Electric-quadrupole coupling between the ionic-core electron and the circular Rydberg electron of an alkaline-earth atom

Andrea Muni

PSL UNIVERSITÉ PARIS

THÈSE DE DOCTORAT
DE L'UNIVERSITÉ PSL

Préparée à l'ÉCOLE NORMALE SUPÉRIEURE
au sein du LABORATOIRE KASTLER-BROSSEL

Electric-quadrupole coupling between the ionic-core electron and the circular Rydberg electron of an alkaline-earth atom

Soutenue par
Andrea MUNI
Le 15 Novembre 2021

École doctorale n° 564
« PHYSIQUE EN ÎLE-DE-FRANCE »

Spécialité
PHYSIQUE QUANTIQUE

Composition du jury :

Prof. Frédéric CHEVY ENS, LKB	*Président*
Dr. Patrick CHEINET Laboratoire Aimé Cotton	*Rapporteur*
Dr. Bruno LABURTHE-TOLRA Laboratoire de Physique des Lasers	*Rapporteur*
Prof. Dr. Christiane KOCH Freie Universität Berlin	*Examinatrice*
Dr. Jérôme LODEWYCK Observatoire de Paris	*Examinateur*
Dr. Sébastien GLEYZES ENS, LKB	*Directeur de thèse*
Dr. Michel POIRIER CEA	*Membre Invité*

COLLÈGE DE FRANCE 1530

Département de Physique
École normale supérieure

ENS ÉCOLE NORMALE SUPÉRIEURE

Laboratoire Kastler Brossel
Physique quantique et applications

PSL RESEARCH UNIVERSITY PARIS

SORBONNE UNIVERSITÉ

A mamma e papá,

e alla mia sorellina Cristina.

CONTENTS

TABLE OF FIGURES

INTRODUCTION

> Indeed it is probable [...] that stellar astronomy and atomic physics are the only sciences which stand higher in popular estimation.
>
> *G.H. Hardy, A Mathematician's Apology.*

Experimental atomic physics is an excellent ground for proof-of-principle investigations. Atoms allow us to push the boundaries of our understanding of fundamental properties of nature. Also, they often represent an ideal platform for the first tests of a new technology.

In this work, we examine some fundamental properties of the circular Rydberg states with high principal quantum number of an alkaline-earth atom, with the long-term goal to use them as the qubits of a Rydberg quantum simulator. More specifically, this work presents three main results. First, we prepare the circular Rydberg states of Strontium (chapters 1, 2). Second, we prove that these circular states are impervious to the autoionization effect when the ionic core of the two-electron atom is excited to a metastable $|4d_{3/2}\rangle$ state (chapter 3). Third, we show that the energy difference between the $|4d_{3/2}\rangle$ states of the ionic-core electron depends upon the state of the circular electron (chapter 4). These experiments pave the way to non-destructive experiments with the Rydberg atoms. Ultimately, we discuss how these three experiments enable us to control the state of the Rydberg electron with a laser pulse.

As an introduction to the dissertation, we briefly go through the recent use of alkaline-earth atoms in many experiments. Next, we explain how our own experiment is connected to that playground and how it brings us closer to the final goal of our research group, being the realization of an efficient Rydberg quantum simulator.

Alkaline-earth Rydberg atoms

Rydberg atoms have remarkable properties. Due to their dipole-dipole interactions and lifetime, both scaling very fast with the principal quantum number n, they have attracted a strong interest.

As a consequence, many research groups started to exploit Rydberg atoms to build quantum technologies [1-5].

Following this intense activity, a number of Rydberg experiments, typically using alkali atoms, achieved important results. Most importantly, those investigations established the Rydberg atoms as front-runners in the realization of quantum technologies within the network of the atomic-molecular-optical (a.m.o.) physics community. However, the strategy to push the boundaries set by those results was soon understood to be the full and precise quantum control of as many individual degrees of freedom of the atoms as possible. Therefore, the a.m.o. physics community looked for ways to improve the control of the atoms, for instance via some quantum control algorithms like the Krotov [6,7] method or dCRAB [8], or for ways to increase the atomic degrees of freedom to be manipulated, resulting in an escalating interest for more complex atoms as compared to Alkali.

Following this evolution, alkaline-earth Rydberg atoms are now the focus of an intense experimental activity [9]. Calcium [10,12] and Strontium [13,17] are the ones that inspired most experiments. Also more complex atoms, Ytterbium [18,19] and Erbium [20] above all, attracted a lot of attention. In the context of alkaline-earth-based optical atomic clocks, dressing with or excitation to Rydberg states open promising perspectives for noise reduction by the preparation of non-classical states of an atomic ensemble [21,22]. The spectroscopy of Rydberg states also provides accurate methods to estimate the systematic shift of these clocks induced by the blackbody radiation or by residual electric fields [23,25]. More importantly, once in the Rydberg state, alkaline-earth atoms feature an optically active ionic core that makes it possible to image [26,27] or trap [28,29] them, opening interesting perspectives for quantum simulation [30,32].

Note that most alkaline-earth experiments exploiting Rydberg atoms so far access low angular-momentum Rydberg states [33,35], for which an excitation of the ionic-core electron quickly leads to autoionization [36,37]. In order to overcome this limit, it is instrumental to increase the angular momentum of the Rydberg electron [28]. Up to now, moderately large-l states have been produced using microwave transfer [38] or Stark switching methods [39,42]. These early studies have evidenced the reduction of the autoionization rate when increasing the principal quantum number of the Rydberg electron but extending these techniques to $n > 10$ is challenging [43].

In contrast with these techniques, the "circularization" would allow us to prepare a "circular" Rydberg state [44,45] with both high principal quantum number n and maximum angular and magnetic quantum numbers, $l = m = n - 1$. Historically, circular states were used extensively to manipulate the microwave fields of superconducting cavities [46]. More recently, they have attracted a broader interest, from cold atom physics [47] to quantum metrology [3,48] or quantum simulation [49]. This enthusiasm for the circular states is motivated by their remarkable

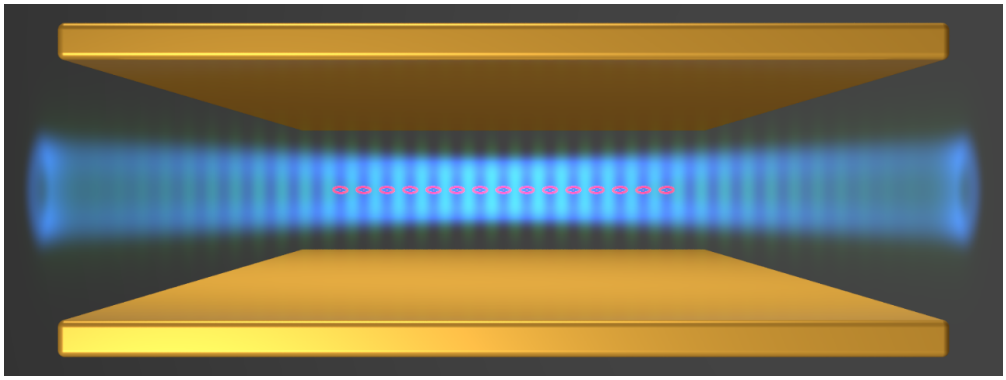

Figure 0.1: Scheme of the quantum simulator [49]. Each Rydberg atom occupies a site of the trapping potential.

properties. For instance, they possess a very long intrinsic lifetime, evolving as n^5 (30 ms for $n \sim 50$). Also, their wavefunction is localized at a large distance from the nucleus. Thus, the outer electron of an alkaline-earth circular state has a very small overlap with the ionic core and the autoionization rate is expected to be extremely low. Consequently, the circular states of alkaline-earth atoms are expected to offer the best protection against autoionization. An early study of the $n = 21$ circular state of Barium has already exhibited reduced autoionization for a core in one of its metastable levels [50]. Their low autoionization rate, combined with their unique properties, explains the interest for circular states of alkaline-earth atoms in recent proposals [30,51].

Our research group shares this interest for alkaline-earth atoms. This is why we recently started a new experiment on Strontium. The perspective is to use this atom as a "workhorse" of a programmable Rydberg quantum simulator, whose realization is the long-term goal of our research group. The choice of Strontium is due to the relatively simple laser excitation of this atom to the Rydberg states. In general, Strontium presents a number of atomic transition frequencies [9, 52, 53] laying within the visible range of the electromagnetic spectrum of light, making it possible to manipulate the atoms with laser beams whose sources are commercially available.

The route towards a Rydberg quantum simulator

The ideal tool to address many-body physics is an analog ‘quantum simulator’ [54, 56], transcribing the dynamics of the system of interest into another one that is under complete experimental control. A number of research groups are pursuing the realization of such a machine [57, 59], some already achieved very interesting results [60, 61].

In our research group as well, we plan to build a quantum simulator based on a chain of

single atoms (figure 0.1) confined close to an axis by a Laguerre-Gauss 'hollow beam' and held in a periodic atomic lattice in the longitudinal direction. The atoms are first excited to the Rydberg states and then circularized. The trapped circular states will ultimately be the qubits of this simulator [62]. Their suitability as qubits is well established by their long lifetimes, that can even be improved in a cryogenic environment by two parallel plates, inhibiting the dominant spontaneous decay channel, the microwave emission towards the lowest circular state. Moreover, the large dipole matrix element between circular levels makes them particularly sensitive to dipole-dipole interactions.

This simulator would allow us to study a spin-1/2 XXZ chain Hamiltonian, where the role of spin-up and spin-down states would be played by two circular states with $n \sim 50$. Their energy difference is within decades of GHz ($\sim$ 105.3 GHz between $|51c\rangle$ and $|49c\rangle$) and accessible via commercially available microwave sources.

An important advantage of the quantum simulator exploiting circular states would be the full tunability of its parameters. The Ising coupling J_z between the spins would be set by moderate applied electric and magnetic fields, the Rabi frequency Ω between the circular states would depend on the frequency of a microwave field driving the transition between the two circular states. Governing these parameters would allow us to tune the spin chain so as to emulate the behaviour of several "exotic" phases of matter (figure 0.2), like Neel phases ($N_{y,z}$), Luttinger liquids, ferromagnetic structures (F) or long-range-order phases (P_x) and thus to explore, with this atomic physics system, some fundamental problems of condensed matter physics.
However, a quantum simulator using Rubidium would suffer from a destructive detection of the Rydberg states. This is usually performed by ionizing all the atoms together and associating the ionization field to the quantum state of the atoms. Even accepting a destructive detection, the simulator would still be strongly limited by two heating mechanisms of the spin chain, both potentially causing a leak of the atom from its trap. One derives from the coupling between the spin exchange of an atom and its motion in the trap. When flipping the spin state of an atom, its interaction with its neighbours, hence its position of equilibrium in the trap, changes and the atom starts oscillating in the trapping potential. When extending this mechanism all over the spin chain, a heating process arises. The second heating mechanism is parametric heating. This is caused by the intensity noise of the laser beams forming the trapping potential that confines the atoms in the optical lattice, which becomes relevant at a timescale comparable with the lifetime of the circular states.

Both the problem of the destructive detection of the Rydberg state and that of heating can be overcome when working with an alkaline-earth atom as a platform for the qubits. One can then exploit the two electrons in the outer filled shell. With one electron excited to a circular

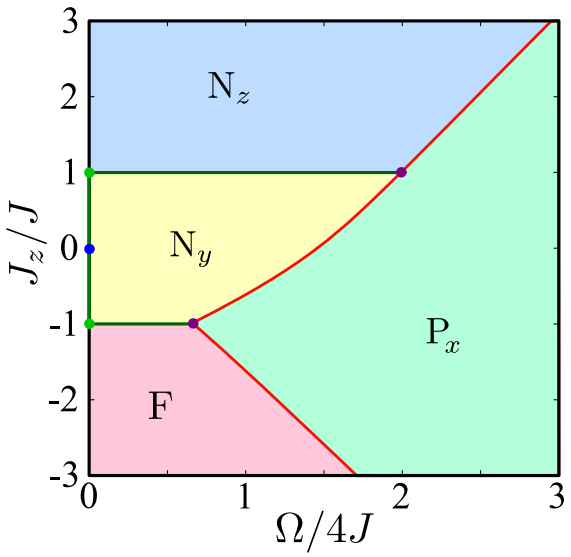

Figure 0.2: Phase diagram of the chain Hamiltonian dressed by the MW [49].

Rydberg state with large enough radius, the physics of the remaining valence electron can be well approximated with that of the Sr^+ ion, hence the chance to work on the ionic core as on a simple ion. One can therefore import the experimental techniques [10, 63] developed for the manipulation of ions into the Rydberg community, like cooling or detection protocols.

As for detection, for instance, the ionic-core electron can be used as a fluorescent, non-destructive probe of the circular state of the other valence electron. The fluorescence is a consequence of the spontaneous decay between two quantum states of the ionic core. The non-destructive nature of this experiment is based on the fact that the optical excitation of one valence electron preserves the circular Rydberg state of the other valence electron, due to the weak autoionization of the electron-electron system. The optical resonance of the ionic core would also allow one to apply standard laser cooling schemes and thus fight efficiently the heating sources of the spin chain.

The implementation of all these improvements for the Rydberg quantum simulator must overcome some difficulties. First, there is that of preparing the circular Rydberg states of Strontium. Second, one must prove that the circular states are impervious to the autoionization effect. Finally, before the implementation of Strontium in the quantum simulator, it is of paramount importance to have a full understanding of the physics of two-electron atoms. It is therefore critical to study the electron-electron interaction between the valence electrons when one is circularized. All these challenges are tackled and solved in this work.

The organization of this work

This work is organized in four chapters, six appendixes, a conclusion and a bibliography.

Chapter 1 is about the theory behind the physics of Rydberg atoms. The dissertation starts from the simple case of Hydrogen. We first discuss the structure of its energy levels and how they are affected by the interaction with a static electric field or a radio-frequency field. Next, we formally introduce the technique of "circularization", being the transfer from a low-l Rydberg state to the circular state of the same manifold. As a second step, we study Rubidium, which presents a more complex core. This last fact requires that we adapt the Hydrogen model in order to understand the energy levels of the Alkali atom. We also explain the extension of the circularization process, introduced for Hydrogen, to Rubidium. Finally, we increase again the complexity of the problem by discussing the Rydberg-excited Strontium atom. Its energy-level structure displays a stronger discrepancy with respect to that of Hydrogen. Moreover, the presence of two electrons requires the introduction of the physics of spins, thus the distinction between singlet and triplet Rydberg states.

Chapter 2 is about the preparation of the circular Rydberg states of Strontium. We first discuss the experimental set-up and next present the experimental results. The circularization is explained step-by-step, starting from the three-photon Rydberg excitation of Strontium to a low-l state, passing through the transfer of the population from a low-l state to the circular state by a radio-frequency pulse and arriving to the detection of that circular state via microwave probes.

Chapter 3 discusses the autoionization effect for a Rydberg-excited Strontium atom. We prove that this effect does not take place if one of the two valence electrons is excited to the circular Rydberg state and the other valence electron is in a metastable $|4d_{3/2}\rangle$ or $|4d_{5/2}\rangle$ state.

Chapter 4 explains some optical manipulations enabling us to quantify the energy difference between the sub-levels of the $|4d_{3/2}\rangle$ states of the ionic core and to show that that energy difference depends on the principal and magnetic quantum numbers of the Rydberg electron. We show that the degeneracy lifting among the $|4d_{3/2}\rangle$ states is caused by the electric-quadrupole term of the multipole expansion of the electron-electron potential governing the interaction between the valence electrons. This experiment leads us to a Ramsey experiment where we control the state of the Rydberg atom with a laser pulse.

The appendices of this work complement the experiments presented in the four chapters. Appendix A shows that our Rydberg excitation concerns only the isotope ^{88}Sr, with zero nuclear spin, so that we work with quantum states whose angular momenta are not affected by the hyperfine coupling with the nuclear spin. Appendix B presents the preparation of a circular

state via an adiabatic passage. Appendix C is an insight on a laser spectroscopy experiment aimed at identifying the resonance frequencies of the laser beams exciting the ionic-core electron. Appendix D complements chapter 3 by showing how to calibrate some microwave pulses enabling us to distinguish between singlet and triplet states of Strontium. Appendix E attaches to chapter 4 the calibration of a short optical pulse exciting the ionic-core electron. Appendix F presents an experiment allowing us to associate an elliptical Rydberg state with the duration of the radio-frequency pulse which leads to its preparation.

The conclusion summarizes the main results of this work, explains why the achievements presented in this doctoral thesis will be important for the realization of the next generation quantum simulator and also presents some short-term perspectives for the experiment to be pursued in the next years.

Note on the outreach activity

This Ph.D. program has received full support from the European Union's Horizon 2020 grant agreement (QuSCo project). Following the guidelines of the project, an intense outreach activity, aiming to encourage young students to join the STEM community during their careers, complemented the experimental results exposed in this work. A portfolio of the outreach items produced under the supervision of the experts from Aarhus University, Denmark, is available here: https://qusco-itn.eu/outreach-3/.

CHAPTER 1

RYDBERG ATOMS

> Mathematics is the art of assigning the same name to different realities.
>
> *Prof. Henri Poincaré*

The Rydberg states of an atom are electronically, highly excited states where the electron perceives only a Coulomb potential from the core. The name derives from Johannes Rydberg, who finds, in 1888, a formula describing the energies of Hydrogen,

$$\frac{1}{\lambda} = R_H\left(\frac{1}{n_1^2} - \frac{1}{n_2^2}\right), \quad n_2 > n_1, \tag{1.1}$$

where λ is the wavelength of the radiation emitted in vacuum, R_H indicates the Rydberg constant for the same atom and n_1, n_2 are the principal quantum numbers of two given energy levels. In general, we address as Rydberg atoms those with the most hydrogenic structure. For them, this formula can be applied as a very first approximation to calculate the energy of the quantum states with very high principal quantum number n. This motivates the definition of Hydrogen as the ideal Rydberg atom. Besides this, the alkali atoms are also suitable candidates for such a title, since they all present one valence electron only. Another fitting choice is an atom belonging to the alkaline-earth set, if one of the two outer electrons is in its ground state and the other is promoted to a very excited one. Given the similarities with Hydrogen, the physics of Rydberg atoms is tackled through the Hydrogen model [64].

In this chapter, we present the Hydrogen model and its extension to the more intricate physics of the Rydberg-excited Strontium. The exposition of such an apparently long jump proceeds gradually throughout the text. After investigating the picture of the Hydrogen atom, we step on the

simpler case of the alkali atoms, with particular attention devoted to Rubidium, and use such a passage as a basis of the analysis pursuing Strontium.

This chapter is therefore split in three sections. Sec. 1.1 presents the model of the Hydrogen atom. We first introduce the wavefunction Ψ_{nlm} and the set of discretized energies E_n predicted by the Schrödinger equation. Next, we study the action of a static electric field on these energy levels, the "DC Stark effect" (paragraphs 1.1.1 - 1.1.2) [65, 66]. Finally, we detail the picture of spin-coherent-states to describe the set of energy levels and introduce a general method of preparation of circular Rydberg states (paragraphs 1.1.3 - 1.1.7). Sec. 1.2 discusses the extension of the Hydrogen model to the alkali atoms. We present a correction term to the Hydrogen energies to model the energy levels of Rubidium with high-n (paragraph 1.2.1). We use this model to briefly investigate the Stark effect and the circularization of Rubidium (paragraphs 1.2.2 - 1.2.3). Sec. 1.3 concludes the chapter. There, we broaden our vision to the physics of Strontium. We describe its Hamiltonian and the implications of working with an alkaline-earth atom, featuring two electrons in the last filled shell. This leads us to include the spin in the treatment of the Hamiltonian. We therefore discuss the exchange energy and the spin-orbit coupling (paragraphs 1.3.1 - 1.3.5) terms of the spin Hamiltonian and see how they affect the energy levels. A brief analysis of the Stark effect for Strontium concludes the section (paragraph 1.3.6).

1.1 The Hydrogen atom

1.1.1 The wavefunction Ψ_{nlm} and the eigenvalues E_n

We begin this work with a brief discussion of the Hydrogen model. For the Hydrogen atom, the stationary Schrödinger equation reads

$$\hat{H}_0\Psi = E\Psi, \tag{1.2}$$

where $\hat{H}_0$ is the Hamiltonian of the atom and E the eigenvalues of the equation, i.e. the set of available energies for the electron. Among these, we ignore those laying in the continuum. We express $\hat{H}_0$ as

$$\hat{H}_0 = \frac{\hat{P}^2}{2\mu} + \hat{V}(\mathbf{r}). \tag{1.3}$$

Here, $\hat{P}^2/2\mu$ indicates the kinetic term, with $\hat{P}$ being the momentum and μ the reduced mass of the electron, whereas $\hat{V}$ represents the Coulomb potential governing the interaction between the proton and the electron. It is a function of the space vector $\mathbf{r}$ describing the distance between the two. The solution Ψ_{nlm} is factorized as

$$\Psi_{nlm} = R_{nl}(r)Y_{lm}(\theta,\phi), \tag{1.4}$$

where $R_{nl}(r)$ indicates the radial component and $Y_{lm}(\theta,\phi)$ stands for the spherical harmonics defining the angular component and dependent upon the spherical coordinates θ,ϕ. Here, n,l,m are the principal, angular and magnetic quantum numbers respectively. They obey the well-known selection rules

$$0 \leq l \leq n-1, \quad -l \leq m \leq +l. \tag{1.5}$$

These wavefunctions are eigenstates of $\{\hat{L}^2,\hat{L}_z\}$, where $\hat{\mathbf{L}}$ is the operator of the angular momentum and $\hat{L}_z$ is its component along the $\mathbf{z}$ axis. The discretized set E_n of energies available for the electron reads

$$E_n = -\frac{\mu c^2 \alpha^2}{2n^2} = -\frac{hcR_H}{n^2}, \tag{1.6}$$

where c is the speed of light, $\alpha \sim 1/137$ is the fine structure constant and h indicates the Planck's constant. Notably, the energy levels depend only on the positive integer n.

1.1.2 The interaction with a static electric field

We consider the perturbation induced when applying a static electric field. This is taken into account by an additional term in the Hamiltonian,

$$\hat{H}_{St} = \hat{\mathbf{d}} \cdot \mathbf{F}, \tag{1.7}$$

where $\hat{\mathbf{d}}$ is the electric-dipole operator and $\mathbf{F}$ is the electric field vector. In this context, the Hamiltonian is unsolvable but with perturbation theory. This technique yields a set of eigenvalues

$$E = E_0 + E_{st}^{(1)} + E_{st}^{(2)} + o(F^3), \tag{1.8}$$

where E_0 is the energy of an unperturbed atom and $E_{st}^{(i)}$ are the correction factors describing the effect of the electric field. They are named linear and quadratic Stark effects respectively,

$$E_{St}^{(1)} = -\frac{3ea_0}{2} n(n_1-n_2)F, \quad E_{St}^{(2)} = -\frac{(ea_0F)^2}{32E_{R_H}} n^4(17n^2 - 3(n_1-n_2)^2 - 9m^2 + 19), \tag{1.9}$$

where E_{R_H} is the ground state energy of the Hydrogen atom, F is the amplitude of the electric field, $e>0$ is the elementary charge and a_0 the Bohr radius. To describe such a new energy level set, we make use of a parabolic basis $|n,n_1,n_2\rangle$, where n_1 and n_2 are the parabolic quantum numbers. Another equivalent choice may be $|n,n_1,m\rangle$. Note that, unlike l, m is still a good quantum number. We have the relations

$$n = n_1 + n_2 + |m| + 1, \quad 0 \leq n_1 \leq n-1, \quad 0 \leq n_2 \leq n-1. \tag{1.10}$$

From (1.9), we infer that a static electric field lifts the degeneracy of the quantum states with different m. The separation between these levels increases with the amplitude of the electric

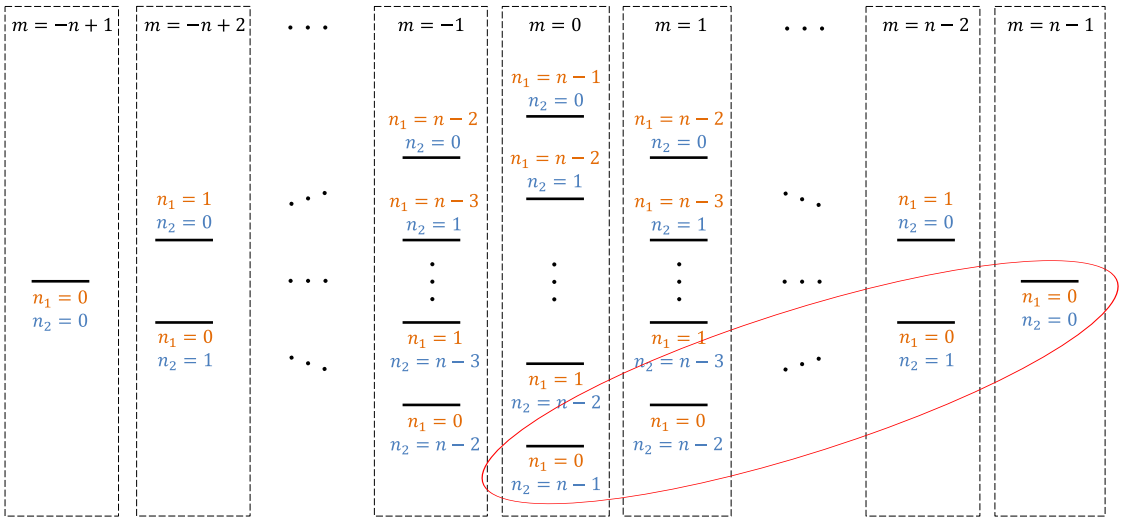

Figure 1.1: Manifold of Rydberg states sharing the same principal quantum number n and undergoing the interaction with a static electric field. All levels are organized from left to right according to the magnetic quantum number m, ranging from $1-n$ to $n-1$. The number of levels associated to the same m is $n-|m|$. The distinction between them is performed either by n_1 or n_2 depending on the choice of the preferred basis. This image is taken from [67].

field.

Figure 1.1 shows the Stark diagram for a given manifold, i.e. the distribution of the energy levels with same n but different n_1, n_2 and m, when they undergo the interaction with a static electric field. Each quantum state is labelled via the set of quantum numbers $|n,n_1,m\rangle$ or $|n,n_1,n_2\rangle$. The manifold has a diamond shape and contains n^2 states. Among these, the set of states with $n_1 = 0$, composing the lowest-right diagonal, are of particular interest for us. They are equidistant between each other and coupled via $\sigma+$ polarized photons. We define the angular, Stark frequency ω_{St} as the spacing, in units of $\hbar = h/2\pi$, between two of these consecutive states. This quantity is in the radio-frequency domain for the range of values of n under interest ($n \sim 50$). More precisely, around $\omega_{St}/2\pi = 100$ MHz for an electric field of 1 V/cm.

At the end of the ladder, we find the state with maximum m. Due to the peculiar, toroidal shape of its wavefunction, we refer to it as the "circular" Rydberg state. We use the notation $|nC\rangle$ to express the circular state of the manifold with principal quantum number n. Given its very high $|m|$, this state cannot be prepared by laser excitation only. A possible strategy is to access by laser a low-m Rydberg state and to apply a radio-frequency field to transfer the quantum population to the circular state of the same manifold.

1.1.3 The Laplace-Runge-Lenz labelling of Stark states

We define here an alternative representation of the parabolic basis: the Laplace-Runge-Lenz (LRL) representation. This is of particular interest to model the interaction of Hydrogen with a static electric field in a more intuitive way, but also completely equivalent from a physical point of view. On top of that asset, the LRL representation also allows one to efficiently study the interaction between the atom and a radio-frequency field.

The LRL representation makes use of the so-called "ladder operators", $\hat{\mathbf{J}}_1$ and $\hat{\mathbf{J}}_2$, defined as

$$\hat{\mathbf{J}}_1 = \frac{\hat{\mathbf{L}} - \hat{\mathbf{a}}}{2}, \quad \hat{\mathbf{J}}_2 = \frac{\hat{\mathbf{L}} + \hat{\mathbf{a}}}{2}. \tag{1.11}$$

where $\hat{\mathbf{L}}$ is the angular momentum operator and $\hat{\mathbf{a}}$ is the the normalized Laplace-Runge-Lenz operator,

$$\hat{\mathbf{a}} = \sqrt{-2\mu E_n}\left(\frac{1}{2}\left[\hat{\mathbf{p}} \times \hat{\mathbf{L}} - \hat{\mathbf{L}} \times \hat{\mathbf{p}}\right] - \mu K \frac{\hat{\mathbf{r}}}{r}\right) = \sqrt{-2\mu E_n}\,\hat{\mathbf{A}}. \tag{1.12}$$

Here, K is the strength of the central force, equal to $e^2/4\pi\epsilon_0$ for the Coulomb force, where ϵ_0 is the dielectric constant in vacuum, and $\hat{\mathbf{A}}$ is the un-normalized LRL operator. This is associated to the classical LRL vector $\mathbf{A}$, which is a conserved physical quantity for a particle interacting with a potential of symmetry $1/r$. Furthermore, inside a given manifold, it is related to the position operator $\hat{\mathbf{r}}$ through the Pauli replacement

$$\hat{\mathbf{r}} = \frac{-3\pi a_0 n}{h}\hat{\mathbf{a}}. \tag{1.13}$$

This is an instrumental result to mathematically relate the ladder operators with the Cartesian components of the position operator. For example, it allows us to express the Stark Hamiltonian in terms of the ladder operators, as

$$\hat{H}_{St} = \frac{h\omega_{St}}{2\pi}\left(\hat{J}_{1,z} - \hat{J}_{2,z}\right). \tag{1.14}$$

Here, we have used $\hat{J}_{i,z}$ to indicate the component of the i_{th} ladder operator along the $\mathbf{z}$ axis.

The mathematics of the ladder operators is very insightful. Inside a given manifold, $\{\hat{J}_1^2, \hat{J}_{1,z}, \hat{J}_2^2, \hat{J}_{2,z}\}$ form a complete set of independent observables. Also, $\hat{J}_1^2$ and $\hat{J}_2^2$ are constant, for a given n, and equal to $(n-1)/2$. Basing on this, we can use the ladder operators as our preferred representation of the parabolic basis, which is equivalent to that presented in sub-section 1.1.2 but provides a more geometric visualization of the eigenstates of the Hydrogen atom. Thus, the energy levels of Hydrogen can be represented as $|j_1, m_1, j_2, m_2\rangle$, where $\hbar m_1$ and $\hbar m_2$ are the eigenvalues of $\hat{J}_{1,z}$ and $\hat{J}_{2,z}$ respectively. Mathematically, the passage from $|n, n_1, n_2\rangle$ to $|n, m_1, m_2\rangle$ is done by imposing

$$\begin{cases} n_1 = \frac{n-1}{2} + m_1 \quad if \quad m \leq 0 \\ n_2 = \frac{n-1}{2} + m_2 \end{cases} \tag{1.15}$$

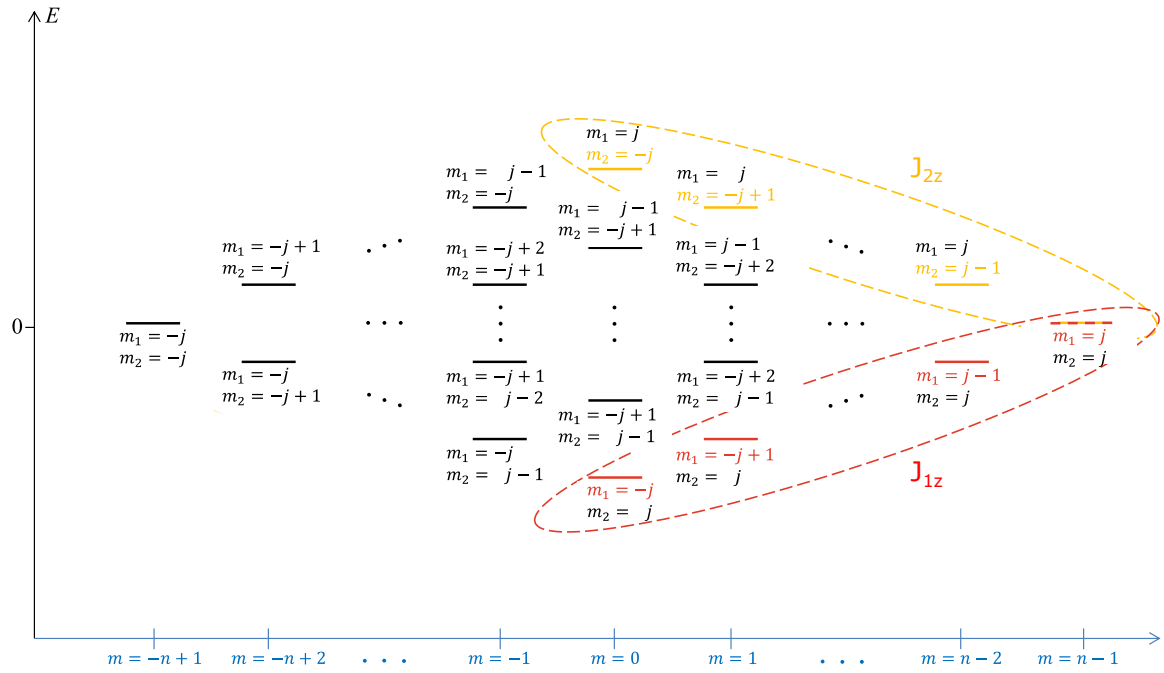

Figure 1.2: Manifold of Rydberg states labelled by use of the Laplace-Runge-Lenz representation.

$$\begin{cases} n_1 = \frac{n-1}{2} - m_2 \quad if \quad m \geq 0 \\ n_2 = \frac{n-1}{2} - m_1 \end{cases}$$

and solving such a system to find m_1 and m_2. Figure 1.2 shows the same manifold already presented in figure 1.1 but with the energy levels labelled via the new set of quantum numbers $|n, m_1, m_2\rangle$.

1.1.3.1 Conversion from the parabolic to the spherical basis

It is instrumental to define the passage from the parabolic basis $|n, m_1, m_2\rangle$ to the spherical basis $|n, l, m\rangle$. This conversion is done by using the algebra of coupling of angular momenta via Clebsch-Gordan coefficients as,

$$|n, l, m\rangle = \sum_{m_1} \sum_{m_2} |n, m_1, m_2\rangle \langle j_1 m_1 j_2 m_2 | j_1 j_2 l m\rangle \tag{1.16}$$

1.1.4 Interaction with a radio-frequency field

We include in the analysis the interaction with a radio-frequency field of frequency ω_{rf} and phase ϕ. This is modelled in the Hamiltonian by the term $\hat{V}_{rf}$. We express it in the form

$$\hat{V}_{rf} = -e\mathbf{F}_{rf} \cdot \mathbf{r}, \tag{1.17}$$

where $\mathbf{F}_{rf}$ describes the electric field vector of the radio-frequency field. It is decomposed into the sum of a σ+ and a σ- polarized component,

$$\mathbf{F}_{rf}(t) = \mathbf{F}^{+}_{rf}(t) + \mathbf{F}^{-}_{rf}(t), \tag{1.18}$$

where we have used t to indicate the time parameter and

$$\mathbf{F}^{\pm}_{rf}(t) = \frac{1}{2} A^{\pm}_{rf} \left[(\mathbf{u}_x \mp i\mathbf{u}_y) e^{i(\omega_{rf} t + \phi)} + (\mathbf{u}_x \pm i\mathbf{u}_y) e^{-i(\omega_{rf} t + \phi)} \right]. \tag{1.19}$$

We have used the notation $\mathbf{u}_i$ to indicate the unit vector along the $\mathbf{i}$ axis and the letters $A^{\pm}_{rf}$ for the amplitudes of the field. When we insert the two components $\mathbf{F}^{\pm}_{rf}(t)$ into (1.18) and next include $\mathbf{F}_{rf}(t)$ into (1.17), we obtain two contributions to the Hamiltonian term $\hat{V}_{rf}$, being

$$\hat{V}_{rf} = \hat{V}^{+}_{rf} + \hat{V}^{-}_{rf}, \tag{1.20}$$

where

$$\hat{V}^{\pm}_{rf} = \frac{1}{2} e A^{\pm}_{rf} \left[(\hat{\mathbf{x}} \mp i\hat{\mathbf{y}}) e^{i(\omega_{rf} t + \phi)} + (\hat{\mathbf{x}} \pm i\hat{\mathbf{y}}) e^{-i(\omega_{rf} t + \phi)} \right]. \tag{1.21}$$

We can express $\hat{V}^{\pm}_{rf}$ in terms of the Cartesian components of the ladder operators $\hat{J}^{\pm}_1 = \hat{J}_{1,x} \pm \hat{J}_{1,y}$, $\hat{J}^{\pm}_2 = \hat{J}_{2,x} \pm \hat{J}_{2,y}$ via the Pauli replacement, as

$$\hat{V}^{\pm}_{rf} = \frac{1}{2} \Omega^{\pm}_{rf} \left[(\hat{J}^{-}_1 - \hat{J}^{-}_2) e^{\pm i(\omega_{rf} t + \phi)} + (\hat{J}^{+}_1 - \hat{J}^{+}_2) e^{\mp i(\omega_{rf} t + \phi)} \right], \tag{1.22}$$

where we define $\Omega^{\pm}_{rf}$ as the Rabi frequencies associated to the radio-frequency field

$$\Omega^{\pm}_{rf} = \frac{3\pi e a_0 n}{h} A^{\pm}_{rf}. \tag{1.23}$$

In the condition of resonance between states with same n and consecutive m numbers and the radio-frequency field, thus $\omega_{rf} = \omega_{St}$, equation (1.22) is simplified,

$$\hat{V}^{+}_{rf} = \frac{1}{2} \Omega^{+}_{rf} \left[\hat{J}^{+}_1 e^{-i(\omega_{rf} t + \phi)} + \hat{J}^{-}_1 e^{+i(\omega_{rf} t + \phi)} \right], \tag{1.24}$$

$$\hat{V}^{-}_{rf} = \frac{1}{2} \Omega^{-}_{rf} \left[\hat{J}^{+}_2 e^{+i(\omega_{rf} t + \phi)} + \hat{J}^{-}_2 e^{-i(\omega_{rf} t + \phi)} \right],$$

from which it is clear that a σ+ (σ-) polarized, radio-frequency field couples neighboring states with $\Delta m = +1$ ($\Delta m = -1$) (figure 1.3). The radio-frequency field therefore needs to satisfy two requirements to successfully transfer the population from one quantum state to another: the resonance with the Stark frequency of the ladder and a σ+ (σ-) polarization.

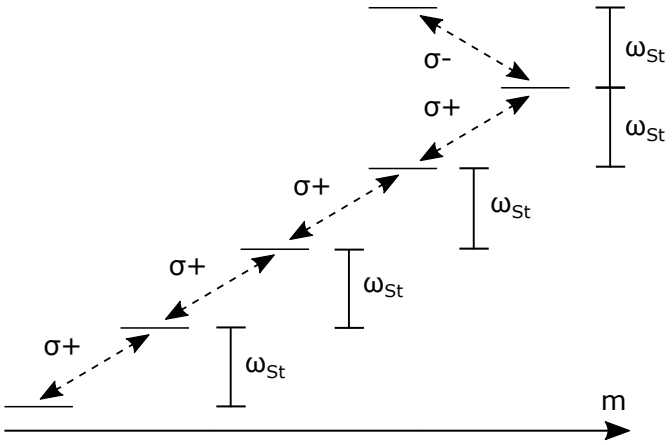

Figure 1.3: Coupling between the ladder of Rydberg states and a resonant radio-frequency field. The polarization σ+ enables to couple neighboring states of the ladder, whereas a σ- polarization allows to couple a given m state with the upper neighbor with lower m.

1.1.5 Spin-coherent-states

The complete Hamiltonian of the Hydrogen atom is the sum of all the terms presented to this point,

$$\hat{H} = \hat{H}_0 + \hat{H}_{St} + \hat{V}_{rf}^{+} + \hat{V}_{rf}^{-}. \tag{1.25}$$

In the latter expression, we distinguish two components of the Hamiltonian, $\hat{H}_1$ and $\hat{H}_2$, and express them in the rotating frame at the radio-frequency ω_{rf}. We write

$$\tilde{\hat{H}}_1 = \frac{h\Delta}{2\pi}\hat{J}_{1,z} + \frac{\Omega_{rf}^{+}}{2\pi}\Big[i\hat{J}_1^{+}e^{i\phi} - i\hat{J}_1^{-}e^{-i\phi}\Big]. \tag{1.26}$$

The term $\tilde{\hat{H}}_2$ is similarly defined by use of the ladder operator $\hat{\mathbf{J}}_2$. We have introduced the detuning Δ between the radio-frequency field and the spacing of consecutive m states of a given manifold. Notably, the terms $\tilde{\hat{H}}_1$ and $\tilde{\hat{H}}_2$ depend on the ladder operators $\hat{\mathbf{J}}_1$ and $\hat{\mathbf{J}}_2$ respectively. They therefore act on different Hilbert spaces and are independent from each other. In this work, we consider, from now on, the only term $\hat{H}_1$, which couples to σ+, radio-frequency fields.

We set Δ to zero to the obey the resonance condition. This simplifies (1.26) into

$$\tilde{\hat{H}}_1 = \Omega_{rf}^{+}\Big[-\sin(\phi_1)\hat{J}_{1,x} + \cos(\phi_1)\hat{J}_{1,y}\Big]. \tag{1.27}$$

The evolution operator corresponding to this Hamiltonian, after a certain interaction time T_{int} between the radio-frequency field and the atom, is the rotation operator

$$\hat{R}_1 = e^{-\frac{i}{\hbar}\tilde{\hat{H}}_1 t} = e^{\frac{i}{\hbar}\theta_i\hat{\mathbf{J}}_1\cdot\mathbf{n}_1} = e^{\frac{-i\theta_i}{\hbar}\Big[-sin(\phi_1)\hat{J}_{1,x}+\cos(\phi_1)\hat{J}_{1,y}\Big]}, \tag{1.28}$$

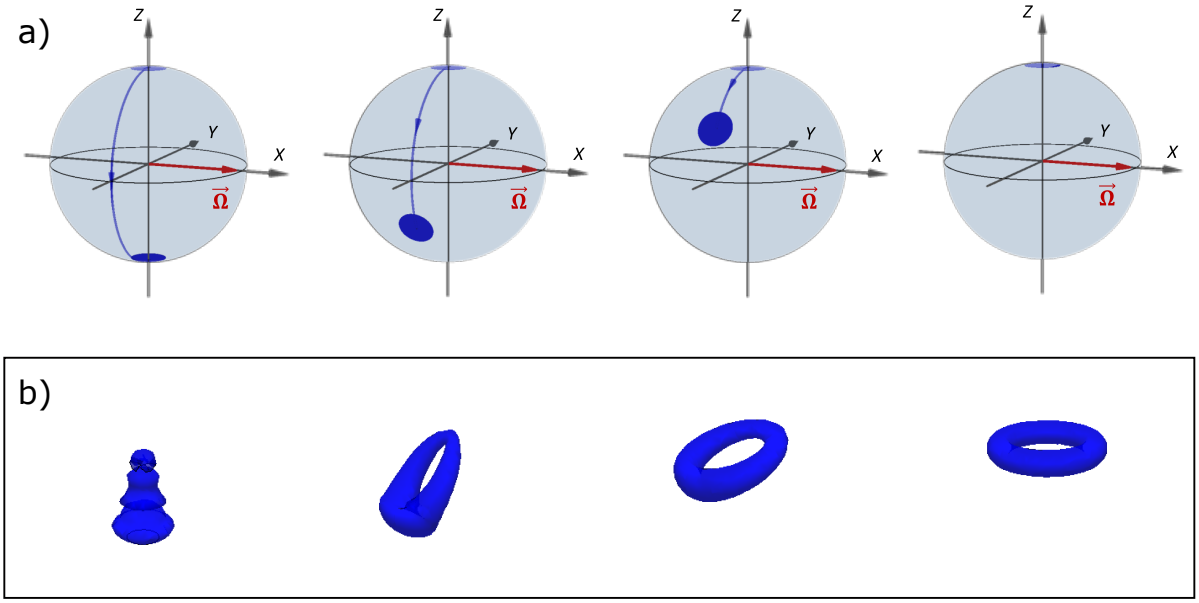

Figure 1.4: a) Spin-coherent-states on the Bloch sphere. We have spin-coherent-states with higher m components when proceeding from left to right. The one on top right is centered on the circular Rydberg state. b) Wavefunction associated to the spin-coherent-state represented in the upper panel. This image is taken from [68].

where $\theta_1 = \Omega_{RF}^{+} T_{int}$ is the rotation angle and $\mathbf{n}_1 = (-\sin\phi_1, \cos\phi_1, 0)$ is the rotation axis. When applied on a state $|j_1, m_1\rangle$, the rotation operator produces a spin-coherent-state $|\theta_1, \phi_1\rangle$ composed by a a superposition of independent states $|j_1, m_1\rangle$, each weighted by the coefficient c_{m_1},

$$|\theta_1,\phi_1\rangle = \sum_{m_1=-j_1}^{j_1} c_{m_1} |j_1, m_1\rangle, \quad c_{m_1} = \sqrt{\binom{2j_1}{j_1+m_1}} \cos\left[\frac{\theta_1}{2}\right]^{j_1+m_1} \sin\left[\frac{\theta_1}{2}\right]^{j_1-m_1} e^{i(j_1-m_1)\phi_1} \tag{1.29}$$

1.1.6 The preparation of the circular Rydberg state

The action of $\hat{R}_1$ on a quantum state can be visualized through the "generalized Bloch sphere" model. This derives from the common Bloch sphere picture. There, the state of a two-level system is indicated by a Bloch vector. The ground state of such a system is located at the south pole, the excited state at the north pole.

The generalized Bloch sphere can be used for systems with multiple excited states, each associated to an horizontal layer. Within this playground, we consider an atom initially prepared in the quantum state located at the south pole of the sphere, noted as $|j_1, m_1 = -j_1\rangle$, and apply $\hat{R}_1$ on it. Its action makes the Bloch vector perform a rotation, thus producing a spin-coherent-state $|\theta_1, \phi_1\rangle$. Notably, a rotation of $\theta_1 = 2\pi$ returns the population to the initial state, whereas, when

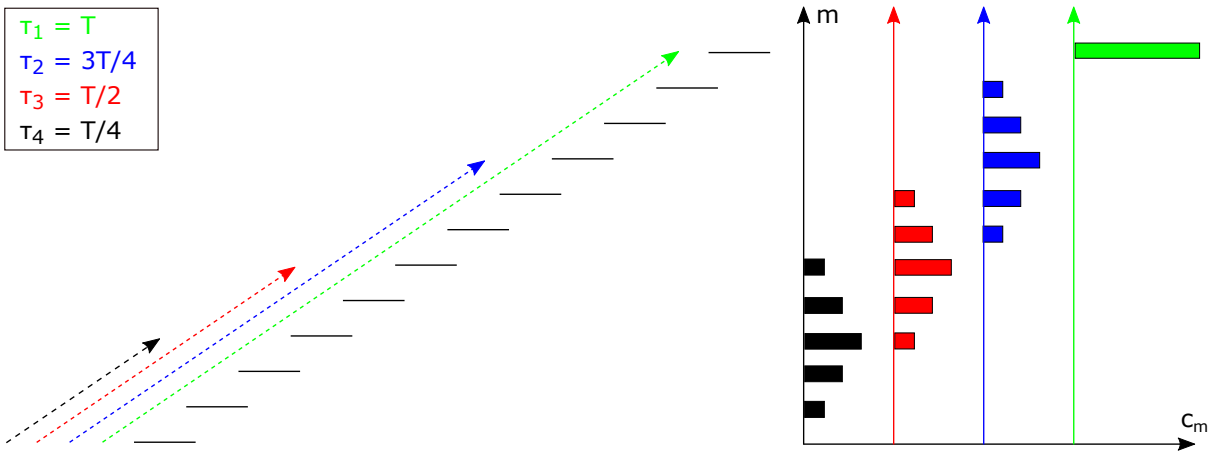

Figure 1.5: Evolution of the population, initially laying in a low-m state of a given manifold, as a function of the duration of a σ+, rf pulse. Each radio-frequency pulse is associated to a duration τ_i, determining the composition of the spin-coherent-state produced. Here, we sketch the preparation of four spin-coherent-states, each centered on a different point of the ladder and associated to a different radio-frequency event. The optimal circularization, associated to an optimal duration T of the rf pulse (π pulse), is given by the green arrow.

$\theta_1 = \pi$, the operator $\hat{R}_1$ centers the resulting spin-coherent-state on the north pole of the Bloch sphere, where the circular Rydberg state lays. This case is of special interest for us. We refer to it as "circularization" (figure 1.4).

The action of the rotation operator can be observed also when discussing the evolution of the population on a manifold of states with same n. We consider a purely σ+ polarized, pulsed, radio-frequency field and the population concentrated on a low-m state of preference. The action of $\hat{R}_1$ is mediated by the radio-frequency field, which moves the atoms away from the given level along the ladder (figure 1.5). The duration and the amplitude of the radio-frequency pulse impose the range of m states present in the final spin-coherent-state, as it determines the rotation angle when considering the Bloch sphere model. Hence, the circularization involves dragging the population until the end of the ladder, where the atoms acquire the maximum magnetic quantum number. This happens for a specific duration of the radio-frequency pulse. A longer pulse causes the atoms to leave the circular state, descending the ladder while revisiting the same states they encountered during the climb.

1.2 Alkali atoms: the Rubidium atom

The Hydrogen model provides us with a very elementary version of the Hamiltonian of more complex, Rydberg-excited atoms. We focus here on its extension to the alkali atoms. The price to pay is taking into account a more complex core than one composed by a single proton. This is

done by introducing a correction factor, named quantum defect, in the formula for the atomic energies at zero electric field. Among the alkali atoms, the case-of-study concerned in this section is Rubidium. Both experiments and theoretical studies solidly confirmed the suitability of the quantum defect theory to model its quantum states.

1.2.1 The quantum defect

The quantum defect is introduced as a dimensionless term $\delta(n,l,J)$ in the denominator of E_n, representing the discrepancy between the energies of a given Rydberg-excited atom and the counterparts in Hydrogen. The equation (1.6) is therefore transcribed in

$$E_{n,l,J} = -\frac{R_H}{\big(n-\delta(n,l,J)\big)^2}. \tag{1.30}$$

As a first approximation, the quantum defect depends on l. It follows that the degeneracy between l states belonging to the same manifold is lifted. Then, it is also sensitive to the fine structure of the atom, hence the dependency on the quantum number J. This derives from the operator $\hat{\mathbf{J}} = \hat{\mathbf{L}} + \hat{\mathbf{S}}$, where $\hat{\mathbf{S}}$ is the spin operator and $\hat{\mathbf{J}}$ is the total angular momentum operator, for an atom with one valence electron only in the outer shell. An approximate expression of the quantum defect reads

$$\delta(n,l,J) = \delta_0 + \frac{\delta_2}{(n-\delta_0)^2}. \tag{1.31}$$

The term δ_0 is a constant in first approximation, whereas δ_2 accounts for the small variation of δ as a function of n. For the Rubidium atom, these parameters are measured for the levels characterized by $l < 7$. All the other Rydberg states, with higher angular quantum numbers, are considered as degenerate at zero electric field. Table 1.1 reports the state-of-the-art quantum defect of the Rydberg states of Rubidium [69].

Table 1.1: Quantum defects of the Rubidium atom for the Rydberg states with $n > 20$.

l	δ_0	δ_2	l	δ_0	δ_2
0	3.131145	0.195	3 (J = 5/2)	0.0165192	-0.085
1 (J = 1/2)	2.65486	0.280	3 (J = 7/2)	0.0165437	-0.086
1 (J = 3/2)	2.64165	0.318	4	0.004	0
2 (J = 3/2)	1.34807	-0.603	5	0.001	0
2 (J = 5/2)	1.34642	-0.545	6	0.0006	0

1.2.2 The numerical simulation of Stark diagrams

We discuss here the method to evaluate numerically the Stark effect of the Rydberg levels of Rubidium [70]. This is based on the numerical diagonalization of the Rubidium Hamiltonian.

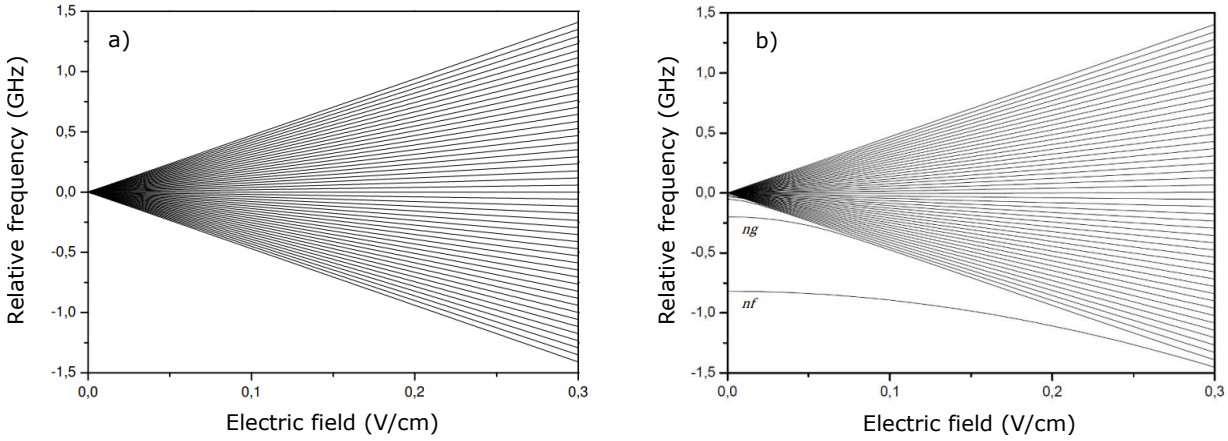

Figure 1.6: Stark diagrams of the $n = 51$ manifold of Rydberg states for Hydrogen (a) and Rubidium (b). We plot the states with $m = 2$ only. All energies are scaled so as to have the energy of the circular Rydberg state with $n = 51$ as zero. This image is taken from [71].

We are interested in the Stark effect of a given manifold of states, with $n = 51$. We set a minimum $n_{min} = 30$ and a maximum $n_{max} = 70$ for the principal quantum numbers, in order to assign a finite dimension to our Hilbert space and the Hamiltonian matrix. Also, we implement a list of quantum defects for all values of $l < 7$ and a frequency window Δf. We consider the contribution of the only states within $\pm\Delta f$ around the central manifold with $n = 52$. We choose Δf large enough so that the Stark effect becomes independent of Δf, thus that the calculated energies vary by less than 1 MHz if we increase Δf further. Typically, we need to consider eight manifolds (four above, four below) around the one whose Stark effect is simulated. This implies a final value of $\Delta f \sim 200$ GHz.

The Hamiltonian at zero electric field, in matrix form, is defined as $\mathbf{H_0}$. Its diagonal entries are computed via the implementation of (1.30). The Stark component $\mathbf{H_{St}}$ is computed by multiplying the dipole matrix $\mathbf{D}$, expressed in atomic units, with the vector of the electric field $\mathbf{F} = (0, 0, F_z)$. The quantity F_z spans from 0 V/m to an arbitrary value F_{max}, representing the highest electric field of interest. The dipole matrix is obtained by the product of a radial and a spherical harmonic component. The matrix elements of the radial component are computed via the Numerov method. The spherical harmonic component is implemented via the 3j formalism. The Hamiltonian is then obtained by summing the two components,

$$\mathbf{H} = \mathbf{H_0} + \mathbf{H_{St}} = \mathbf{H_0} - \mathbf{D} \cdot \mathbf{F}, \tag{1.32}$$

and finally diagonalized.

Figure 1.6 shows the Stark diagrams for Hydrogen and Rubidium for $n = 51$. For Hydrogen, at zero electric field, all the levels are degenerate. When the Stark effect is active, those energy

levels characterized by different m are distanced from one another. The same manifold in the Rubidium atom appears different. At zero electric field, the energies of the $|G\rangle$, $|F\rangle$, $|D\rangle$, $|P\rangle$ and $|S\rangle$ states differ from the energies of those belonging to the manifold. Also, when the Stark effect is considered, those energy levels with different m split and the $|G\rangle$, $|F\rangle$, $|D\rangle$, $|P\rangle$ and $|S\rangle$ states tend progressively to join the manifold.

Understanding the Stark effect for the Rydberg states matters in the perspective to access the circular state of a given manifold. The Stark diagram can indicate the electric field where the energy differences between neighboring m states become independent from m, thus where the coupling of the energy levels with an external, $\sigma+$ polarized, radio-frequency field is efficient to circularize.

1.2.3 The state-of-the-art preparation of a circular Rydberg state of Rubidium

Here, we briefly present the sequence of events applied to access the circular Rydberg state of Rubidium (figure 1.7). A detailed insight on this matter is presented in [68].

The experimental sequence of events used to prepare the circular Rydberg state is made of three steps. To start, the laser preparation of a low-m Rydberg state takes place. Three infrared photons (780 nm, 776 nm and 1258 nm) are employed to that end. The level $|52F, m = +2\rangle$ is chosen to avoid the anharmonicity of the lowest levels ($|m = +1\rangle$ and $|m = 0\rangle$) due to the quantum defect (figure 1.8). Second, the electric field is increased to 235 V/m so as to make the $|F\rangle$ levels join their respective manifold and set the energy difference between neighboring levels of the ladder around 230 MHz. We name this step "Stark switching". Third and last, a radio-frequency pulse at 230 MHz is applied to the atoms to transfer the population along the ladder until reaching the circular Rydberg state at its top. The polarization of such a pulse is calibrated to be $\sigma+$ and its frequency matches the spacing between neighboring states of the ladder.
This strategy allows us to prepare the circular Rydberg state with $> 80\%$ of efficiency.

1.3 The Strontium atom

1.3.1 The notation for the physics of two-electron atoms

We define here the notation for the physical quantities in use when we discuss the physics of the Rydberg-excited Strontium. Unless otherwise specified, we are using lower case letters to indicate the quantum numbers of an individual electron between the two populating the outer shell of Strontium. The index of the quantum number indicates which electron we refer to. The number 1 refers to the Rydberg electron, the number 2 to the ionic core. For instance, the angular momenta of the two electrons are associated to the operators $\hat{\mathbf{l}}_1$ and $\hat{\mathbf{l}}_2$, whereas the spins of the two electrons to $\hat{\mathbf{s}}_1$ and $\hat{\mathbf{s}}_2$. Also, we use capital letters to indicate the operators and the quantum

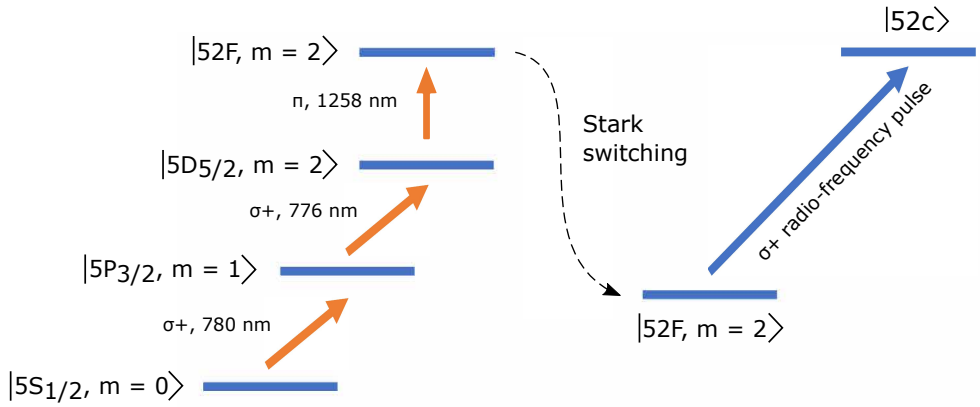

Figure 1.7: Sequence of events to access the circular Rydberg state of Rubidium with $n = 52$.

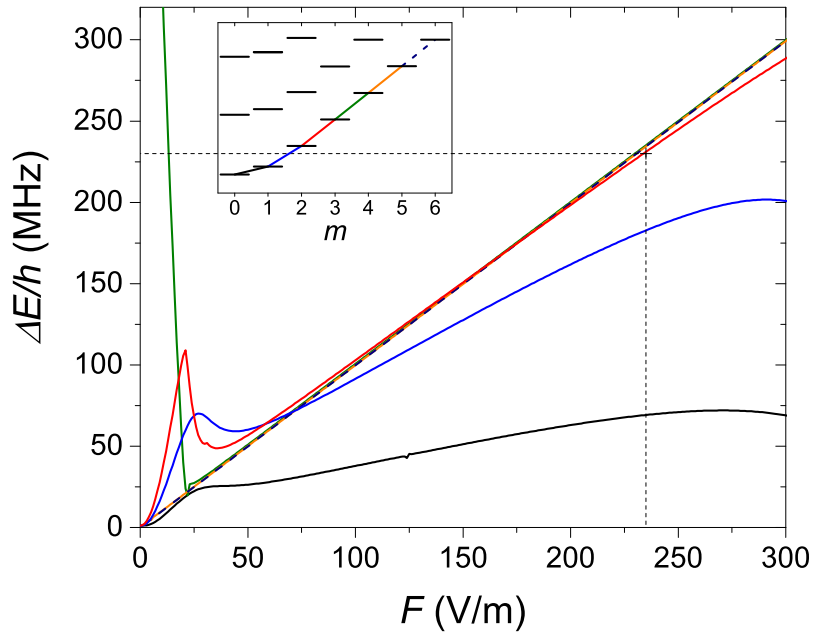

Figure 1.8: Energy difference between neighboring m states along the Rydberg ladder. The colors of the solid lines correspond to the transitions depicted in the inset. The quantum defect drags the lowest energy levels out of resonance with the upper ones, hence the necessity to prepare the atoms in a $|m = +2\rangle$ state before applying the radio-frequency field to circularize. The $|m = +2\rangle$ state involved in this circularization protocol belongs to the $|52F\rangle$ set of Rydberg states. This image is taken from [67].

numbers referring to the collective, two-electron system. For instance, $\hat{\mathbf{L}} = \hat{\mathbf{l}}_1 + \hat{\mathbf{l}}_2$ represents the angular momentum of the two-electron system and $\hat{\mathbf{S}} = \hat{\mathbf{s}}_1 + \hat{\mathbf{s}}_2$ indicates the total spin.

We report a modification of the notation of the magnetic quantum number. We name m as m_{l_i}, to label the magnetic quantum number associated to the angular momentum l_i, and introduce m_{s_i} to indicate the magnetic quantum number associated to the projection of the spin along the $\mathbf{z}$ axis for the i_{th} electron. Also, following the rule of before, $m_L = m_{l_1} + m_{l_2}$ and $m_S = m_{s_1} + m_{s_2}$.

The same rules are applied to the position vector of each electron. The number 1, used as an index of $\hat{\mathbf{r}}$, $\hat{x}$, $\hat{y}$ and $\hat{z}$, indicates the Rydberg electron. The number 2 refers to the ionic-core electron.

1.3.2 The Hamiltonian

We are going to adapt the mathematics of the Hydrogen atom, the quantum defects theory and the technique of circularization to Strontium. The latter atom presents a more complex energy-level structure than Alkali, due to the presence of two electrons in the outer shell.
A possible first approach to investigate this physics requires first to extend the Hamiltonian of the Hydrogen atom by including the potential describing the interaction between the two valence electrons, as

$$\hat{H} = \frac{\hat{P_1}^2}{2\mu} + \frac{\hat{P_2}^2}{2\mu} + \hat{V}_{Sr^{2+}}(\mathbf{r}_1) + \hat{V}_{Sr^{2+}}(\mathbf{r}_2) + \hat{V}_{12}, \tag{1.33}$$

and next to solve the Schrödinger equation. In (1.33), $\hat{V}_{Sr^{2+}}(\mathbf{r})$ is the potential of the Sr^{2+} ion and $\hat{V}_{12}$ is the term governing the interaction between the two electrons and inducing the well-known process of autoionization in alkaline-earth atoms,

$$\hat{V}_{12} = \frac{1}{4\pi\epsilon_0}\frac{e^2}{|\mathbf{r}_1 - \mathbf{r}_2|}. \tag{1.34}$$

This strategy is hard to pursue already at zero electric field without the assistance of perturbation theory. This enables to solve the Hamiltonian for two non-interacting particles and to consider $\hat{V}_{12}$ as a mere perturbation to that scenario. In the context of Rydberg atoms only, an alternative approach is provided by the Multichannel Quantum Defect Theory (MQDT) [73-76], which generalizes the quantum defect approach introduced for alkali atoms. There, the outer electron, prepared in a given Rydberg state $|\Psi_1\rangle$, penetrates the core and exits in a different Rydberg state $|\Psi_1'\rangle$, expressed in a complicated basis. The initial state of the atom therefore evolves from $|\Psi_1, \Psi_2\rangle$ to $|\Psi_1', \Psi_2'\rangle$, where Ψ_2 and Ψ_2' represent the state of the core before and after the interaction. Different couplings $|\Psi_1, \Psi_2\rangle \rightarrow |\Psi_1', \Psi_2'\rangle$ of the active electron and the core are referred as "channels".

Our strategy is simpler and more empiric but works for the range of Stark manifolds we are interested in. Those gather the Rydberg states with $48 < n < 54$. Their evolution is well understood via our picture.
We assume that the ionic-core electron remains in the ground state and we compute the energy level of the Rydberg electron in the effective potential created by the core Sr^{2+} and the ionic-core electron. Since the Rydberg electron is far away, we have $|\mathbf{r}_1 - \mathbf{r}_2| \sim \mathbf{r}_1$ and the potential $\hat{V}_{Sr^{2+}}(\mathbf{r}_1) + \hat{V}_{12} \sim -1/(4\pi\epsilon_0|\mathbf{r}_1|)$. The potential of the Sr^{2+} core, screened by the ionic core, is very close to the Hydrogen atom potential. We thus expect the dynamics of the Rydberg electron of Strontium to be described by the model based on single quantum defects, in the same way as for the Rydberg states of alkali atoms. However, the price to pay is that the quantum defects are larger, since the interaction between two valence electrons is stronger than that among Rydberg filled shells. Also, we need to take into account the spin degrees of freedom of the two valence electrons. The energy of the quantum states of the spin ("spin states") is influenced by two more contributions to the Hamiltonian, being the exchange energy and the spin-orbit coupling.

The exchange energy represents the energy difference between two families of states with equivalent set of quantum numbers but different total spin states ("singlet" and "triplet" states). Both obey the Pauli principle. When diagonalizing (1.33), the exchange energy is accounted as the off-diagonal term deriving from the presence of (1.34) in the Hamiltonian. It reads

$$E_{ex} = \langle n_1 l_1, n_2 l_2 | \frac{1}{|\mathbf{r}_1 - \mathbf{r}_2|} | n_2 l_2, n_1 l_1 \rangle . \tag{1.35}$$

On the contrary, the spin-orbit coupling is not included in the electron-electron potential of (1.33). However, we can define a new Hamiltonian component, describing the spin-orbit coupling, of the form

$$\hat{H}_{so} = A^{(1)}_{n,l_1} \hat{\mathbf{l}}_1 \cdot \hat{\mathbf{s}}_1 + A^{(2)}_{n,l_1} \hat{\mathbf{l}}_1 \cdot \hat{\mathbf{s}}_2, \tag{1.36}$$

where $A^{(i)}_{n,l_1}$ are the spin-orbit constants. Notably, the terms including the angular momentum of the core electron are not reported, since that electron is considered, at this stage, in the ground state $|5S, l_2 = 0\rangle$.

1.3.3 The uncoupled, spin eigenstates

The competition between the exchange energy and the spin-orbit coupling term in the Hamiltonian make us distinguish among three situations. If we assume the spin-orbit coupling to be zero and the exchange energy to represent the only spin-dependent term of the Hamiltonian, we can distinguish two classes of energy levels, differentiated by the total spin of the electronic system, the singlet ($S = 0$) and triplet states ($S = 1$). For the singlet states, the wavefunction Ψ of the entire electronic system is composed by a symmetrical spatial component ψ and an anti-symmetrical spin component χ. Note that Ψ must be anti-symmetrical, given the fermionic

nature of the electrons. In this case, the anti-symmetry of the final wavefunction is inherited from its spin component,

$$\Psi_A^{(S)} = \psi_S(\mathbf{r}_1, \mathbf{r}_2)\chi_A(1,2). \tag{1.37}$$

For the triplet states, the final anti-symmetrical wavefunction of the electronic system is composed by an anti-symmetrical spatial component and a symmetrical spin component.

$$\Psi_A^{(T)} = \psi_A(\mathbf{r}_1, \mathbf{r}_2)\chi_S(1,2). \tag{1.38}$$

For what concerns this work, the exchange energy is taken into account as a contribution to the quantum defect. Table 1.2 reports a table of the quantum defects for some Rydberg series [72]. There, the quantum states are reported by use of the common notation

$$n^{2S+1}X_J, \tag{1.39}$$

where the letter X is replaced by S,P,D,F,G,H, if $L = 0,1,2,3,4,5$ respectively.

Table 1.2: Quantum defects of the Strontium atom.

Serie	δ_0	δ_2	Serie	δ_0	δ_2
$5sns\,^1S_0$	3.26896	-0.138	$5snp\,^3P_0$	2.8866	0.44
$5snp\,^1P_1$	2.7295	-4.67	$5snd\,^3D_3$	2.63	-42.3
$5snd\,^1D_2$	2.3807	-39.41	$5snd\,^3D_2$	2.636	-1
$5snf\,^1F_3$	0.089	-2	$5snd\,^3D_1$	2.658	3
$5sns\,^3S_1$	3.371	-0.5	$5snf\,^3F_4$	0.12	-2.4
$5snp\,^3P_2$	2.8719	0.446	$5snf\,^3F_3$	0.12	-2.2
$5snp\,^3P_1$	2.8824	0.407	$5snf\,^3F_2$	0.12	-2.2

Note that if the spin-orbit coupling is symmetrical (i.e $A^{(1)}_{n,l_1} = A^{(2)}_{n,l_1}$) it is possible to write (1.36) as

$$\hat{H}_{so} = A_{n,l_1}\hat{\mathbf{L}}\cdot\hat{\mathbf{S}}. \tag{1.40}$$

This Hamiltonian commutes with the total spin operator. The spin orbit coupling does not mix a singlet and a triplet level, it only lifts the degeneracy between the triplet states, hence the different quantum defect for $^3P_2$, $^3P_1$, $^3P_0$ or $^3D_3$, $^3D_2$, $^3D_1$ for instance.

1.3.4 The asymmetrical spin-orbit coupling

We consider here the opposite scenario, where the exchange energy is zero and the spin-orbit coupling is asymmetrical. We need to introduce a new basis to diagonalize the Hamiltonian of Strontium taking into account the spin-orbit coupling. Therefore, we define the total angular momentum operator $\hat{\mathbf{j}}_1$ for the Rydberg electron, as

$$\hat{\mathbf{j}}_1 = \hat{\mathbf{l}}_1 + \hat{\mathbf{s}}_1. \tag{1.41}$$

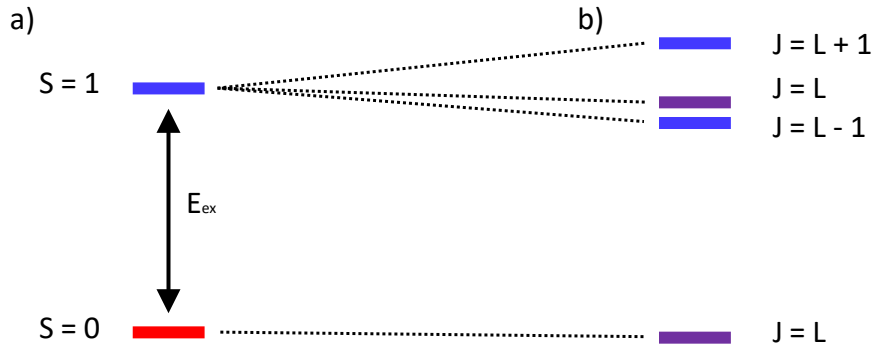

Figure 1.9: Classes of eigenstates of the Strontium Hamiltonian when the exchange energy is the only spin dependent term considered (a) and when the asymmetrical spin-orbit coupling is included in the analysis (b).

Its projection along the **z** axis and its square commute between each other and with the Hamiltonian. We therefore choose the $\{\hat{j}_1^2, \hat{j}_{1,z}\}$ as a basis for the new energy levels.

In this context, the distinction between singlet and triplet levels is irrelevant: the absence of the exchange energy implies no shift of one class with respect to the other. Instead, we make the distinction between two states, one with $j_1 = l_1 + 1/2$, the other with $j_1 = l_1 - 1/2$.

1.3.5 General case: exchange energy and spin-orbit coupling

In the most general case, the exchange energy and the spin-orbit coupling term are both non-zero. To model such a case, we define the total angular momentum of the second electron as $\hat{\mathbf{j}}_2$, as previously done for the first electron, and, following our notation, the total angular momentum operator associated to the entire electronic system as

$$\hat{\mathbf{J}} = \hat{\mathbf{j}}_1 + \hat{\mathbf{j}}_2. \tag{1.42}$$

To model the physics of two, coupled spins, we choose the basis $\{\hat{J}^2, \hat{J}_z\}$. At this stage, we keep the distinction between singlet and triplet states. Contrary to the case where the only exchange energy is considered, here, we can make two points. First, we have no degeneracy of the triplet states sharing the same n but different J. However, the triplet states with same n, J but different m_J are still degenerate. Second, states with identical J are distanced between one another, regardless of the singlet or triplet nature (figure 1.9). Notably, this mutual displacement ΔE_{so} is a function of n, l and derives from the spin-orbit coupling. We anticipate that for $|F\rangle$ states, the spin-orbit coupling is low enough to make the displacement ΔE_{so} between states with identical n, J negligible. It becomes larger for $|G\rangle$ states and then completely dominant over the exchange energy term for the $|H\rangle$ states, where we cannot distinguish anymore an internal structure for the states located in the energy range of the were-triplets (figure 1.10).

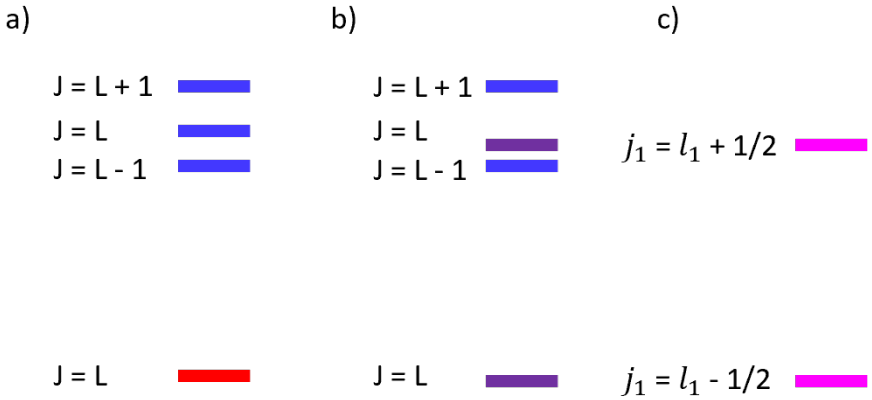

Figure 1.10: Structure of the spin states undergoing the asymmetrical spin-orbit coupling. When the coupling is weak but not negligible, the triplets (blue lines) are not degenerate. This is the case for the Rydberg states of Strontium with $l_1 = 3$ ($|F\rangle$ states). Next, with increasing strength of the asymmetrical spin-orbit coupling, the J states start to mix and loose their singlet (violet lines) or triplet character. This is the case for the Rydberg states with $l_1 = 4$ ($|G\rangle$ states). Finally, when it is completely dominant over the exchange energy, we distinguish just two states (pink lines) at zero electric field. This is the case for the Rydberg states with $l_1 = 5$ ($|H\rangle$ states).

1.3.6 Interaction with a static electric field

The discussion of the two-electron atom physics has so far considered the only scenario where no static electric field interacts with the atom. We briefly discuss here the opposite case, where the interaction with a static electric field is taken into account.

At low electric field, the Stark effect lifts the degeneracy of each J state into m_J sub-levels, as it happened for the Hydrogen atom when considering l and m. Here, m_J is

$$m_J = m_L + m_S, \tag{1.43}$$

and represents, in this context, a good quantum number. In the most general case, where both the exchange energy and the spin-orbit coupling are taken into account, the admitted values of m_J are in the $[-J, J]$ range for both the singlet and triplet branch. In the case where the only exchange energy is entirely neglected, the level with $j_1 = l_1 + 1/2$ ($j_1 = l_1 - 1/2$) ramifies into its m_{j_1} sub-levels, where $m_{j_1} = [-j_1, +j_1]$.

At higher electric field, m_J is still a good quantum number. The Stark splitting among the m_J levels increases. Finally, the levels with same m_L gather. We therefore pass from a description in terms of m_J to one in terms of m_L, in use for Rubidium and Hydrogen.

1.4 Discussion

In this chapter, we present the basic elements of the physics concerning the Rydberg-excited Strontium. To that end, we initially generalize the description of Hydrogen to alkali atoms by introducing the quantum defect, a dimensionless parameter accounting for the discrepancy between the Hydrogen energy levels with their counterpart for alkali atoms at zero electric field. In the same section, we also describe the process of circularization, being the transfer of the population from a low-l_1 Rydberg state to that with maximum l_1 and m_{l_1} of a given manifold. The latter state is named as the circular Rydberg state, due to its toroidal wavefunction.

The formalism and the mathematics already used for alkali atoms is then adopted, as a first approximation, to describe the eigenstates of the Rydberg-excited Strontium. We then include the spins of the two valence electrons of Strontium in our analysis. This is done by defining the exchange energy, deriving from the Coulomb potential governing the electric interaction between the two electrons, and the spin-orbit Hamiltonian, coupling spins and angular momenta. Overall, we see two classes of states resulting from the diagonalization of the complete Strontium Hamiltonian: singlet and triplet states. We conclude by analysing the interaction between the Rydberg-excited Strontium and a static electric field. The Stark effect is showed to lift the degeneracy between states with different m_J.

All the elements presented so far come together in the next chapter, where we are going to present the experimental preparation of the circular Rydberg states of Strontium.

CHAPTER 2

THE PREPARATION OF THE CIRCULAR RYDBERG STATE OF STRONTIUM

> In the study of nature, as in the practice of art, it is not given to man to achieve the goal without leaving a trail of dead ends he had pursued.
>
> *Baron Louis Bernard Guyton de Morveau*

The former chapter introduced the Hydrogen model and outlined its extension to the physics of multi-electron atoms excited to Rydberg states.

In this chapter, we present the procedure to prepare and manipulate the circular Rydberg state of Strontium for the first time. The chapter is split in three parts. We first introduce the experimental set-up. Next, we detail the sequence of laser, microwave (MW) and radio-frequency (rf) pulses used to prepare and detect the circular states. Once we have explained the experimental sequence, we focus on the results of the circularization. Finally, as a conclusion, we discuss some optimisations performed by use of the circular Rydberg state.

2.1 Experimental set-up

2.1.1 Overview

We detail here the experimental set-up used to prepare the Rydberg atoms of Strontium. A scheme of its main mechanical components is presented in figure 2.1. We start by discussing the

Strontium oven (paragraph 2.1.2) and next the cryogenic environment (paragraph 2.1.3) where the experiment takes place. At that point of the discussion, we explain our detection method and its limitations. Next, we present the radio-frequency source (paragraph 2.1.4) and the laser diodes at 461 nm, 767 nm, 896 nm performing the Rydberg excitation (paragraph 2.1.5).
The cryogenic environment, the detector and the radio-frequency source were inherited from a former series of experiments on the circular Rydberg states of Rubidium. On the contrary, the oven and the laser beams are specific for Strontium and were built from scratch to obtain the results exposed in this work.

2.1.2 The oven

The oven is a 132 mm stainless tube with a built-in CF40 flange (figure 2.2a). A sample of metallic Strontium is heated into its main chamber at 582°C and converted into vapor. At that temperature, the sample of Strontium is not yet liquid. The melting point of Strontium is at 777°C at the standard atmospheric pressure. The Strontium vapor thus exits the oven as an atomic beam. Its minimal divergence of ~ 70 mrad is guaranteed by some microtubes with 130 μm and 300 μm of internal and external diameters (figure 2.2b), cut by the manufacturer in 8 mm pieces with a pulsed high power laser. They collimate and align the beam towards the cryostat. They are heated at 639°C to prevent the deposition of the Strontium atoms on their walls.

The oven is a attached to a CF40 chamber provided with two windows parallel to the propagation axis of the atoms and internal diaphragms further refining the collimation of the beam. The windows allow us to perform laser spectroscopy to verify the presence of an atomic beam ejected from the oven. Finally, a valve separates the chamber from the cryostat, enabling us to vent them independently and facilitating the refilling of the oven.

2.1.3 The cryogenic environment

We are provided with a cryostat kept at 4 K by liquid Helium 4 (figure 2.3). It uses liquid Nitrogen for thermal shielding. This low temperature environment aims to protect the Rydberg atoms from black-body radiation. It is pumped by a turbo-molecular pump to 10^{-7} mbar, enough to prevent some residual gas inside the cryostat from scattering against the atomic beam. We estimate the internal pressure to be further reduced by the cryo-pumping in the inner part of the cryostat. It is however hard to predict the exact value of the pressure reached via this mechanism.

The experiment itself takes place in a structure named "core of the cryostat". It is located at the bottom of the cryogenic environment and aligned in-axis with the oven. The walls of this structure are four ring-shaped electrodes, which are used to apply electric fields along the horizontal axis and rf pulses to the atoms, whereas the floor and the roof are composed by two

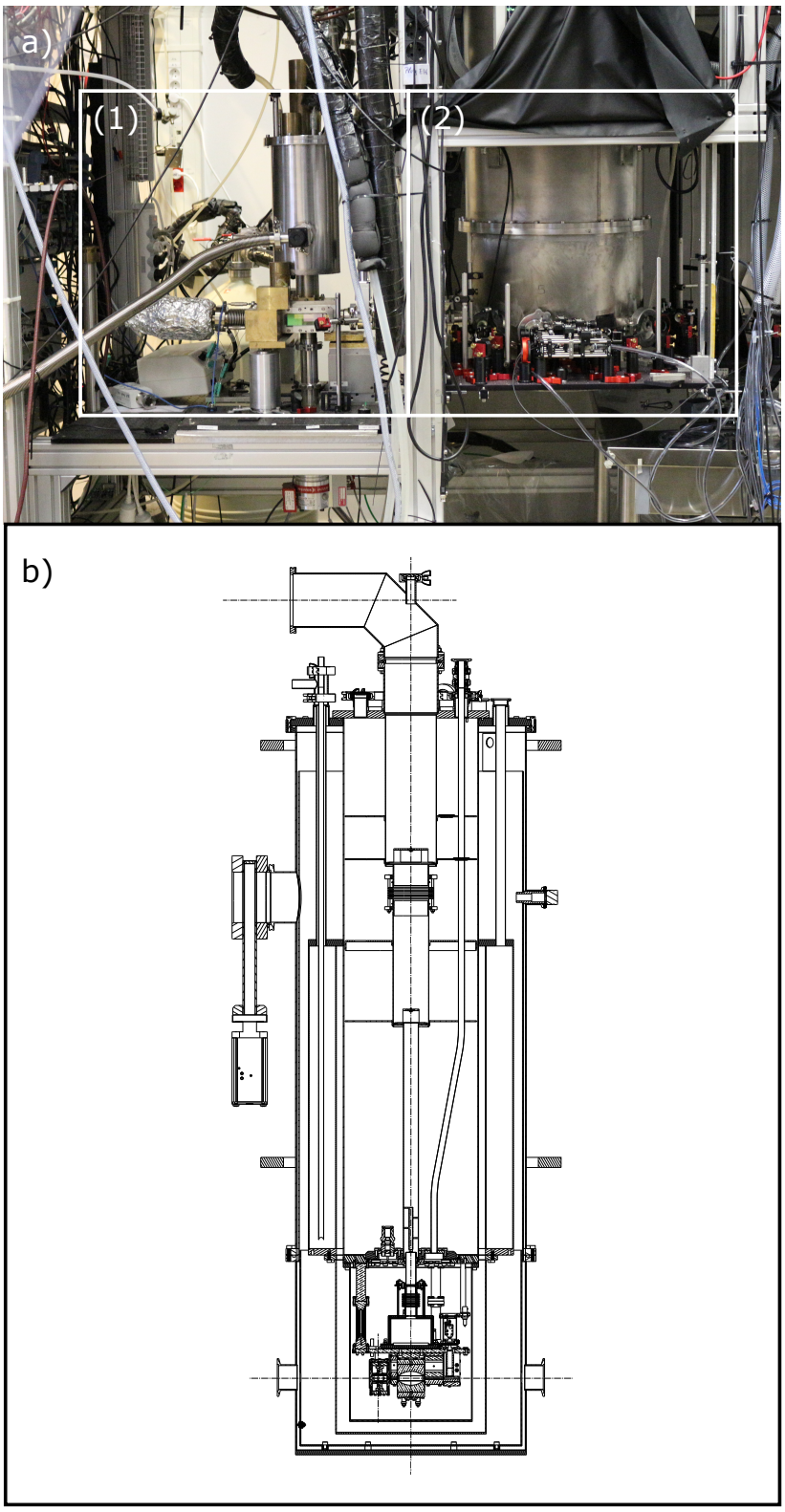

Figure 2.1: a) Photography of the main mechanical components, the oven (1) and the cryostat (2), of the experimental set-up. b) Scheme of the main mechanical components of the cryostat.

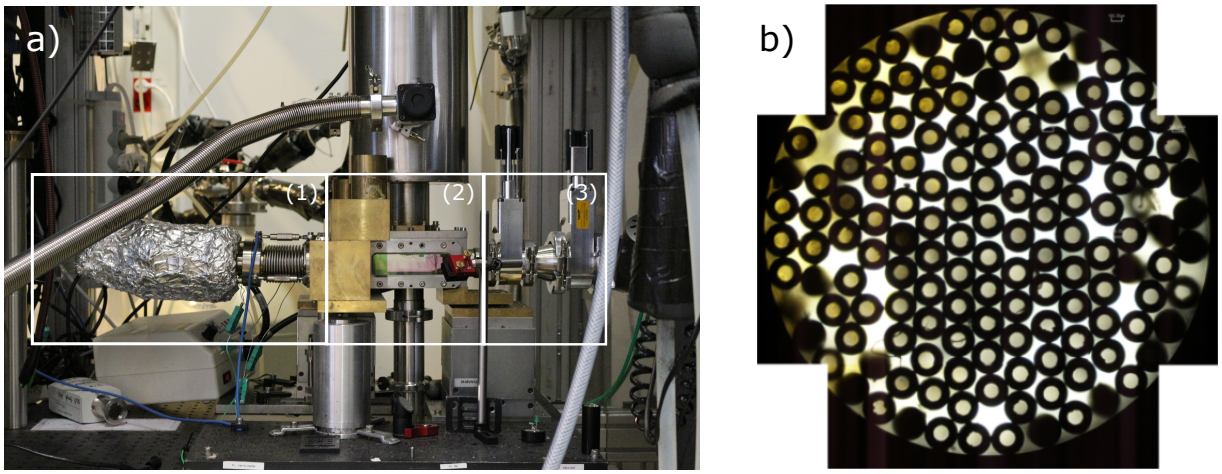

Figure 2.2: a) Photography of the oven (1). the CF40 cube (2) and the valve (3). b) Photography of the transversal section of the microtubes of an oven built following the same design. This panel is taken from [77].

parallel, plane electrodes, allowing us to set electric fields along the vertical axis.

The cryogenic environment holds the detector. In our set-up, the Rydberg atoms are detected by ionization. This is accomplished by use of two horizontal plates whose spacing varies along the trajectory of the atomic beam. We set an ionization voltage on these two plates and count the atoms ionizing at that value of the voltage by collecting the electrons expelled. They are accelerated to a channel electron multiplier (CEM) by use of some electrostatic lenses. Next, the CEM acts as the amplifying stages in a photomultiplier tube, producing a signal when hit by an electron. A set of amplifiers enhances the signal before its transmission to the computer.

We relate the input voltage $V^{(det)}_{n,l_1,m_{l_1}}$ applied on the plates of the detector with the electric field $F^{(det)}_{n,l_1,m_{l_1}}$ ionizing the atoms by use of a simple formula,

$$F^{(det)}_{n,l_1,m_{l_1}} = K_{det}\frac{V^{(det)}_{n,l_1,m_{l_1}}}{d_{det}}, \tag{2.1}$$

where $K_{det} = 50$ is a calibration factor taking into account the amplification stage and $d_{det} = 3.74$ mm is a parameter approximating the distance between the two plates by use of a constant value.

The ionization field of a given state is a function of its set of quantum numbers. Rydberg states with high-n are farther from the nucleus and therefore easier to ionize. They consequently have lower ionization thresholds. On the contrary, low-n states feel a stronger attraction from

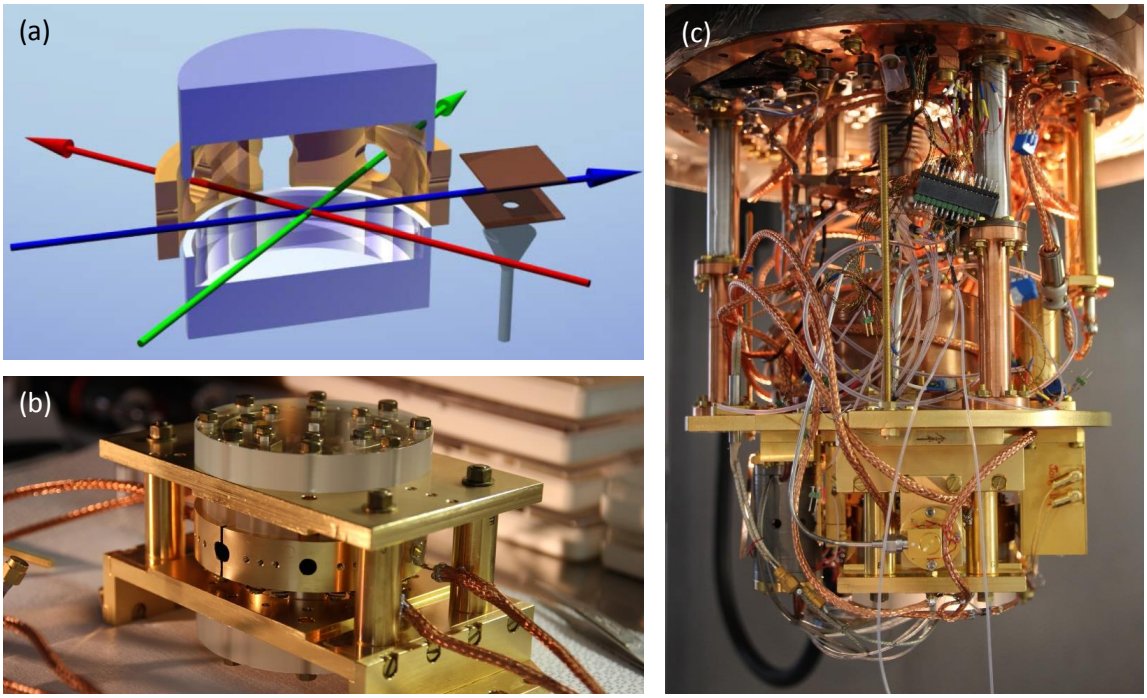

Figure 2.3: a) Sketch of the experiment, illustrating the "core of the cryostat", where the path of the atoms (blue arrow) intersects that of the lasers (red and green arrow for the 461 nm and the infrared lasers respectively). The walls of the structure are the electrodes employed to the generation of the horizontal component of the electric field and the radio-frequency fields (yellow electrodes in panel a)). The roof and the floor are the electrodes employed to produce electric fields along the vertical axis (blue electrodes in panel a)). b) Photography of the core of the cryostat, where the experiment takes place. c) Photography of the cryostat. This image is taken from [67].

the core and the valence electron requires a higher field to be extracted.

States with different magnetic quantum numbers also ionize differently. A semi-classical interpretation of this fact derives from a simple analysis of the electric potential perceived by the atoms at the detection stage. The detector adds a eFz term to the Coulomb potential (figure 2.4) and creates a saddle point in the overall potential perceived by the atom. When increasing the electric field, the state of the electron adiabatically evolves in another Rydberg state, sharing the same n and m_{l_1} with the original one but different parabolic quantum number n_1. This new state has a wavefunction partially localized in the $z < 0$ region, where the saddle point lays. This fact allows the electron to escape the core, if the electric field of the detector overcomes the binding energy. Note that the wavefunction of the Rydberg state produced after increasing the electric field of the detector explores an area of space in the $z < 0$ region which depends on the quantum number m_{l_1}. As a result, once set n, the Rydberg states in the highest positions of the ladder need a higher electric field to be ionized with respect to those located in the lowest positions.

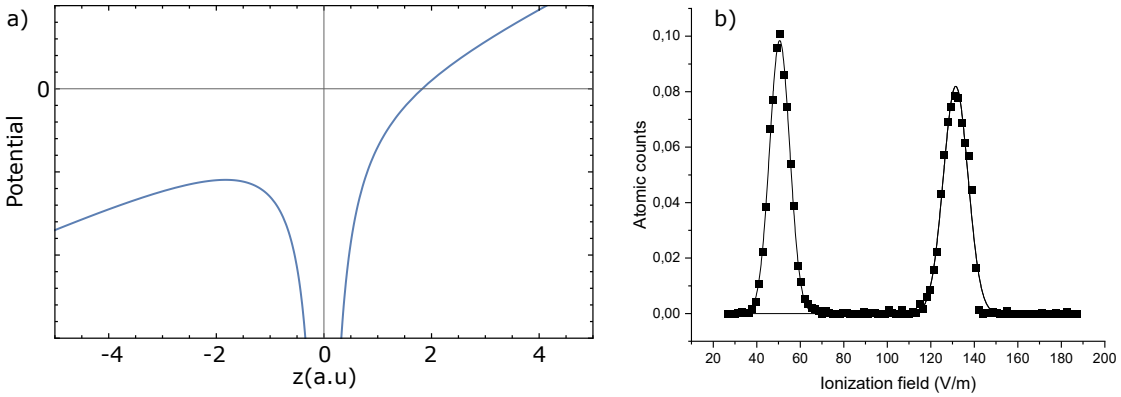

Figure 2.4: a) Electric potential applied on the atoms, made up by a Coulomb component and a linear electric field imposed by the detector [67]. b) Ionization signal (black points) of atoms prepared in a low-m_{l_1} Rydberg state (left, bell-shaped signal) and of atoms in a high-m_{l_1} state (right, bell-shaped signal). The solid line is a guide for the eye.

Such a method to measure the Rydberg atoms production is not immune to drawbacks. In a first place, it is a destructive technique. Secondly, Rydberg atoms belonging to the same level distribute over a bell-shaped curve as a function of the detection field. This may involve a non-negligible overlap between the bells of two states and consequently cause background counts when measuring one of the two.

2.1.4 The radio-frequency synthesizer

The rf pulses are produced by a synthesizer H provided with four channels, noted H_1, H_2, H_3, H_4, each connected to one of the four ring-shaped electrodes inside the cryostat. The free parameters of each channel are the frequency ω_{rf}, power P_{rf} and phase ϕ_{rf} of the output radio-frequency field. Notably, varying ω_{rf} makes the instrument lose the calibration of ϕ_{rf}. Therefore, ω_{rf} cannot be scanned but must be set by hand before each sequence.
The pulse envelope is chosen via a programmable, high-resolution, arbitrary wave generator (AWG) connected to the synthesizer. If not otherwise specified, all the rf pulses mentioned in this work have a square shape.
Figure 2.5 presents a basic scheme of the electronic connections of each channel to the corresponding electrode inside the cryostat.

2.1.5 The laser beams for the Rydberg excitation

Rydberg states have a high principal quantum number. This involves an atomic transition frequency of the order of several hundreds of THz with respect to the ground state. Such a massive

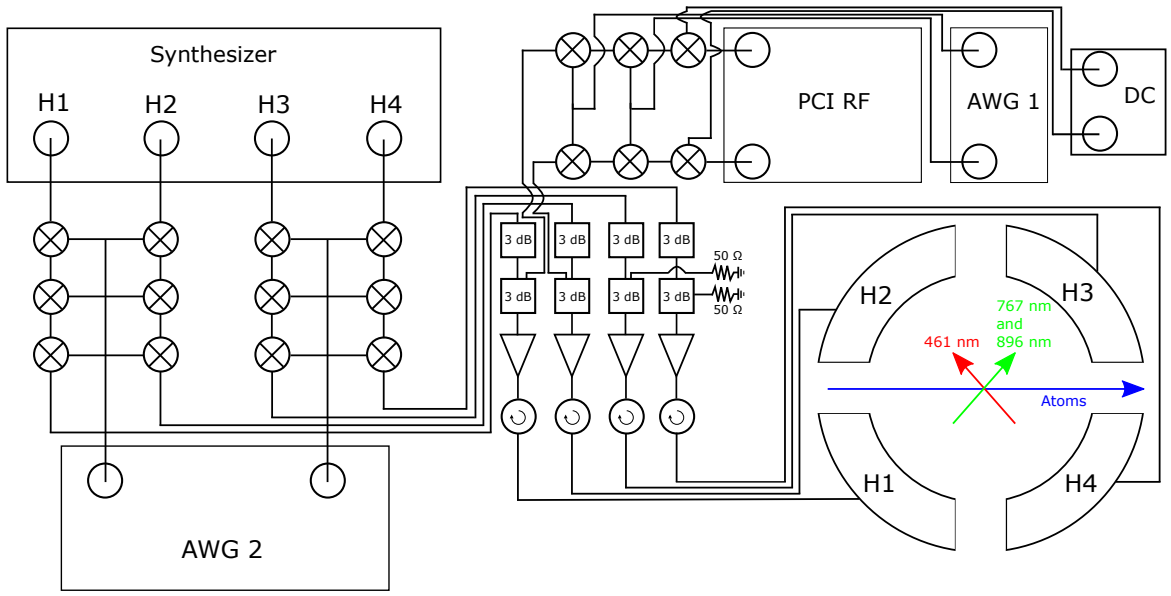

Figure 2.5: Scheme of the radio-frequency set-up. We use a synthesizer connected to an arbitrary wave generator to produce rf, single frequency, square pulses. The connections between the two are made by coaxial cables. Each channel of the synthesizer is connected to a ring-shaped electrode in the cryostat (H_1, H_2, H_3, H_4), here sketched from above.

frequency step can be accomplished by lasers only. Therefore, once inside the cryostat, the atoms are excited by three laser beams at 461 nm, 767 nm and 896 nm (figure 2.6).

All the laser sources are placed on top of an optical table preventing the vibrations from the environment from affecting the stability of each beam. The preparation of every laser features four steps: the beam shaping, the adjustment and lock of the frequency, the selection of continuous wave mode or pulsing mode and the definition of the intersection geometry with the atomic beam.

Each laser is prepared as a collimated Gaussian beam by a telescope made up of cylindrical lenses. We use two plano-convex lenses to fine-tune the shape of a given laser beam and a final plano-concave lens to collimate it. The 461 nm laser beam uses a combination of lenses with 100/150/-50 mm as focal lengths. Instead, the 767 and 896 nm use a combination with 200/75/-50 mm as focal lengths. After the telescope, the beam is split. One branch goes to a wave-meter, a second one is directed to an ultra-stable cavity and a third one reaches a small board, placed in the proximity of the cryostat, via a polarization-maintaining optical fiber. There, the 461 nm beam goes through a selection of the polarization. The 767 nm and 896 nm beams are overlapped through a beam-splitter. Also, for this last laser only, we have a last plano-convex lens, with 400 mm as a focal length, to focus the 896 nm beam at the intersection with the atomic beam. After these last refinements, each beam enters and exits the core of the cryostat through round holes made on the ring-shaped electrodes. Figure 2.7 presents the optical paths of all laser beams,

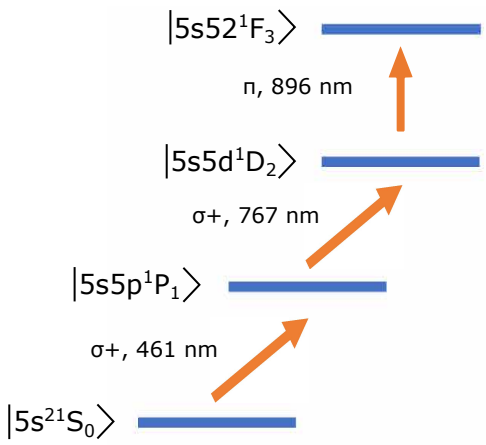

Figure 2.6: Three-photon laser excitation to the Rydberg states of Strontium. The first step is performed by a laser beam at 461 nm and $\sigma+$ polarized, the other two by laser beams at 767 nm and 896 nm respectively. We make use of the $\sigma+$ and π components of their polarizations. We ultimately access the $|52^1F_3, m_{l_1} = +2\rangle$ Rydberg state.

figure 2.8 displays the optical path of those branches which are brought to the cryostat.

The frequency of every beam is individually adjusted to meet the resonance of the corresponding transition. The 461 nm is brought to 650.5024 THz to excite the ground state $|5s5s^1S_0\rangle$ to $|5s5p^1P_1\rangle$, the 767 nm to 390.6000 THz to prepare $|5s5d^1D_2\rangle$ and finally the 896 nm to 334.6883 THz to ultimately access the state $|52^1F_3, m_{l_1} = +2\rangle$. The ultra-stable cavity (finesse $\sim$ 10000) enables us to lock these frequencies by the standard Pound-Drever-Hall (PDH) method. Notably, the combination of laser frequencies reported here works well for the Rydberg excitation of the only isotope ^{88}Sr. While our experiment does not use an isotopically pure sample, we focus our experimental activity on the only ^{88}Sr. We leave to appendix A the proof of this statement via standard laser spectroscopy of the atomic beam.

The treatment of the 461 nm beam differs. The portions of this beam arriving to the ultra-stable cavity and to the wavelength meter have a wavelength of 922 nm. This is because the 461 nm beam is produced by frequency-doubling a 922 nm laser beam. Our strategy involves using a branch of this last infrared beam, not undergoing the frequency-doubling stage, to lock the frequency of the 461 nm laser. This choice is motivated by the coating of the cavity mirrors, which work only for wavelengths within the infrared range, and by a band-pass effect of the wave-meter.

The 461 nm and 767 nm laser beams work in continuous wave mode. On the contrary, the 896 nm laser is pulsed. The pulse production requires the laser beam to cross an AOM whose power supply is connected to a fast switch. The power supply is a rf source emitting a single-frequency wave with few dBm of power, which is then increased by an amplifier to reach around 33 dBm.

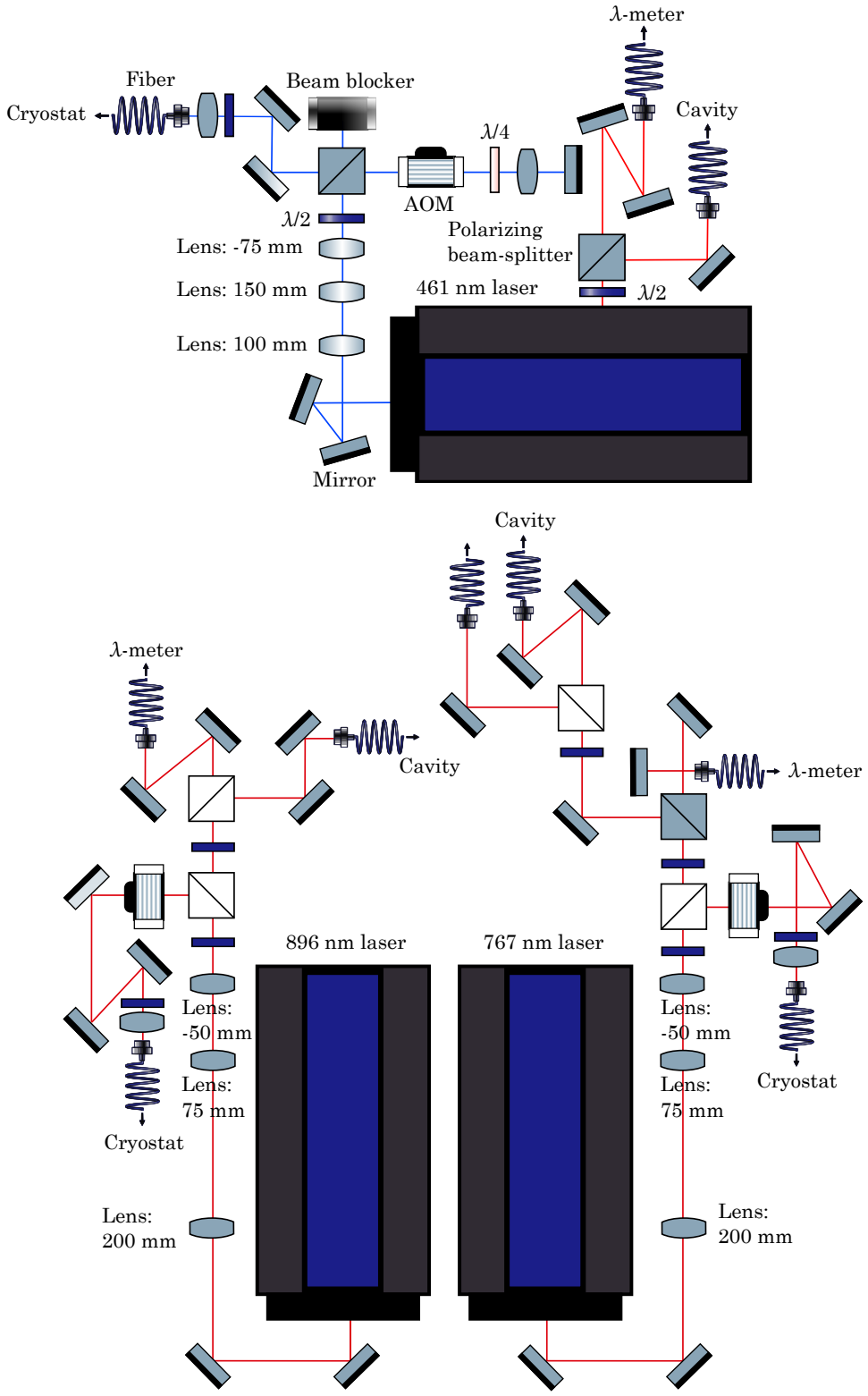

Figure 2.7: a) Optical path of the 461 nm laser beam. b) Optical paths of the 767 nm (right) and 896 nm (left) laser beams.

The interaction of each laser with the atomic beam depends on the direction of the laser propagation, its power and Gaussian diameter. All these parameters are kept stable throughout the experiments. The power is recorded by a light sensor working within the 400 nm - 1100 nm range. The diameter is measured by deviating the laser path with a pair of mirrors and next placing a camera at a distance which matches that between the last mirror and the intersection point of the laser beam with the atoms.
The 461 nm laser arrives to the cryostat with an angle of incidence of 135^o with respect to the direction of the atomic beam and 90^o with respect to the infrared lasers. The direction of propagation of this beam is parallel to the quantization axis, defined by a small, horizontal electric field at this stage of the experiment. The 461 nm beam has a Gaussian diameter of ~ 900 μm at the atomic beam position and an optical power of ~ 0.9 mW. The polarization is selected to be $\sigma+$ by a beam-splitter cube and a $\lambda/4$ wave-plate placed before the window of the cryostat.
The 767 nm and 896 nm lasers are parallel and collinear. The anti-reflection coating of the cryostat windows motivates a different entry path for these two beams. The respective Gaussian diameters on the atoms are ~ 1100 μm and ~ 490 μm whereas their optical powers are ~ 7.3 mW and ~ 34 mW. We make use of the σ component of the 767 nm laser polarization and the π component for the 896 nm laser.

2.1.5.1 The ultra-stable cavity

We use a high-finesse cavity, characterized by a free-spectral-range (FSR) of 1.5 GHz in vacuum, to lock the frequency of the lasers by standard PDH method. The cavity is made up of two mirrors 10 cm away from each other, both protected by a cylindrical, metallic shield. This has two holes on its walls, enabling the beams to enter the cavity from one side and exit from the other. The closest mirror to the entry is plane, the opposite one is convex. The cavity is kept under vacuum ($P \sim 10^{-7}$ mbar) by an ionic pump.

Each laser beam is brought to the cavity through an optical fiber equipped with an electro-optical-modulator (EOM). By applying a sinusoidally varying potential voltage on the EOM, we generate sidebands to the frequency of the laser entering the fiber. In this way, we are able to control and sweep the frequency of the beam going to the cavity independently from the main line going to the cryostat. After the EOM, at the exit of the fiber, the diameter of each beam directed to the cavity is 900 μm. Next, each laser goes through a mode-matching stage and is then aligned with the cavity. We are interested in the reflections, produced after that the beams bounce off the plane mirror at the cavity entry. Each reflection is first separated from the others by dichroic mirrors or polarizing beam-splitters and next recorded via a fast photo-diode. The photo-diodes and the cavity require low optical power for the beams under use. We therefore tune the power of each laser line to be < 1 mW for safety. Figure 2.9 shows the optical path.

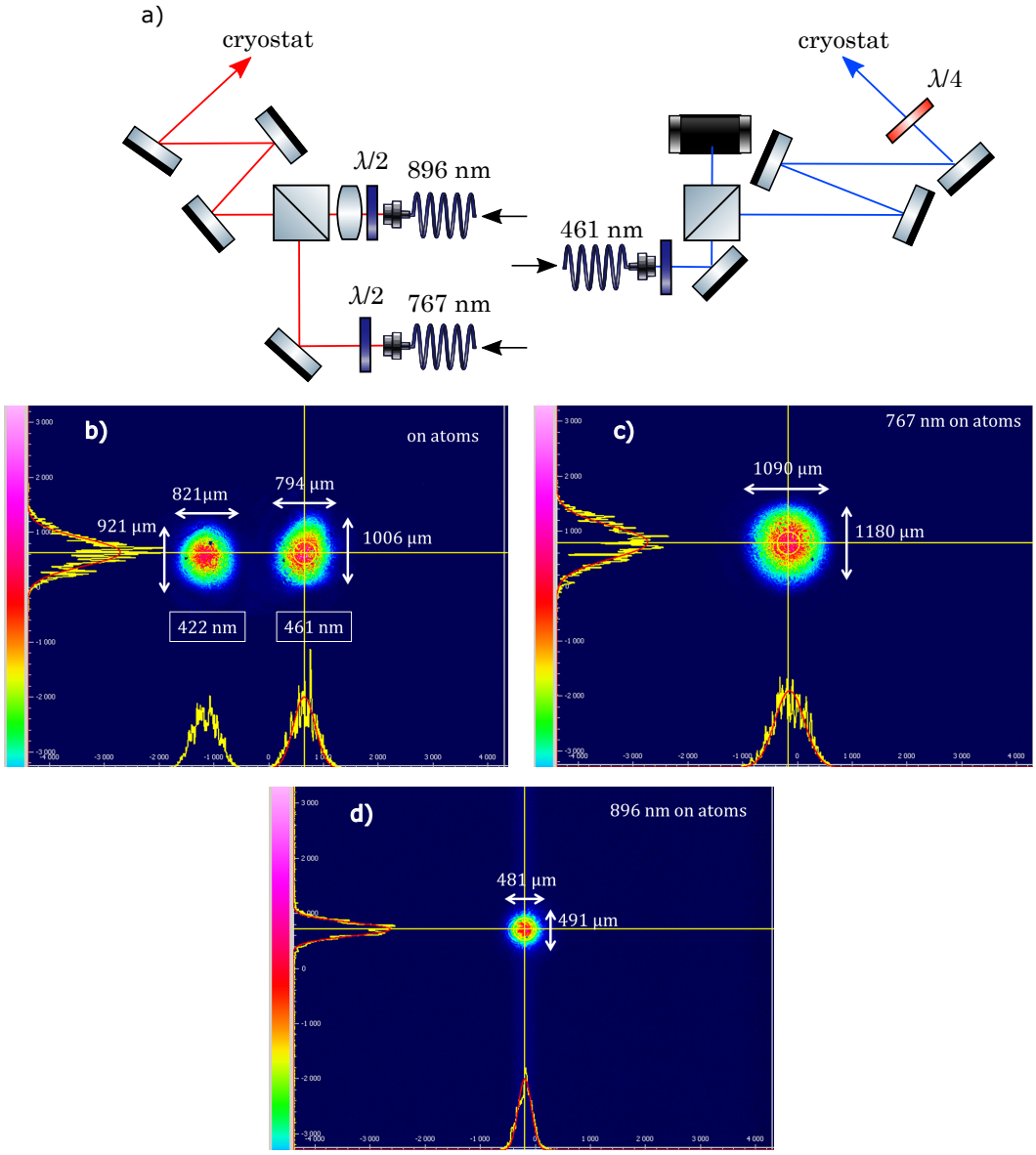

Figure 2.8: a) Optical path of the laser beams in the proximity of the cryostat. The two infrared lasers overlap. The blue laser undergoes a polarization selection via a beam-splitter and a wave-plate $\lambda/4$. b-c-d) Gaussian profiles of the 461 nm, 767 nm, 896 nm laser beams at the point of the intersection with the atomic beam. Panel b) reports the profile of an additional laser beam at 422 nm, used for the core excitation. We leave the description of the core excitation and the 422 nm laser beam to chapter 3.

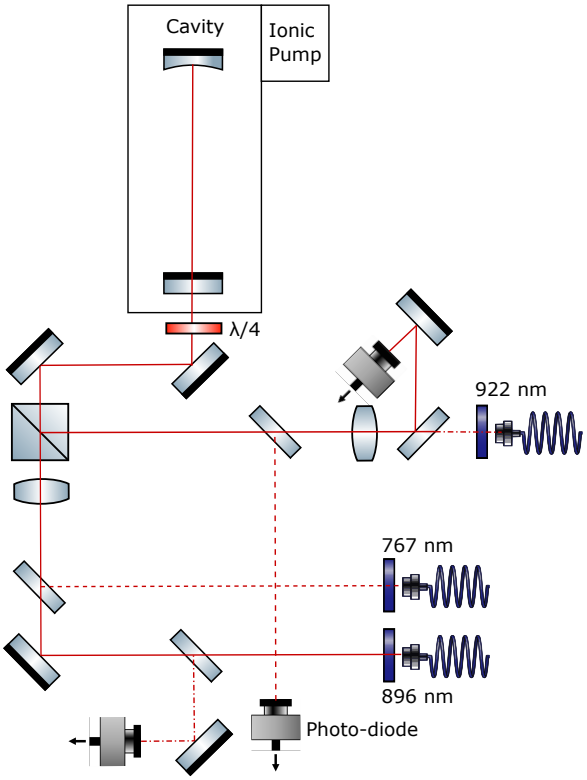

Figure 2.9: Optical path of the 767 (dashed, red line), 896 (solid, red line), 922 nm (dashed-dotted, red line) laser beams in the proximity of the ultra-stable cavity. Every laser beam undergoes a mode-matching lens, a dichroic mirror (a cubic beam-splitter alternatively) and a fast photo-diode to obtain its reflection from the first mirror of the cavity following the optical path.

2.2 Experimental results

2.2.1 Overview

In this section, we discuss the procedure to access the circular Rydberg states of Strontium. We decompose this procedure into its main events, graphically summarized in figure 2.10. We begin by accessing $|52^1F_3, m_{l_1} = +2\rangle$ (paragraph 2.2.2) and discussing the selection of the velocity class (paragraph 2.2.3). Next, we transfer the population to $|51^1G_4, m_{l_1} = +2\rangle$ (paragraph 2.2.4) and investigate the harmonicity of the $|n = 51, n_1 = 0, m_{l_1} > 0\rangle$ ladder (paragraph 2.2.5). Once identified the Stark frequency, we prepare a $\sigma+$ polarized, single-frequency, radio-frequency pulse (paragraph 2.2.6) allowing us to climb the ladder and prepare a superposition of high-l_1 states (paragraph 2.2.7). We measure the population of its components by use of microwave pulsed probes. The probe for the circular state is also used to determine the optimal duration of the rf-driven Rabi pulse that maximizes the circular population (paragraph 2.2.8). Notably, we also achieve the preparation of $|51c\rangle$ via an adiabatic passage from the $|51^1G_4, m_{l_1} = +2\rangle$ state. It is a complementary result which is not used to get the results of chapters 3 and 4. Therefore,

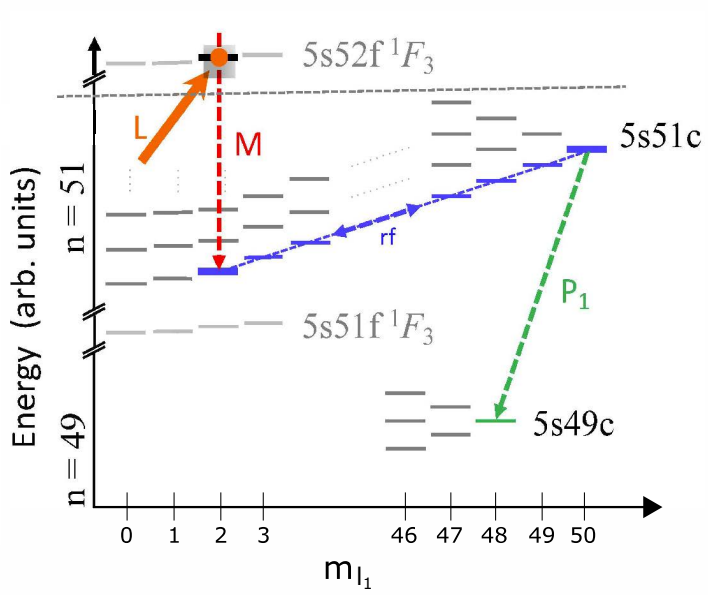

Figure 2.10: The principle of the experimental circularization of Strontium.

we leave the explanation of the adiabatic circularization to appendix B. In Sec. 2.3, we present some further optimisations on the circular Rydberg state. We start from the fine-tuning of the $\sigma+$ polarization of the rf pulse (paragraph 2.3.1) and conclude by showing how to use a Ramsey experiment to compensate for the gradient of the electric field perceived by the atoms (paragraph 2.3.2).

2.2.2 The preparation of the $|52^1F_3, m_{l_1} = +2\rangle$ Rydberg state

In our group, most previous experiments on circular states of Rubidium used principal quantum numbers $n \sim 50$. Those states are well suited for our purposes, since the atomic transitions between such neighboring manifolds are in the $44-60$ GHz range by one- or two-photon transitions. These frequencies are easily accessible via our MW sources. We aim for the manifold with $n = 52$ by scanning the frequency of a 1 μs long 896 nm laser pulse. The duration of the pulse derives from a compromise between saving enough time for the next MW, rf or laser pulses and having a large enough atomic sample to get a satisfactory signal-to-noise-ratio.

The extension of the frequency sweep is set to include the theoretical values of the atomic transition frequencies between the $|5s5d^1D_2\rangle$ state and the $|52^1F_3\rangle$ levels. The electric field is horizontal and imposes the quantization axis along the laser propagation. Its amplitude is of 60 V/m. We want it high enough so as to lift the degeneracy among the m_{l_1} levels of the $|52^1F_3\rangle$ group and to resolve the transitions leading to their preparation. We finally detect the Rydberg atoms by initially setting as a threshold for the detector the ionization voltage of the same states

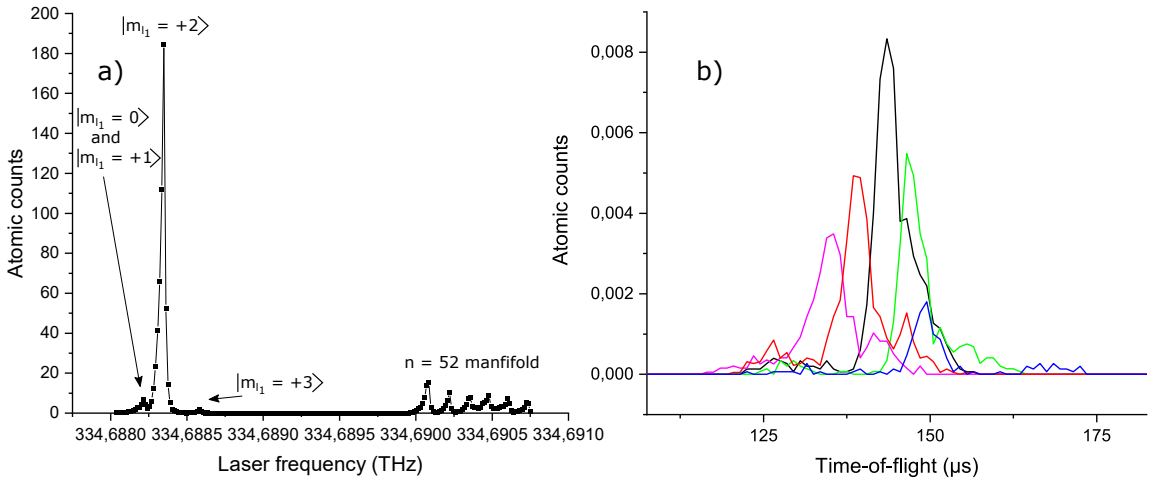

Figure 2.11: Laser spectrum of the Rydberg excitation to the $|52^1F_3\rangle$ states. The highest peak represents the transition to the $|52^1F_3, m_{l_1} = +2\rangle$ state. There are the $|52^1F_3, m_{l_1} = 0\rangle$, $|52^1F_3, m_{l_1} = +1\rangle$ transitions on its left (unresolved by our laser) and the $|52^1F_3, m_{l_1} = +3\rangle$ on the right. At very high frequency, we see the manifold of states with $n = 52$. We lock the frequency of our laser at the top of the $|52^1F_3, m_{l_1} = +2\rangle$ transition. The solid line is a guide for eye. b) Atomic counts as a function of the time-of-flight. We repeat the measurement for different Doppler corrections of the 896 nm laser frequency (black: 474 MHz, red: 479 MHz, green: 469 MHz, blue: 464 MHz, pink: 484 MHz). We set the Doppler correction in correspondence of the maximum atomic count recorded, centered upon a time of flight of (143.910 ± 0.057) μs from the Rydberg excitation. The 461 nm and 767 nm laser frequencies are both kept locked throughout the measurement.

for Rubidium. This ionization voltage is then optimized for Strontium.

Figure 2.11a shows the laser spectrum around the frequencies of the $|5s5d^1D_2\rangle \rightarrow |52^1F_3\rangle$ atomic transitions. We notice multiple peaks and attribute the highest to the $|52^1F_3, m_{l_1} = +2\rangle$ state, since the combination $\sigma+/\sigma+/\pi$ for the polarizations of the lasers performing the Rydberg excitation is set to maximize its population. The minor peak on its left is associated the transitions leading to the $|52^1F_3, m_{l_1} = +1\rangle$ and $|52^1F_3, m_{l_1} = +0\rangle$ states. The Doppler width of the atoms, together with the electric field inhomogeneity, does not allow us to resolve them individually. The peak on the right is attributed to the transition to the $|52^1F_3, m_{l_1} = +3\rangle$ state. At higher laser frequencies, we excite the $n = 52$ manifold. We lock the laser to the frequency of the maximum transfer to $|52^1F_3, m = +2\rangle$.

2.2.3 The selection of the velocity class

The oven ejects a flux of atoms, with very broad thermal distribution, which undergo the Doppler effect. This is a combination of the individual Doppler effects, each related to a laser beam contributing to the Rydberg excitation. To select the velocity class, we fine tune the 896 nm frequency. We do this by scanning the frequency of the EOM, which acts on the portion of the

beam directed to the cavity, and by recording a time-of-flight experiment for each laser frequency. Thus, we set the $|52^1F_3, m_{l_1} = +2\rangle$ ionization field on the detector and measure the amount of Rydberg atoms as a function of a time window. We repeat this experiment and draw a curve for various frequency corrections of the EOM to study the velocity profile (figure 2.11b). We finally set the Doppler correction so as to work with a velocity class with a time-of-flight of (143.910 ± 0.057) μs from the Rydberg excitation. Counting 61 mm of distance from the lasers crossing point to the detector, this time-of-flight corresponds to a velocity of the atom of around $v_0 = 423.87$ m/s along the direction of propagation of the atomic beam.

2.2.4 The preparation of the $|51^1G_4, m_{l_1} = +2\rangle$ Rydberg state

The $|F\rangle$ levels of Strontium join the manifold at very high electric field. This is an important complication with respect to the circularization of Rubidium. The solution to this problem would be to access, by use of laser pulses, a state which joins the manifold at lower electric field. Since the number of lasers at our disposal enables us to prepare $|F\rangle$ states only (it is possible to perform only a step of $\Delta l_1 = 1$ for each beam), we optically access $|52^1F_3, m_{l_1} = +2\rangle$ and transfer the population via a MW pulse to another class of states which joins the manifold at lower electric field. Given the accessible frequency range of our MW sources, we can only produce one-photon transitions to $n = 51$ or $n = 53$ states or two-photon transitions to $n = 50$ or $n = 54$. There is no reason to prefer a two-photon transition. The logical choice is therefore to transfer the atoms from $|52^1F_3, m_{l_1} = +2\rangle$ to the $n = 53$ or $n = 51$ manifold via a one-photon transition. We risk to slightly exit the range of available frequencies if we opt for $n = 53$, either at this stage of the experiment or when other MW transitions between the same manifolds are induced. We therefore go for the $n = 51$ manifold.

To understand the Stark effect of the $n = 51$ manifold and consequently find our route to the circular Rydberg state, we record some MW spectra of the atomic transitions having $|52^1F_3, m_{l_1} = +2\rangle$ as an initial state and the $n = 51$ manifold as a target. The MW spectra are collected in the Stark diagram reported in figure 2.12. Around 48 GHz of distance from $|52^1F_3, m_{l_1} = +2\rangle$, we find the $|51^1F_3\rangle$ set of states, at around 46 GHz we see the $|51^1G_4\rangle$ states and finally between 44 and 45 GHz, we detect the $|51^1H_5\rangle$ states.

We aim to access a $|G\rangle$ state. The selection rule narrows down the choice to $|51^1G_4, m_{l_1} = +1\rangle$, $|51^1G_4, m_{l_1} = +2\rangle$ or $|51^1G_4, m_{l_1} = +3\rangle$. We opt for $|51^1G_4, m_{l_1} = +2\rangle$ since it presents an excellent transfer when prepared from $|52^1F_3, m_{l_1} = +2\rangle$. To access $|51^1G_4, m_{l_1} = +2\rangle$, we apply a MW pulse after the lasers. Its duration is 0.2 μs only, so as to mitigate the effect of the electric field noise that broadens the peaks. The detector is set at an ionization threshold slightly increased with respect to that of $|52^1F_3, m_{l_1} = +2\rangle$, since we expect a state with $n = 51$ to be harder to ionize.

We record the spectrum of the MW driving the transition between $|52^1F_3, m_{l_1} = +2\rangle$ and

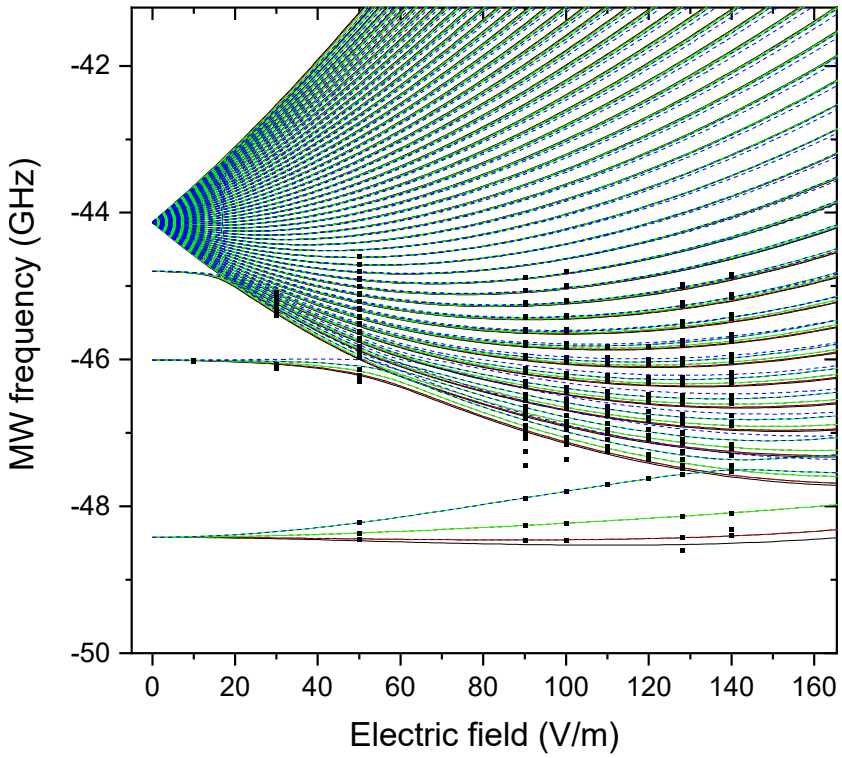

Figure 2.12: Data of spectroscopy experiments (black points) and calculations (lines) on the atomic transition frequencies from $|52^1F_3, m_{l_1} = +2\rangle$ to the $n = 51$ manifold. The set of states whose position at zero field is at a distance around 48 GHz from $|52^1F_3, m_{l_1} = +2\rangle$ is the $|F\rangle$ set. Above, we have first the $|G\rangle$, around 46 GHz, and finally the $|H\rangle$ states close to 45 GHz. The experimental points unfitted by the calculations are consistent with the expected frequency distance between the $|52^1F_3, m_{l_1} = +2\rangle$ Rydberg state and some energy levels of the $n = 53$ manifold.

the $|51^1G_4\rangle$ states (figure 2.13). We associate the peak to the transition $|52^1F_3, m_{l_1} = +2\rangle \rightarrow |51^1G_4, m_{l_1} = +2\rangle$, following the indications given by the simulations of the same Stark diagram for Rubidium and after verifying the ionization voltages of all the other accessed levels (not displayed here) appearing in the MW spectrum. We set the frequency of the MW to the transfer peak. This yields around 87.3% of transfer efficiency. This value is retrieved as the simple ratio between the atomic counts detected at the ionization threshold of $|51^1G_4, m_{l_1} = +2\rangle$ after the MW pulse and the atomic counts detected at the ionization threshold of $|52^1F_3, m_{l_1} = +2\rangle$ before the MW pulse.

Up to this point, all laser and MW manipulations were performed in a horizontal electric field. Yet, the polarization of the rf field is defined as $\sigma+$ with respect to the vertical axis of the system. The horizontal electric field is therefore ramped down in 1 μs while the vertical electric field is raised in 0.5 μs. The latter duration is a compromise between saving enough time for next events and make the atoms follow adiabatically the rotation of the quantization axis. When this

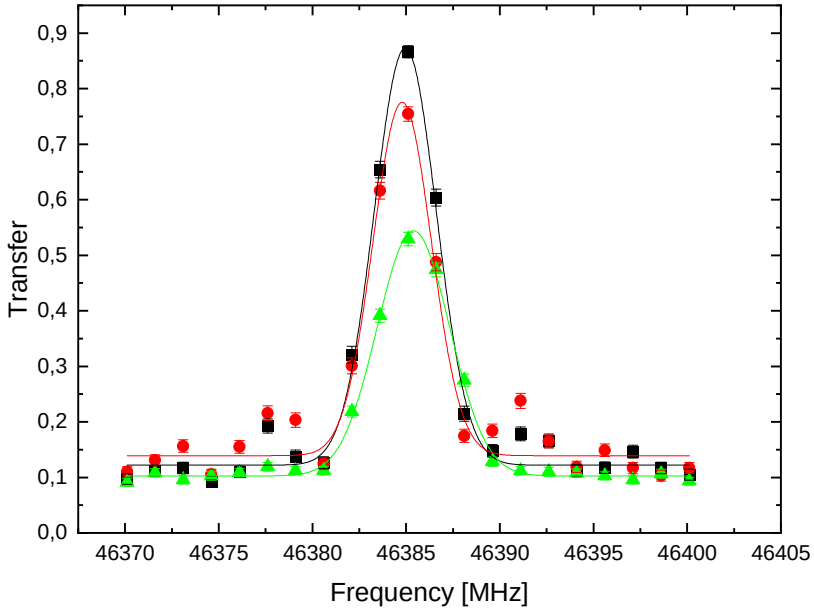

Figure 2.13: MW spectrum of the $|52^1F_3, m_{l_1} = +2\rangle \rightarrow |51^1G_4, m_{l_1} = +2\rangle$ transition. Colored points are the data, the lines are Gaussian fits. We repeat the experiment for various MW powers to maximize the transfer. The power of the MW source is lowered by 2 dBm from the black curve to the red curve and again from the red and green one. The MW pulse duration is 0.2 μs. This explains the large width of the transition.

transformation is accomplished, the quantization axis will have the same direction of the vertical electric field. It will be maintained this way for the rest of this work. After the ramp, the final amplitude of the vertical electric field depends on the manipulation we want to do on the atoms: the circularization requires an electric field which makes the Rydberg ladder resonant with the rf pulse we are going to apply. Our next step is therefore selecting this value for the amplitude of the electric field.

2.2.5 The harmonicity of the $|n = 51, n_1 = 0, m_{l_1} > 0\rangle$ ladder

Our goal is to have a rf field with single frequency that couples neighbouring Rydberg states with $m_{l_1} \geq 2$ along a ladder. It needs a pure $\sigma+$ polarization and a frequency resonant with the same ladder. Therefore, we look for an electric field which satisfies two conditions. First, the atomic transition frequency between the Rydberg state with magnetic quantum number $|m_{l_1}\rangle$ and that with number $|m_{l_1} + 1\rangle$ must be always the same for all values of $m_{l_1} \geq 2$. Second, the rf field should not induce the transition from $|n = 51, n_1 = 0, m_{l_1} = +2\rangle$ to $|n = 51, n_1 = 0, m_{l_1} = +1\rangle$. We

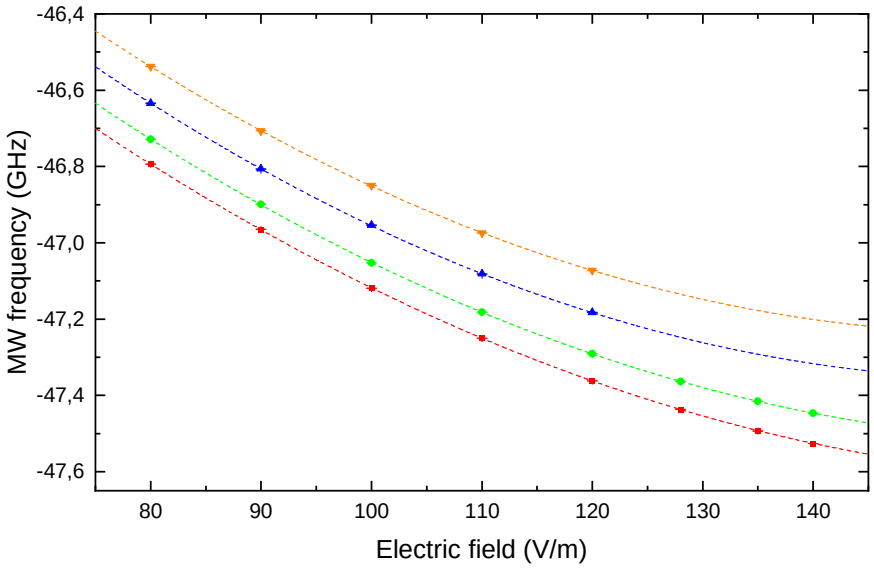

Figure 2.14: Energy difference between the $|51^1G_4\rangle$ states and the $|52^1F_3, m_{l_1} = +2\rangle$ state as a function of the electric field. The points are experimental data (red: $|51^1G_4, m_{l_1} = +1\rangle$, green: $|51^1G_4, m_{l_1} = +2\rangle$, blue: $|51^1G_4, m_{l_1} = +3\rangle$, orange: $|51^1G_4, m_{l_1} = +4\rangle$), whereas the lines indicate parabolic fits. At 112.2 V/m, the energy difference between neighboring states is similar for all states from $|m_{l_1} = +2\rangle$ on.

thus select an electric field for which, due to the quantum defects of the lowest-m_{l_1} states, that transition is out of resonance with respect to the transitions between all the other neighbouring states of the ladder.

The easiest way to obtain the electric field of interest is to study the spacing between neighbouring m_{l_1} states of the Rydberg ladder of the $n = 51$ manifold as a function of the electric field amplitude. We do this by first preparing the state $|52^1F_3, m_{l_1} = +2\rangle$, next scanning the frequency of a MW pulse and finally detecting the atoms prepared in any of the $|51^1G_4\rangle$ states as a function of the MW frequency. The sequence is repeated for several values of the vertical electric field applied by the electrodes in the cryostat.

Figure 2.14 reports the atomic transition frequencies of those transitions observed when recording the spectrum of a MW pulse transferring the atoms to the $|51^1G_4\rangle$ states. According to the selection rule, we detect the atoms arriving in the only $|51^1G_4, m_{l_1} = +1\rangle$, $|51^1G_4, m_{l_1} = +2\rangle$, $|51^1G_4, m_{l_1} = +3\rangle$ states. The data on $|51^1G_4, m_{l_1} = +4\rangle$ are instead retrieved after preparing $|52^1F_3, m_{l_1} = +3\rangle$ instead of $|52^1F_3, m_{l_1} = +2\rangle$ via the laser beams and next scanning the MW pulse frequency.

Overall, we see that the spacing between neighboring m_{l_1} levels becomes similar around 110

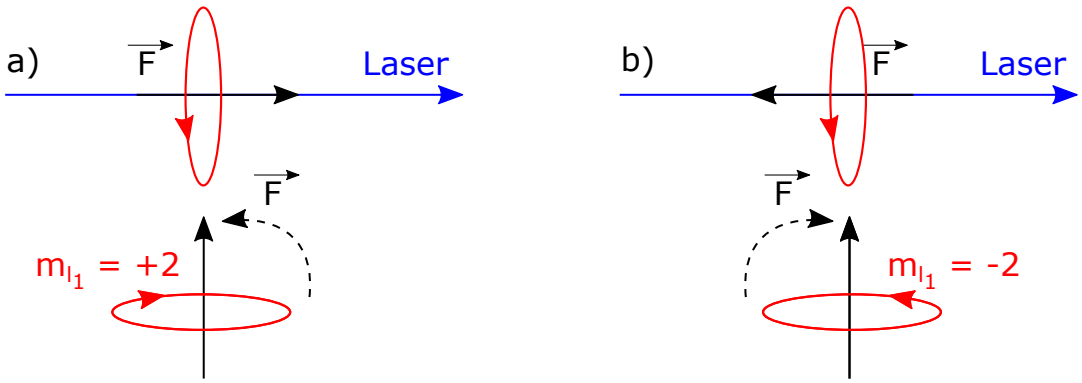

Figure 2.15: Rotation (dashed line) of the horizontal electric field (solid, black line) applied on the atomic beam, starting from a parallel (a) or anti-parallel (b), horizontal orientation of the electric field with respect to the direction of the 461 nm laser beam (solid, blue line). Case a) leads to the preparation of a $|m_{l_1} > 0\rangle$ state, case b) to the preparation of a $|m_{l_1} < 0\rangle$ state. For the purpose of our experiment, we are interested in accessing $|52^1F_3, m_{l_1} = -2\rangle$.

V/m. Next, we fine-tune the electric field so as to optimize the hamornicity of the Rydberg ladder from $|m_{l_1} = +2\rangle$ on. Following this, the selected value of the electric field is 112.2 V/m. The Stark frequency at that value of the electric field is 110 MHz. When resonant at that frequency, the rf field can now couple the levels from $|m_{l_1} = +2\rangle$ on, until the highest point of the same ladder, which is the circular state $|51c\rangle$. We have now a candidate for the electric field and one for the rf frequency.

2.2.6 The optimization of the σ+ component of the polarization for the radio-frequency field

Obtaining the resonance frequency of the ladder is not sufficient to circularize, we also need to optimize the polarization of the rf pulse. Only an ideal σ+ pulse guarantees the preparation of the circular states. This subsection discusses this aspect of the experiment. To make the notation simpler, we omit the parabolic quantum number when we report the quantum states. Also, the principal quantum number of the states mentioned in this section is always $n = 52$.

To have a pure σ+ rf field, we need to minimize the σ- component. To that end, we look for a two-level system coupled to a σ- field. Unfortunately, all energy levels accessible from $|m_{l_1} = +2\rangle$ along the ladder can be coupled with a σ+ field only. However, all transitions from $|m_{l_1} = -2\rangle$ need a σ- field. Therefore, our strategy is to laser excite $|m_{l_1} = -2\rangle$ and set the electric field so that the $|m_{l_1} = -2\rangle \rightarrow |m_{l_1} = -3\rangle$ transition frequency is 110 MHz.

Thus, we invert the electric field with respect to the direction of the 461 nm laser propagation and apply the laser beams. In this way, we prepare $|52^1F_3, m_{l_1} = -2\rangle$ (figure 2.15). Next, we ramp

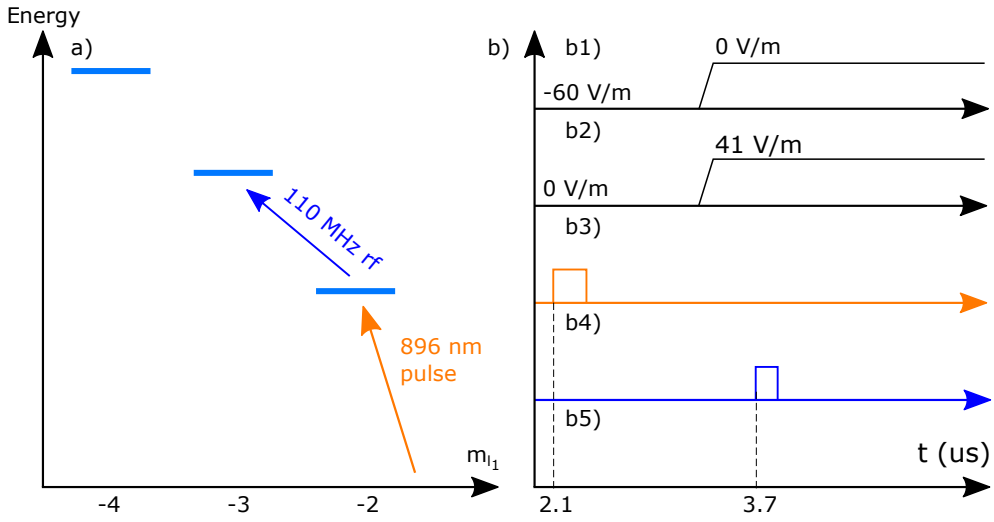

Figure 2.16: Energy levels scheme of the $|m_{l_1} < 0\rangle$ Rydberg states on use for the calibration of the rf polarization. We need the $|52^1F_3, m_{l_1} = -2\rangle \rightarrow |52^1F_3, m_{l_1} = -3\rangle$ transition resonant at 110 MHz. To that end, we vary the electric field until finding the value making the spacing between the two Rydberg states equal to 110 MHz. Then, we are ready to work on the power and phase of the rf pulse to suppress the σ- component of its polarization. b) Sequence of events applied for the optimization of the polarization of the rf pulse. b1) indicates the horizontal component of the electric field, b2) the vertical component, b3) the MW pulse, b4) the rf pulse and b5) the time axis.

down (up) the horizontal (vertical) component of the electric field. We set a rf pulse to induce the $|52^1F_3, m_{l_1} = -2\rangle \rightarrow |52^1F_3, m_{l_1} = -3\rangle$ transition (figure 2.16) and record, for several values of the electric field, the Rabi oscillations. They evolve in time at a frequency equal to $\sqrt{\Omega_{rf}^2 + \Delta_{rf}^2(F)}$, where $\Delta_{rf}(F)$ is the detuning of the rf pulse. Our goal is to identify the minimum frequency of the Rabi oscillations, yielding the optimal electric field that makes the atomic transition $|52^1F_3, m_{l_1} = -2\rangle \rightarrow |52^1F_3, m_{l_1} = -3\rangle$ resonant at 110 MHz (figure 2.17). That optimal electric field has 41 V/m as amplitude. The duration of the rf pulse is chosen long enough so as to isolate a two-level system out of the $|52^1F_3, m_{l_1} = -2\rangle$, $|52^1F_3, m_{l_1} = -3\rangle$ levels. This duration is 200 ns.

We can now work with the two-level system composed by the $|52^1F_3, m_{l_1} = -2\rangle$, $|52^1F_3, m_{l_1} = -3\rangle$ levels. We set the electric field at 41 V/m, apply a 200 ns long, rf pulse, produced by the ring electrodes H_1 and H_2, and measure the transfer efficiency of the pulse as a function of the power or phase imposed by one electrode. The power and phase of the other are varied synchronously with the same step and number of steps. The population $|52^1F_3, m_{l_1} = -3\rangle$ is minimized when the rf field has the minimal σ- component. Therefore, we set the power and phase of the two rf channels in use at the minimum transfer between the two Rydberg levels (figure 2.18a). In this way, we achieve an optimal σ+ polarization of the rf field.

In principle, H_1 and H_2 are sufficient to provide a satisfactory $\sigma+$ polarization. However, the amplitude of the rf field depends on the distance between the electrodes on use and the atoms. Since the atoms propagate from left to right in the Cartesian reference of the experiment, the rf field produced by H_1 and H_2 becomes less efficient as a function of the space travelled by the atoms, whereas that produced by H_3 and H_4 becomes more efficient. For the sake of homogeneity of the rf field perceived by the atoms in each position of the trajectory, we repeat the procedure with H_4 and H_3 and balance the power of the pairs H_1, H_2 and H_3, H_4 to have the most homogeneous rf field along the trajectory of the beam. Ultimately, the atoms perceive a total, homogeneous rf field resulting from the constructive interference between the two rf pulses. To verify this, we switch back to the preparation of $|52^1F_3, m_{l_1} = +2\rangle$, apply a rf pulse exciting the atoms to $|52^1F_3, m_{l_1} = +3\rangle$ and measure the Rabi frequency of the $|52^1F_3, m_{l_1} = +2\rangle \rightarrow |52^1F_3, m_{l_1} = +3\rangle$ transition as a function of the application time of the rf field. This is done when all four ring electrodes producing the rf pulse are switched on simultaneously (figure 2.18b). The measured Rabi frequency now shows a steady behaviour as a function of time. We conclude that we can work with a homogeneous rf field when exciting the atoms along the Rydberg ladder.

2.2.7 The preparation of a high-l_1 state

The rf pulse, if properly polarized and resonant with the ladder, prepares the circular state. Unfortunately, it also populates other Rydberg states with high l_1 and similar m_{l_1} to that of the circular state. Since the circular state and the undesired elliptical states with high-l_1 share a similar range of ionization voltages, we are unable to distinguish them at the detection stage (figure 2.19a). To do that, we make use of MW pulsed probes.

The principle of a MW probe is to transfer the population from a state ψ_{in} to another one ψ_{tg}, ionizing at a quite different electric field. This technique is useful when the detection threshold of ψ_{in} is too close to that of other states to measure its population independently.

In our experiment, we often make use of probes transferring the population of a quantum state by two manifolds. To prepare a probe accomplishing this task, we need to settle a frequency, a starting time and a duration for our MW pulse. For the frequency, we start by preparing the $|n = 51, n_1 = 0, m_{l_1}\rangle$ Rydberg state via a rf pulse of duration τ. Next, we sweep the frequency of a MW pulse and detect the Rydberg atoms transferred to the $n = 49$ manifold. We finally set the frequency of the MW at the transfer peak. This is chosen after fitting the transition line by a Gaussian curve. Note that the MW frequency sweep takes place at an electric field of 144.6 V/m since the Rydberg-to-Rydberg transitions between the $n = 51$ manifold and the $n = 49$ manifold are well known at this field. Afterwards, we work on the starting time t_P of the probe. This parameter is determined by a map, recorded when the MW pulse is in resonance with the atomic

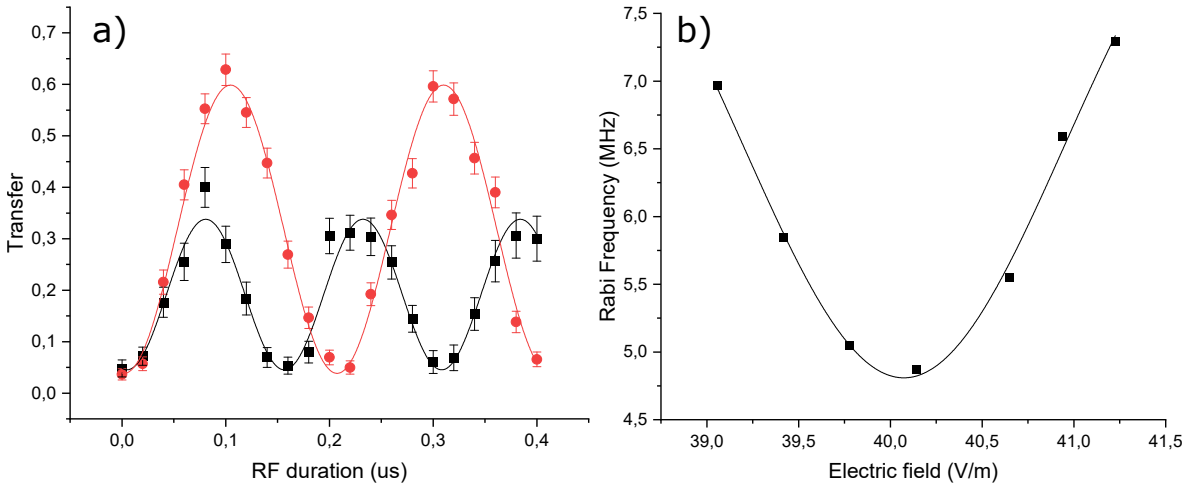

Figure 2.17: a) Rabi oscillations between the $|52^1F_3, m_{l_1} = -2\rangle$, $|52^1F_3, m_{l_1} = -3\rangle$ states. Black squares indicate the result of the experiment at the guess value of the electric field whereas the red circles when the resonant field is found. Solid lines are sinusoidal fits. For each of them, we extract the Rabi frequency. b) Rabi frequency as a function of the electric field. We fit the data with a parabolic lineshape for simplicity. The minimum frequency yields the optimal electric field.

transition frequency of interest, of the spatial structure of the mode produced by the MW source. As a last optimization, we perform a Rabi experiment by sweeping the MW pulse duration at constant power. We choose the duration which maximizes the transfer.

Figure 2.19b presents the results of this experiment for several values of τ. We identify the two-photon transitions between the ladder of Rydberg states in the $n = 51$ and that of the $n = 49$ manifold. Notably, each detected transition between $|n = 51, n_1 = 0, m_{l_1}\rangle$ and $|n = 49, n_1 = 0, m_{l_1} - 2\rangle$ is a good candidate to calibrate a MW probe for the Rydberg state $|n = 51, n_1 = 0, m_{l_1}\rangle$. For the moment though, we are interested only in those transitions useful to prepare the probes of the circular state and the elliptical states with $m_{l_1} \sim n$. Table 2.1 summarizes the specifics of each probe calibrated for the transitions of interest. We also report that for $|n = 51, n_1 = 1, m_{l_1} = 49\rangle$, which is the first level met along the Rydberg ladder above the circular state. It will be useful in the final section of this work.

Table 2.1: Specifics of the probes for high-l_1 Rydberg states of Strontium.

Transition	MW Frequency (GHz)	Pulse duration (μs)
$\|51c\rangle \rightarrow \|49c\rangle$	52.67877376	1.05
$\|n = 51, n_1 = 0, m_{l_1} = 49\rangle \rightarrow \|n = 49, n_1 = 0, m_{l_1} = 47\rangle$	52.67600493	1.06
$\|n = 51, n_1 = 0, m_{l_1} = 48\rangle \rightarrow \|n = 49, n_1 = 0, m_{l_1} = 46\rangle$	52.67321504	1.23
$\|n = 51, n_1 = 1, m_{l_1} = 49\rangle \rightarrow \|n = 49, n_1 = 1, m_{l_1} = 47\rangle$	52.68154241	1.05

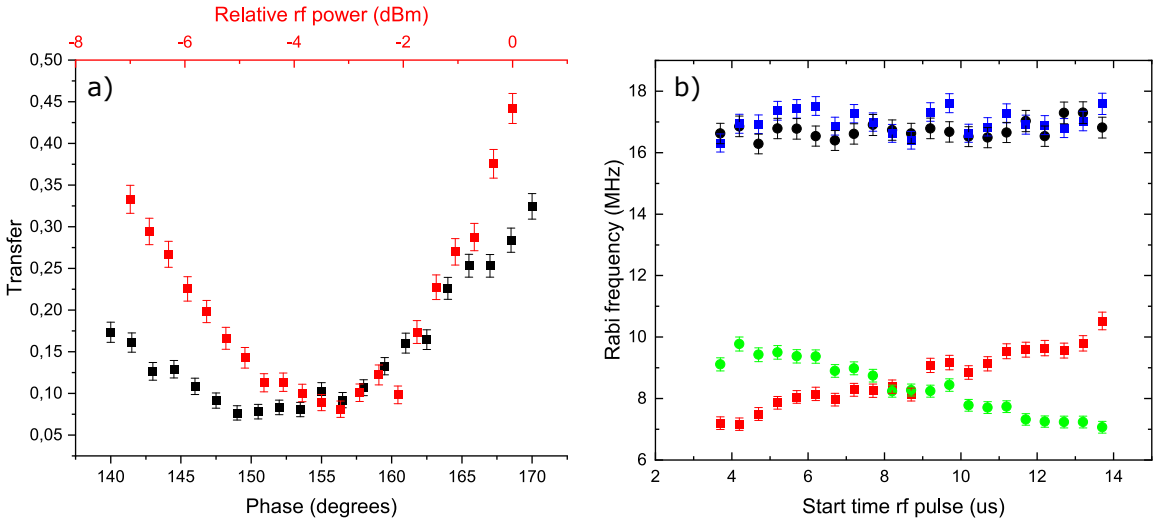

Figure 2.18: a) Transfer from $|52^1F_3, m_{l_1} = -2\rangle$ to $|52^1F_3, m_{l_1} = -3\rangle$ as a function of the phase (black squares) or the power (red squares) of the rf pulse produced by the H_i channel. b) Test of the homogeneity of the rf field perceived by the atoms after the calibration, as a function of the position along their trajectory. Green data are recorded for a rf pulse produced by H_1 and H_2, red data when produced by H_3 and H_4. Black data are recorded when all the electrodes are switched on at the same time. Blue data are an arithmetical sum of green and red data, to check for the consistency of the black data.

2.2.8 The preparation of the circular state by Rabi pulse

It is time to make use of the probes. We use that of the circular state to optimize the duration of the rf field transferring the population from $|m_{l_1} = +2\rangle$ to the high-l_1 state. We sweep the duration of this rf pulse and measure the population of $|51c\rangle$ and the elliptical states with the closest m_{l_1} via the respective probes. The timing of the sequence is presented in figure 2.20.

Figure 2.21a shows the result of this experiment. Increasing the duration of the rf pushes the population away from the level $|n = 51, n_1 = 0, m_{l_1} = 2\rangle$ to higher m_{l_1} states progressively. The optimal rf duration, 189 ns, allows us to arrive close to the north pole of the Bloch sphere where we prepare the circular state. The estimated efficiency of the Rabi passage at its best is 85%. Note that, even at the optimized duration, some undesired elliptical components with m_{l_1} close to that of the circular state still perturb the circularization. The presence of $|n = 51, n_1 = 0, m_{l_1} = 48\rangle$ is an example of these resilient, elliptical components. We estimate the population left in $|n = 51, n_1 = 0, m_{l_1} = 48\rangle$ to be around 5%. A further increase of the rf duration pushes the population in the direction of the south pole, visiting the same elliptical levels already accessed during the climb, reversely. This explains the two side-peaks for the elliptical states $|n = 51, n_1 = 0, m_{l_1} = 49\rangle$ and $|n = 51, n_1 = 0, m_{l_1} = 48\rangle$.

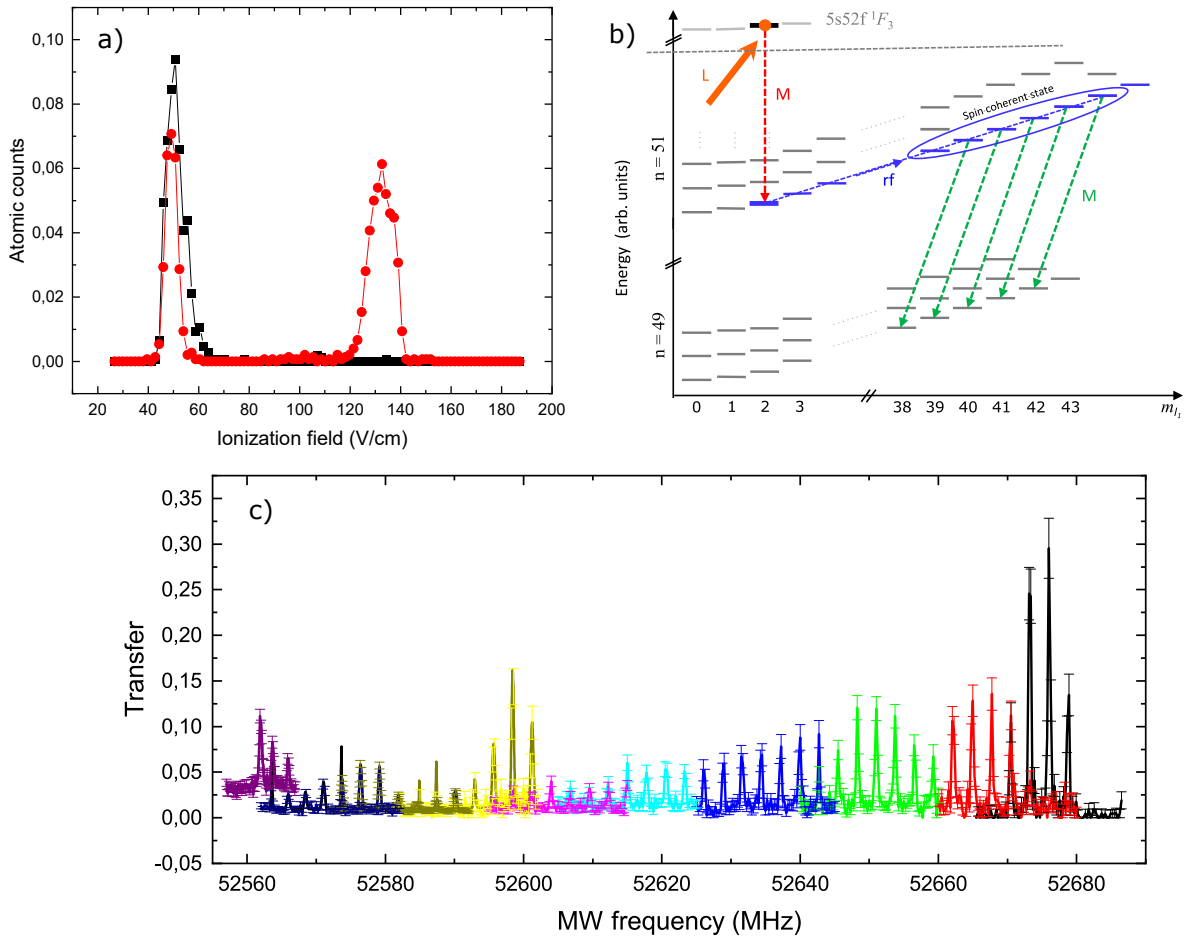

Figure 2.19: a) Ionization signal showing the preparation of a superposition of high-l_1 Rydberg states (red points), from a low-l_1 state (black points). The preparation is not optimal given the amount of population not transferred by the rf pulse. Solid lines are guides for the eye. b) Navigation in the Hilbert space following our laser, MW and rf events for the calibration of the probes. c) Two-photon MW transitions from the $|n = 51, n_1 = 0, m_{l_1}\rangle$ states to the $|n = 49, n_1 = 0, m_{l_1} - 2\rangle$ states. The experiment is performed for several values of the rf pulse duration (black data: 190 ns, red data: 160 ns, green data: 140 ns, blue data: 120 ns, light blue data: 100 ns, pink data: 90 ns, yellow data: 80 ns, dark yellow data: 60 ns, dark blue data: 40 ns, violet data: 30 ns).

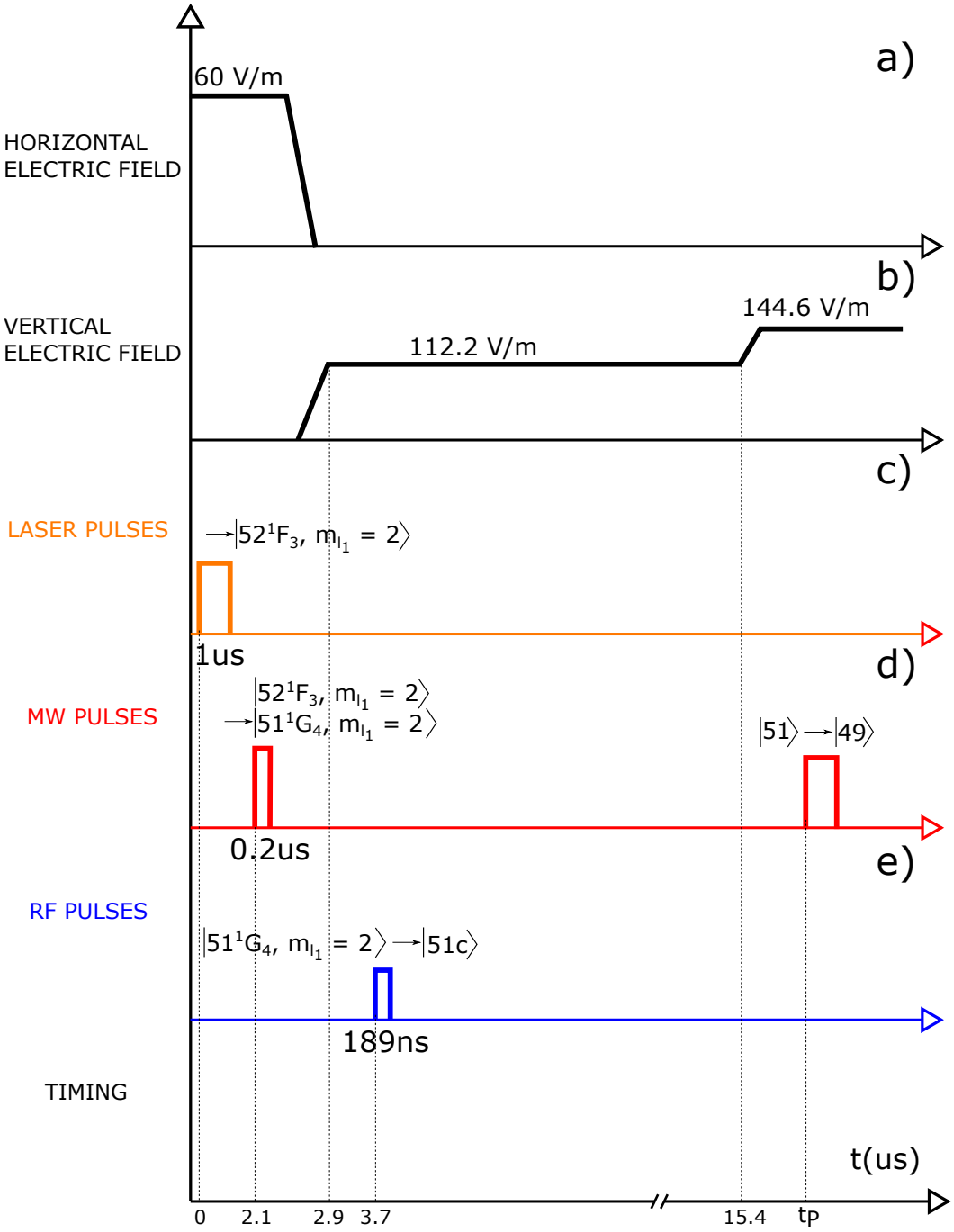

Figure 2.20: The sequence enabling the circularization of Strontium. At 60 V/m, a 1 μs 896 nm π polarized pulse c) prepares the atoms in a low-l_1 state. Next, the horizontal field a) is ramped down while the vertical component b) is switched on. A 200 ns MW pulse d) transfers the population in the $n = 51$ manifold and finally a rf pulse e) finalizes the preparation of the circular state. We apply a MW probe to measure the population of $|51c\rangle$.

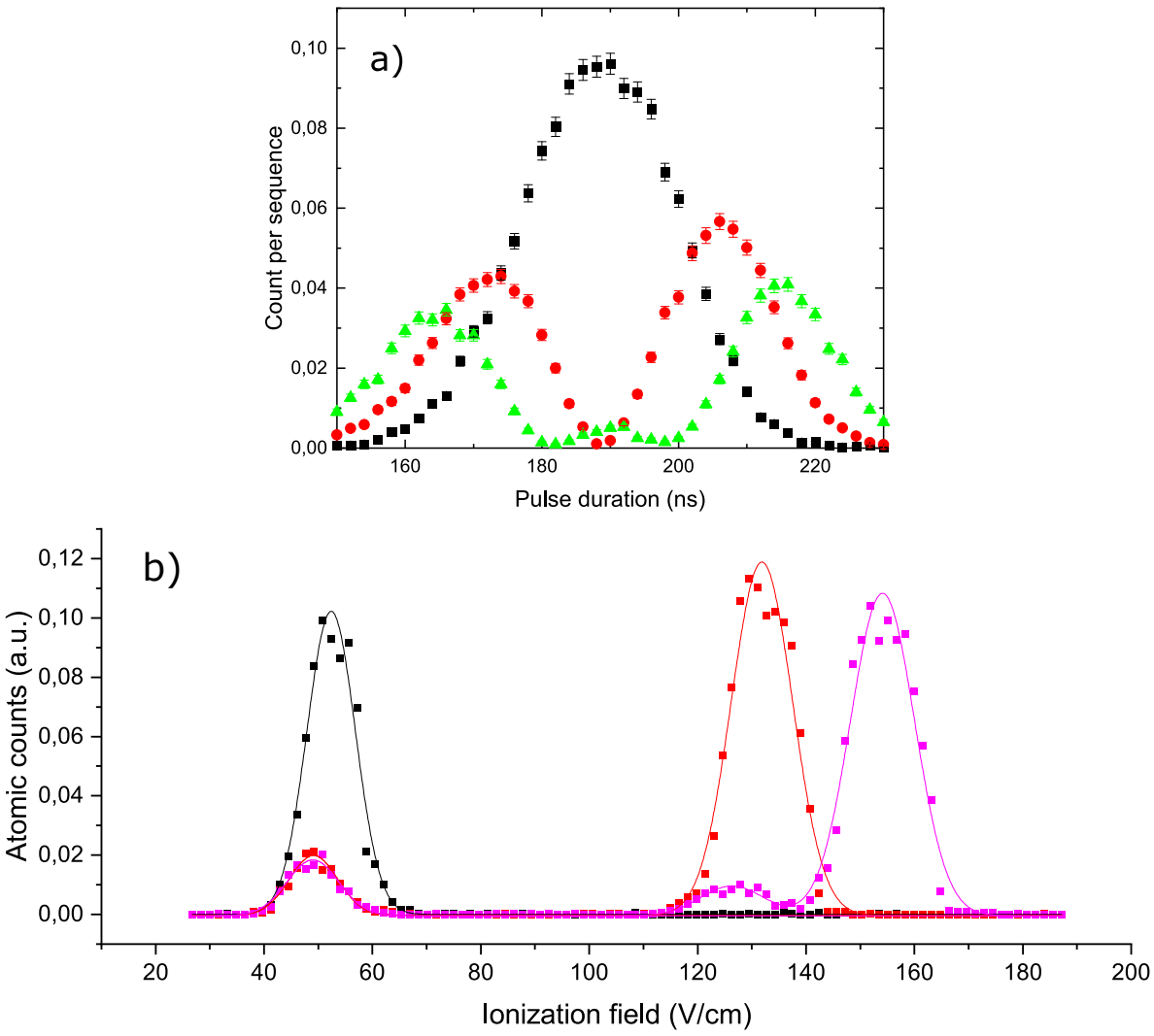

Figure 2.21: a) Circularization by Rabi π pulse. We measure the population of $|51c\rangle$ (black points), $|n=51, n_1=0, m_{l_1}=49\rangle$ (red points) and $|n=51, n_1=0, m_{l_1}=48\rangle$ (green points) by use of MW pulsed probes. b) Ionization signals. Black data indicate the starting level of the circularization $|51^1G_4\rangle$. Red data show the preparation of $|51c\rangle$. Note that the remaining ionization signal at low voltage indicates both the atoms not transferred by the MW pulse at 2.1 μs and those not transferred by the rf pulse to $|51c\rangle$. Violet data display the effect of the MW probe on $|51c\rangle$: the population is transferred to $|49c\rangle$, at higher ionization fields. Solid lines are Gaussian fits

Figure 2.21b displays the effect of a probe applied on the circular state. The rf field prepares a superposition of high-l_1 states dominated by the circular component. Such a state ionizes at a threshold of (131.86 ± 0.11) V/cm. The probe transfers the $|51c\rangle$ population to the $|49c\rangle$ state, which ionizes at (154.11 ± 0.12) V/cm where none of the other levels of the superposition ionize. The remaining atoms at (126.34 ± 1.28) V/cm belong to the elliptical components of the superposition not affected by the probes.

2.3 Final optimizations

Before switching to the core manipulation experiments reported in the next chapter, we perform some final optimizations on the experiment. The next section presents the fine-tuning of the rf polarization, this time optimized by suppressing the efficiency of preparation of a high-l_1 Rydberg state, and the compensation, via a Ramsey experiment, of the electric field gradient perceived by the atomic packet.

2.3.1 The suppression of the $|n = 51, n_1 = 1, m_{l_1} = 49\rangle$ signal

We perform a fine tuning of the rf polarization. This is now done while recording the population of a high-m_{l_1} state instead of a low-m_{l_1} state. As before, we scan phase and power of H2 and H4 together. The difference between the phase of H2 and that of H4, as well as the ratio between the powers, is maintained constant throughout the scan. We record the population of $|n = 51, n_1 = 1, m_{l_1} = 49\rangle$, which we prepare by use of a 189 ns long rf pulse and detect with a probe (figure 2.22a). The state $|n = 51, n_1 = 1, m_{l_1} = 49\rangle$, as all the energy levels of the upper diagonal, couples to the residual σ- component of the rf pulse. This implies that, as the phase moves away from the optimal value (~ 152.7 °C) during the scan, eventually the polarization of the Rabi pulse is so wrong that the rf field starts populating the energy levels of the upper diagonal (figure 2.22b). We set the phases of our electrodes at the value corresponding to the minimum amount of atoms prepared in $|n = 51, n_1 = 1, m_{l_1} = 49\rangle$.

Figure 2.22c presents an evidence of the improvement of the circular-to-circular transfer once the rf pulse is finely tuned. The transfer, at the atomic transition frequencies corresponding to the transitions $|n = 51, n_1 = 1, m_{l_1} = 49\rangle \rightarrow |n = 49, n_1 = 1, m_{l_1} = 47\rangle$, $|n = 51, n_1 = 1, m_{l_1} = 48\rangle \rightarrow |n = 49, n_1 = 1, m_{l_1} = 46\rangle$, is suppressed since no important amount of atoms is pushed by the rf pulse on the upper ladder when the σ- component is minimized. This MW scan is a valid check of the fulfillment of the optimization of the rf field.

2.3.2 The gradient field compensation

To have a good transfer efficiency from $|51^1G_4, m_{l_1} = +2\rangle$ to $|51c\rangle$, one needs to have a homogeneous electric field at the position of the atomic beam.

The circular Rydberg state is insensitive to the linear Stark effect. On the contrary, the state $|n = 52, n_1 = 0, m_{l_1} = 50\rangle$ presents a non-zero linear dependency upon the electric field amplitude along the quantization axis. This fact suggests to use the atomic transition frequency between $|51c\rangle$ and $|n = 52, n_1 = 0, m_{l_1} = 50\rangle$ via a Ramsey experiment to measure if the electric field perceived by our atomic packet of finite size presents any inhomogeneity.

We model the two-level system by a Bloch sphere with the south and north poles occupied by $|51c\rangle$ and $|n = 52, n_1 = 0, m_{l_1} = 50\rangle$ respectively. We apply a MW $\pi/2$ pulse between these levels at a moment t_0 and a second one at $t_0 + \Delta t$. Let τ_1 and τ_2 be their lengths. The first pulse prepares the atom in a quantum, balanced superposition of $|51c\rangle$ and $|n = 52, n_1 = 0, m_{l_1} = 50\rangle$. Its phase Φ precesses around the $\mathbf{z}$ axis of the Bloch sphere during Δt. The precession frequency, in the rotating frame, is $\delta\omega = \omega_{St}(F) - \omega_{MW}$, thus the difference between the atomic transition frequency between the two Rydberg levels, which depends on the electric field, and the MW frequency. If the number of phase cycles around the equator is an integer, the second $\pi/2$ pulse finalizes the preparation of $|n = 52, n_1 = 0, m_{l_1} = 50\rangle$. If it is instead a half-integer, the atoms go entirely back to $|51c\rangle$.

If the field is homogeneous, the phases of all the atoms precess at the same frequency. They do not accumulate any phase difference between one another before the second $\pi/2$ pulse, hence all producing the same superposition $\alpha|51c\rangle + \beta|n = 52, n_1 = 0, m_{l_1} = 50\rangle$, eventually with $\alpha = 0$ or $\beta = 0$ if the phase is set accordingly, at the end of the sequence. What we measure is the average $\overline{T}$ of the transfers of all the atoms. In this ideal case, this quantity evolves between 0 and 1.

If the field is not homogeneous, each atom perceives a slightly different value of the electric field, adjusts its energy accordingly, resulting into a different transition frequency between its two Rydberg levels and therefore a different precession frequency. The ith atom thus oscillates around the equator at frequency ω_i, ending up with a corresponding phase Φ_i, and produces a superposition $\alpha(\Phi_i)|51c\rangle + \beta(\Phi_i)|n = 52, n_1 = 0, m_{l_1} = 50\rangle$. Next, we apply the second MW pulse. We measure again the average of the transfers. This time, $\overline{T}$ is not ideally spanning the range $[0, 1]$ but is reduced. The contrast of $\overline{T}$ is proportional to the dispersion of the precession frequencies, thus determined by the discrepancy between the electric field perceived by one atom and the other.

We approach as close as possible to the first situation of a homogeneous electric field. To that end, we repeat the Ramsey experiment for several values of the DC voltage applied on the ring electrodes, in order to make the electric field as homogeneous as possible along the horizontal axis, until reaching the maximum Ramsey contrast.

We prepare two $\pi/2$, MW pulses. By construction of our set-up, it is easier for us not to scan

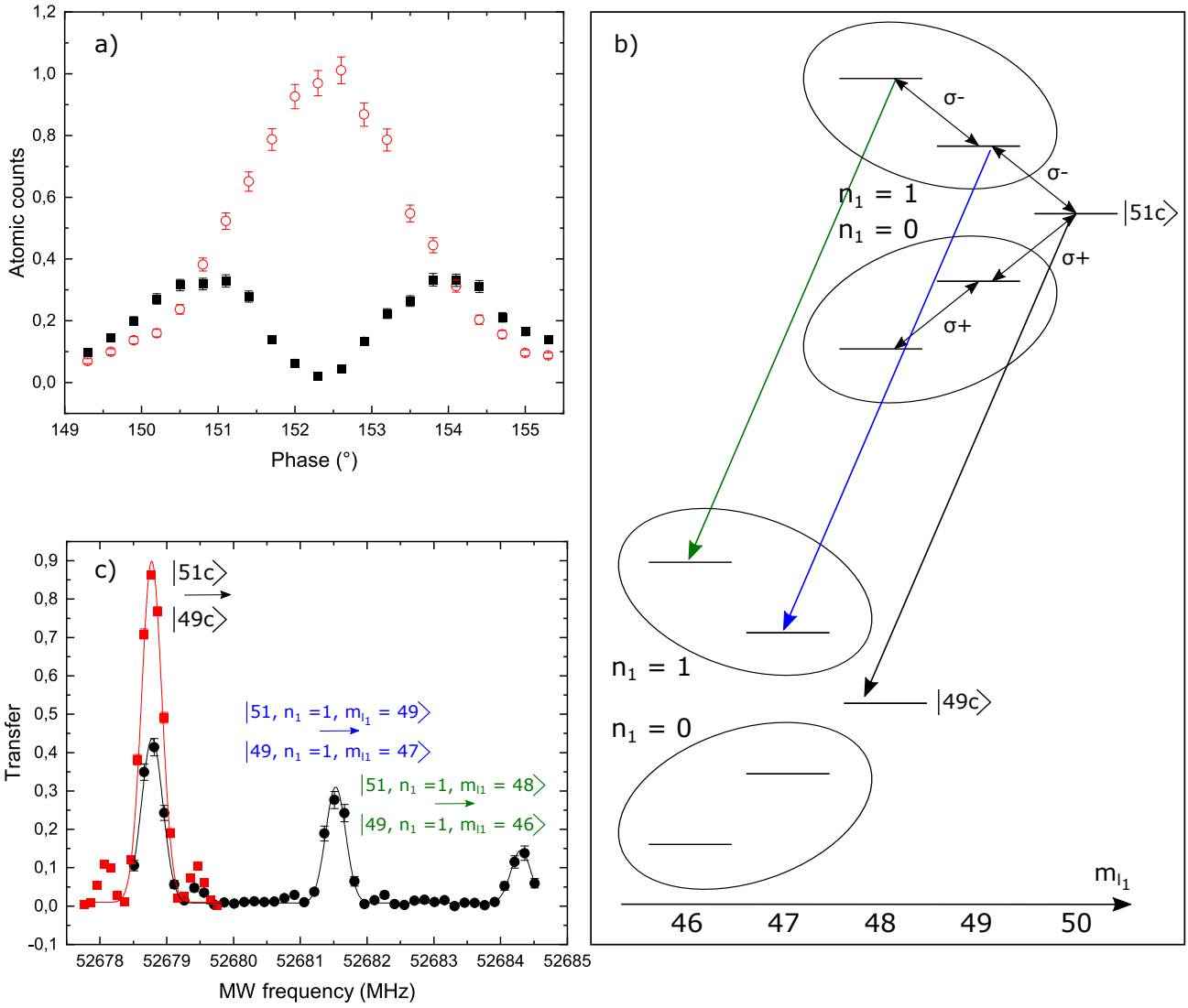

Figure 2.22: a) Population of $|51c\rangle$ (empty, red points) and $|n = 51, n_1 = 1, m_{l_1} = 49\rangle$ (full, black points) as a function of the phase of the rf produced by H_2 and H_4. The states are prepared via a rf pulse performing a Rabi passage. b) Coupling of the energy levels with the $\sigma+$ and $\sigma-$ components of the rf field. c) Evidence of the improvement of the circular-to-circular MW transfer after fine tuning the rf polarization. Black points indicate the data on the transfer before the optimization, red points after. Solid lines are Gaussian fits.

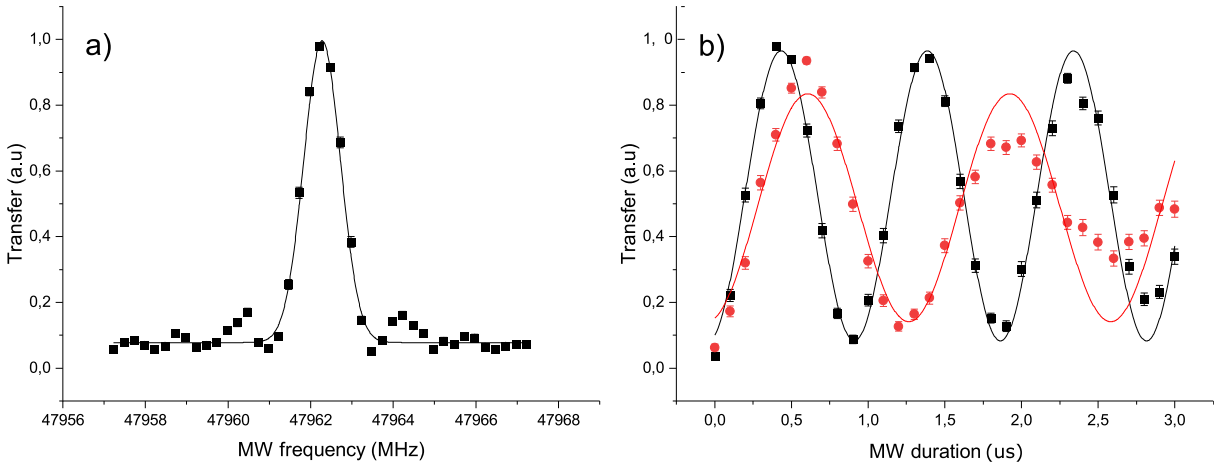

Figure 2.23: a) MW spectrum of the $|51c\rangle \rightarrow |n = 52, n_1 = 0, m_{l_1} = 50\rangle$ transition (black squares). We set the MW frequency at ~ 47.962 GHz, i.e. the maximum of the transfer fitted by a Gaussian lineshape (solid line). b) Rabi experiments performed at the arrival time of the $\pi/2$ pulses of the Ramsey experiment. Black squares refer to the Rabi oscillations performed with the first MW pulse, red data to those performed with the second one. Solid lines are a guide for the eye.

Δt but the frequency of the MW source producing the pulses in order to scan the phase values. We therefore perform the Ramsey experiment with these two pulses at fixed positions and separated by 6.5 μs. We set their lengths to be 0.43 μs and 0.59 μs respectively (figure 2.23). These values are chosen so as to broaden the transition enough not to make the transfer between the Rydberg levels considerably diminished when the frequency of the pulse is scanned over ± 0.25 MHz across the resonance. The MW source we use is the same for both pulses.

Figure 2.24 provides an evidence of the improvement on the contrast of the fringes before and after the field gradient compensation. It is easy to access the coherence time of our experiment by repeating the Ramsey sequence for different Δt values after properly adjusting the second $\pi/2$-pulse duration for all the delay values. We fit the contrast with a Gaussian lineshape centered in zero and with null offset (figure 2.25). Its width indicates that the coherence time is (24.66 ± 0.72) μs.

The choice of a Gaussian fit derives from the mathematics of the Ramsey fringes contrast C, after assuming a Gaussian distribution of the electric field noise. The contrast of the Ramsey fringes is formulated as

$$C = Re\left(e^{i(\omega-\omega_{St})\Delta t}\right). \tag{2.2}$$

What we measure is the average of the contrast of all the atoms, i.e.

$$\overline{C} = \overline{Re\left(e^{i(\omega-\omega_{St})\Delta t}\right)} = Re\left(\overline{e^{i(\omega-\omega_{St})\Delta t}}\right). \tag{2.3}$$

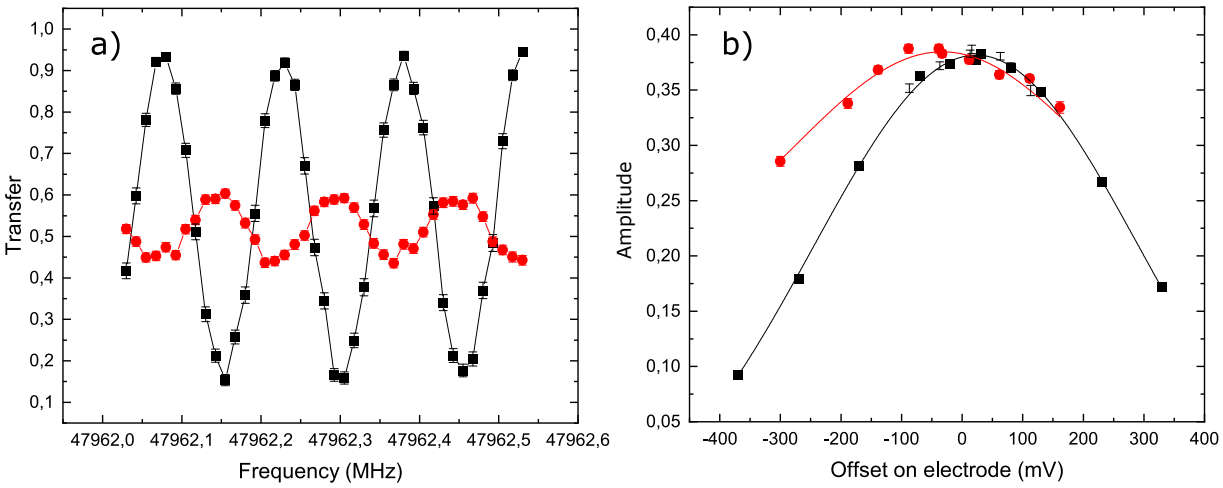

Figure 2.24: a) Ramsey oscillations before (red points) and after (black points) the gradient field compensation. Solid lines are guides for the eye. b) Amplitude of the Ramsey fringes as a function of an offset applied on H_1 (black points) and next on H_2 (red points) to compensate for the undesired gradient of the electric field. The maximum value of the amplitude is an indication of the quality of the gradient compensation. The solid lines are Gaussian fits.

We write the Stark frequency as the sum of a term $\omega_{St,0}$ indicating the Stark frequency when the electric field is homogeneous and a term $\delta\omega_{St}(F)$ indicating the broadening of the Stark frequency when the electric field is not homogeneous.

$$\omega_{St} = \omega_{St,0} + \delta\omega_{St}(F), \tag{2.4}$$

The term accounting for the broadening is written as

$$\delta\omega_{St}(F) = \alpha_S \delta F, \tag{2.5}$$

where α_S is $\Delta\omega_{St}/\Delta F$ and δF comes from the inhomogeneity of the electric field. We can therefore write $\overline{C}$ as

$$\overline{C} = Re\left(\overline{e^{i(\omega-(\omega_{St,0}+\delta\omega_{St}(F)))\Delta t}}\right) = Re\left(\overline{e^{i(\omega-\omega_{St,0})\Delta t}e^{-i\alpha_S\delta F\Delta t}}\right). \tag{2.6}$$

The first exponential is not dependent on the electric field. We can therefore apply the average operation to the second one only,

$$\overline{C} = Re\left(e^{i(\omega-\omega_{St,0})\Delta t}\overline{e^{-i\alpha_S\delta F\Delta t}}\right). \tag{2.7}$$

The term $\overline{e^{-i\alpha_S\delta F\Delta t}}$ is now cast, assuming a Gaussian dispersion of the field distribution, as

$$\overline{e^{-i\alpha_S\delta F\Delta t}} = \frac{1}{N}\int d(\delta F)e^{-i\alpha_S\delta F\Delta t}e^{-\frac{\delta F^2}{\sigma_F^2}} = e^{-\frac{1}{2}\alpha_S^2\sigma_F^2\Delta t^2} = e^{\frac{2\Delta t^2}{t_{coh}^2}}. \tag{2.8}$$

Here, σ_F indicates the dispersion of the electric field and N is a normalization factor. We can infer σ_F from the coherence time t_{coh} as

$$\sigma_F = \frac{2}{\alpha_S t_{coh}}. \tag{2.9}$$

In this work, for simplicity, we use the theoretical value of $\alpha_S = 3ea_0n/2\hbar$. By use of this, the calculation leads us to estimate a standard deviation of the electric field noise of $\sigma_F = (12.86 \pm 0.37)$ mV/m

2.4 Discussion

In this chapter, we present the experimental circularization of Strontium. We begin with the presentation of the experimental set-up. This is composed by a high temperature oven, a cryogenic environment and three laser diodes producing the beams for the Rydberg excitation. The oven produces a vapour of Strontium atoms, which is then collimated and directed to the cryostat. Inside this environment, protecting the atoms from black-body radiations, we can safely prepare and manipulate the Rydberg states. The preparation is performed via three optical photons whose frequencies are locked on an ultra-stable cavity. The manipulations are done via static electric fields, MW and rf pulses. We have four ring-electrodes able to apply horizontal electric fields and radio-frequency pulses on the atoms, two plane electrodes allowing us to set vertical electric fields and four MW sources. After the manipulations, the atoms arrive to the detector. This works by simple ionization of the Rydberg atoms. The measurement by ionization allows us to infer the quantum state of the atoms ionized in a destructive way.

Next, we switch to the discussion of the experimental circularization of Strontium. We first prepare the Rydberg state $|52^1F_3, m_{l_1} = +2\rangle$, by use of three $\sigma+/\sigma+/\pi$ polarized optical photons. Unfortunately, any $|F\rangle$ level is known to join the manifold of states with same n at very high electric field. Therefore, we decide to transfer the population to $|51^1G_4, m_{l_1} = +2\rangle$ via a short MW pulse exploiting a one-photon transition. The $|G\rangle$ states are known to reach their manifold at a lower electric field. They are thus a suitable entry point to the Rydberg ladder of the circularization.

We design a single-frequency, $\sigma+$ polarized, rf pulse to climb the $n_1 = 51, \hat{J}_1$ ladder. As for the frequency, we retrieve the spacing between neighboring levels of the ladder by use of MW spectroscopy, which suggests to work at 112.2 V/m. At this value, the ladder is resonant. Next, we discuss the optimization of the polarization of the rf pulse. We minimize its $\sigma-$ component on the transfer between two low-m_{l_1} Rydberg states. We finally apply the rf pulse on the atoms and climb the ladder until preparing the circular state. We determine the optimal duration, 189 ns, of the rf pulse maximizing the circular population. We use MW pulsed probe to measure the

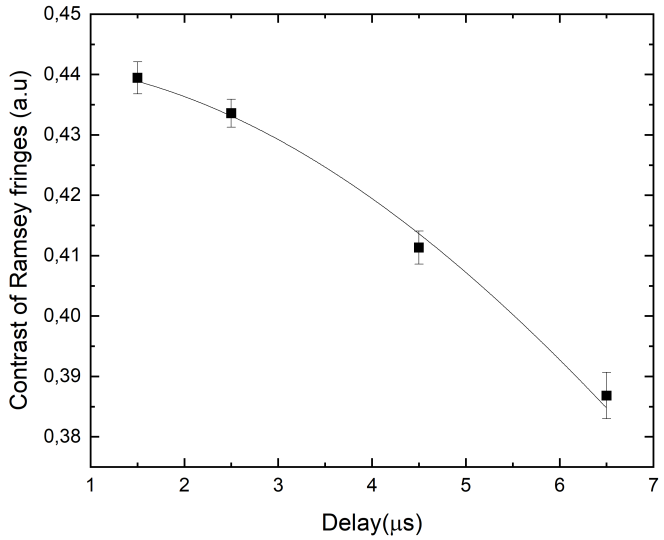

Figure 2.25: Contrast of the Ramsey fringes for different values of the delay between the $\pi/2$ pulses (black squares). The solid line is a Gaussian fit with set null offset and center. The width returns a coherence time of (24.66 ± 0.72) μs, corresponding to a standard deviation of the electric field noise of $\sigma_F = (12.86 \pm 0.37)$ mV/m.

population of any high-l_1 Rydberg state featuring in the calibration of the rf duration. The probes target the $n_1 = 49$ manifold and guarantee an optimal signal-to-noise-ratio for our measurements. The circularization presented in this work is estimated to be 85% effective.

Before addressing the core electron, we perform a few more optimisations. First, we fine-tune the rf polarization by detecting the population of $|n = 51, n_1 = 1, m_{l_1} = 49\rangle$ as a function of the rf phase and power. Next, we make use of the outer electron states to perform a Ramsey experiment across the $|51c\rangle \rightarrow |n = 52, n_1 = 0, m_{l_1} = 50\rangle$ transition. This technique enables us to compensate for the gradient of the electric field perceived by the atoms and obtain a coherence time of (24.66 ± 0.72) μs, corresponding to a standard deviation of the electric field noise of $\sigma_F = (12.86 \pm 0.37)$ mV/m.

It is now time to switch to the description of those experiments where both the Rydberg electron and the ionic-core electron are manipulated. They are the focus of the experimental activity to be presented in chapters 3 and 4. There, we are going to show the advantages of working with circular states of an alkaline-earth atom with respect to those of an alkali atom, starting from the absence of autoionization effect and arriving to the possibility of optically manipulating the ionic-core electron while preserving the circular states.

CHAPTER 3

THE AUTOIONIZATION EFFECT

> An atom with two electrons has one electron too many.
>
> *Prof. Jean-Michel Raimond, adapting a quote from Prof. Arthur Schawlow.*

We have established a protocol to prepare the circular Rydberg states of Strontium. As for Rubidium, the circularization of Strontium involves the manipulation of one valence electron only. However, Strontium possesses two electrons in the last filled shell. With one excited to the Rydberg state, there is still a remaining electron at our disposal to be optically manipulated. In principle, this fact provides a broader range of physical investigations. Unfortunately, doubly-excited states of alkaline-earth atoms are well known to autoionize, since the excitation energy of the ionic-core electron exceeds the ionization energy of the Rydberg electron.

Fortunately though, the autoionization effect depends on the overlap between the wavefunctions of the two valence electrons. Where there is overlap (figure 3.1a), a scattering event between the two particles takes place, followed by an electron expulsion, turning the neutral atom into an ion. On the contrary, in absence of any overlap (figure 3.1b), the electrons do not scatter against each other. The whole system does not consequently present any autoionization effect. This is the case of the circular state.

We are interested in the few excited states of the core electron depicted on figure 3.2. When the first electron is excited to a high-n Rydberg state, the structure of the core electron energy levels is, at very good approximation, that of the Sr^+ ion. We consequently have the state $|5p_{1/2}\rangle$

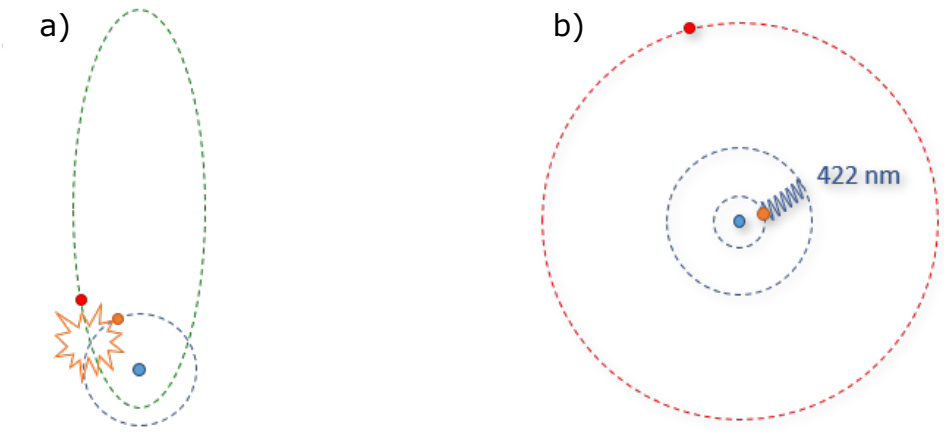

Figure 3.1: a) Collision between the excited core electron and the Rydberg electron prepared in a low-l_1 state. The scattering event is caused by the overlap of the wavefunctions. b) Absence of collision between the excited core and the circular state, due to the absence of overlap between the wavefunctions.

($|5p_{3/2}\rangle$) at 422 (408) nm above the $|5s_{1/2}\rangle$ ground state, the $|4d_{3/2}\rangle$ metastable states at 1092 nm below the $|5p_{1/2}\rangle$ state and similarly the $|4d_{5/2}\rangle$ metastable states at 1033 nm below the $|5p_{3/2}\rangle$ state.

With a 1/17 branching ratio, the $|5p_{1/2}\rangle$ state decays into the $|4d_{3/2}\rangle$ state, which is metastable. The spontaneous emission lifetime of the $|5p_{1/2}\rangle$ states is 7 ns only, whereas the lifetimes of the $|4d_{3/2}\rangle$ states are in the milliseconds range. Thus, in a few tens of nanoseconds only, a resonant illumination on the $|5s_{1/2}\rangle \rightarrow |5p_{1/2}\rangle$ transition results in the atom being optically pumped in the $|4d_{3/2}\rangle$ states. Similarly, the $|5p_{3/2}\rangle$ state decays into $|4d_{3/2}\rangle$, with rate r, and $|4d_{5/2}\rangle$, with rate r_0. The branching ratio r_0/r is 8.4. Therefore, an analogous optical pumping process allows one to populate the $|4d_{5/2}\rangle$ state from the ground state.

When the core electron is excited to any of these states, its wavefunction can potentially overlap with that of the Rydberg electron and cause autoionization. In this chapter, we are going to explore this physics. In particular, we are interested in studying the absence of autoionization for the circular state for the core excited to $|4d_{3/2}\rangle$ or $|4d_{5/2}\rangle$ states (paragraphs 3.3.2 - 3.3.5 for the first case, paragraph 3.3.6 for the second case), and the presence of autoionization for a Rydberg state with low angular momentum. We are therefore going to prepare the Rydberg state of interest, excite the core and test whether the amount of Rydberg atoms drops when the core is in any of the $|4d\rangle$ states.

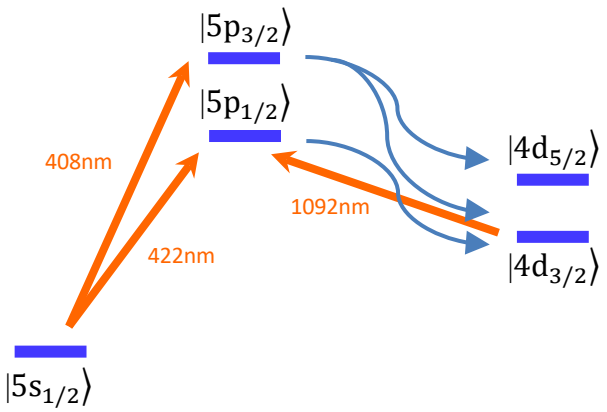

Figure 3.2: Diagram of the energy levels of the Sr^+ ion which we consider in this work.

3.1 The optical set-up for the ionic core manipulation

Here, we go through the technical details of the optical set-up used for the manipulations of the ionic-core electron. We first describe the optical path of each laser, from the initial beam shaping to the optical branch directed to the experiment. Then, we discuss the geometry of the intersection between the lasers and the atomic beam. Finally, we give the parameters of the laser beams: the optical power, the Gaussian diameter and the resonance frequency.

We use a 422 nm laser beam to perform the $|5s_{1/2}\rangle \rightarrow |5p_{1/2}\rangle$ excitation (figure 3.3a). As the lasers performing the Rydberg excitation, the 422 nm beam is first shaped as a Gaussian beam by a telescope made up of three cylindrical, plano-convex lenses with 150 mm, 75 mm and 75 mm of focal lengths respectively. After the beam shaping, the laser is split in four branches.
The first branch addresses a transfer cavity. Notably, for this laser only, we cannot use the ultra-stable cavity for the frequency locking, due to the coating of its internal mirrors. Therefore, to achieve a stable frequency locking, we lock the length of the transfer cavity on the signal of a 767 nm beam, itself locked on the ultra-stable cavity. We tune the frequency of the 422 nm laser by changing the frequency of the 767 nm beam on which the cavity is locked by use of an EOM.
A second branch makes the 422 nm laser do a double-pass across a Rubidium cell. Historically, we performed standard saturated-absorption spectroscopy on the Rubidium vapor to detect the hyperfine transitions of Rubidium between $|5s\rangle$ and $|6p\rangle$ (coincidentally close to the resonance frequency between $|5s_{1/2}\rangle$ and $|5p_{1/2}\rangle$ of Strontium) and used them as an initial reference for the frequency of the laser.
A third branch leads the laser beam to the wave-meter, which is now the main reference for the wavelength.
Finally, we prepare a fourth branch of the 422 nm beam, collecting the majority of the light power. This portion of the laser is pulsed, sent in the direction of the cryostat via an optical fiber and

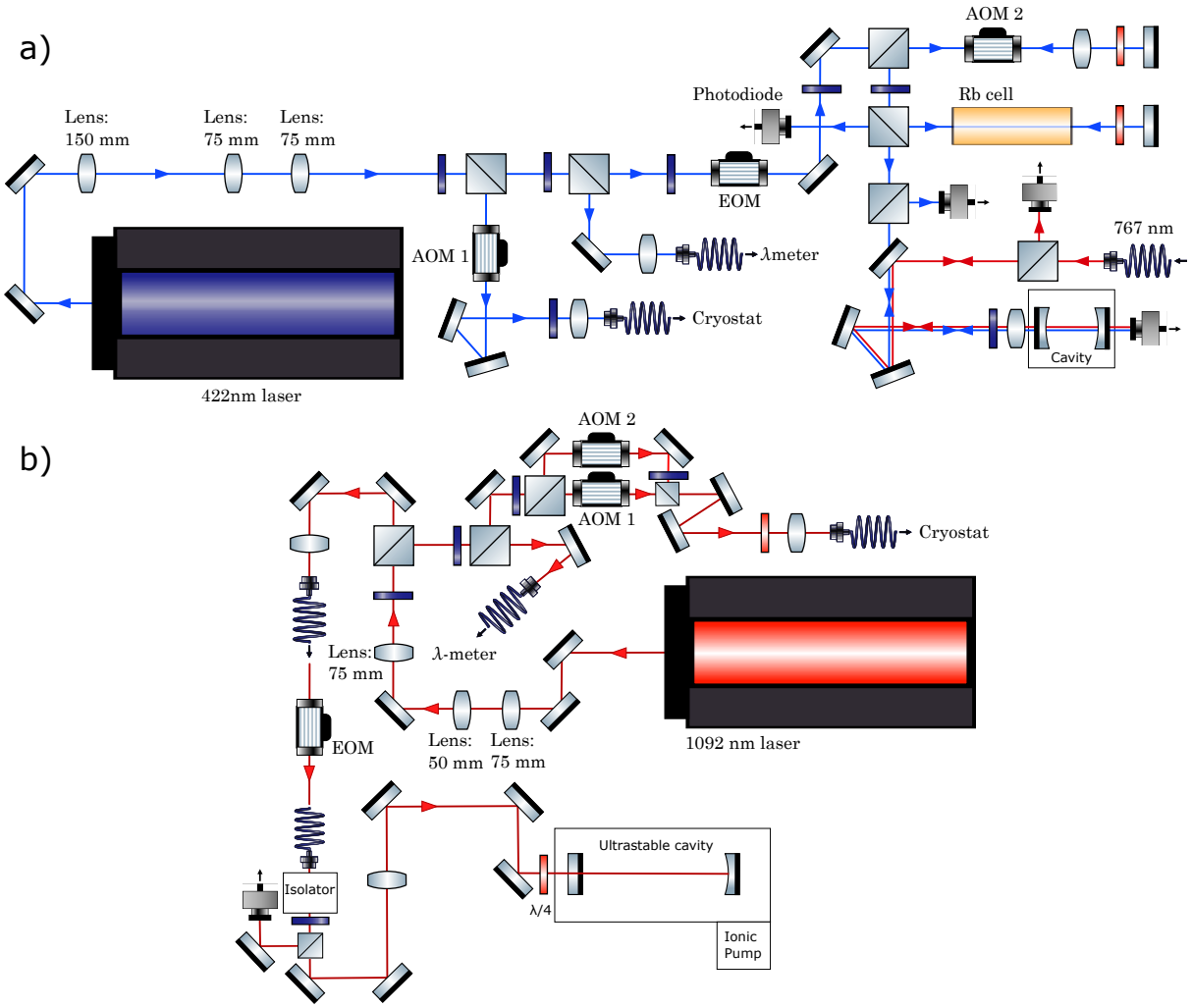

Figure 3.3: a) Optical set-up of the 422 nm and b) 1092 nm laser beams [78].

ultimately aligned towards the experiment. Note that the laser crosses the same beam-splitter and wave-plate already used for the 461 nm laser. These two beams consequently have orthogonal polarizations when meeting the atoms.

We use a 1092 nm laser acting as a repumper, emptying the $|4d_{3/2}\rangle$ states when they are populated via the spontaneous decay from the $|5p_{1/2}\rangle$ state (figure 3.3b). Again, the 1092 nm beam is shaped as a Gaussian beam by a telescope made up of cylindrical, plano-convex lenses with 75 mm, 50 mm and 75 mm as focal lengths. Next, it is split in three lines. One goes to the wave-meter, another to an ultra-stable cavity, identical to that presented in chapter 2, for the frequency lock via standard PDH method.
A last branch is further divided in two linearly and orthogonally polarized beams by a wave-plate and a beam-splitter and finally directed to the cryostat. Note that we pulse both beams

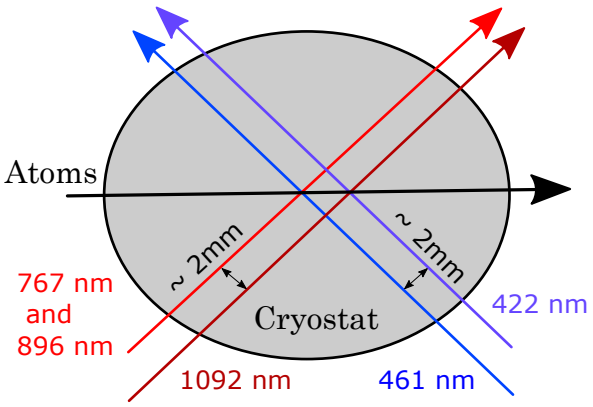

Figure 3.4: Crossing paths of the laser beams with the atomic beam.

independently. Each of them uses an electronic set-up (rf source + coaxial cable + amplifier + AOM) similar to that of the 896 nm and 422 nm beams. The two orthogonal beams are frequency shifted via a pair of AOMs by 3 MHz, to efficiently empty the $|4d_{3/2}\rangle$ states [79], then overlapped and finally coupled within the same polarization-maintaining optical fiber directing them to the experiment. The need of two optical branches derives from the energy levels structure of the Sr^+ ion. When exciting the atoms from a set of states with $j_2 = 3/2$ to a set with $j_2 = 1/2$, one always runs into atomic dark states for the laser driving the transition. This happens if the laser has a pure polarization, either σ or π. The solution to this problem is detuning the two σ and π components of the laser beam with respect to each other so that their phases change rapidly. In this context, when the laser is applied on the atoms, there is no state which is dark all the time.

The 422 nm and 1092 nm laser beams cross each other orthogonally on the atoms but do not share the same crossing point with the Rydberg lasers. The 422 nm and 1092 nm beams meet the atoms later along their trajectory, so as to be able to first produce the Rydberg states and only next act on the core. The 422 nm beam runs parallel but shifted by ~ 2 mm with respect to the 461 nm beam. The 1092 nm beam is built with a analogous arrangement, as displayed in figure 3.4.

The 422 nm laser reaches a maximum light power of ~ 20 mW on the atoms and has a broad Gaussian diameter, ~ 850 μm. The 1092 nm laser has a maximum power of ~ 20 mW on the atoms as well but a larger Gaussian diameter, 1500 μm, on the position of the atoms (figure 3.5). The resonance frequencies of both the 422 nm and 1092 nm laser beam are determined via a series of laser spectroscopy experiments, which are presented in appendix C. The resonance frequencies are 710.9618 THz and 274.5894 THz at 206.6 V/m (we want the electric field to be high enough so as to lift the degeneracy of the states composing the Rydberg ladder) for the 422 nm and 1092 nm laser beams respectively. The Doppler corrections are already taken into account in these values.

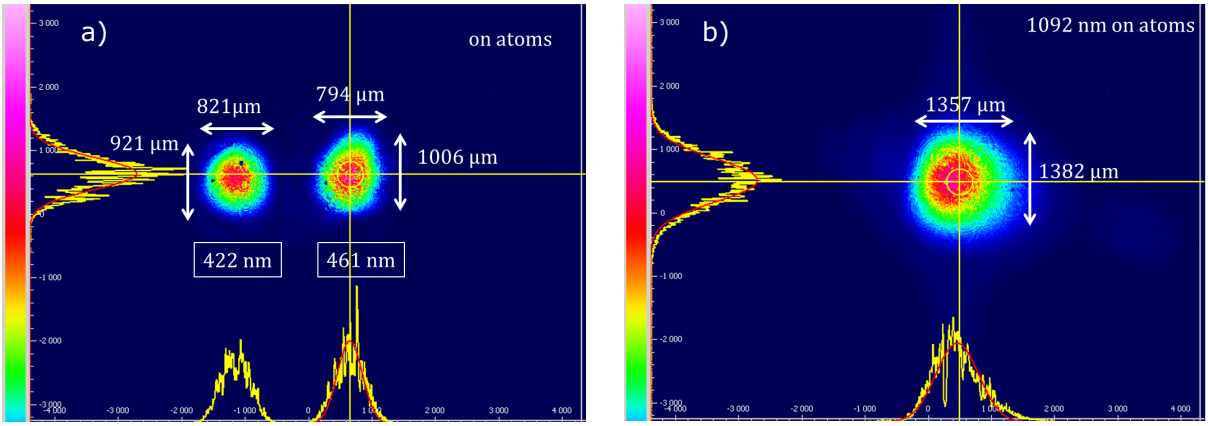

Figure 3.5: a) Profiles of the 422 nm and 461 nm laser beams. b) Profile of the 1092 nm laser beam.

The last laser used to manipulate the core is a beam at 408 nm, able to drive the transition $|5s_{1/2}\rangle \rightarrow |5p_{3/2}\rangle$. This beam is produced by a free-running frequency doubled Ti:Sa laser. Its power is on the order of a mW, sufficient to optically pump the atoms in the metastable state $|4d_{5/2}\rangle$. Notably, the 408 nm beam is not pulsed. It does not interact with the atoms in low-l_1 states since this laser beam crosses the atomic beam when the atoms have already been circularized. This laser is the only one borrowed from another experimental set-up for a short period and not built from scratch.

3.2 Principle and technical tools of the experiment

3.2.1 Overview

The principle of the experiment consists of three steps. We circularize, excite the core electron with a 422 nm laser pulse and observe if the optical pumping in the $|4d_{3/2}\rangle$ states involves any loss of circular states. We are going to see that no variation in the atomic counts is detected, therefore that the circular state is not perturbed by the excitation of the core (sections 3.3.2 - 3.3.4). Note that the absence of a drop in the atomic counts is obviously observed also if the laser beam never meets the atoms or is off-resonant. We therefore need to perform the experiment while checking that we indeed excite the core in its metastable level. To that end, we make use of low-l_1 states. We rely on them to verify that we have changed the state of the core. Thus, we perform the same experiment with an additional rf pulse after the excitation of the core, therefore reducing the angular momentum of the Rydberg electron, and monitoring the population in the final low-l_1 state. We are going to see that, in this context, the atomic counts drop, since the two electrons scatter and one of the two is expelled.

In the second part of the chapter (sections 3.3.5 and 3.3.6), we are going to include the singlet-triplet nature of the quantum states into the discussion. Due to the spin-orbit coupling of the ionic-core electron in the $|5p_{1/2}, nl_1\rangle$ state, scattering photons at 422 nm may flip the spin of the ionic-core electron, thus inducing a transition from $|5p_{1/2}, nl_1\rangle$ to the $|5s_{1/2}, nl_1\rangle$ triplet state. Thus, as a final result, we are going to quantify the decay of the $|5p_{1/2}, 51c\rangle$ state into the triplet state of $|5s_{1/2}, 51c\rangle$ as a function of the 422 nm laser frequency.

In order to discuss this experiment, we detail in advance the preparation of the rf pulse lowering the angular momentum of the Rydberg electron. We coin a term, the "decircularization", to address this action on the atoms.

3.2.2 The decircularization

In principle, a simple application of the same rf pulse optimized for the circularization should work to decircularize with the same efficiency. Notably, to produce this second rf pulse, we use the same synthesizer already employed to prepare that performing the circularization. The second rf pulse is therefore already produced with a pure $\sigma+$ polarization and a frequency of 110 MHz as well. It is applied 11 μs after the first one to leave enough time between the two rf events for the 422 nm laser pulse manipulating the core. However, during that time, the atoms move inside the cryostat. In the region of space where the decircularization takes place, the static electric field has a different value than where the circularization occurs. In principle, this fact implies that the second rf pulse, despite being at the same frequency of the first one, might not be efficient to decircularize. Fortunately, the variation of the electric field is not expected to be very large.

We start by optimizing the duration of the decircularization on the transfer $|51c\rangle \rightarrow |51^1G_4, m_{l_1} = +2\rangle$ (figure 3.6a) by detecting the low-l_1 population as a function of the duration of the second rf pulse (figure 3.6b). This is optimal at 179 ns. On a second step, we carry out a fine tuning of the electric field by repeating the decircularization for several electric field amplitudes and determining that yielding the highest transfer. This is 112.4 V/m.

From the data, it is clear that the decircularization is not as efficient as the circularization (figure 3.6c). The second rf field indeed leaves an amount of atoms in a Rydberg state ionizing around 90 V/cm. However, the majority of the atoms returns to the $|51^1G_4, m_{l_1} = 2\rangle$ state where the circularization process started.

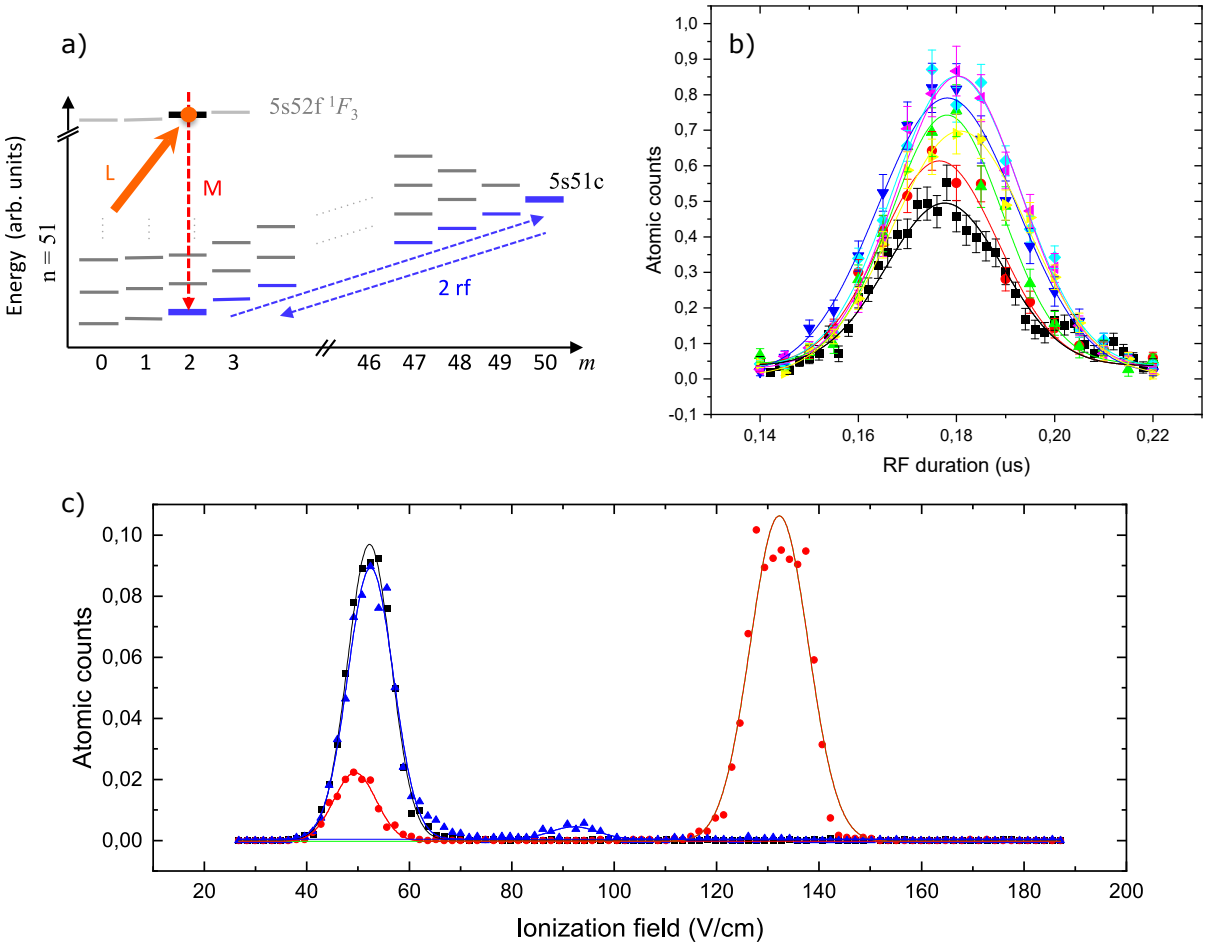

Figure 3.6: a) Navigation in the Hilbert space. b) Scan of the duration of the rf pulse decircularizing the atoms and detection of the population brought back to the $|51^1G_4, m_{l_1} = +2\rangle$ state for several values of the electric field (black points: 112.0 V/m, red points: 112.1 V/m, green points: 112.2 V/m, blue points: 112.3 V/m, light blue points : 112.4 V/m, pink points : 112.5 V/m, yellow points : 112.6 V/m). c) Ionization signal before the circularization (black data), after the circularization (red data, with some atoms ionizing at around 50 V/cm, not transferred by the rf field, but a vast majority are circularized) and after the decircularization (blue data). We also record some atoms ionizing around 90 V/cm, therefore in intermediate m_{l_1} states. Solid lines are Gaussian fits.

3.3 Experimental results

3.3.1 Overview

We present here the results proving that the circular states are unaffected by the autoionization effect. We focus on this aspect when the core is either excited to the $|4d_{3/2}\rangle$ state (paragraph 3.3.2) or to the $|4d_{5/2}\rangle$ state (paragraph 3.3.7). For the first case, we present the numerical model (paragraph 3.3.3 - 3.3.4) used to fit the data. Next, we discuss the decay from the $|5p_{1/2}, nl_1\rangle$ state to the triplet state of $|5s_{1/2}, nl_1\rangle$, caused by the spin flip of the core following the interaction with the 422 nm photons (paragraphs 3.3.5 - 3.3.6).

3.3.2 The absence of autoionization for the $|4d_{3/2}, 51c\rangle$ state

We discuss here the absence of autoionization effect for the $|4d_{3/2}, 51c\rangle$ state. The investigation proceeds as follows. We apply a 5 μs long, 422 nm laser pulse at maximum power ($\sim$ 16 mW) after the circularization and sweep the laser frequency around the resonance (figure 3.7). The circular population N^c is measured and normalized by the amount of circular states N_0^c which is recorded if the 422 nm laser beam is not applied on the atoms. The measurement shows that the signal does not drop within error bars, whether the 422 nm is on or off resonance with the $|5s_{1/2}\rangle \rightarrow |5p_{1/2}\rangle$ transition (figure 3.8). This implies that there is negligible autoionization for the circular states. Such a conclusion is compatible with our initial expectations, which predict the autoionization rate to decrease by one order of magnitude for each increase of l.

We repeat the same sequence but, this time, we add a decircularization pulse after the core excitation and record the population of the $|51^1G_4, m_{l_1} = +2\rangle$ state (figure 3.9). Decircularizing after the 422 nm pulse makes the outer electron get through levels with decreasing l_1 quantum numbers while the core is excited. Lowering l_1 implies increasing the ellipticity of the Rydberg electron's orbital, hence the probability of scattering between the valence electrons. Consequently, only very few atoms reach the lowest states of the ladder if the core is in the $|4d_{3/2}\rangle$ metastable state. We therefore expect a drop of the number of atoms N detected at the $|51^1G_4, m_{l_1} = +2\rangle$ ionization threshold when the 422 nm beam matches the $|5s_{1/2}\rangle \rightarrow |5p_{1/2}\rangle$ resonance and optically pumps the core electron in $|4d_{3/2}\rangle$.

Figure 3.10 presents the number N of atoms detected in $|5s_{1/2}, 51^1G_4 m_{l_1} = +2\rangle$, normalized by the amount N_0 of atoms detected in the same level when the 422 nm laser is not applied. As expected, we observe a dip around the resonance, with a depth increasing with the blue laser power. The asymmetry of the signal detected is due to the Doppler effect induced at the moment of the laser excitation of the atoms. As an additional check, we perform the same experiment with the 1092 nm repumper laser resonant with the $|4d_{3/2}, 51c\rangle \rightarrow |5p_{1/2}, 51c\rangle$ transition. It efficiently empties $|4d_{3/2}, 51c\rangle$. We then observe a flat signal, close to 100%, confirming the dip to

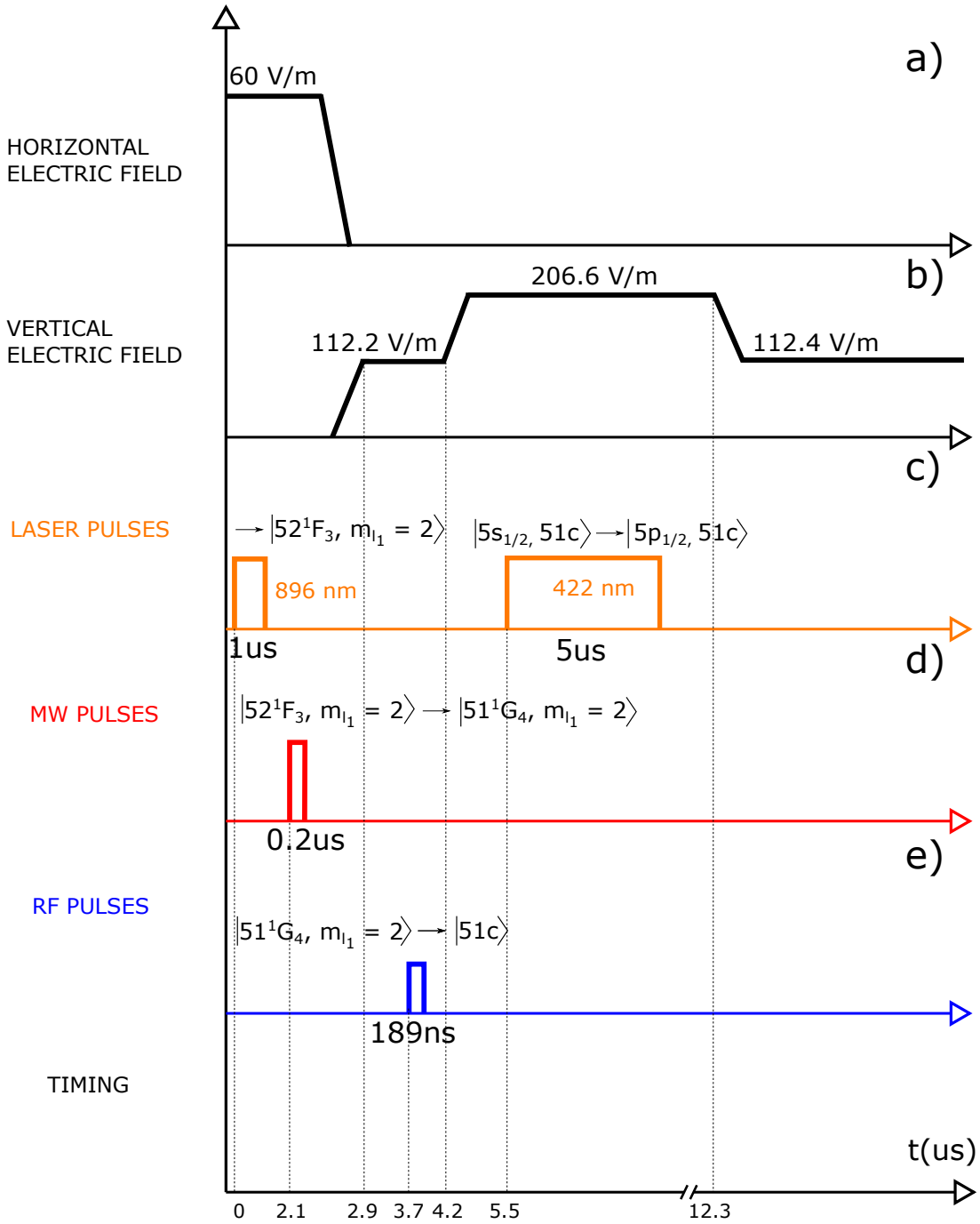

Figure 3.7: Sequence of laser, MW, rf and static electric fields used to measure the absence of autoionization for $|4d_{3/2}, 51c\rangle$ state.

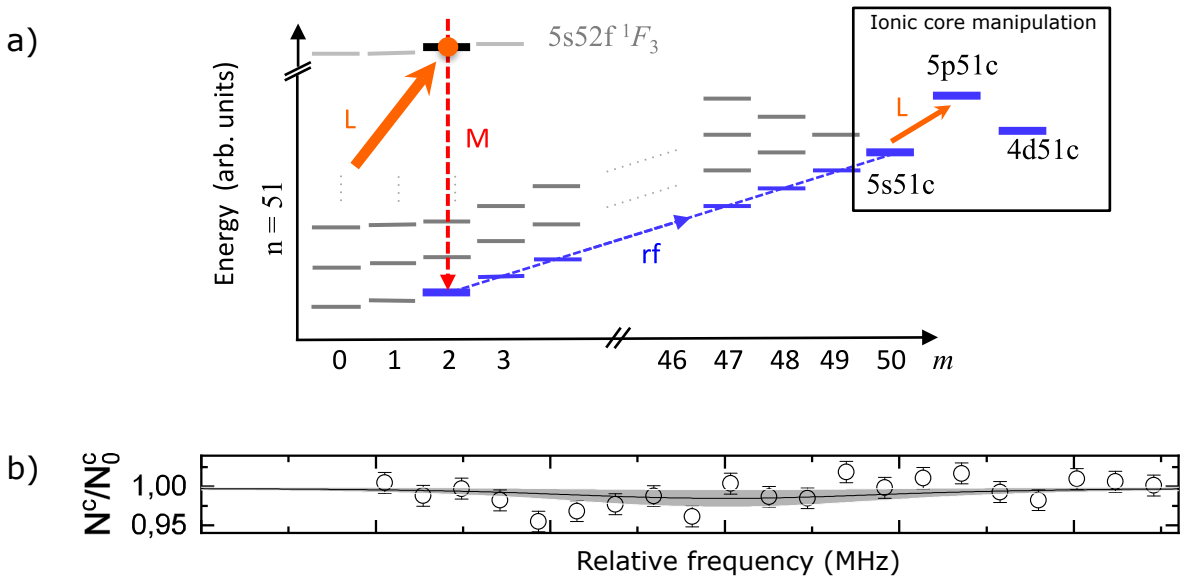

Figure 3.8: a) Navigation in the Hilbert space following the sequence of events designed to test the absence of autoionization for the circular state. b) Survival probability of the circular Rydberg state to the autoionization effect as a function of the 422 nm laser. The white points are experimental data with statistical error bars. The shadow area corresponds to the 95% confidence band of the fit of the survival probability.

be caused by the pumping in $|4d_{3/2}, 51c\rangle$. The data are in excellent agreement with the numerical simulations, presented in the next paragraph, computing the population remaining in $|5s_{1/2}, 51c\rangle$ before the second rf pulse.

3.3.3 The numerical model

Until this point, we have discussed the physics of the autoionization effect without taking into account the singlet or triplet nature of the quantum states. We did this since we could not attribute a singlet or triplet character when the core is in the $|p\rangle$ and $|d\rangle$ states. For these states, the fine structure component of the Hamiltonian is indeed dominant over the exchange energy. On the contrary, it is possible to assign a spin class to the atoms whose core is in the ground state $|5s_{1/2}\rangle$. In the latter case, when the Rydberg electron is circularized, the exchange energy is zero and the singlet and triplet states are degenerate. Therefore, if the Rydberg electron is in the circular state, the distinction between singlet and triplets is formally valid but we have no experimental way to discriminate the two spin classes even with the core in the ground state. All these features on the spin nature of the quantum states are taken into account in our numerical model fitting the data on the autoionization effect. The reason is that we use this same model to fit also another set of data, to be presented later in this work, whose interpretation involves explicitly the spin of the quantum states.

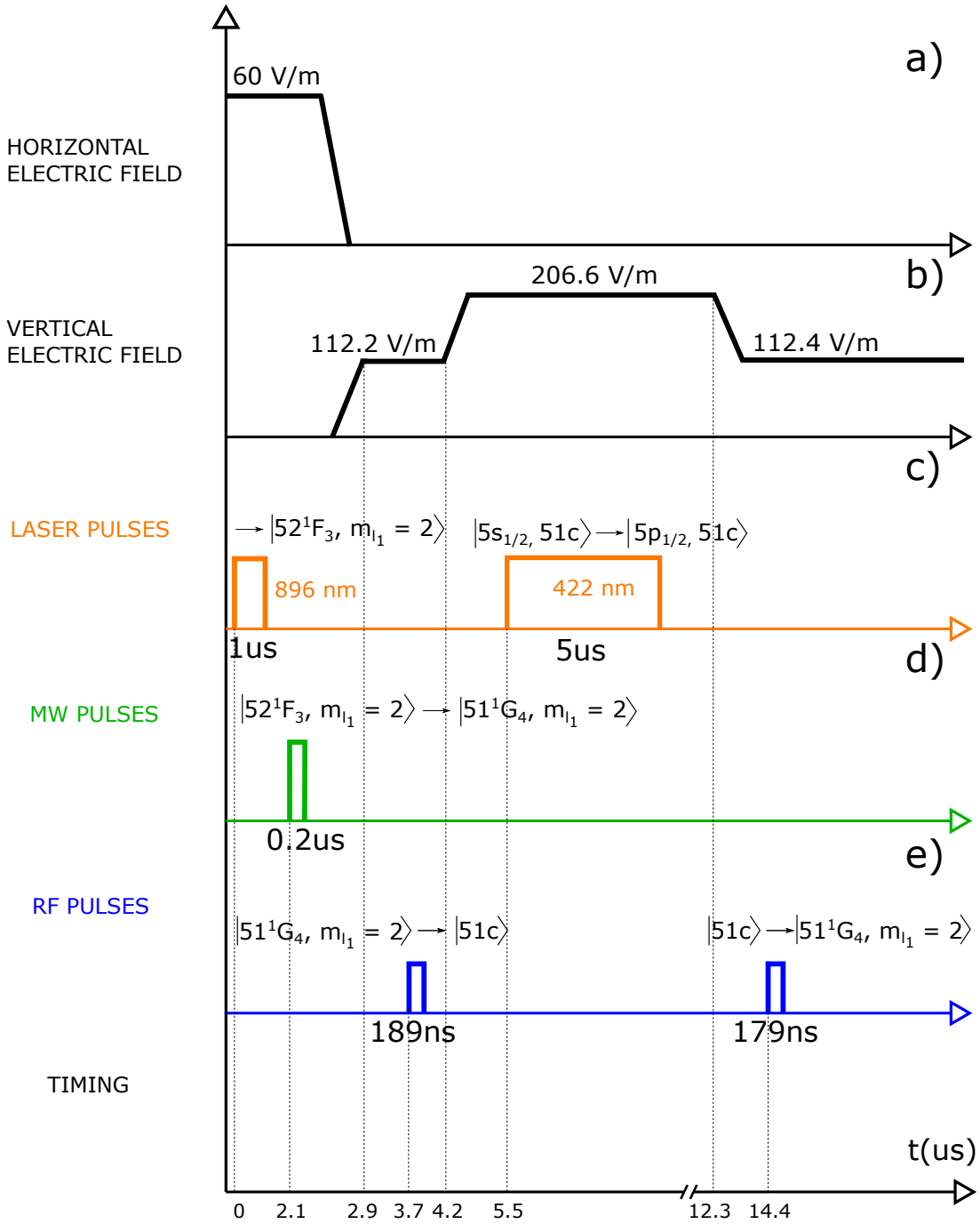

Figure 3.9: Sequence of laser, MW, rf and static electric fields used to measure the autoionization effect for a low-l_1 Rydberg state.

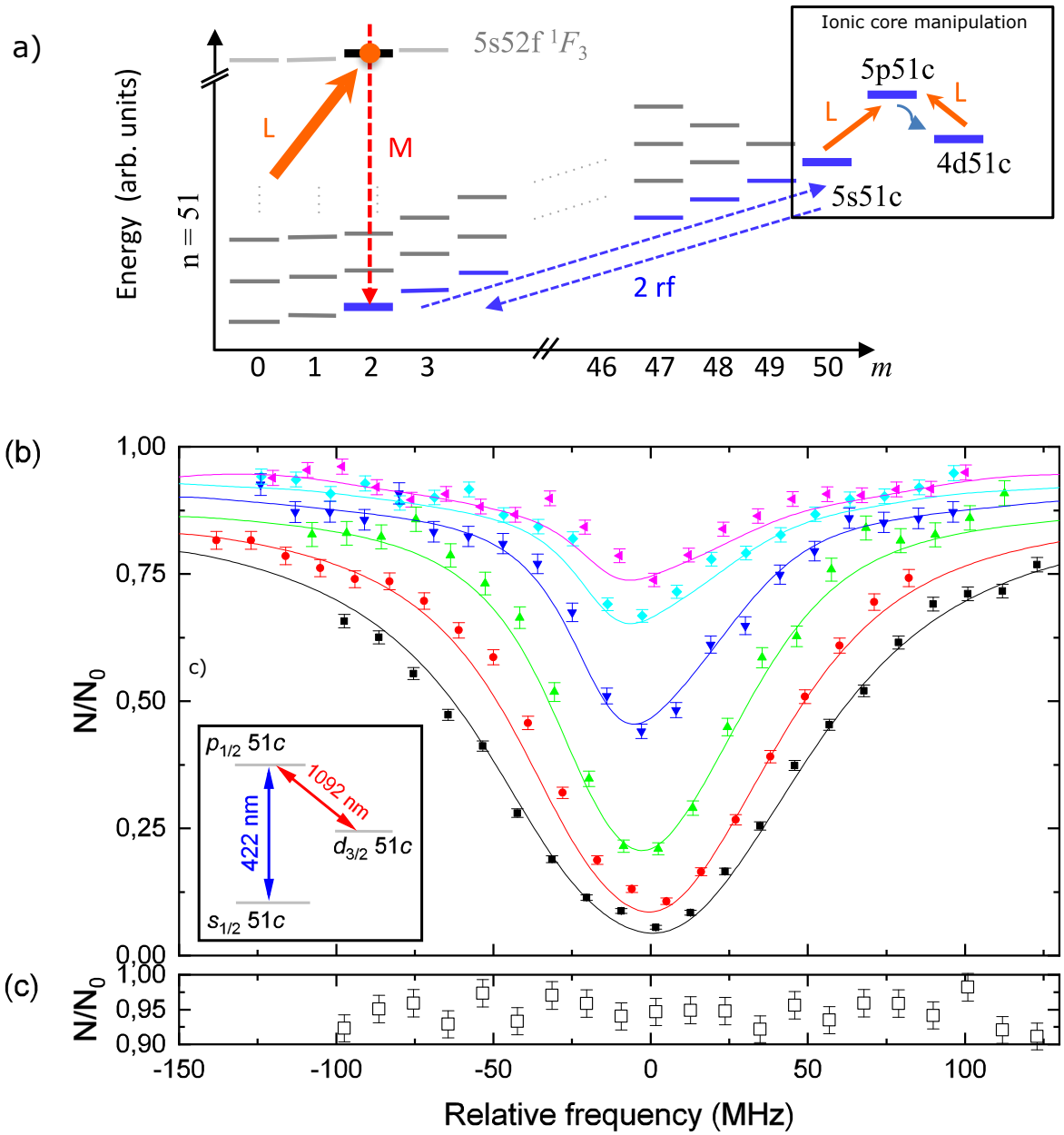

Figure 3.10: a) Navigation in the Hilbert space following the sequence of events designed to test the presence of autoionization for $|4d_{3/2}, 51^1G_4 m_{l_1} = 2\rangle$. b) Evidence of autoionization of a low-m_{l_1} Rydberg state, for several 422 nm laser powers (black: 16 mW , red: 9.5 mW , green: 4.0 mW, blue: 1.3 mW, cyan: 0.5 mW, pink: 0.3 mW). We plot the probability that the atom ends up in $|5s_{1/2}, 51^1G_4 m_{l_1} = +2\rangle$ after the decircularization, as a function of the laser frequency. Solid lines indicate numerical simulations. c) Survival to the autoionization after the application of the repumper.

The model is based on the integration of the density matrix master equation under the action of the 422 nm laser beam detuned by $\Delta/2\pi$ from the $|5s_{1/2},51c\rangle \rightarrow |5p_{1/2},51c\rangle$ transition frequency.

The energy levels, written in the uncoupled spin basis, and the couplings taken into account are depicted in figure 3.11. The states of interest are

$$|5s_{1/2}m_{j_2} = -1/2,51c,\downarrow\rangle, |5p_{1/2}m_{j_2} = -1/2,51c,\downarrow\rangle,$$

$$|5s_{1/2}m_{j_2} = -1/2,51c,\uparrow\rangle, |5p_{1/2}m_{j_2} = -1/2,51c,\uparrow\rangle,$$

$$|5s_{1/2}m_{j_2} = +1/2,51c,\downarrow\rangle, |5p_{1/2}m_{j_2} = +1/2,51c,\downarrow\rangle,$$

$$|5s_{1/2}m_{j_2} = +1/2,51c,\uparrow\rangle, |5p_{1/2}m_{j_2} = +1/2,51c,\uparrow\rangle,$$

where the arrow depicts the spin of the Rydberg electron, with a quantization axis chosen along the direction of the 422 nm laser. We also include a ninth state "$|d_{3/2}\rangle$", which formally represents all the $|4d_{3/2}\rangle$ levels in which the $|5p_{1/2}\rangle$ sub-levels can decay with the same rate.

The decay rates from $|5p_{1/2} \pm m_{j_2}\rangle$ to $|5s_{1/2} \pm m_{j_2}\rangle$ and $|5s_{1/2} \mp m_{j_2}\rangle$ are named Γ_π and Γ_σ respectively. We have $\Gamma_\sigma/2\pi$ = 13.6 MHz, $\Gamma_\pi/2\pi$ = 6.8 MHz. The decay rate γ accounting for the decay from $|5p_{1/2} \pm m_{j_2}\rangle$ into $|d_{3/2}\rangle$ is set as $\gamma/2\pi$ = 1.2 MHz. The Rabi frequencies Ω+ and Ω-, associated to the $|5s_{1/2}\rangle|51c\rangle \rightarrow |5p_{1/2}\rangle|51c\rangle$ transitions with $\Delta m_{j_2} = 1$ or -1 respectively, depend on the amplitude of the σ+ or σ- polarization component of the 422 nm laser at the position of the atoms and on the square root of the local laser intensity $I(x,z)$. They also vary along the atomic trajectory. We measure Ω+ = Ω-/6. The 422 nm laser polarization is indeed selected to be as pure σ- as possible. The ratio between the σ+ and σ- intensities is measured to be $1:36$ via a beam-splitter and a photo-diode temporarily set at the exit of the cryostat.

Next, we take into account the characteristics of the 422 nm laser beam driving the $|5s_{1/2}\rangle$ to $|5p_{1/2}\rangle$ transitions. We assume that the dynamics of the atom crossing a beam with a Gaussian width $\sqrt{2}w_x = 580$ μm can be approximated by that of an atom staying at the point of maximum intensity $I(0,z)$ for a time t_{eff}. The factor $\sqrt{2}$ takes into account the angle between the atomic beam and the laser. To determine the value of t_{eff}, we first assume the Rabi frequency to have a Gaussian dependence with respect to time and next compute the probability for the atoms to end up in the triplet $|5s_{1/2}\rangle$ state as a function of the Rabi frequency calculated at the maximum of the Gaussian. This computation is done by numerical integration of the master equation. We set a constant Rabi frequency for a given amount of time and compute the again the probability for the atoms to end up in the triplet $|5s_{1/2}\rangle$ state. The two probabilities, computed with two different dependencies of the Rabi frequency with respect to time, match each other when the Rabi frequency is set as a constant for an "effective" time of 1.8 μs, for a velocity class moving at 418 m/s.

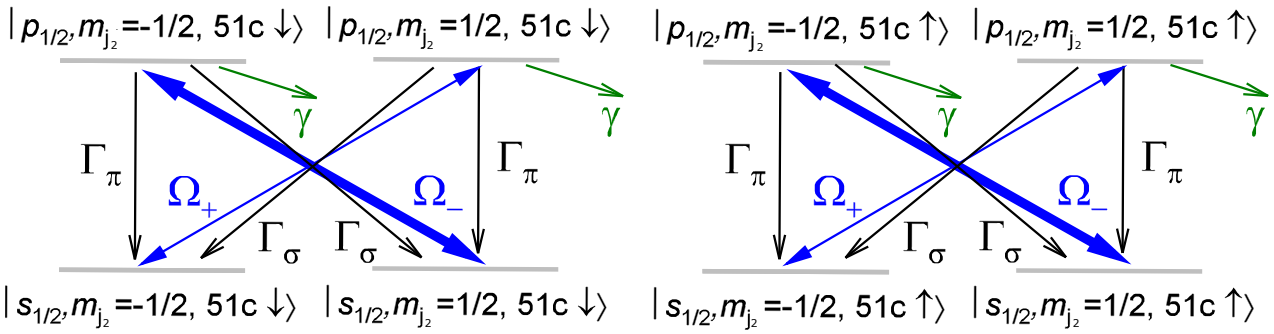

Figure 3.11: Decay trajectories from the $|5p_{1/2}\rangle$ states. Blue arrows indicate the 422 nm laser drive, black arrows indicate the decays from the $|5p\rangle$ states to the $|5s\rangle$ states, green arrows stand for the decay from each $|5p\rangle$ level to the metastable $|4d\rangle$ states. We consider the same decay rates for the same channel when the spin is oriented up or down.

Once all these parameters are set, we compute the probabilities $P_s(I(0,z),\Delta)$ and $P_t(I(0,z),\Delta)$ for an atom initially in the singlet state

$$\frac{1}{\sqrt{2}}\left[|5s_{1/2}m_{j_2}=-1/2,51c,\uparrow\rangle-|5s_{1/2}m_{j_2}=+1/2,51c,\downarrow\rangle\right]$$

to end up in a singlet or triplet state respectively, after interacting for at time t_{eff} with a laser of intensity $I(0,z)$ and detuning Δ. For this calculation, we neglect the velocity dispersion of the atomic beam, hence the associated dispersion of t_{eff}. Instead, we take into account the profile of the laser beam in the direction perpendicular to the atomic beam. To this end, we average the result over the spatial extension of the atomic sample along the **z** axis. Next, we convolute the result with the velocity distribution of the atoms. Such a step allows us to include in the model the Doppler effect on the laser detuning Δ. We finally perform a convolution between the frequency response of the atom and a Gaussian lineshape of 3 MHz width modelling the frequency noise of the laser. This procedure allows us to compute the probability for the atom to be stored in the metastable $|4d_{3/2}\rangle$ level and the average probabilities $P_s(I_0,\Delta)$ and $P_t(I_0,\Delta)$ to be in a singlet or triplet state before the decircularization pulse, as a function of the laser intensity I_0 at the center of the beam.

The numerical model matches very well with the data of figure 3.10. Still, the proportionality factor between the peak intensity I_0 and the power P of the laser beam is fitted to be 26% smaller than the result of an ab initio calculation from the estimated size of the laser beam at the atomic position. This proportionality factor is the only free parameter.

3.3.4 The autoionization lifetime of the $|4d_{3/2},51c\rangle$ state

It is possible to estimate a lower bound for the lifetime of the $|4d_{3/2},51c\rangle$ level from the experimental data. The survival probability N^c/N_0^c of the circular state is

$$\frac{N^c}{N_0^c} = P_{s_{1/2}} + P_{d_{3/2}} e^{\frac{-t}{\tau_{d_{3/2}}}} \tag{3.1}$$

where $P_{s_{1/2}}$ ($P_{d_{3/2}}$) is the probability to find the atoms in the $|5s_{1/2},51c\rangle$ ($|4d_{3/2},51c\rangle$) state and $\tau_{d_{3/2}}$ is the autoionization lifetime of the $|4d_{3/2},51c\rangle$ state. By considering $P_{s_{1/2}} = 1 - P_{d_{3/2}}$, we get

$$\frac{N^c}{N_0^c} = 1 - P_{d_{3/2}} \left[1 - e^{\frac{-t}{\tau_{d_{3/2}}}} \right]. \tag{3.2}$$

We fit the data of figure 3.8b with the formula

$$\frac{N^c}{N_0^c} = 1 - \beta P_{d_{3/2}} \tag{3.3}$$

where $P_{d_{3/2}}$ is computed via the numerical model. From the fitted 95% confidence band, we find that

$$0.004 < \beta < 0.028 \tag{3.4}$$

providing a lower bound on the auto-ionization lifetime $\tau_{d_{3/2}} > 5$ ms. We cannot do better than a lower bound for the lifetime given the finite time-of-flight of the atoms of 140 μs. A cold circular Rydberg state of Strontium would certainly allow us to measure more precisely the lifetime.

3.3.5 Probing the spin dynamics of the ionic-core electron

From the $|5p_{1/2},51c\rangle$ state, the atoms can decay in the $|4d_{3/2},51c\rangle$ states, in the triplet $|5s_{1/2},51c\rangle$ state or also back in the singlet $|5s_{1/2},51c\rangle$ state. To measure the amount of those decaying in these two last states, we use the decircularization and two MW probes discriminating between the singlet and triplet states. We leave to appendix D the description of the calibration of these two probes.

The corresponding data are divided in two sections, one where the singlet-triplet dynamics is investigated as a function of the laser power, the other where we set the laser power and vary the laser detuning.

3.3.5.1 Singlet to triplet $|5s_{1/2},51c\rangle$ state transfer

The experiment is very similar to that performed to verify the survival of the circular states to the autoionization effect. We circularize, excite the core, thus inducing the optical pumping from $|5p_{1/2},nC\rangle$ to the $|4d_{3/2},nC\rangle$ states and to the triplet $|5s_{1/2},nC\rangle$ state, decircularize and finally

apply the probes. The repumper is left on all the time.

The excitation of the core is done via a 5 μs pulse of the 422 nm laser with σ- polarization, kept in resonance with the $|5s\rangle \rightarrow |5p\rangle$ transition. While the 422 nm laser power is scanned from 0 to 10 mW, we measure the decircularized singlet and triplet populations by use of the corresponding MW probes.

Figure 3.12a shows the results of this experiment. Up to $P = 0.1$ mW, the singlet $|5s_{1/2}, 51c\rangle$ state population decreases as a function of the laser power down to $\sim 25\%$, while the population of the triplet state rises to $\sim 75\%$. The core electron is promoted from $|5s_{1/2}, m_{j_2} = +1/2\rangle$ to $|5p_{1/2}, m_{j_2} = -1/2\rangle$ and then optically pumped in the $|5s_{1/2}, m_{j_2} = -1/2\rangle$ sub-level after a few absorption-spontaneous emission cycles only. $|5s_{1/2}, m_{j_2} = -1/2\rangle$ is almost a dark state, for the selected configuration of the polarization (figure 3.12b). The result of this redistribution is therefore a $1:3$ mixture of singlet and triplet states.

For $P > 0.1$ mW, the minor $\sigma+$ component of the 422 nm laser polarization becomes large enough to have a sizable effect. The $|5s_{1/2}, m_{j_2} = -1/2\rangle$ state is no longer a dark state (figure 3.12c). Absorption and spontaneous emission cycles repeat until the atoms decay in the $|4d_{3/2}, 51c\rangle$ metastable state. The decircularization leads to the autoionization effect. Accordingly, both singlet and triplet populations decrease as a function of the laser power.

The numerical model predicts very well the dependency of the singlet and triplet populations as a function of the laser power, as showed by the solid lines of figure 3.12. Note that, to obtain a good fit of the data, we have to compensate for the lower detection efficiency of the triplet probe. Also, the transfer efficiency of the decircularization rf pulse is different for an atom in the singlet or triplet state. This implies that an efficient -π pulse decircularizing the singlet population is less efficient for the triplet population. The atoms belonging to that spin class are indeed accumulated along the low-l_1 states visited during the action of the second rf pulse. This explains the lower number of triplets detected at low-l_1. We calibrate the detection efficiency of the triplet probe by assuming that, for a large 422 nm laser power and in the presence of repumper light, the population of the triplet state is 75%.

3.3.5.2 Singlet-triplet dynamics as a function of the laser detuning

We now discuss the optical pumping in the triplet state of $|5s_{1/2}, 51c\rangle$ as a function of the 422 nm laser detuning.

We first reduce the power of the 422 nm laser, to avoid transferring atoms to the $|4d\rangle$ levels,

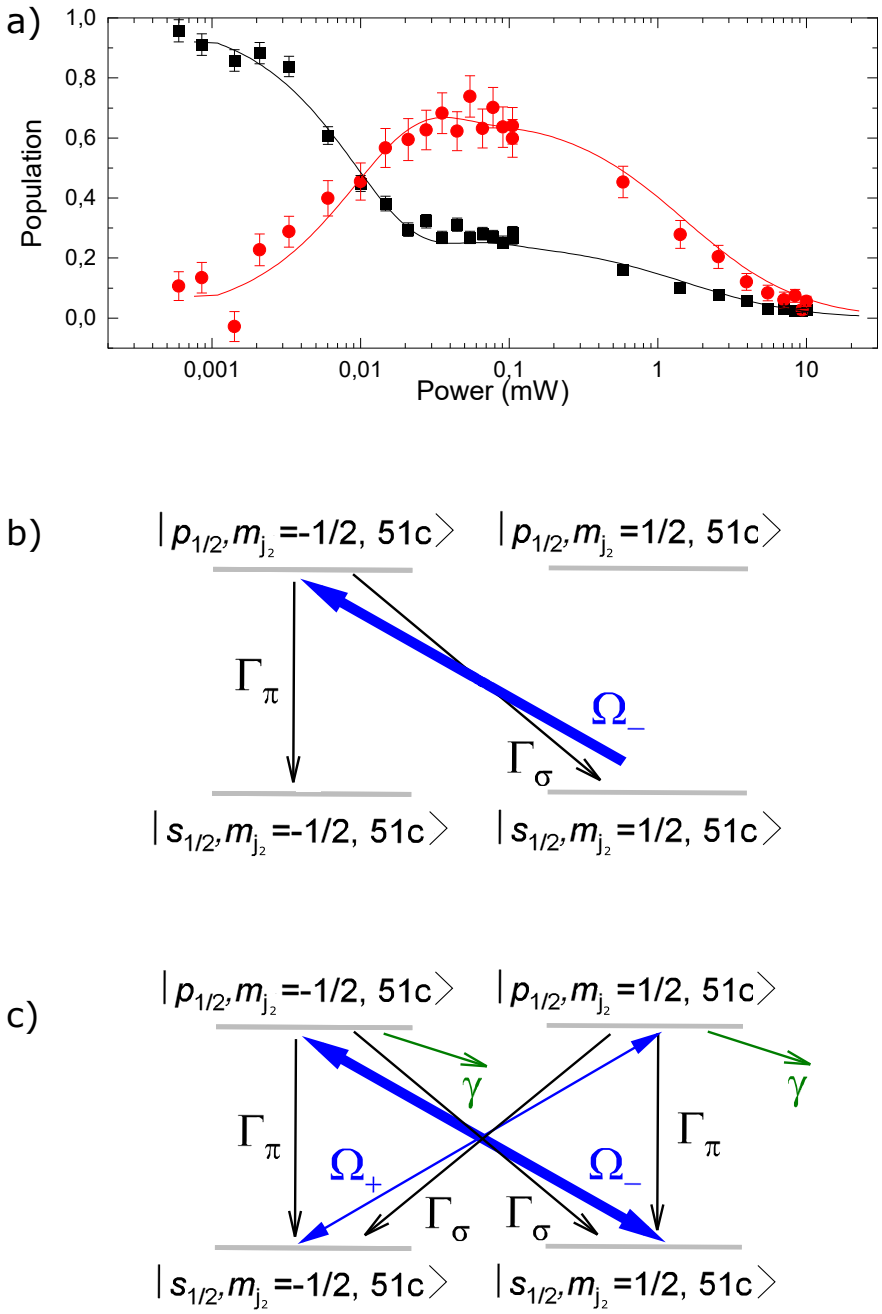

Figure 3.12: a) $|5s_{1/2},51c\rangle$ singlet and triplet populations (black and red points respectively), detected after the decircularization, as a function of the laser power. The solid lines present the predictions of the numerical model. b-c) Schemes of the dynamics following the interaction between the laser beam and the atoms, for low and high laser power respectively.

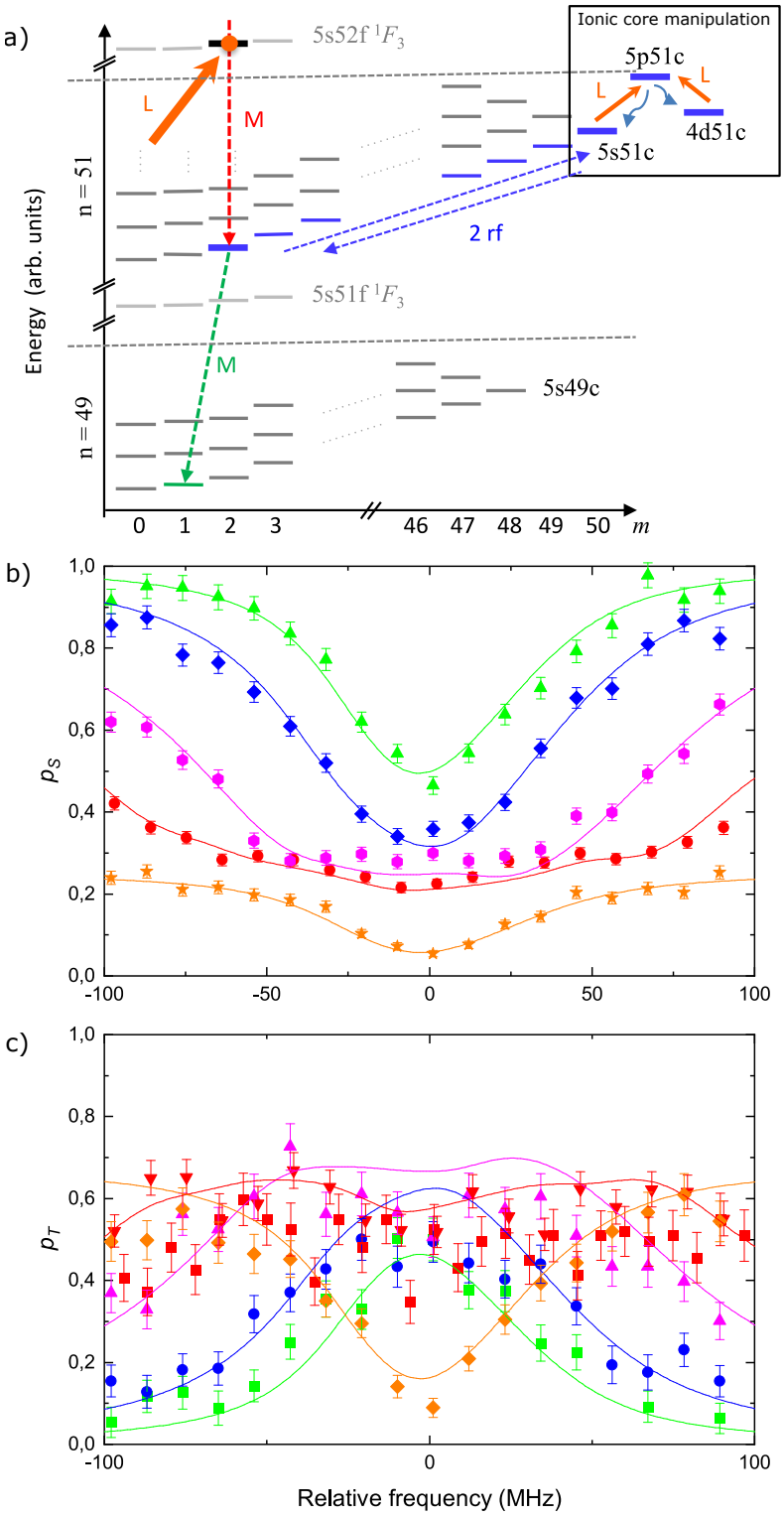

Figure 3.13: a) Navigation in the Hilbert space. b) - c) Singlet and triplet populations (ρ_S, ρ_T) as a function of the 422 nm laser frequency, for different laser powers (orange points: 4 mW, red points: 0.29 mW, pink points: 43 μW, blue points: 19 μW, green points: 9.6 μW). Solid lines are the theoretical predictions made by the numerical model.

and repeat the experiment demonstrating the autoionization for a low-l_1 state. We detect the singlet and the triplet populations returning in a low-l_1 state by use of the respective probes (figure 3.13a). We observe a dip in the singlet population when the 422 nm crosses the resonance, which broadens when increasing the laser power, (figure 3.13b). This drop results from the decay in the triplet state, whose population rises when the laser is resonant, (figure 3.13c). When the singlet dip is sufficiently broad, it appears as the background of the autoionization dip evidenced in figure 3.10b.

We then increase the laser powers. Initially, this results in a broadening of the singlet dip and triplet peak. Around 4 mW instead, both signals present a central dip, around the $|5s_{1/2}\rangle \rightarrow |5p_{1/2}\rangle$ resonance frequency. This is due to the fact that, from this laser power on, the atoms are pumped in the $|4d_{3/2}, 51c\rangle$ states and the decircularization consequently causes the autoionization of those atoms and a reduction of counts both for the singlet and the triplet populations. The numerical model predicts again very well the evolution of the singlet and triplet populations (see solid lines of figure 3.13), both when the laser power is not sufficient to excite the atoms in the metastable $|4d_{3/2}, 51c\rangle$ levels (green, blue and pink points) and when we lose atomic counts for the decay in those states (red and orange points).

3.3.6 The absence of autoionization for the $|4d_{5/2}, 51c\rangle$ state

We investigate the autoionization effect for $|4d_{5/2}, 51c\rangle$. We proceed as we did when performing the experiment for the atoms in $|4d_{3/2}, 51c\rangle$.

We prepare a similar sequence (figure 3.14) to that displayed in figure 3.9. The only difference is that we replace the 422 nm laser pulse with a 408 nm laser in continuous wave mode, exciting the atoms into the $|5p_{3/2}, 51c\rangle$ level, from which the population spontaneously decays onto the $|4d_{5/2}, 51c\rangle$ state and the $|4d_{3/2}, 51c\rangle$ state. We also perform analogous measurements to those presented for $|4d_{3/2}\rangle$. As there, we present the circular state survival probability, (figure 3.15a), as well as the number of atoms detected in the low-l_1 state after the decircularization, as a function of the laser frequency (figure 3.15b). These two curves are recorded simultaneously to eliminate the effect of the slow drift of the 408 nm laser frequency, which is not locked due to experimental limitations. Results are analogous to the $|4d_{3/2}\rangle$ case. We observe no significant variation on the atomic signal for the circular state and a drop of the counts due to autoionization effect when we return the atoms to the low-l_1 state after the core excitation.

We estimate the population of the $|4d\rangle$ states from the dip in the N/N_0 signal showed in figure 3.15b. At the lowest point of the Lorentz fit, the ratio N/N_0 is 8%. Part of the atom count reduction can be due to a transfer of the atoms into the $|5s_{1/2}, 51c\rangle$ triplet state. 85% of the population is instead optically pumped in the $|4d\rangle$ states. From the branching ratio, we deduce

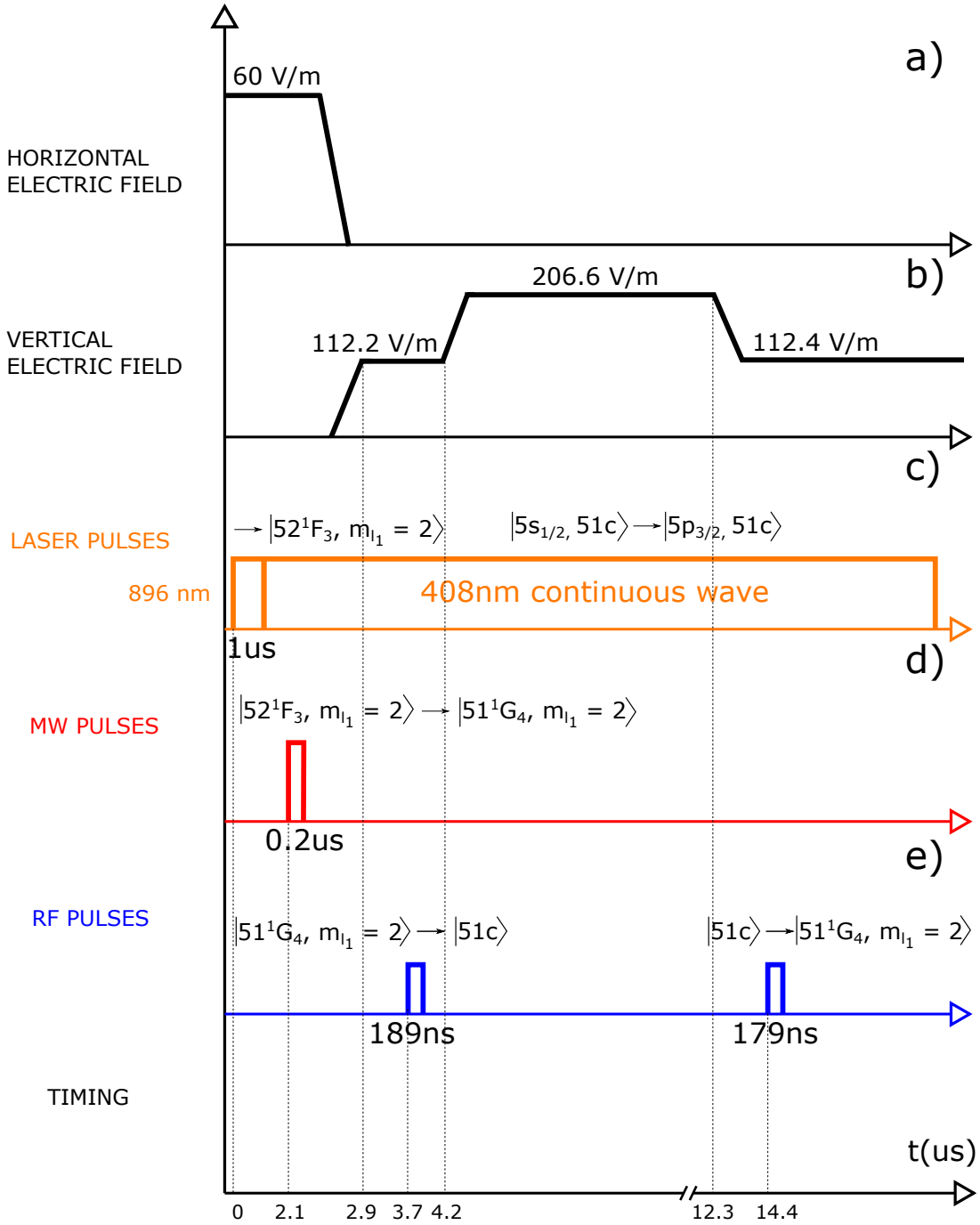

Figure 3.14: Sequence of laser, MW, rf and static electric fields used to measure the autoionization effect for the $|4d_{5/2}, 51c\rangle$ state.

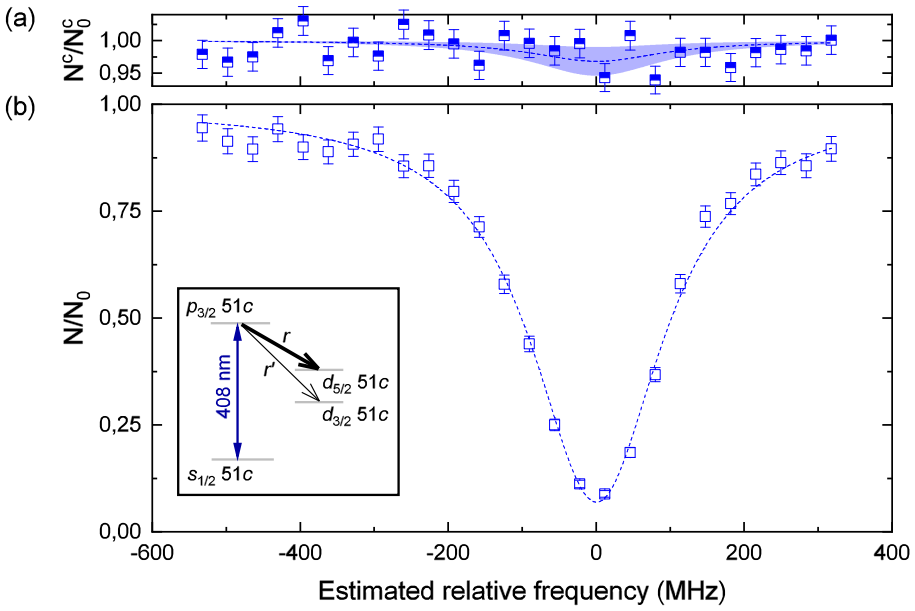

Figure 3.15: a) Absence of autoionization effect for the $|4d_{5/2},51c\rangle$ state (blue, full points). b) Presence of autoionization effect for the $|4d_{5/2},51^1G_4,m_{l_1}=+2\rangle$ state accessed by decircularization (blue, empty points).

that at least 76% of the population is in the $|4d_{5/2}\rangle$ level and 9% is in $|4d_{3/2}\rangle$. These amounts derive from the branching ratio between the decay channels from the state $|5p_{3/2}\rangle$. We then write the survival probability of the circular state as

$$\frac{N^c}{N_0^c} = P_{s_{1/2}} + P_{d_{3/2}} e^{\frac{-t}{\tau_{d_{3/2}}}} + P_{d_{5/2}} e^{\frac{-t}{\tau_{d_{5/2}}}}, \tag{3.5}$$

where $P_{d_{5/2}}$ is the probability to find the atoms in the $|4d_{5/2}\rangle$ state and $\tau_{d_{5/2}}$ is the autoionization lifetime of the same state. To get a lower bound on $\tau_{d_{5/2}}$, we assume $\tau_{d_{3/2}} = \infty$ and that all the loss is due to the population in the $|4d_{5/2}\rangle$ state. With this assumption, we deduce from the Lorentz fit $N^c/N_0^c > 0.946$ at the minimum of the curve with more than 95% probability. This value leads to $\tau_{d_{5/2}} > 2$ ms. As for the measurement of the $|4d_{3/2},51c\rangle$ lifetime, we are strongly limited by the time-of-flight of the atoms.

3.4 Discussion

In this chapter, we present our study on the autoionization effect for the Rydberg states of Strontium. As a central result, we report the evidence of the survival of the circular Rydberg states of Strontium to the autoionization effect, whether the ionic core is promoted to the $|4d_{3/2}\rangle$ or $|4d_{5/2}\rangle$ state. We check that we change the state of the core via the optical excitation by testing the presence of autoionization for a low-l_1 Rydberg state synchronously with the measurement

on the circular state. Our data are first fitted via a numerical model of the optical pumping and then used to estimate some lower bounds for the autoionization lifetimes of $|4d_{3/2},51c\rangle$ and $|4d_{5/2},51c\rangle$, of 5 ms and 2 ms respectively. The main experimental limitation, preventing us from measuring these quantities further, is the finite time-of-flight of the atoms.

As a second set of results, we observe a decay of the $|5p_{1/2},nl_1\rangle$ in the $|5s_{1/2},nl_1\rangle$ triplet state. This dynamics is dominant for low 422 nm laser power whereas the spontaneous decay in the $|4d\rangle$ states from the $|5p\rangle$ level governs at high laser powers. The measurements on the singlet and triplet populations is achieved via individual, spin-sensitive, MW pulsed probes calibrated between low-l_1 Rydberg states.

The results on the autoionization effect described in this chapter pave the way to optical cooling and trapping of long-lived circular state atoms with considerable, potential impact on quantum metrology and quantum simulation. The interaction between the core and Rydberg electron leads us to envision quantum logic operations between them. Importing optical manipulation techniques developed for ion trap experiments makes it possible to use these quantum gate operations to detect or manipulate the outer Rydberg electron. Following this research line, we are going to present, in the next chapter, some optical manipulations on the atoms once the Rydberg electron is circularized, thus preserving the atoms from autoionization.

CHAPTER 4

THE COUPLING OF THE IONIC-CORE ELECTRON WITH THE CIRCULAR RYDBERG ELECTRON

Try again. Fail again. Fail better.

Samuel Beckett

We proved that the circular Rydberg states of Strontium are impervious to the autoionization effect when the core electron is excited to the $|4d_{3/2}\rangle$ or $|4d_{5/2}\rangle$ states. The absence of autoionization gives us the opportunity to optically manipulate the core while preserving the circular state of the Rydberg electron. We focus on this aspect in this chapter. We perform optical manipulations to measure the splitting between neighboring $|m_{j_2}|$ states within the $|4d_{3/2}\rangle$ set of energy levels of the core, while the Rydberg electron is prepared in the circular state.

Note that, in the former chapter, the $|4d_{3/2}\rangle$ states of the core electron were assumed degenerate and equivalent to those of the Sr^+ ion. Here, on the contrary, we distinguish two, non-degenerate sets of sub-levels within the $|4d_{3/2}\rangle$ states, differentiated by the quantum number $|m_{j_2}|$. The sub-levels with $|m_{j_2}| = 3/2$ are now energy shifted by hundreds of kHz with respect to those with $|m_{j_2}| = 1/2$. The lift of the degeneracy results from the inclusion of the electric-quadrupole term of the electron-electron interaction between the two valence electrons in the Hamiltonian of the atom. Note that this electric coupling does not allow us to distinguish among those states with $+m_{j_2}$ or $-m_{j_2}$. Thus, the levels with opposite m_{j_2} values are still degenerate.

We split this chapter in three parts. The initial section is a theoretical introduction to the electric coupling between the ionic-core electron and the Rydberg electron (section 4.1). There, we first show that the electric coupling is dominated by the electric-quadrupole term of the

multipole expansion of the Coulomb potential. We then introduce some numerical calculations of the splitting $\delta^{(12)}_{n,m_{l_1}}$ between the $|4d_{3/2}\rangle$ core states resulting from the interaction with the circular state of the Rydberg electron. The second part of the chapter discusses the principle of two experiments and the respective experimental results (sections 4.2 - 4.3). One experiment concerns the splitting $\delta^{(12)}_{n,m_{l_1}}$ between the $|4d_{3/2}\rangle$ states of the core ("direct electric-quadrupole effect"), the other is about the differential splitting $\Delta\delta^{(12)}_{n,m_{l_1}}$. The latter quantity is the difference between the value of $\delta^{(12)}_{n,m_{l_1}}$ associated to a Rydberg state and that of another Rydberg state ("differential electric-quadrupole effect"). Initially, we show how to measure the differential and direct electric-quadrupole effects, in this order, by manipulating the atoms after they are circularized. Next, we perform the same experiments while the Rydberg electron is excited to an intermediate Rydberg state along the ladder of the $n = 51$ manifold. Since we focus on the only circularization ladder for this analysis, we are going to omit the quantum number $n_1 = 0$ of the parabolic basis to make the quantum states notations simpler.
As a conclusion, we show how these experiments lead us to a Ramsey experiment, performed on a circular-to-circular transition, demonstrating that we can control the state of the Rydberg atom with a laser pulse (section 4.4).

4.1 Theory

We detail here the mathematical tools needed to understand the coupling between the ionic-core electron and the circular Rydberg electron. We start by discussing the multipole expansion of the electron-electron potential. We then introduce the Hamiltonian associated to the electric-quadrupole term of the multipole expansion and calculate its expectation value when the Rydberg electron is circularized. This calculation proves that the contribution of the electric-quadrupole Hamiltonian to the energy of the $|4d_{3/2}\rangle$ core states is measurable in the experiment.

4.1.1 The multipole expansion

The Coulomb potential governing the interaction between the two valence electrons was already presented in chapter 1 in equation (1.33). Here, we apply the multipole expansion to the Coulomb potential. This allows us to decompose the coupling between the valence electrons in a series of terms expressed by spherical harmonics [80] (we omit the term $1/(4\pi\epsilon_0)$),

$$\frac{e^2}{|r_1 - r_2|} = e^2 \sum_{k=0}^{\infty} \sum_{m=-k}^{m=k} \frac{4\pi}{2k+1} \frac{r_2^k}{r_1^{k+1}} Y_{k,m}(\theta_2, \phi_2) Y^*_{k,m}(\theta_1 \phi_r), \quad r_1 > r_2, \tag{4.1}$$

The indexes 1 and 2 refer to the Rydberg and core electron respectively, the term $Y_{k,m}$ is the spherical harmonic component of the kth term and θ_i, ϕ_i are the spherical coordinates of the ith electron. The multipole expansion at order k is therefore a sum of $2k+1$ terms. The zeroth-order term ($k = 0$) is called the monopole moment, the first-order ($k = 1$) term is called the dipole moment, the second-order ($k = 2$) is called the electric-quadrupole moment, the third-order term

($k = 3$) is called the octupole moment and so on. Equation (4.1) can be reformulated as a scalar product of tensors of rank k of the form

$$W = \sum_{k=0}^{\infty} \sum_{m=-k}^{m=k} (-1)^m C_{k,-m} Q_{k,m}, \tag{4.2}$$

where

$$C_{k,m} = -e\sqrt{\frac{4\pi}{2k+1}}\, r_1^{-k-1} Y^*_{k,m}(\theta_1, \phi_r) \quad Q_{k,m} = -e\sqrt{\frac{4\pi}{2k+1}}\, r_2^k Y_{k,m}(\theta_2, \phi_2). \tag{4.3}$$

In (4.2) and (4.3), the parameter m indicates the component of a given tensor. The term with $k = 0$ is the screening of the charge of the Sr^{2+} core by the ionic-core electron. It is the reason why the Rydberg levels of Strontium are almost hydrogenoid. Instead, we are going to discuss in detail the influence of other two terms, the electric-dipole term $W_{k=1}$ and the electric-quadrupole term $W_{k=2}$, on the energy levels $|4d_{3/2}\rangle$ of the core.

4.1.2 First-order perturbation theory

Due to the symmetry of the ionic-core wavefunction, the expectation value of $Q_{1,0}$, therefore of the first order of $W_{k=1}$, is zero. The first non-zero term in the first order perturbation theory is thus the electric-quadrupole term. Therefore, we start by discussing its contribution to the energy of the atom. We set $k = 2$ in our calculations and define the electric-quadrupole Hamiltonian as

$$\hat{W}_2 = \sum_{m=-2}^{m=2} (-1)^m \hat{C}_{2,-m} \hat{Q}_{2,m}, \tag{4.4}$$

which derives from (4.2) once passing from tensors to quantum operators. Following [81], expression (4.4) can be cast as

$$\hat{H}_Q = \nabla\hat{\mathbf{F}}^{(2)} \cdot \hat{\Theta}^{(2)}, \tag{4.5}$$

where the tensor operator $\nabla\hat{\mathbf{F}}^{(2)}$, representing the gradient field operator, plays the role of $\hat{C}_{2,-m}$ and the tensor operator $\hat{\Theta}^{(2)}$, being the electric-quadrupole moment operator, of $\hat{Q}_{2,m}$. The components of $\nabla\hat{\mathbf{F}}^{(2)}$ are

$$\begin{cases} \nabla\hat{F}^{(2)}_0 = -\frac{1}{2}\frac{\partial F_z}{\partial z}, \\ \nabla\hat{F}^{(2)}_{\pm 1} = \pm\frac{\sqrt{6}}{6}(\frac{\partial}{\partial x} \pm i\frac{\partial}{\partial y})F_z, \\ \nabla\hat{F}^{(2)}_{\pm 2} = -\frac{\sqrt{6}}{12}(\frac{\partial}{\partial x} \pm i\frac{\partial}{\partial y})(F_x \pm iF_y), \end{cases} \tag{4.6}$$

whereas those of $\hat{\Theta}^{(2)}$ ([82]) are

$$\begin{cases} \hat{\Theta}^{(2)}_0 = -\frac{e^2}{2}(3\hat{z_2}^2 - \hat{r_2}^2), \\ \hat{\Theta}^{(2)}_{\pm 1} = -e^2\sqrt{\frac{3}{2}}\,\hat{z_2}(\hat{x_2} \pm i\hat{y_2}), \\ \hat{\Theta}^{(2)}_{\pm 2} = -e^2\sqrt{\frac{3}{8}}\,(\hat{x_2} \pm i\hat{y_2})^2. \end{cases} \tag{4.7}$$

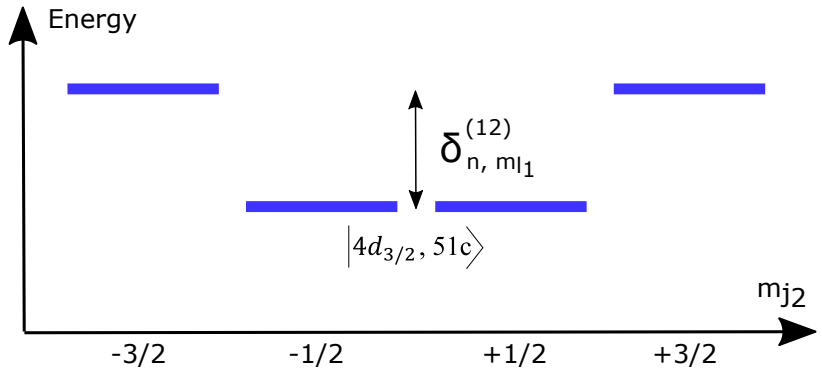

Figure 4.1: Lift of the degeneracy between the $|4d_{3/2}\rangle$ quantum states of the ionic-core electron due to the electric-quadrupole coupling with the Rydberg electron.

Here, $\mathbf{F}$ is the electric field at $r = 0$ created by the Rydberg electron in the position r_1. The first effect of the electric-quadrupole Hamiltonian on the energy levels is to lift the degeneracy between the $|4d_{3/2}\rangle$ states (figure 4.1). They are split in two sets, one with $|m_{j_2}| = 3/2$ and the other with $|m_{j_2}| = 1/2$. When the Rydberg electron is in the state $|n, l_1, m_{l_1}\rangle$, those two sets are energy shifted by an amount

$$V_{12} = \begin{cases} +\hbar\delta^{(12)}_{n,m_{l_1}}/2 & if \quad |m_{j_2}| = 3/2 \\ -\hbar\delta^{(12)}_{n,m_{l_1}}/2 & if \quad |m_{j_2}| = 1/2 \end{cases} . \tag{4.8}$$

We use the term "splitting" to refer to $\delta^{(12)}_{n,m_{l_1}}$. To calculate its value, we must compute the expectation value of (4.5). The main complication is that all components presented in (4.6) have non-zero contributions to the calculation of $\delta^{(12)}_{n,m_{l_1}}$. Still, as a very first approximation, we perform the calculation with the only operator $\nabla\hat{F}^{(2)}_0$. We anticipate that this approximation leads to reliable theoretical predictions for high-m_{l_1} Rydberg states and that is gradually less efficient when m_{l_1} is lowered. Furthermore, it can be proven that the overall computation of $\delta^{(12)}_{n,m_{l_1}}$ comes down to calculating the expectation value of the only gradient field operator, since the matrix elements of the electric-quadrupole moment operator can be computed via the Wigner-Eckart theorem. The next paragraph goes through this discussion.

4.1.3 The Wigner-Eckart theorem

The Wigner-Eckart theorem [80, 83] states that, given a tensor operator $\hat{\mathbf{T}}^k_q$ and two state subspaces of angular momenta j and j', there exists a constant $\langle j\|\hat{\mathbf{T}}^k_q\|j'\rangle$ such that for all m, m', q, the matrix elements of $\hat{\mathbf{T}}^k_q$ can be expressed as the product of $\langle j\|\hat{\mathbf{T}}^k_q\|j'\rangle$ and a scalar quantity,

$$\langle j, m|\hat{\mathbf{T}}^k_q|j', m'\rangle = \langle j'm'kq|jm\rangle\,\langle j\|\hat{\mathbf{T}}^k_q\|j'\rangle\,. \tag{4.9}$$

The term $\langle j'm'kq|jm\rangle$ is the Clebsch-Gordan coefficient which couples j' with k to get j. The constant $\langle j\|\hat{\mathbf{T}}^k_q\|j'\rangle$ is the reduced matrix element of the tensor operator.

We make use of this theorem to compute the matrix elements of the electric-quadrupole tensor operator $\hat{\Theta}^{(2)}$. For a given j_2, the tensor is diagonal with respect to $|m_{j_2}|$ and the elements along the diagonal read

$$\langle n_2, j_2, m_{j_2}|\hat{\Theta}_0^{(2)}|n_2, j_2, m_{j_2}\rangle = \langle j_2 m_{j_2} 20|j_2 m_{j_2}\rangle \langle j_2|\|\hat{\Theta}_0^{(2)}\||j_2\rangle . \tag{4.10}$$

where $\langle j_2 m_{j_2} kq|j_2 m_{j_2}\rangle$ is the Clebsch-Gordan coefficient and $\langle j_2|\|\hat{\Theta}^{(2)}\||j_2\rangle$ is the reduced matrix element of the electric-quadrupole moment operator. We set $j_2 = 3/2$. Now, the Clebsch-Gordan coefficient depends on the only magnetic quantum number of the $|4d_{3/2}\rangle$ state. It is

$$\langle j_2 = \frac{3}{2}, m_{j_2}, k = 2, q = 0|j_2 = \frac{3}{2}, m_{j_2}\rangle = \begin{cases} +\frac{1}{\sqrt{5}} & if \quad |m_{j_2}| = 3/2, \\ -\frac{1}{\sqrt{5}} & if \quad |m_{j_2}| = 1/2. \end{cases} \tag{4.11}$$

Instead, the reduced matrix element of the electric-quadrupole moment operator is given in [84] as

$$\langle j_2 = \frac{3}{2}|\|\hat{\Theta}_0^{(2)}\||j_2 = \frac{3}{2}\rangle = \sqrt{5}\Theta(4d_{3/2}), \tag{4.12}$$

where $\Theta(4d_{3/2})$ is the electric-quadrupole moment. It is as well reported by [84] as

$$\Theta(4d_{3/2}) = \frac{e}{5}\langle 4d_{3/2}|r_2^2|4d_{3/2}\rangle \tag{4.13}$$

for an electron in a $|4d_{3/2}\rangle$ state and outside a filled shell. Theoretical predictions give $\Theta(4d_{3/2})$ at $2.029(12)ea_0^2$ [85], for all $|d_{3/2}\rangle$ states, very close to the values indicated by [84] ($2.107ea_0^2$) or by [86] ($2.12ea_0^2$).

4.1.4 Calculation of the electric-quadrupole Hamiltonian expectation value

We have simplified the mathematics enough to tackle the computation of the expectation value of the electric-quadrupole Hamiltonian. We must now multiply $\Theta(4d_{3/2}) = 2.029(12)ea_0^2$ by the expectation value of the gradient field operator to obtain $\delta^{(12)}_{n,m_{l_1}}$ (the factor $\sqrt{5}$ is simplified with the Clebsch-Gordan coefficient). It can be proven that, in the specific case of the circular Rydberg state, the only component of the gradient with a non-zero contribution to the expectation value is the component $\nabla\hat{F}_0^{(2)}$ of the gradient field operator. Therefore, for the calculations on the circular state presented in this paragraph, we have

$$\delta^{(12)}_{n,m_{l_1}} = \frac{2}{\hbar}\langle \Psi_{nl_1m_{l_1}}|\nabla\hat{F}_0^{(2)}|\Psi_{nl_1m_{l_1}}\rangle \Theta(4d_{3/2}), \tag{4.14}$$

where $\Psi_{nl_1m_{l_1}}$ is the wavefunction of the circular state. The electric field gradient is written in spherical coordinates in the form

$$\nabla\hat{F}_0^{(2)} = \frac{3\cos^2\theta_1 - 1}{2r_1^3}, \tag{4.15}$$

and its expectation value is computed by the triple integral

$$\langle \Psi_{nl_1m_{l_1}} | \nabla \hat{F}_0^{(2)} | \Psi_{nl_1m_{l_1}} \rangle = \int_0^\infty dr_1 \int_0^{2\pi} d\phi_1 \int_0^\pi d\theta_1 \Psi^*_{nl_1m_{l_1}} \frac{3\cos^2\theta_1 - 1}{2r_1^3} \Psi_{nl_1m_{l_1}} r_1^2 \sin(\theta_1), \tag{4.16}$$

We express $\Psi_{nl_1m_{l_1}}$ as a product of a spatial and an angular component and we insert them in (4.14). We get

$$\langle \Psi_{nl_1m_{l_1}} | \nabla \hat{F}_0^{(2)} | \Psi_{nl_1m_{l_1}} \rangle = \int_0^\infty dr_1 \int_0^{2\pi} d\phi_1 \int_0^\pi d\theta_1 R^*_{n,l_1}(r_1) Y^{*,l_1}_{m_{l_1}}(\theta_1,\phi_1) \frac{3\cos^2\theta_1 - 1}{2r_1^3} \cdot \tag{4.17}$$

$$R_{n,l_1}(r_1) Y^{l_1}_{m_{l_1}}(\theta,\phi) r_1^2 \sin(\theta_1),$$

which can be decomposed into two separate integrals I_r, depending on the spatial coordinate r_1, and I_a, depending on the angular coordinates.
The first integral reads

$$I_r = \int_0^\infty dr_1 R^*_{n,l_1}(r_1) \frac{1}{r_1^3} R_{n,l_1}(r_1) r_1^2, \tag{4.18}$$

and is solved via the standard formula

$$I_r = \frac{1}{n^3 \left[l_1(l_1 + \frac{1}{2})(l_1 + 1) \right]}. \tag{4.19}$$

The second integral is

$$I_a = -\int_0^{2\pi} d\phi_1 \int_0^\pi d\theta_1 Y^{*,l_1}_{m_{l_1}}(\theta_1,\phi_1) \frac{3\cos^2\theta_1 - 1}{2} Y^{l_1}_{m_{l_1}}(\theta_1,\phi_1) \sin(\theta_1). \tag{4.20}$$

The integrand is simplified via the mathematics of the spherical harmonics. We recall that

$$Y^{*,l_1}_{m_{l_1}} = (-1)^{m_{l_1}} Y^{l_1}_{-m_{l_1}}. \tag{4.21}$$

Next, we compute the spherical harmonic with $l_1 = 2$ and $m_{l_1} = 0$. This reads

$$Y^2_0 = \sqrt{\frac{5}{4\pi}} \frac{3\cos^2\theta_1 - 1}{2}. \tag{4.22}$$

The equations (4.21) and (4.22) allow us to express (4.20) as an integral of the product of three spherical harmonics,

$$I_a = -(-1)^{m_{l_1}} \left(\sqrt{\frac{5}{4\pi}} \right)^{-1} \int_0^{2\pi} d\phi_1 \int_0^\pi d\theta_1 Y^{l_1}_{-m_{l_1}}(\theta_1,\phi_1) Y^2_0 Y^{l_1}_{m_{l_1}}(\theta_1,\phi_1) \sin(\theta_1). \tag{4.23}$$

This formulation of the integrand allows us to apply the formula

$$\int_0^{2\pi} d\phi_1 \int_0^\pi d\theta_1 \sin(\theta_1) Y^{l_1^A}_{m_{l_1^A}}(\theta_1,\phi_1) Y^{l_1^B}_{m_{l_1^B}}(\theta_1,\phi_1) Y^{l_1^C}_{m_{l_1^C}}(\theta_1,\phi_1) = \tag{4.24}$$

$$\sqrt{\frac{(2l_1^A+1)(2l_1^B+1)(2l_1^C+1)}{4\pi}}\begin{pmatrix} l_1^A & l_1^B & l_1^C \\ 0 & 0 & 0 \end{pmatrix}\begin{pmatrix} l_1^A & l_1^B & l_1^C \\ m_{l_1^A} & m_{l_1^B} & m_{l_1^C}, \end{pmatrix},$$

to solve I_a by use of the 3j-symbols formalism. Here, $l^{A,B,C}$ and $m_{l^{A,B,C}}$ are the angular momentum and the magnetic quantum numbers associated to the spherical harmonic $Y^{l^{A,B,C}}$ respectively.

After computing the integrals I_r and I_a, multiplying the result by the electric-quadrupole moment and converting the result in SI units, we obtain the splitting of the $|4d_{3/2},51c\rangle$ states caused by the electric-quadrupole term of the coupling between the electrons. It is of 760 kHz.

We can make two points about this electric-quadrupole splitting. The first is that it is large enough to be measured in the experiment. The second is that it depends on the principal quantum number of the circular state, following a n^{-6} power law. This results from (4.19), showing that I_r has a n^{-3} explicit dependency and a l^{-3} dependency deriving from the term $l_1(l_1+1/2)(l_1+1)$. The quantum number l scales as n. Therefore, after writing (4.19) in terms of n only, we retrieve a n^{-6} dependency. We are going to verify this dependency in the experimental data.

4.1.5 Extension of the numerical calculation to the Rydberg states of circularization ladder

The electric-quadrupole coupling between the ionic-core electron and the Rydberg electron does not concern the circular state only. Any elliptical Rydberg state can couple with the core electron. Therefore, we can extend the numerical calculation of $\delta^{(12)}_{n,m_{l_1}}$ to the case of Rydberg states with intermediate or low m_{l_1}. Here, we focus on those states belonging to the circularization ladder.

Unlike the case of the circular state, the calculations now feature elliptical Rydberg states which must be necessarily expressed in the parabolic basis $|n,n_1,m_{l_1}\rangle$. The first step is therefore to convert the latter basis in the spherical one $|n,l_1,m_{l_1}\rangle$. We do this by use of two Clebsch-Gordan coefficients, $\langle nn_1m_{l_1}|nl_1m_{l_1}\rangle^*$ and $\langle nn_1m_{l_1'}|nl_1'm_{l_1'}\rangle$, as discussed in chapter 1. As a consequence, in the case of elliptical Rydberg states, we define the electric-quadrupole splitting of the ionic-core electron states as

$$\delta^{(12)}_{n,m_{l_1}} = \sum_{l_1}\sum_{l_1'}\langle nn_1m_{l_1}|nl_1m_{l_1}\rangle^* \cdot \langle nn_1m_{l_1'}|nl_1'm_{l_1'}\rangle \cdot \tag{4.25}$$

$$\langle \Psi_{nl_1'm_{l_1'}}\Lambda_{n_2l_2s_2m_{j_2}}|\hat{H}_Q|\Psi_{nl_1m_{l_1}}\Lambda_{n_2l_2s_2m_{j_2}}\rangle,$$

where $\Lambda_{n_2l_2s_2m_{j_2}}$ is the wavefunction of the core electron. We then proceed as in the case of the circular state, by first using the Wigner-Eckart theorem for the calculation of the matrix elements of $\hat{\Theta}$ and next computing the expectation value of $\nabla\hat{F}^{(2)}_0$ as the product of two integrals. Fortunately, the solution of I_r does not depend on $m_{l_1'}$. Instead, the calculation of I_a does depend

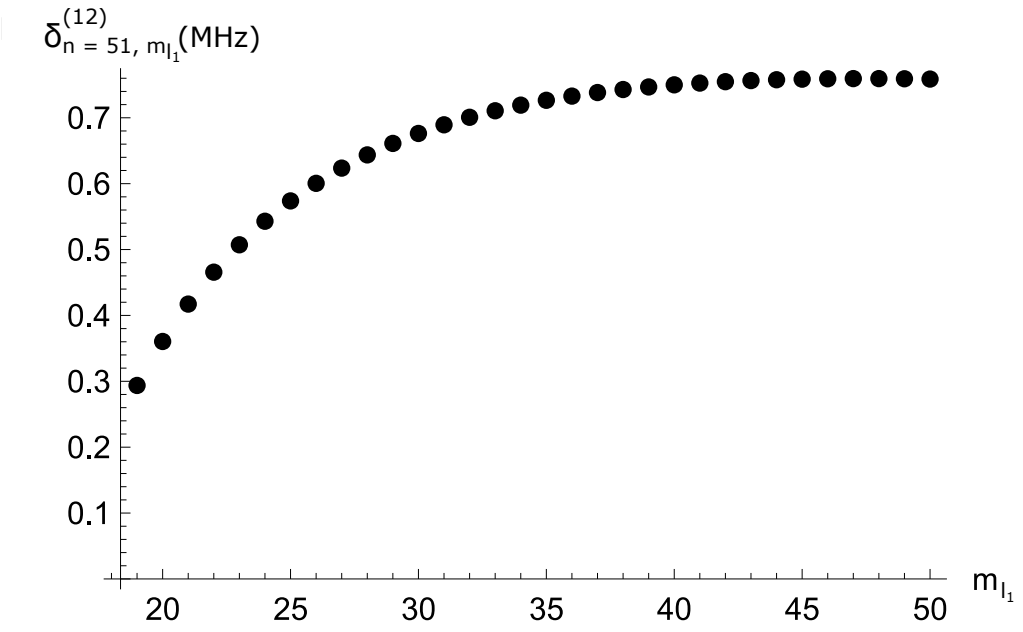

Figure 4.2: Calculation of the electric-quadrupole splitting $\delta^{(12)}_{n=51,m_{l_1}}$ as a function of the magnetic quantum number of the Rydberg electron. Our simulations concern only the Rydberg states of the circularization ladder.

on the magnetic quantum number. This integral is therefore evaluated for all values of m_{l_1}.

We calculate the splitting between the $|4d_{3/2}\rangle$ states of the core for all the Rydberg states belonging to the ladder of the $n = 51$ manifold. Figure 4.2 displays the result of this calculation. The splitting is reported as a function of the magnetic quantum number of the Rydberg electron. We will soon compare the results with the experimental data.

4.1.6 Dipole term contribution to the energy shift of the $|4d_{3/2}\rangle$ states

The electric-quadrupole component of the multipole expansion of the Coulomb potential is not the only term contributing to the energy shift of the $|4d_{3/2}\rangle$ states. Here, we briefly explain the influence of another term, the electric-dipole Hamiltonian $\hat{W}_1$ deriving from (4.2) when $k = 1$, for the circular state case only. Due to the symmetry of the ionic-core wavefunction, the expectation value of $\hat{Q}_{1,0}$, therefore of the first order of $\hat{W}_1$, is zero. However, the shift induced by $\hat{W}_1$ at second order does not vanish. This component mostly comes from the coupling of the circular atom with the core in $|4d_{3/2}\rangle$ to the Rydberg states with the core in $|5p_{1/2}\rangle$. However, it does not change very much the relative energy between the sub-levels with $|m_{j_2}| = 3/2$ and $|m_{j_2}| = 1/2$. We numerically estimate a shift of -3 kHz for $|4d_{3/2}|m_{j_2}| = 1/2, 51c\rangle$ and -6 kHz for $|4d_{3/2}|m_{j_2}| = 3/2, 51c\rangle$.

Another higher order contribution derives from the coupling between the circular state and

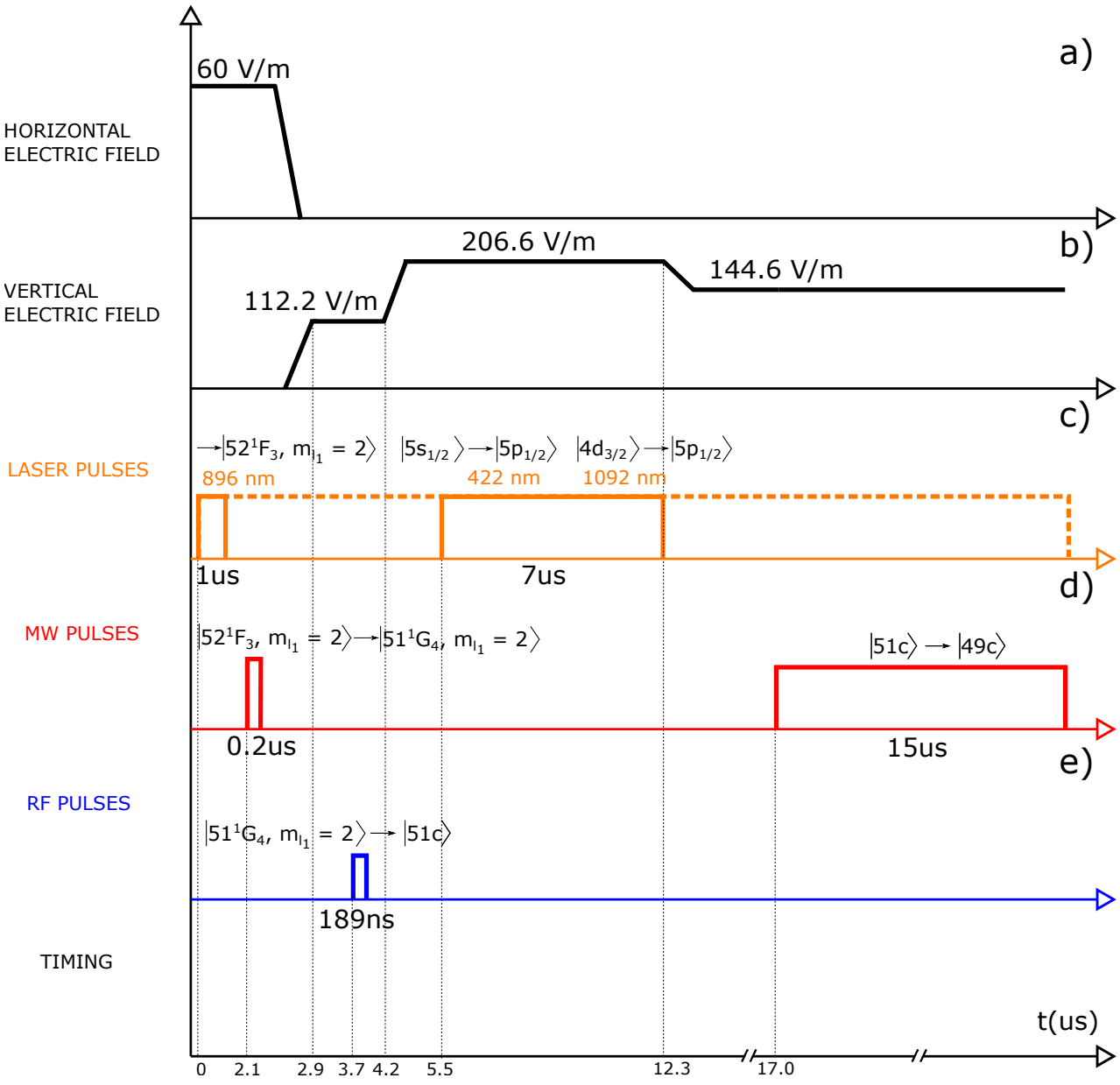

Figure 4.3: Sequence of laser, MW, rf and static electric fields used to measure the circular-to-circular frequency shift. We add the repumper in continuous wave mode (dashed, orange square in c)) to identify which frequency shift is associated to $|4d_{3/2}|m_{j_2}| = 1/2\rangle$ and which one to $|4d_{3/2}|m_{j_2}| = 3/2\rangle$ (see subsection 4.3.3 for details).

other Rydberg states of the same manifold. Note that, although the static electric field lifts the degeneracy between the circular state and the Rydberg levels with $m_{l_1} = n-2$ by more than 100 MHz, one of the Stark levels with $m_{l_1} = n-3$ is a few kHz away from the circular state. However, the coupling induced to this level by $\hat{W}_2$ is small and shifts the energy of the circular state by less than a kHz. Thus, the electric-quadrupole effect is dominant within correction of the order of one percent.

4.2 Principle of the experiment on the differential electric-quadrupole effect

The theoretical introduction makes it clear that the electric-quadrupole coupling between the ionic-core electron and the Rydberg electron governs the splitting between the $|4d_{3/2}\rangle$ ionic-core states. However, the splitting between the states of the core with the Rydberg electron in $|n, m_{l_1}\rangle$ is expected to differ from that between the same states when the Rydberg electron is instead in $|n-2, m_{l_1}-2\rangle$. The difference between the two values of the splitting is named here as $\Delta\delta^{(12)}_{n,m_{l_1}}$. This quantity is expected to be in the 100 kHz range. We are going to measure it via MW spectroscopy of the Rydberg-to-Rydberg atomic transition.

The strategy is straightforward. We prepare the $|n, m_{l_1}\rangle$ Rydberg state, optically pump the atoms in the $|4d_{3/2}\rangle$ states and finally apply a MW pulse. We record the spectrum of the Rydberg-to-Rydberg transition and show how the atomic transition frequency changes when the ionic core is excited. We expect to observe a different atomic transition frequency for the Rydberg-to-Rydberg transition depending on the state of the core, therefore three transfer lines in total. One will be associated to the core in the ground state, the other two to the core in the metastable, excited states.

4.3 Experimental measurement of the differential electric-quadrupole effect

4.3.1 Overview

In this section, we present the measurements of $\Delta\delta^{(12)}_{n,m_{l_1}}$. First, we discuss the data concerning the circular states. We measure $\Delta\delta^{(12)}_{n,m_{l_1}}$ for the transition $|51c\rangle \rightarrow |49c\rangle$ and compare the result with the value predicted by the theoretical model (paragraphs 4.3.2 - 4.3.3). Second, we focus on the measurement of $\Delta\delta^{(12)}_{n,m_{l_1}}$ for Rydberg states with intermediate m_{l_1}. In particular, we are interested in the values of $\Delta\delta^{(12)}_{n,m_{l_1}}$ between states belonging to the lowest-right Rydberg ladder of the $n = 51$ manifold and that of the $n = 49$ manifold (paragraph 4.3.4). After presenting the data, we assess their consistency by comparing the measured $\Delta\delta^{(12)}_{n,m_{l_1}}$ values with theory. Third and last,

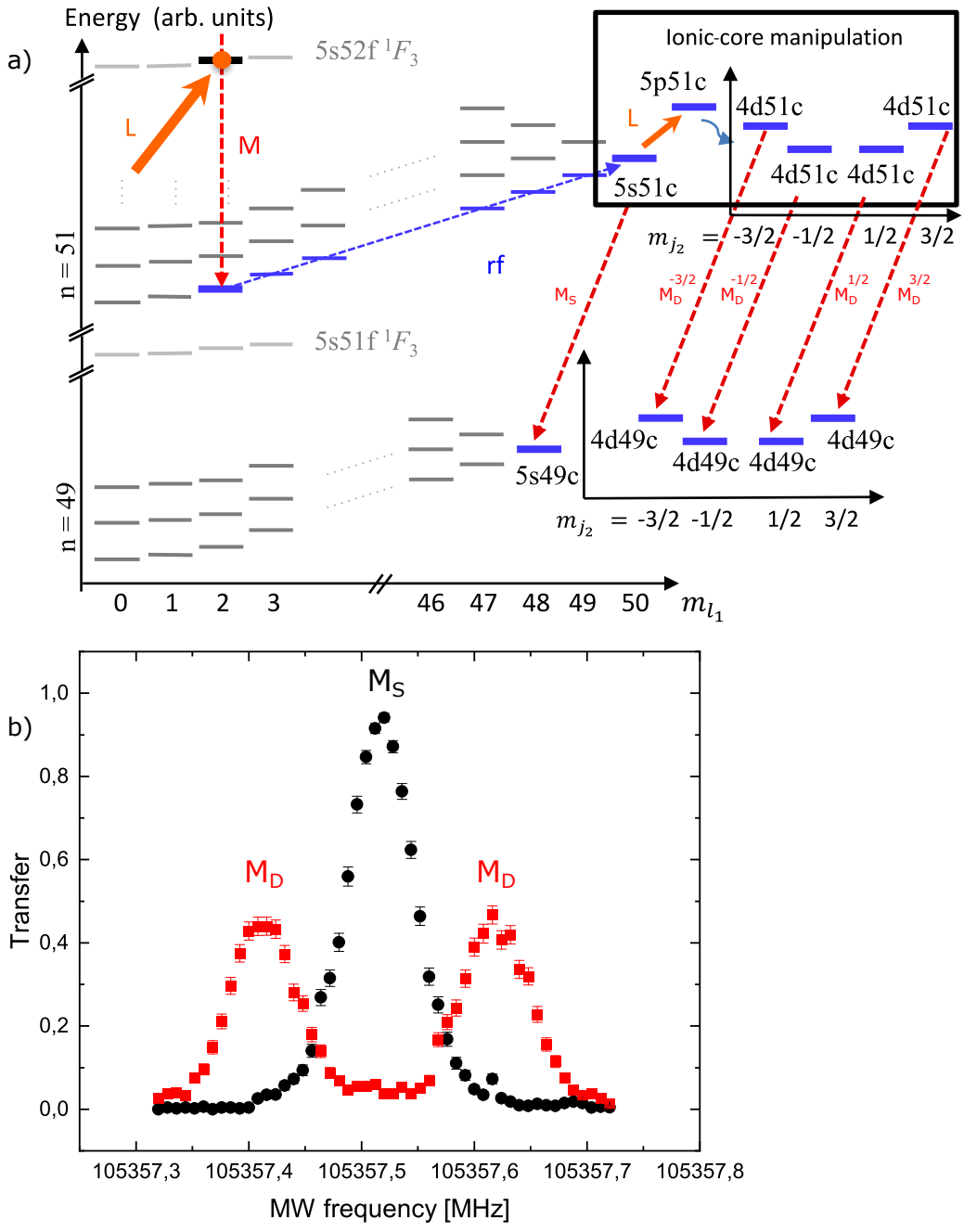

Figure 4.4: a) Scheme of the energy levels undergoing our manipulation with rf, laser and MW pulses. b) MW spectra of the $|51c\rangle \rightarrow |49c\rangle$ transition without (black squares) and with the excitation of the core (red circles).

we briefly show an evidence of the electric-quadrupole coupling between the circular state and the core in $|4d_{5/2}\rangle$ (paragraph 4.3.5). This set of data leads us to evaluate the electric-quadrupole moment of the $|d_{5/2}\rangle$ states. We discuss the agreement between the value retrieved by fitting the experimental data and the theoretical expectation in [87].

4.3.2 Measurements on the circular states

To measure the differential electric-quadrupole effect, we circularize, optically pump the atoms in the $|4d_{3/2},51c\rangle$ states with a 7 μs pulse at 422 nm and apply a MW pulse (figure 4.3). Its duration is set to be 15 μs long to resolve the $|51c\rangle \rightarrow |49\rangle$ transition line where the core is in $|4d_{3/2}|m_{j_2}| = 1/2\rangle$ from that where the core is in $|4d_{3/2}|m_{j_2}| = 3/2\rangle$. The MW power is optimized on the transfer between the two circular states. The time of the MW application is chosen via a map of the MW mode along the atomic beam. We scan the frequency of the MW pulse over ± 0.25 MHz around the $|5s_{1/2},51c\rangle \rightarrow |5s_{1/2},49c\rangle$ transition, since the differential electric-quadrupole effect is expected to be relatively small with respect to the circular-to-circular transition frequency. We ionize the atoms transferred to the $n = 49$ manifold. The experiment is finally repeated without the excitation of the core.

Figure 4.4a shows the navigation in the Hilbert space of the Rydberg electron during the experimental sequence, together with the manipulation of the core. Figure 4.4b presents the MW spectra. When the 422 nm laser is not applied, we detect only one peak, associated to the $|5s_{1/2},51c\rangle \rightarrow |5s_{1/2},49c\rangle$ transition. On the contrary, when the 422 nm laser is applied, we observe two peaks, associated to the $|4d_{3/2}|m_{j_2}| = 1/2,51c\rangle \rightarrow |4d_{3/2}|m_{j_2}| = 1/2,49c\rangle$ transition and to the $|4d_{3/2}|m_{j_2}| = 3/2,51c\rangle \rightarrow |4d_{3/2}|m_{j_2}| = 3/2,49c\rangle$ transition. They are (204.04 ± 1.66) kHz far from each other and equidistant from the $|5s_{1/2},51c\rangle \rightarrow |5s_{1/2},49c\rangle$ peak. The distance between the two transfer peaks matches the difference between $\delta^{(12)}_{n,m_{l_1}}$ for the circular state of the $n = 51$ manifold and $\delta^{(12)}_{n,m_{l_1}}$ for the circular state of the $n = 49$ manifold. To verify that, we compare the data with the theoretical expectation of the model. The calculated value for $\Delta\delta^{(12)}_{n,m_{l_1}}$ (retrieved by calculating $\delta^{(12)}_{n,m_{l_1}}$ for $|51c\rangle$ and $|49c\rangle$ and making the difference) is 205.6 kHz, in excellent agreement with the value measured here.

Note that this measurement shows that the resonance frequency of the MW returns information on the state of the core and therefore that the MW pulse is now core-selective. It means that we have now a way to distinguish the circular atoms whose core lays in $|4d_{3/2}|m_{j_2}| = 1/2\rangle$, $|4d_{3/2}|m_{j_2}| = 3/2\rangle$ or $|5s_{1/2}\rangle$. We coin the term M_S as a name for the MW pulse allowing us to quantify the atoms in $|5s_{1/2}|m_{j_2}| = 1/2,51c\rangle$. We use instead M_D as a general name for a MW pulse measuring the atoms in any $|4d_{3/2},51c\rangle$ state.

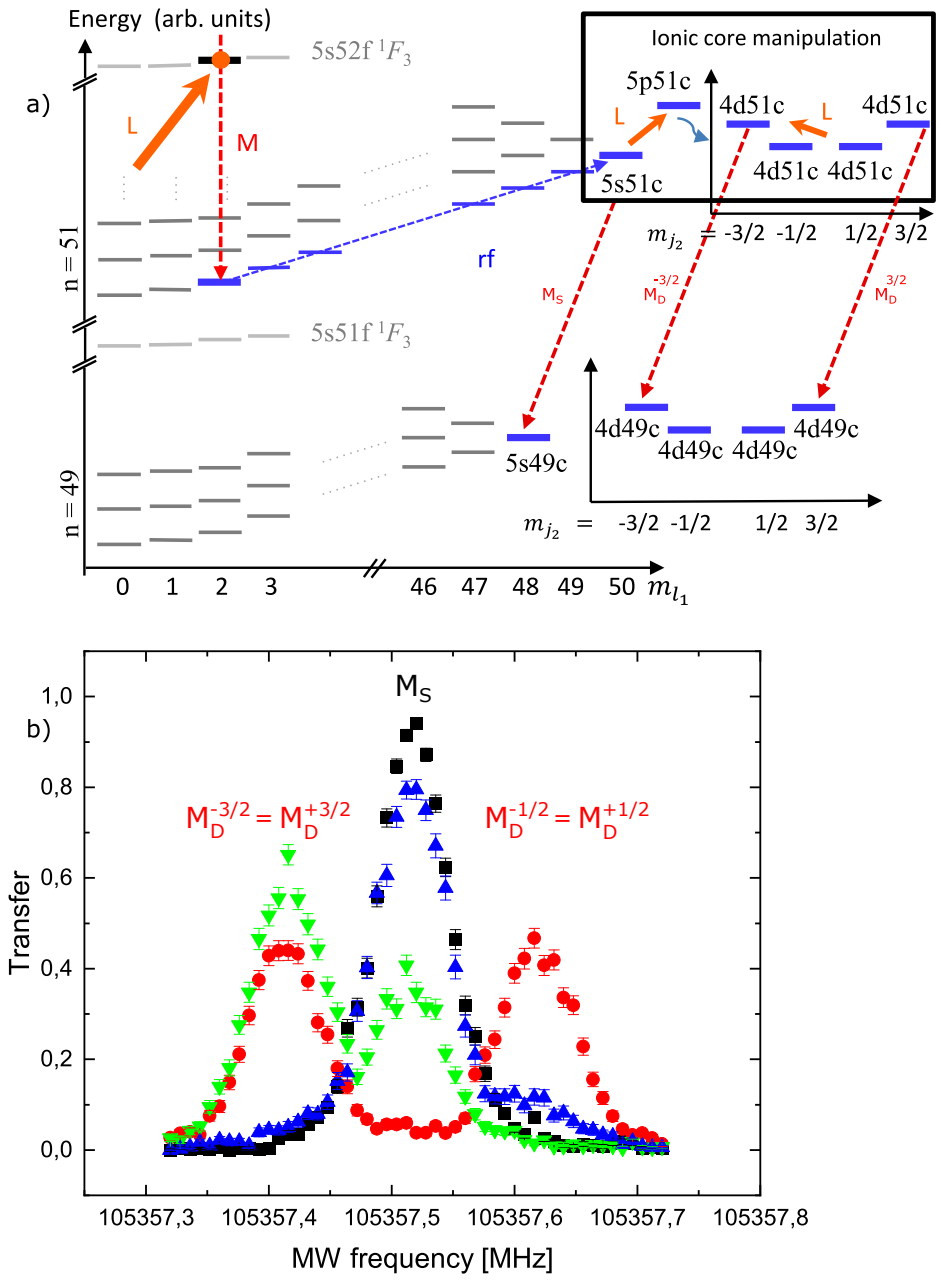

Figure 4.5: a) Scheme of the energy levels undergoing our manipulations with rf, laser and MW pulses aimed to identify the states of the core in the MW spectra. b) MW spectra of the $|51c\rangle \rightarrow |49c\rangle$ transition without the excitation of the core (black squares), with excitation of the core (red circles), with the repumper having an horizontal (blue triangles) or vertical (green triangles) polarization.

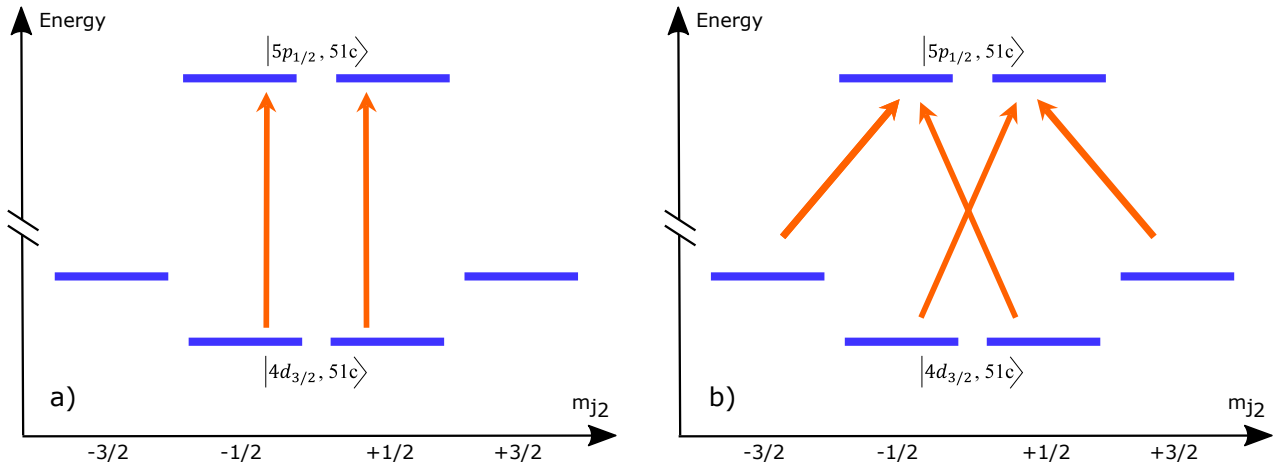

Figure 4.6: Effect of the laser polarization (a) vertical, b) horizontal) on the $|4d_{3/2}\rangle$ sub-levels of the ionic-core electron.

4.3.3 Identification of the $|4d_{3/2}\rangle$ core sub-levels with the repumper

In the condition of an excited core, the former experiment does not yield any information on which of the two transition lines is associated to the state with $|m_{j_2}| = 3/2$ or with $|m_{j_2}| = 1/2$. To do this distinction, we make use of the 1092 nm repumper laser.

We perform the same experiment as that in subsection 4.3.2. while applying the repumper at 1092 nm in continuous wave and at full power (figure 4.5a). The measurements are recorded for both an horizontal and vertical polarization of the repumper beam. At this stage of the experiment, the quantization axis is vertical.

Figure 4.5b presents the results of the experiment when the repumper is applied. When the repumper polarization is horizontal, the population is transferred back from the $|4d_{3/2}, 51c\rangle$ states to the $|5s_{1/2}, 51c\rangle$ state (figure 4.6). In such a case, we detect one transfer peak corresponding to the $|5s_{1/2}, 51c\rangle \rightarrow |5s_{1/2}, 49c\rangle$ transition. On the contrary, with a vertical polarization of the repumper, we expect a depletion of the only $|4d_{3/2}|m_{j_2}| = 1/2, 51c\rangle$ state. This is consistent with our observations, since we see that, after exciting the core and recording the MW spectrum, only one peak of the two involving a core in a $|4d_{3/2}\rangle$ state remains. The population of $|4d_{3/2}|m_{j_2}| = 1/2, 51c\rangle$ is transferred back to the $|5s_{1/2}, 51c\rangle$. Simultaneously, we leave the population of $|4d_{3/2}|m_{j_2}| = 3/2, 51c\rangle$ untouched. We can now associate each transfer peak to a state of the core. Taking as a reference the circular-to-circular transition with unexcited core, the transfer peak at lower frequencies corresponds to the $|4d_{3/2}|m_{j_2}| = 3/2, 51c\rangle \rightarrow |4d_{3/2}|m_{j_2}| = 3/2, 49c\rangle$ transition whereas that at higher frequencies accounts for the $|4d_{3/2}|m_{j_2}| = 1/2, 51c\rangle \rightarrow |4d_{3/2}|m_{j_2}| = 1/2, 49c\rangle$ transition. This fact is consistent with the theoretical predictions of paragraph 4.1.4.

4.3.4 Measurements on elliptical Rydberg states

The effect of the coupling between the two valence electrons can be also observed when performing the experiment with the Rydberg electron in an intermediate Rydberg state along the ladder of the $n = 51$ manifold.

We apply a rf pulse on the atoms prepared in $|5s_{1/2}, 51^1G_4 m_{l_1} = 2\rangle$. By adjusting the rf duration τ, we can prepare a spin-coherent-state centered on any elliptical state $|n, m_{l_1}\rangle$ along the circularization ladder. Next, we apply the 422 nm laser pulse, optically pumping the core in the $|4d_{3/2}\rangle$ states, followed by the frequency scan of a MW pulse across the $|n = 51, m_{l_1}\rangle \rightarrow |n = 49, m_{l_1} - 2\rangle$ Rydberg-to-Rydberg transition. We are interested into the resonance frequency of this MW. This is expected to shift depending on the state of the core as in the circular case. We finally prepare a second sequence, where we omit the excitation of the core. For both sequences, we measure the atoms transferred in the $n = 49$ manifold.

Figure 4.7 shows the MW spectra for six realizations of the experiment. We observe the $|n = 51, m_{l_1}\rangle \rightarrow |n = 49, m_{l_1} - 2\rangle$ transitions for $m_{l_1} = \{49, 48, 37, 17, 10, 9\}$ and the shifts of their resonance frequencies when the core is excited. We note that the core excitation shifts the transition frequencies by a few hundreds of kHz, comparable to the case of the circular state.

Figure 4.8 collects the frequency shifts, when the core is either in $|4d_{3/2}|m_{j_2}| = 3/2\rangle$ or $|4d_{3/2}|m_{j_2}| = 1/2\rangle$, as a function of the magnetic quantum number of the Rydberg state. The graph is very insightful. First, we see the transfer peaks merging and then becoming separated again, which we interpret as they invert their position (as expected from the theory). The cross-point lays around $m_{l_1} = 25$. Second, it is increasingly harder to detect the shift when lowering the magnetic quantum number of the Rydberg state. The most evident reason for this is the autoionization effect, that becomes more relevant for low-m_{l_1} states. Below $m_{l_1} = 11$, the atomic counts become very low due to the autoionization of a majority of atoms. Below $m_{l_1} = 7$, it is not possible to detect a shift. Third, we see that our theoretical model succeeds in predicting the shift of the Rydberg-to-Rydberg transition frequency both for intermediate-m_{l_1} states and for high-m_{l_1} states. However, it is less reliable for very low m_{l_1}.

The reason behind the mismatch between data and numerical model for very low m_{l_1} states is that some components of the electric-quadrupole Hamiltonian are not included in the numerical model. In the calculations, we have only used the $m = 0$ component of equation (4.4). We then argued that the influence of the $m = 2$ term was not important, since it weakly coupled the circular with only one Rydberg state with $m_{l_1} = n - 2$. The effect of the $m = 2$ term of the electric-quadrupole Hamiltonian, as well as that of the $m = 1$ term, becomes instead important when considering low-m_{l_1} Rydberg states. Any Rydberg state with lower angular momentum than that

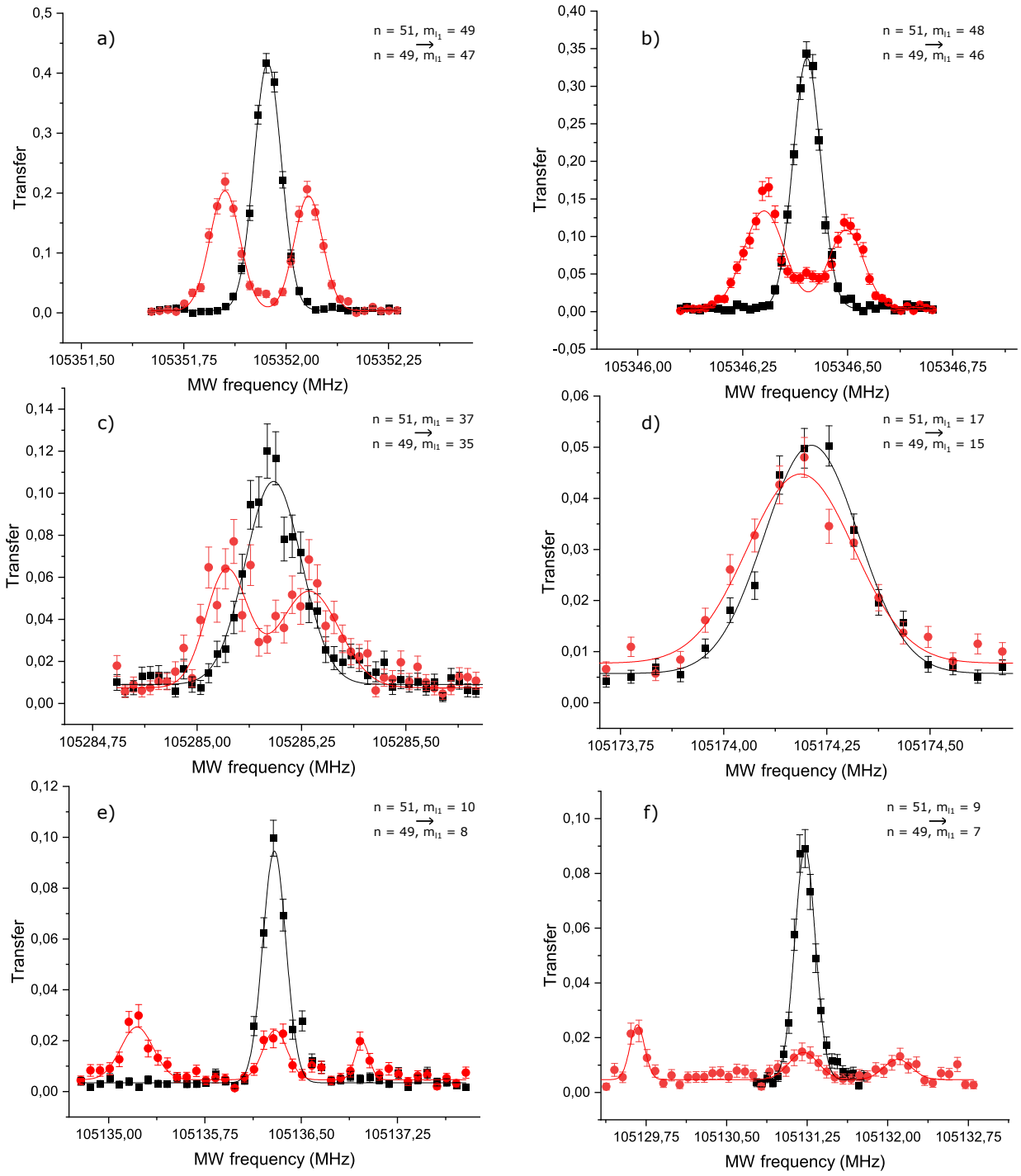

Figure 4.7: Collection of MW spectra of the $|n=51, m_{l_1}\rangle \rightarrow |n=49, m_{l_1}-2\rangle$ atomic transitions for $m_{l_1} = \{49, 48, 37, 17, 10, 9\}$. For a-d) The frequency sweep is ± 0.50 MHz with the center peak as a center. The span is increased for e) to ± 1.60 MHz and for f) to ± 1.90 MHz. Panels a),b),e),f) refer to a MW duration of 15 μs, whereas c) and d) to a MW duration of 10 μs. Black data refer to an unexcited core, red data to an excited core. Solid lines are Gaussian fits.

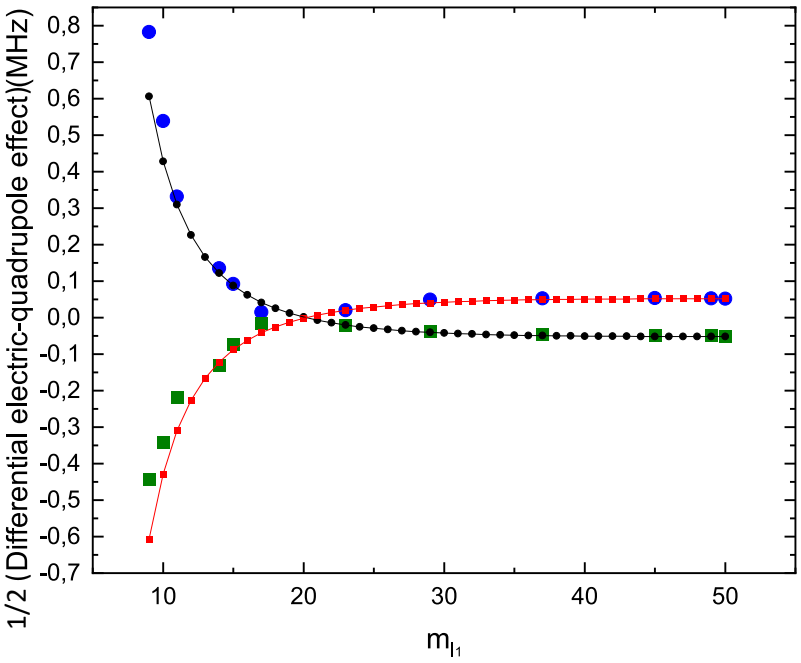

Figure 4.8: Differential electric-quadrupole effect measured on the atomic transition frequency between the $|n = 51, m_{l_1}\rangle$ Rydberg state and the $|n = 49, m_{l_1} - 2\rangle$ Rydberg state, when the core is excited to either $|4d_{3/2}|m_{j_2}| = 1/2\rangle$ (blue circles) or $|4d_{3/2}|m_{j_2}| = 3/2\rangle$ (green squares). Black and red points are the predictions made by the theoretical model for all values of m_{l_1}. Black and red lines are guides for the eye.

of the circular state of the same manifold gets indeed coupled to multiple Rydberg states [88]. Alternatively, the discrepancy between data and simulations can be tracked to the effect of the second-order dipole, which becomes larger when m_{l_1} decreases.
The strategy to improve the match between data and simulations would therefore require us to include the $m = \pm 2, \pm 1$ component of the electric-quadrupole Hamiltonian in the model.

4.3.5 Evidence of the electric-quadrupole coupling on the $|4d_{5/2}\rangle$ states

In chapter 3, we verified the absence of autoionization for $|4d_{5/2}, 51c\rangle$. This makes it possible to test the effect of the electric-quadrupole coupling between the two valence electrons also when the core is excited to a $|4d_{5/2}\rangle$ state.

We repeat the sequence applied to detect the shift of the $|51c\rangle \rightarrow |49c\rangle$ transition with a MW spectrum when the core is excited. This time, after the circularization, we apply a continuous 408 nm laser instead of the 422 nm pulse. Thus, we optically pump the atoms in $|4d_{5/2}, 51c\rangle$ via the spontaneous decay $|5p_{3/2}, 51c\rangle \rightarrow |4d_{5/2}, 51c\rangle$.

Figure 4.9a presents the navigation in the Hilbert space of the Rydberg electron, together

with the manipulations of the core. Figure 4.9b presents the results. We detect three transfer peaks when the 408 nm laser beam interacts with the atoms and one transfer peak only when the laser beam is not applied. In the first case, we interpret the three peaks as the transfer lines of the transitions $|4d_{5/2}|m_{j_2}| = 1/2, 51c\rangle \rightarrow |4d_{5/2}|m_{j_2}| = 1/2, 49c\rangle$, $|4d_{5/2}|m_{j_2}| = 3/2, 51c\rangle \rightarrow |4d_{5/2}|m_{j_2}| = 3/2, 49c\rangle$, $|4d_{5/2}|m_{j_2}| = 5/2, 51c\rangle \rightarrow |4d_{5/2}|m_{j_2}| = 5/2, 49c\rangle$. In the second case instead, we see the only transfer peak corresponding to $|5s_{1/2}, 51c\rangle \rightarrow |5s_{1/2}, 49c\rangle$.

We recall that the optical pumping from $|5s_{1/2}\rangle$ via $|5p_{3/2}\rangle$ populates both the $|4d_{5/2}\rangle$ and $|4d_{3/2}\rangle$ states. In this context, the Rydberg electron couples with the core in $|4d_{3/2}\rangle$ and with the core in $|4d_{5/2}\rangle$. We want to verify that we have truly observed a circular-to-circular frequency shift due to the core in $|4d_{5/2}\rangle$ and not again the shift due to the core in $|4d_{3/2}\rangle$. The problem is that the frequency shifts of the $|51c\rangle \rightarrow |49c\rangle$ transition due to the core in $|4d_{5/2}\rangle$ or $|4d_{3/2}\rangle$ are comparable. Also, the $|4d_{3/2}, 51c\rangle$ and $|4d_{5/2}, 51c\rangle$ states are indistinguishable at the detection stage. Fortunately, the distinction can be done via the repumper at 1092 nm. This is expected to deplete the $|4d_{3/2}, 51c\rangle$ states only.

Figure 4.10 presents two MW spectra. One is performed after the core excitation with only the 408 nm laser, the other is done when the 408 nm laser acts with a synchronous 1092 nm laser pulse. We observe a depletion of the $|4d_{3/2}\rangle$ states when the repumper is applied. Its limited effect is due to the fact that the majority of the atoms are in the $|4d_{5/2}\rangle$ states. However, the results following the application of the repumper confirm that the circular-to-circular shift was mainly due to the core in the $|4d_{5/2}\rangle$ states. We can therefore deduce that the resonance between $|51c\rangle$ and $|49c\rangle$ shifts within a 140 kHz range due to the coupling with the core in the $|4d_{5/2}\rangle$ states (see Table 4.1).

Table 4.1: Frequency shift of the $|51c\rangle \rightarrow |49c\rangle$ transition due to the electric-quadrupole coupling between the Rydberg electron and the core in $|4d_{5/2}\rangle$.

Relative position of the peak	MW frequency (MHz)	Resonance frequency shift (kHz)
Left	105357.38727 ± 0.0016	-129.84
Central	105357.55275 ± 0.00295	35.64
Right	105357.6516 ± 0.00366	134.49

Figure 4.11 shows a comparison between the expected shift of the circular-to-circular atomic transition frequency and our data. Reference [87] claims that the frequency shift, due to the electric-quadrupole coupling to the $|4d_{5/2}\rangle$ states, evolves as

$$\Delta\nu = \frac{1}{2\hbar}\Theta(4d_{5/2})\frac{\partial F}{\partial z}\frac{35 - 12m_{j_2}^2}{40}, \tag{4.26}$$

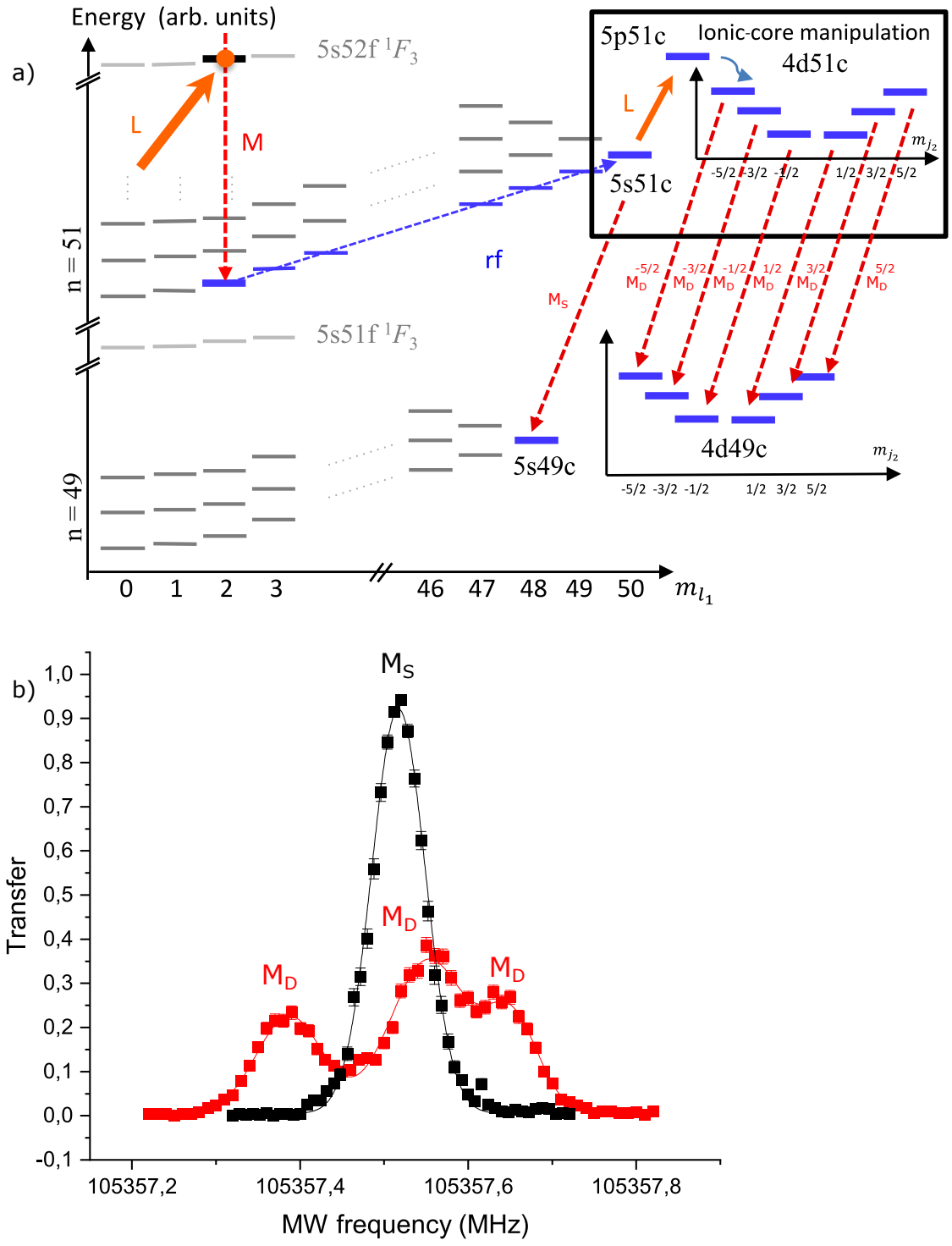

Figure 4.9: a) Navigation in the Hilbert space following our manipulations with rf, laser and MW pulses. b) MW spectra of the $|51c\rangle \rightarrow |49c\rangle$ transition with (red data) and without (black data) the excitation of the core to the $|4d_{5/2}\rangle$ states.

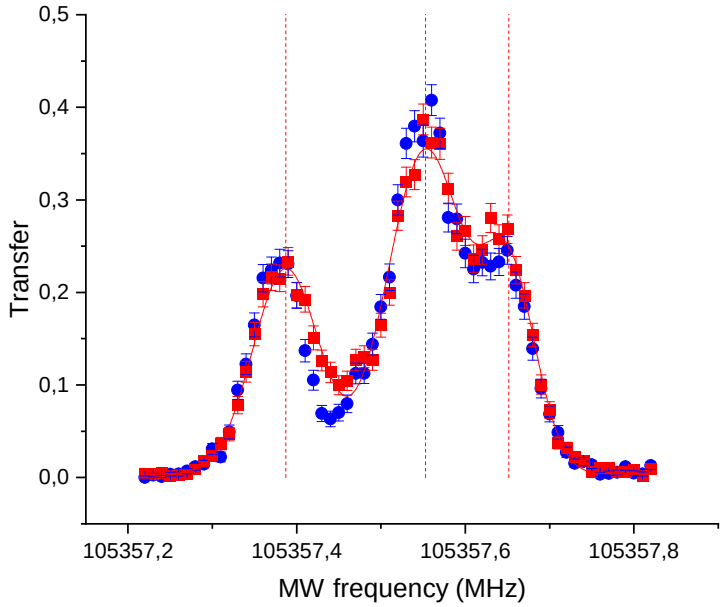

Figure 4.10: MW spectra of the $|51c\rangle \rightarrow |49c\rangle$ transition after the optical pumping in the $|4d_{5/2}\rangle$ and $|4d_{3/2}\rangle$ states performed by the 408 nm laser. Red data show the results when the repumper at 1092 nm is not applied on the atoms, blue data when it is applied. Solid line is a Gaussian fit, dashed lines indicate the transfer peaks.

where $\Theta(4d_{5/2})$ is the electric-quadrupole moment for the $|4d_{5/2}\rangle$ states [84], defined as

$$\Theta(4d_{5/2}) = \frac{2e}{7} \langle 4d_{5/2}|r_2^2|4d_{5/2}\rangle . \tag{4.27}$$

Our experimental results obtained on the differential electric-quadrupole effect for the $|4d_{5/2}\rangle$ states are in excellent agreement with the $m_{j_2}^2$ dependency predicted by equation (4.26) (see figure 4.11). The data on the differential electric-quadrupole shift are well simulated when using $2.973^{(+0.026)}_{(-0.033)}$ atomic units as a value of the electric-quadrupole moment for the $|4d_{5/2}\rangle$ states [87].

4.4 Principle of the experiment on the direct electric-quadrupole effect

We switch to our experimental study of the direct electric-quadrupole effect. The purpose of the experiment is to measure the splitting $\delta^{(12)}_{n,m_{l_1}}$ between the $|4d_{3/2}\rangle$ states of the ionic core. In this section, we discuss the case of the circular state $|51c\rangle$. The principle of the measurement consists in observing the time evolution of two coherent superposition states of $|4d_{3/2}|m_{j_2}| = 1/2, 51c\rangle$ and $|4d_{3/2}|m_{j_2}| = 3/2, 51c\rangle$. These superposition states are initially prepared as dark states of the repumper laser. They are produced by applying a short repumper pulse to the atoms prepared

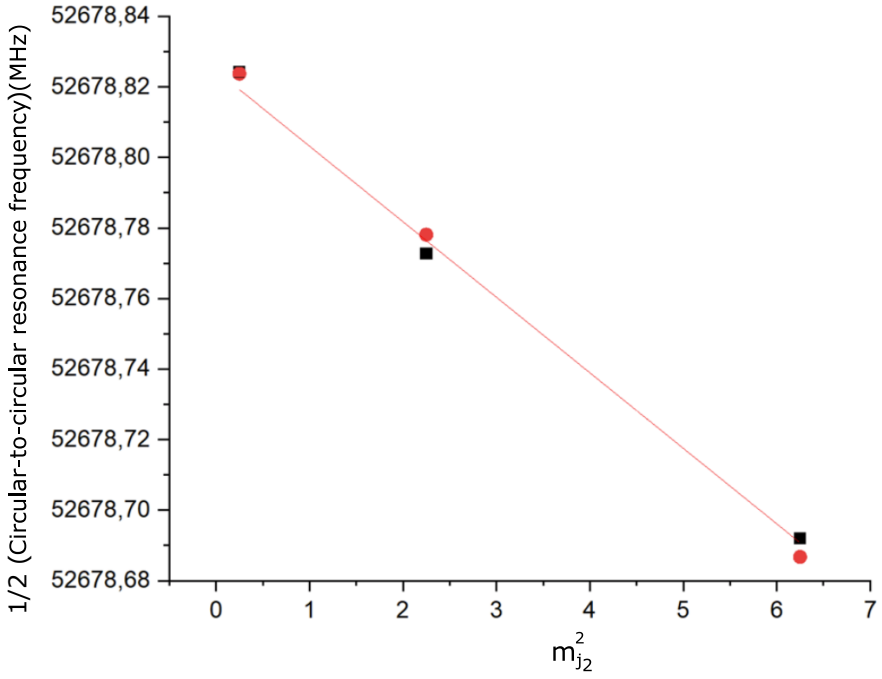

Figure 4.11: Circular-to-circular resonance frequency as a function of the magnetic quantum number m_{j_2} squared. Black squares indicate the experimental data, red circles are the theoretical expectation made by use of (4.26) with $\Theta(4d_{5/2}) = 2.973^{(+0.026)}_{(-0.033)}$ atomic units, the red line is a linear fit.

in $|4d_{3/2}, 51c\rangle$ by the 422 nm laser. Under the effect of electric-quadrupole splitting, these dark states evolve in time and acquire a bright component, which we probe with a second repumper pulse.

We go through this physics in more detail. We start by circularizing the atoms and optically pumping the ionic-core electron in the $|4d_{3/2}, 51c\rangle$ states via the 422 nm laser. Next, we apply a repumper pulse. This laser has a horizontal polarization, perpendicular to the quantization axis. This is imposed by the vertical electric field generated by the plane electrodes of the experimental chamber. The dynamics of the system now concerns two separate three-level systems, one composed by $|4d_{3/2} m_{j_2} = -1/2, 51c\rangle$, $|4d_{3/2} m_{j_2} = +3/2, 51c\rangle$ and $|5p_{1/2} m_{j_2} = +1/2, 51c\rangle$, the other by $|4d_{3/2} m_{j_2} = -3/2, 51c\rangle$, $|4d_{3/2} m_{j_2} = +1/2, 51c\rangle$ and $|5p_{1/2} m_{j_2} = -1/2, 51c\rangle$, as shown in figure 4.12a. There, we neglect the electric-quadrupole coupling. The two three-level systems belong to two independent sub-spaces. It follows that we can discuss the physics of one of the two, the same arguments holding for the other. We choose to discuss that composed by $|4d_{3/2} m_{j_2} = -1/2, 51c\rangle$, $|4d_{3/2} m_{j_2} = +3/2, 51c\rangle$ and $|5p_{1/2} m_{j_2} = +1/2, 51c\rangle$. Within this set of states, the repumper pulse

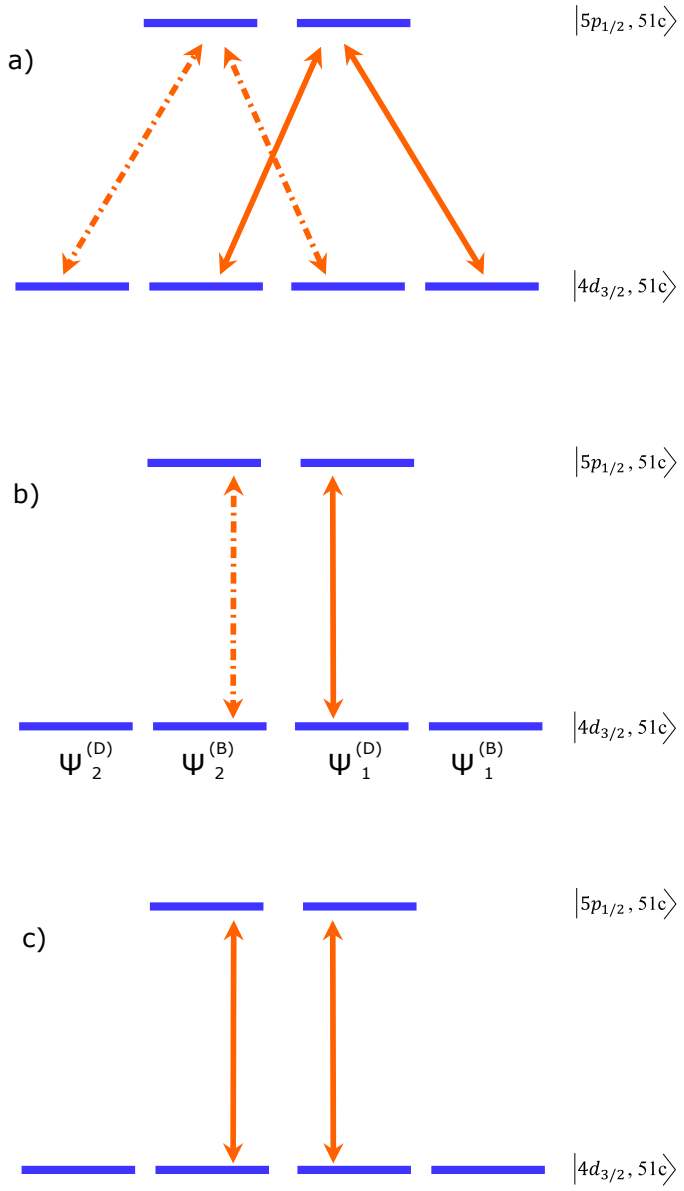

Figure 4.12: Coupling of the repumper laser with the ionic-core states. a) Case of horizontal polarization, distinguishing two three-level systems. b) Distinction of a dark and a bright component, in the case of horizontal polarization of the repumper. c) Case of vertical polarization.

defines a dark state $\Psi^{(D)}$ and a bright state $\Psi^{(B)}$ (figure 4.12b),

$$\Psi^{(D)} = \frac{1}{\sqrt{N_1}}\Big(\alpha\,|4d_{3/2}m_{j_2} = -1/2, 51c\rangle + \beta\,|4d_{3/2}m_{j_2} = +3/2, 51c\rangle\Big), \tag{4.28}$$

$$\Psi^{(B)} = \frac{1}{\sqrt{N_1}}\Big(\beta^*\,|4d_{3/2}m_{j_2} = -1/2, 51c\rangle - \alpha^*\,|4d_{3/2}m_{j_2} = +3/2, 51c\rangle\Big), \tag{4.29}$$

where N_1 is a normalization constant and α, β weight the components. The repumper thus optically pumps the atoms in the bright state $\Psi^{(B)}$ back to $|5s_{1/2}m_{j_2} = 1/2, 51c\rangle$. On the contrary, those in the dark state $\Psi^{(D)}$ are unaffected by the repumper. This implies that the only atoms left in any $|4d_{3/2}, 51c\rangle$ state belong to the dark component. Notably, the dark state is not an eigenstate of the electric-quadrupole Hamiltonian. Therefore, taking into account the electric-quadrupole effect, it evolves in time as

$$\Psi^{(D)}(t) = \frac{1}{\sqrt{N_1}}\Big(\alpha\,|4d_{3/2}m_{j_2} = -1/2, 51c\rangle + \beta e^{-i(2\pi\cdot\delta^{(12)}_{n,m_{l_1}})t}\,|4d_{3/2}m_{j_2} = +3/2, 51c\rangle\Big), \tag{4.30}$$

where $(2\pi\cdot\delta^{(12)}_{n,m_{l_1}})t$ is a phase factor evolving in time at frequency $\delta^{(12)}_{n,m_{l_1}}$. The effect of the phase factor is that the dark state periodically, at frequency $\delta^{(12)}_{n,m_{l_1}}$, acquires a bright component. Next, we apply a second repumper pulse. Again, this pulse transfers the atoms belonging to the bright component in $|5s_{1/2}m_{j_2} = 1/2, 51c\rangle$. Its population is then measured via the MW probe M_S to $|5s_{1/2}m_{j_2} = 1/2, 49c\rangle$, as defined in section 4.3.2. When recording the atomic counts in $|5s_{1/2}m_{j_2} = 1/2, 49c\rangle$, as a function of the delay between the two repumper pulses, one expects to detect the oscillations of the superposition state, periodically passing from a dark to a bright state, and to directly deduce the electric-quadrupole splitting $\delta^{(12)}_{n,m_{l_1}}$ from their frequency. Note that, to succeed in obtaining $\delta^{(12)}_{n,m_{l_1}}$, the duration of the repumper pulses must be short enough so that the electric-quadrupole coupling is negligible during these pulses. The same arguments and the same conclusions hold for the other three-level subspace.

It is important to note that the dynamics of this process strongly depends on the repumper polarization. If we work with a vertical polarization (figure 4.12c), instead of a horizontal one, the first repumper pulse depletes the $|4d_{3/2}|m_{j_2}| = 1/2, 51c\rangle$ states only. In this context, the dark states are indeed the two $|4d_{3/2}|m_{j_2}| = 3/2, 51c\rangle$ sub-levels. However, these dark states are eigenstates of the electric-quadrupole Hamiltonian. It follows that they do not evolve in time. When applying a second repumper pulse, we do not expect to see any modulation of the number of atoms repumped in $|5s_{1/2}|m_{j_2}| = 1/2, 51c\rangle$.

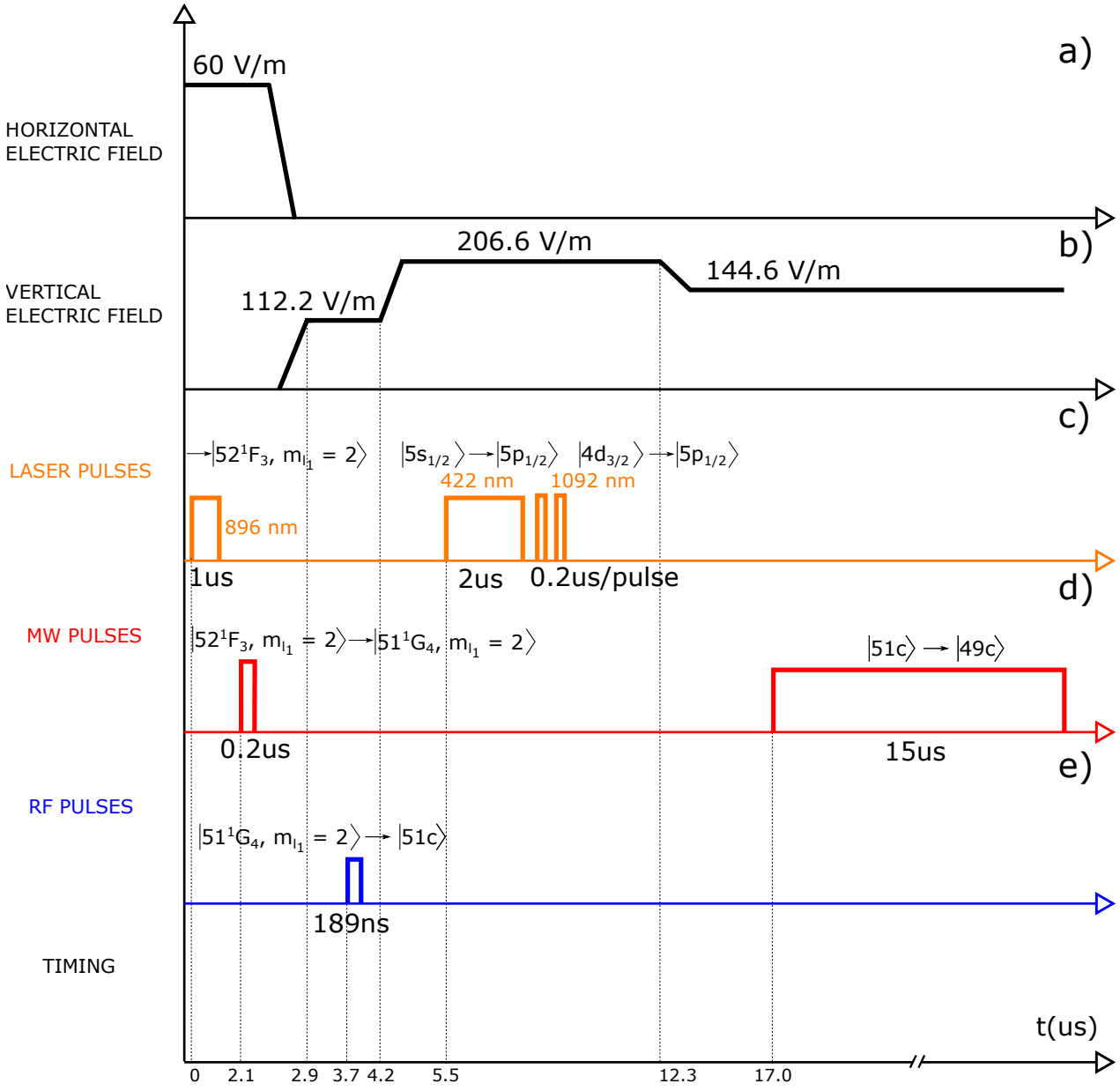

Figure 4.13: Sequence of laser, MW, rf and static electric fields used to detect the oscillations of the repumping efficiency when the Rydberg electron is in $|51c\rangle$.

4.5 Experimental measurement of the direct electric-quadrupole effect

4.5.1 Overview

We are now ready to measure the direct electric-quadrupole effect. The data on the circular state $|51c\rangle$ are first presented (paragraph 4.5.2.1). Next, we are going to perform the experiment for different circular states ($49 \leq n \leq 52$) and retrieve the dependency of $\delta^{(12)}_{n,m_{l_1}}$ as a function of the principal quantum number of these circular states (paragraph 4.5.2.2). Finally, we perform a similar experiment for several Rydberg states with different m_{l_1} along the ladder of the $n = 51$ manifold (paragraph 4.5.3). The latter study allows us to get the dependency of the direct electric-quadrupole effect with respect to the magnetic quantum numbers of the Rydberg states. At the end of the section, we compare the experimental results with the theoretical predictions of our model.

4.5.2 Measurements on the circular states

We gather here the details on the experimental sequence and on the results concerning the direct electric-quadrupole effect, for the case of the circular states.

4.5.2.1 Measurements on $|51c\rangle$

Figure 4.13 presents the experimental sequence of events whereas figure 4.14a shows the corresponding navigation in the Hilbert space. We circularize, optically pump the atoms in the $|4d_{3/2}\rangle$ states via a short 422 nm laser pulse (see appendix E on this matter) and next use the repumper pulses. They are both produced by the same AOM placed along one of the two optical branches of the repumper going to the experiment. The other optical branch is switched off so as to be able to prepare dark states for the repumper in the experiment. We design the sequence so that one of these pulses ends at time $t_1^{(end)}$ and the other starts at time $t_2^{(start)}$. The difference between $t_1^{(end)}$ and $t_2^{(start)}$ is named t_{RR}. The pulses are both 0.2 μs long, so as to be well below 1 μs, which represents the expected order of magnitude of the timescale for the electric-quadrupole coupling. They also share the same polarization and are at maximum power. The sequence is concluded by the long MW probe M_S, transferring the atoms repumped in $|5s_{1/2}|m_{j_2}| = 1/2, 51c\rangle$ to $|5s_{1/2}|m_{j_2}| = 1/2, 49c\rangle$.

Figure 4.14b is a plot of the results. Green data refer to a realization of the experiment where the second repumper pulse is omitted and the polarization of the first one is vertical. The transfer $|5s_{1/2}|m_{j_2}| = 1/2, 51c\rangle \rightarrow |5s_{1/2}|m_{j_2}| = 1/2, 49c\rangle$, proportional to the repumping transfer, is recorded as a function of t_{RR}. It is constant and then drops when the atoms exit the region of space where they interact with the laser. Note that the repumping efficiency is slightly larger

than the expected 50%, probably due to some residual contribution of the electric-quadrupole evolution during the repumper pulse. Blue data are recorded by applying the same sequence of events, but for a horizontal polarization of the repumper. We see no difference between green and blue data because in both cases we do not have a second repumper pulse applied on the atoms. Red data describe the results of the experiment realized when using two repumper pulses with a vertical polarization. As expected, we see no oscillations of the population transferred back to $|5s_{1/2}|m_{j_2}| = 1/2, 51c\rangle$ as a function of the delay between the two repumper pulses. Unlike the former cases though, we always have two pulses acting on the atoms. It follows that the transfer does not drop within the time window where we record the atomic counts. Finally, black data show the results for a pair of horizontal-polarized pulses. Within the time interval of the scan, we observe oscillations of the atoms repumped in $|5s_{1/2}|m_{j_2}| = 1/2, 51c\rangle$. The frequency of these oscillations is $\delta^{(12)}_{n,m_{l_1}} = (753.68 \pm 9.55)$ kHz, very close to the 760 kHz value predicted by the theoretical model.

4.5.2.2 Measurements on $|49c\rangle$, $|50c\rangle$ and $|52c\rangle$

We repeat the same experiment for different circular Rydberg states. The sequence of events is identical to that used for $|51c\rangle$ but for two events. The first difference is an additional MW pulse taking place after the circularization and before the core excitation. This MW pulse transfers the population from $|51c\rangle$ to another circular state. The MW power is calibrated to maximize the transfer between the two circular states, the MW duration is kept very short, 0.5μs, to save time for the core manipulation. The second difference is the M_S probe of the circular state, which is not anymore set on the $|51c\rangle \rightarrow |49c\rangle$ transition, but depends on the circular of interest.

For instance, to test the repumping oscillations while the Rydberg electron is in $|52c\rangle$ ($|49c\rangle$ or $|50c\rangle$), we circularize in the $n = 51$ manifold, transfer the population with a MW pulse from $|51c\rangle$ to $|52c\rangle$ ($|49c\rangle$ or $|50c\rangle$ respectively), apply the 422 nm and 1092 nm pulses and finally use a two-photon MW probe to measure the population repumped in $|5s_{1/2}, 52c\rangle$ ($|5s_{1/2}, 49c\rangle$ or $|5s_{1/2}, 50c\rangle$ respectively). The MW probe transfers the population, in this case, to $|50c\rangle$ ($|51c\rangle$ or $|52c\rangle$ respectively). Note that, when performing the experiment on $|49c\rangle$, we measure the population of $|49c\rangle$ by using a probe transferring the atoms back in $|51c\rangle$. The problem is that $|51c\rangle$ is not an empty target state, since the circularization is always done in the $n = 51$ manifold and the first MW pulse, transferring the population from $|51c\rangle$ to $|49c\rangle$, has not a 100% efficiency. We risk to mix the population of $|51c\rangle$ with that not transferred by the first MW pulse. To solve this issue, we use a rf pulse decircularizing the population in $|51c\rangle$ before using the latter state as the target for the probe of $|49c\rangle$.

Figures 4.15a-c) gather the results for $|49c\rangle$, $|50c\rangle$, $|52c\rangle$. We record the data for the only case of horizontal polarization of the repumper, when two repumper pulses are applied on the

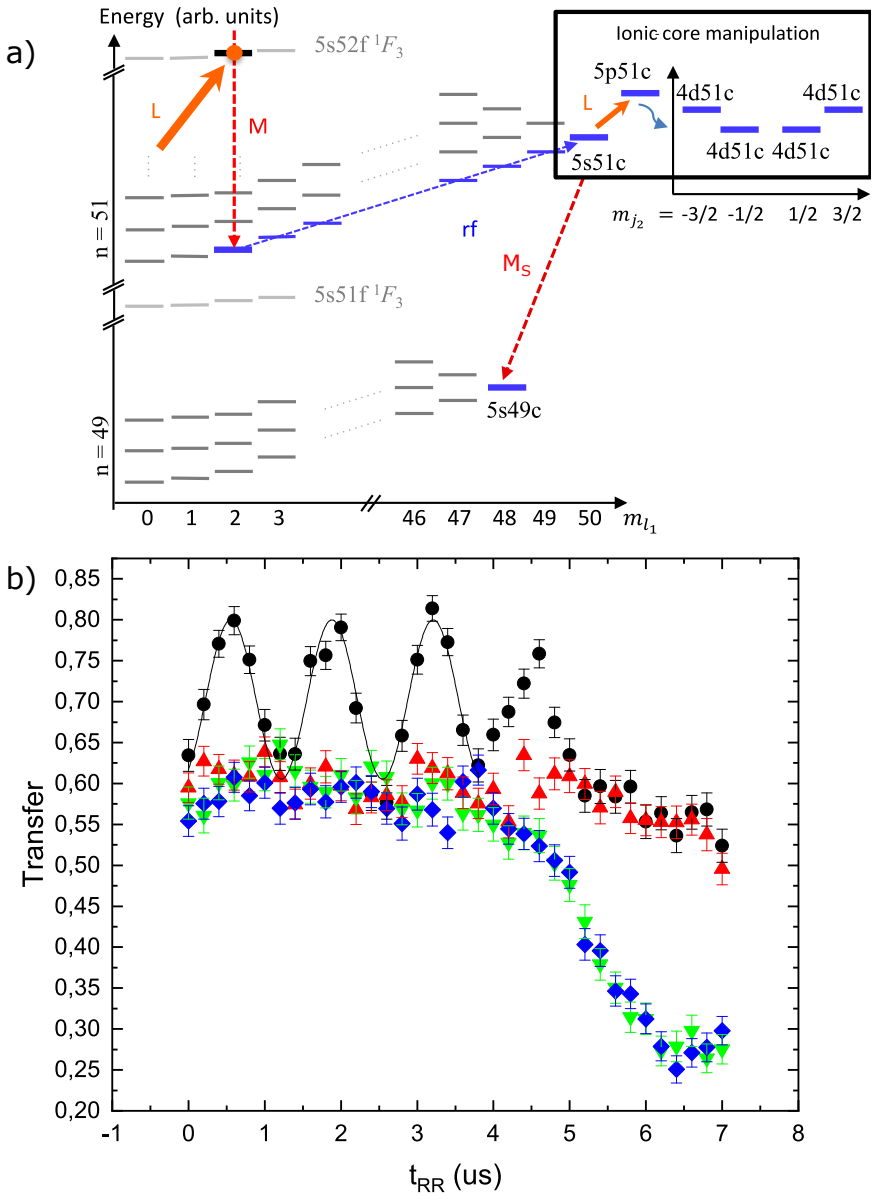

Figure 4.14: a) Navigation in the Hilbert space following our manipulations with rf, laser and MW pulses, aimed to detect the oscillations of the repumping efficiency. b) Variation of the repumping efficiency as a function of temporal distance between the two 1092 nm pulses. The measurements are performed for an horizontal (black), vertical (red) polarization of the two repumper pulses or in presence of only one repumper pulse. In the latter case, blue data refer to an horizontal polarization, green data to a vertical polarization. The solid line is a sinusoidal fit.

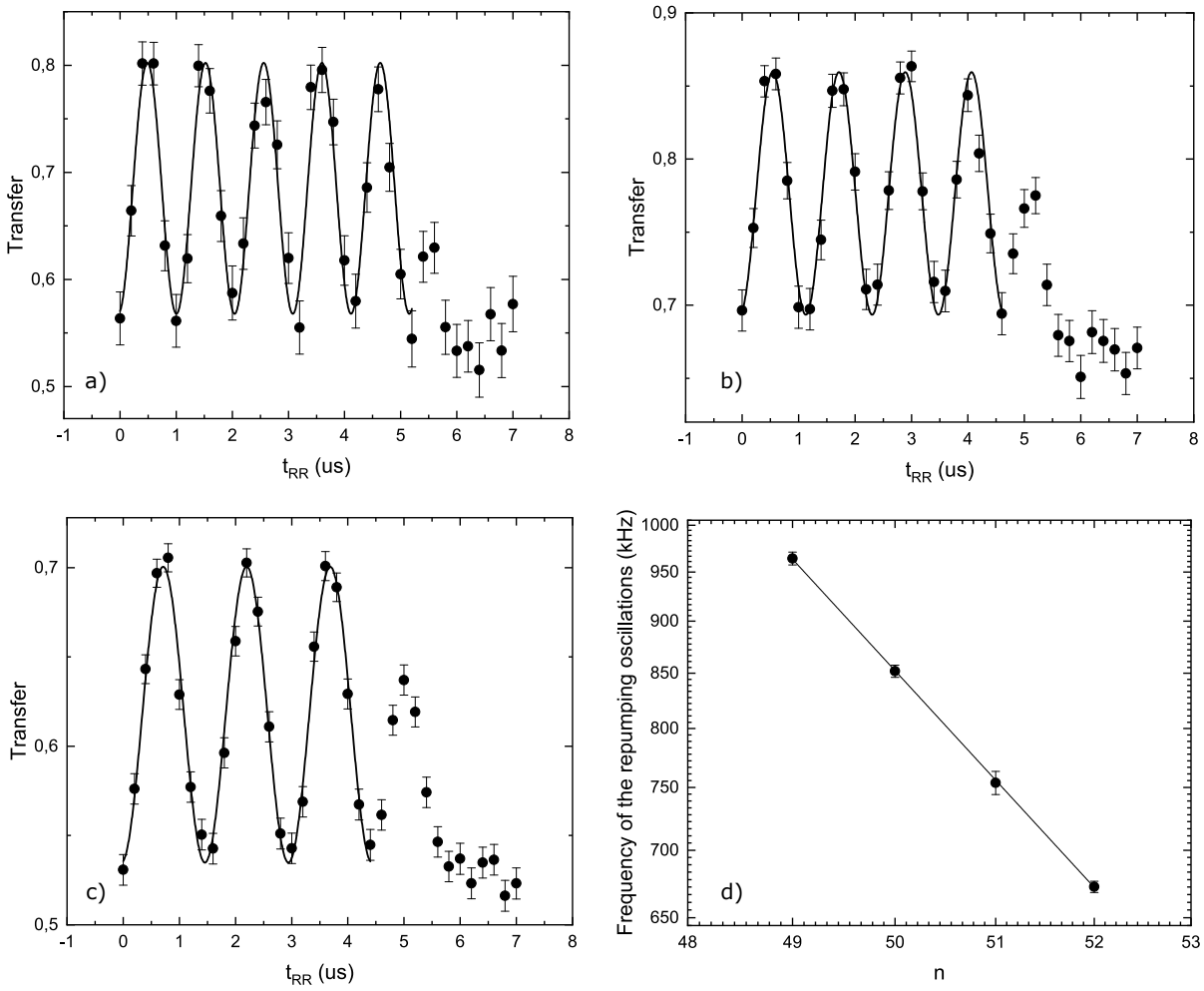

Figure 4.15: a-c) Oscillations of the repumping efficiency for different circular Rydberg states ($|49c\rangle$ top left, $|50c\rangle$ top right, $|52c\rangle$ bottom left). All measurements are performed for an horizontal polarization of the repumper. Black data refer to the experiments involving two repumper pulses. Solid lines are sinusoidal fits. d) Frequency of the oscillations of the repumping efficiency as a function of n. Solid line is a fit following a n^{-6} power law.

atoms. The efficiency of the repumping process oscillates as a function of the delay between the repumper pulses. The frequency of the oscillations is (964.17 ± 6.77) kHz for $|49c\rangle$, (851.98 ± 5.68) kHz for $|50c\rangle$ and (672.39 ± 4.22) kHz for $|52c\rangle$. Figure 4.15d) is a plot of the frequency of the repumping oscillations, therefore of $\delta^{(12)}_{n,m_{l_1}}$, as a function of the principal quantum number of the circular states. This graph shows that the splitting $\delta^{(12)}_{n,m_{l_1}}$ decreases with the principal quantum number of the circular following a power law n^{-6}, as the theoretical model predicts.

4.5.3 Measurements on elliptical Rydberg states

We measured the differential electric-quadrupole effect for several Rydberg states along the ladder of the $n = 51$ manifold and saw that the order of magnitude of the Rydberg-to-Rydberg frequency shift was comparable to the circular case, as theory predicted. We are going to verify that the same agreement holds when measuring the direct electric-quadrupole effect for the $|4d_{3/2}, n = 51, m_{l_1} > 7\rangle$ Rydberg states.

The sequence applied in the experiment is presented in figure 4.16. We apply a rf pulse with duration τ, so as to excite a spin-coherent-state along the ladder. Next, we optically pump the core in the $|4d_{3/2}\rangle$ states. Note that this optical pumping works for the atoms prepared in all the Rydberg states composing the spin-coherent-state at the same time. Some atoms autoionize since we deal with Rydberg states with intermediate m_{l_1}. Afterwards, we apply two short, horizontal polarized repumper pulses and vary their temporal distance. They repump the core electron to the $|5s_{1/2}\rangle$ state. Again, this optical pumping works for all the Rydberg states of the spin-coherent-state. At this point, it would be sufficient to apply the probe to the $n = 49$ manifold to observe the repumping oscillations.

Such a measurement would unfortunately suffer of a low counting rate, as we would detect only one component of the spin-coherent-state. A better strategy is to set a second rf pulse after the repumper pulses. The purpose of this second rf is to conclude the circularization starting from the spin-coherent-state produced along the Rydberg ladder. We refer to this process as "re-circularization". Its duration, in nanoseconds, reads $\tau_{rec} = 189 - \tau$, where 189 ns is the optimal duration of the full circularization. As a final step, after having reached the circular state with the second rf pulse, we use the MW probe driving the transition $|5s_{1/2}, 51c\rangle \rightarrow |5s_{1/2}, 49c\rangle$ to measure the amount of population "recircularized", which is proportional to the number of atoms repumped in the $|5s_{1/2}\rangle$ state of the core.

Figure 4.17a shows the navigation in the Hilbert space of the Rydberg electron and the manipulations of the core when testing $\delta^{(12)}_{n,m_{l_1}}$ for a given spin-coherent-state. Figure 4.17b shows the repumping oscillations for several values of τ. For each curve, we fit the oscillations via a sinusoidal function and extract their frequency. Figure 4.17c reports the frequency of the

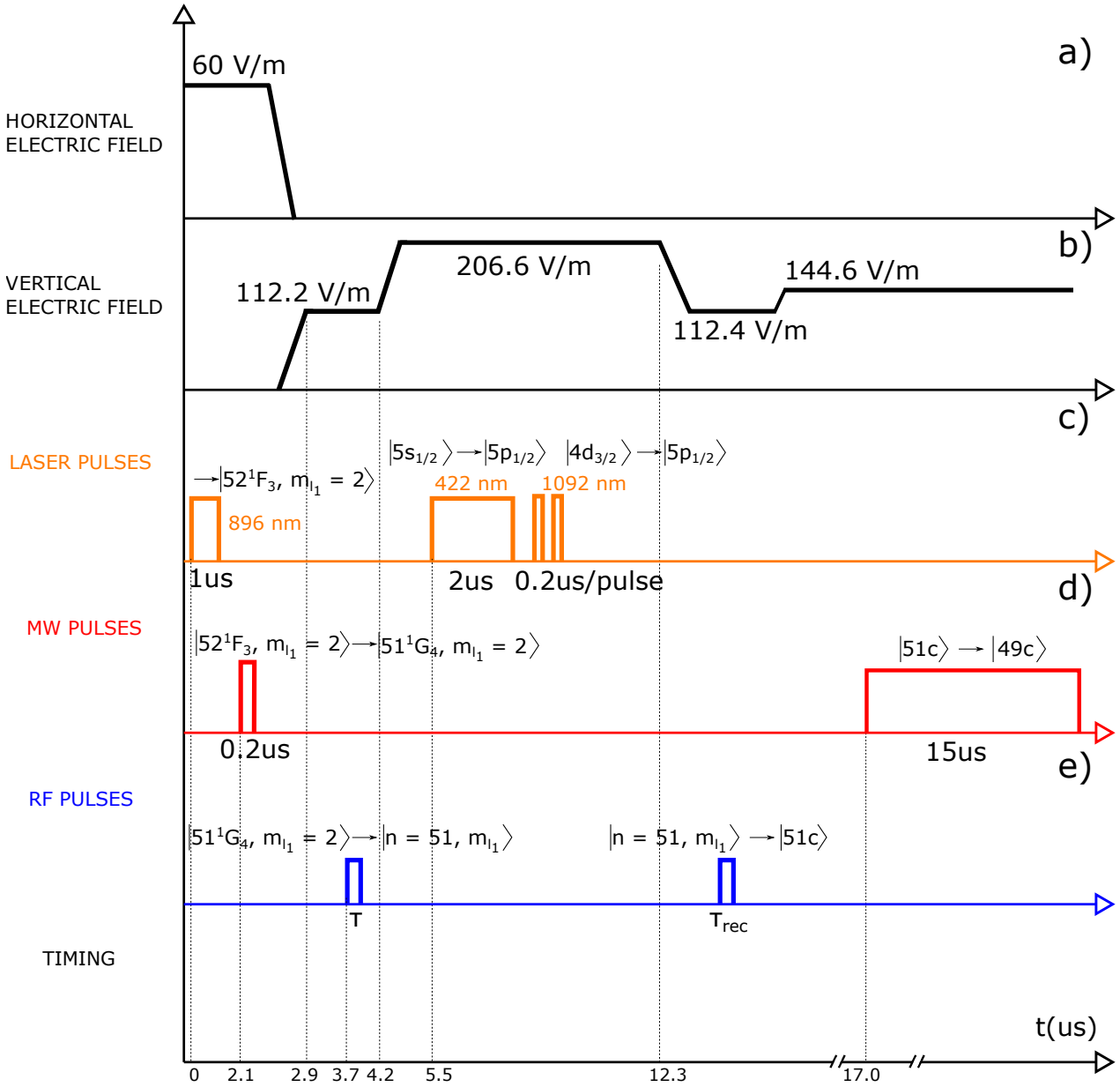

Figure 4.16: Sequence of laser, MW, rf and static electric fields used to detect the oscillations of the repumping efficiency when the Rydberg electron is prepared in different spin-coherent-states along the Rydberg ladder.

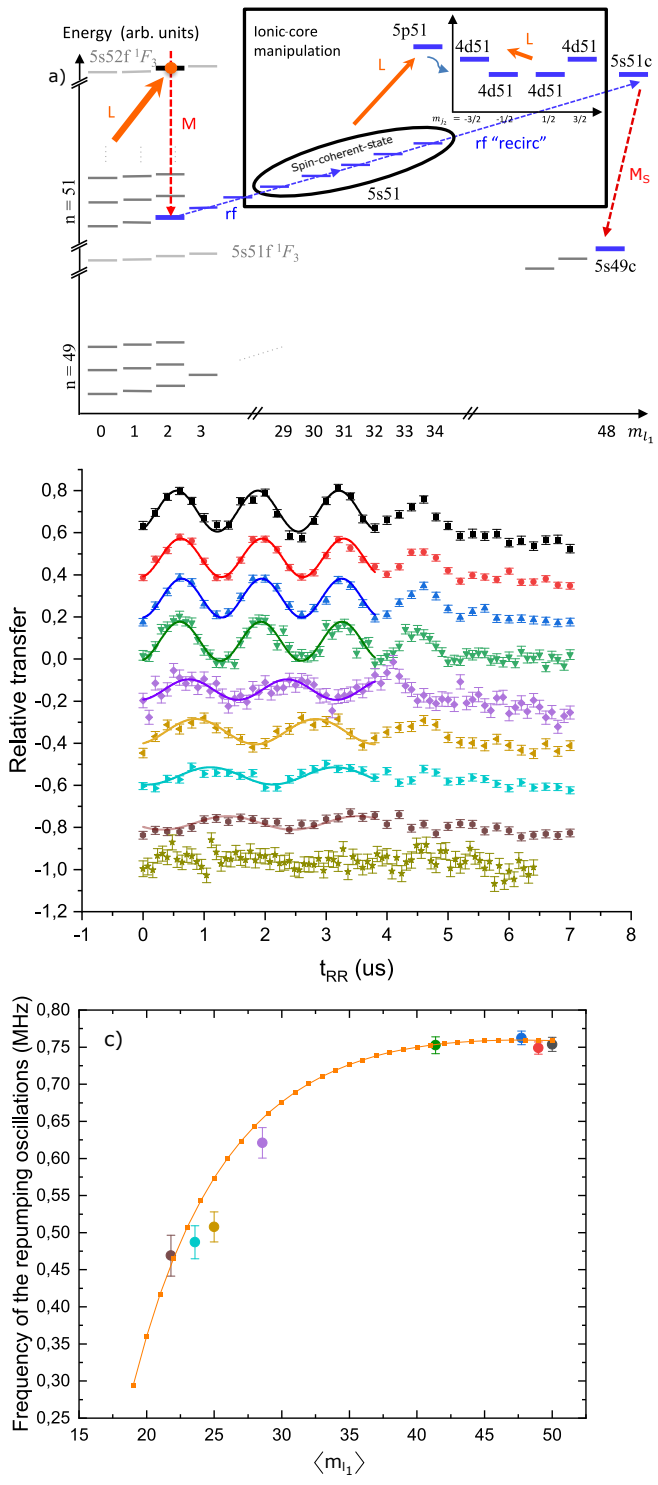

Figure 4.17: a) Navigation in the Hilbert space. b) Oscillations of the repumping efficiency for several spin-coherent-states. Black data for: $\tau = 189$ ns, red: $\tau = 169$ ns, blue: $\tau = 159$ ns, green: $\tau = 129$ ns, violet: $\tau = 89$ ns, yellow: $\tau = 79$ ns, light blue: $\tau = 75$ ns, brown: $\tau = 70$ ns, dark yellow data: $\tau = 50$ ns. Solid lines are sinusoidal fits. c) Frequency of the oscillations as a function of $\langle m_{l_1} \rangle$. Orange points are the theoretical values calculated via the model, orange line is a guide for the eye.

repumping oscillations, as a function of $\langle m_{l_1} \rangle$, obtained from the fit. Here, the quantity $\langle m_{l_1} \rangle$ is an average value of the magnetic quantum numbers associated to the Rydberg components of the spin-coherent-state prepared by the rf pulse. The conversion $\tau \rightarrow \langle m_{l_1} \rangle$ is done via the formula

$$\langle m_{l_1} \rangle = 25 \left(1 + \cos \left(\pi \frac{189 - \tau}{220} \right) \right), \tag{4.31}$$

which derives from the experimental calibration of the recircularization (see appendix F for details). In the same plot, we report the values predicted by our model. The agreement between data and theory is good.

First, the contrast of the repumping oscillations is worse when investigating the electric-quadrupole coupling for Rydberg states with intermediate or low $\langle m_{l_1} \rangle$ with respect to the circular case. The drop of contrast motivates the larger error bar for $\delta^{(12)}_{n,m_{l_1}}$ at low magnetic quantum numbers and makes it hard to detect any repumping oscillation below $\tau = 70$ ns.
Second, it is clear that the frequency of the oscillations depends on $\langle m_{l_1} \rangle$. We deduce that $\delta^{(12)}_{n,m_{l_1}}$ as well varies with the magnetic quantum number. However, associating an individual value of $\delta^{(12)}_{n,m_{l_1}}$ to each Rydberg component of the spin-coherent-state is hard, since the core manipulations concern all the Rydberg states prepared by the rf pulse at the same time and not a single Rydberg state. This is the major difference with respect to the case of the circular state presented in subsection 4.5.2 and also the reason why we are forced to express the dependency of the splitting in terms of an average value of the magnetic quantum number.

4.6 Further development: coherent core state manipulation

The experiments presented so far lead us to some Ramsey experiments where we control the state of the Rydberg electron with a laser pulse. Here, we present this last experiment very briefly. A more detailed description on its realization will be given in the Ph.D. thesis of my colleague Léa Lachaud.

A first development of the electric-quadrupole experiment is a Raman transfer from one $|4d_{3/2}\rangle$ state to another. After the circularization, a 422 nm pulse and a vertical-polarized repumper pulse are applied to optically pump the atoms in the $|4d_{3/2}|m_{j_2}| = 3/2\rangle$ states. Next, two other 1092 nm pulses are used. They are detuned between each other, one π polarized and the other σ polarized, and transfer by a Raman process the atoms from $|4d_{3/2}|m_{j_2}| = 3/2\rangle$ to $|4d_{3/2}|m_{j_2}| = 1/2\rangle$. Note that the Raman experiment allows us to measure $\delta^{(12)}_{n,m_{l_1}}$ in a simpler way than the measurement of the precession of the relative phase factor between the $|4d_{3/2}\rangle$ states. The splitting $\delta^{(12)}_{n,m_{l_1}}$ is measured as a function of the detuning between the last two 1092 nm pulses (figure 4.18).

Next, we map the state of the Rydberg electron onto that of the core. In this experiment, the Raman pulse behaves as an optical switch controlling the final state of the Rydberg atom.

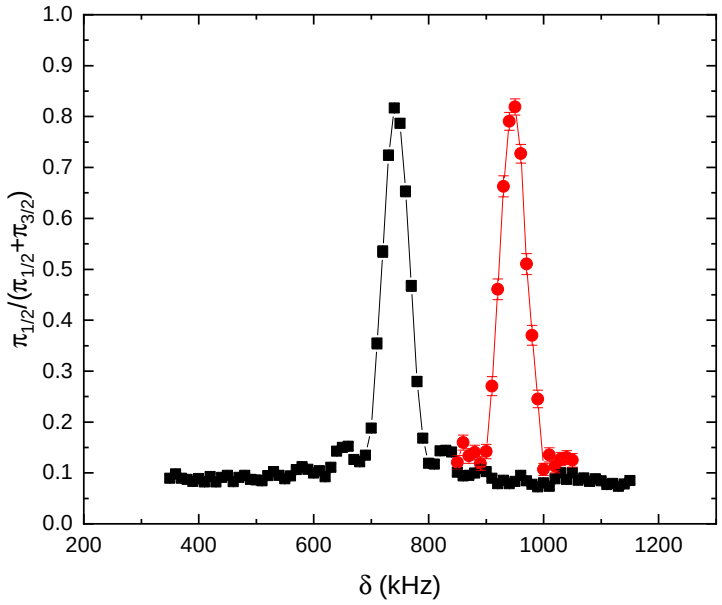

Figure 4.18: Measurement of the Raman transfer between the $|4d_{3/2}|m_{j_2}| = 3/2\rangle$ and $|4d_{3/2}|m_{j_2}| = 1/2\rangle$ states as a function of the detuning δ between the repumper pulses. The experiment is realized while the Rydberg electron is in $|51c\rangle$ (black squares) or $|49c\rangle$ (red circles).

The sequence of events can be summed up as follows. First, the superposition of $|51c\rangle$ and $|49c\rangle$ is prepared. Next, the phase of the circular state coherent superposition is flipped in the time interval between the MW pulses of the Ramsey experiment, by applying a long 2π Raman pulse tuned on the $|4d_{3/2}|m_{j_2}| = 3/2, 49c\rangle \rightarrow |4d_{3/2}|m_{j_2}| = 1/2, 49c\rangle$ transition. Ideally, this pulse should imprint a phase shift of π on the $|4d_{3/2}, 49c\rangle$ component of the superposition without affecting the $|4d_{3/2}, 51c\rangle$ component. Finally, a second $\pi/2$ MW pulse closes the Ramsey interferometer. Its phase is chosen so that the atom exits the interferometer in $|51c\rangle$ in absence of the Raman pulse and in $|49c\rangle$ if the pulse is applied. This allows us to control the final state of the Rydberg electron with the 1092 nm laser.

4.7 Discussion

In this chapter, we present our study on the electric interaction between the two valence electrons of Strontium. The chapter is divided in two parts, a theoretical section, outlining the mathematics needed to understand the experiment, and an experimental section. In the theory section, we first introduce the electron-electron potential governing the electric interaction between the two valence electrons of Strontium. The dominant term is the electric-quadrupole component of the multipole expansion of that potential. This term causes the lift of the degeneracy between the

$|4d_{3/2}\rangle$ states of the core, which are now split in two sets, one with $|m_{j_2}| = 3/2$ and the other with $|m_{j_2}| = 1/2$. We present a theoretical calculation of the energy difference $\delta^{(12)}_{n,m_{l_1}}$ between the two sets of states. As a result, we see that $\delta^{(12)}_{n,m_{l_1}}$ is 760 kHz when the Rydberg electron is in the circular state with $n = 51$. Moreover, the splitting $\delta^{(12)}_{n,m_{l_1}}$ exhibits a n^{-6} dependency.

Next, we discuss the experimental results. They are divided in two macro-sections, one discussing the shift of the circular-to-circular transition frequency after the core excitation (the "differential electric-quadrupole effect"), the other investigating the energy difference between the ionic-core states with $|m_{j_2}| = 3/2$ and the states with $|m_{j_2}| = 1/2$ (the "direct electric-quadrupole effect").

First, we discuss the differential electric-quadrupole effect. We start with the circular states. We record the MW spectra between two circular states and see that the resonance frequency shifts if the core is excited. The measured shift agrees very well with the theoretical prediction of our model. Next, we repeat the experiment after preparing a few spin-coherent-states along the lowest-right Rydberg ladder of the $n = 51$ manifold instead of preparing the circular state. This experiment shows that the Rydberg-to-Rydberg frequency shift varies as a function of the magnetic quantum numbers of the spin-coherent-state components. Again, the data follow the theoretical prediction very well. Yet, the mismatch between experiment and theory increase for very low values of the magnetic quantum number. After completing the discussion on the data concerning the $|4d_{3/2}\rangle$ states, we focus on those about the $|4d_{5/2}\rangle$ states of the ionic core. We present an evidence of the electric-quadrupole coupling between the circular and the core in $|4d_{5/2}\rangle$. The results are consistent with the theoretical prediction of [87].

Second, we switch to the experimental measurement of the direct electric-quadrupole effect, i.e. the splitting $\delta^{(12)}_{n,m_{l_1}}$ between $|4d_{3/2}|m_{j_2}| = 3/2, 51c\rangle$ and $|4d_{3/2}|m_{j_2}| = 1/2, 51c\rangle$. To start, we optically pump the atoms in a statistical mixture of $|4d_{3/2}|m_{j_2}| = 3/2, 51c\rangle$ and $|4d_{3/2}|m_{j_2}| = 1/2, 51c\rangle$. Afterwards, we measure the amount of repumped atoms in $|5s_{1/2}, 51c\rangle$ following the application of two, short repumper pulses. The measurement is performed via the core-sensitive MW probe for $|5s_{1/2}, 51c\rangle$. In conclusion, the amount of repumped atoms is shown to oscillate as a function of the temporal distance between the two repumper pulses. The frequency of the oscillations is proven to be the splitting $\delta^{(12)}_{n,m_{l_1}}$ between the core states. We also perform the experiment after preparing other circular Rydberg states, thus proving that $\delta^{(12)}_{n,m_{l_1}}$ depends on the principal quantum number of the circular state and follows a n^{-6} power law, as theory predicts. Finally, we realize the experiment for several spin-coherent-states along the lowest-right Rydberg ladder. We see that the direct electric-quadrupole effect as well depends on the magnetic quantum number of the Rydberg electron. Our theoretical model succeeds in predicting the evolution of the direct electric-quadrupole effect as a function of m_{l_1}.

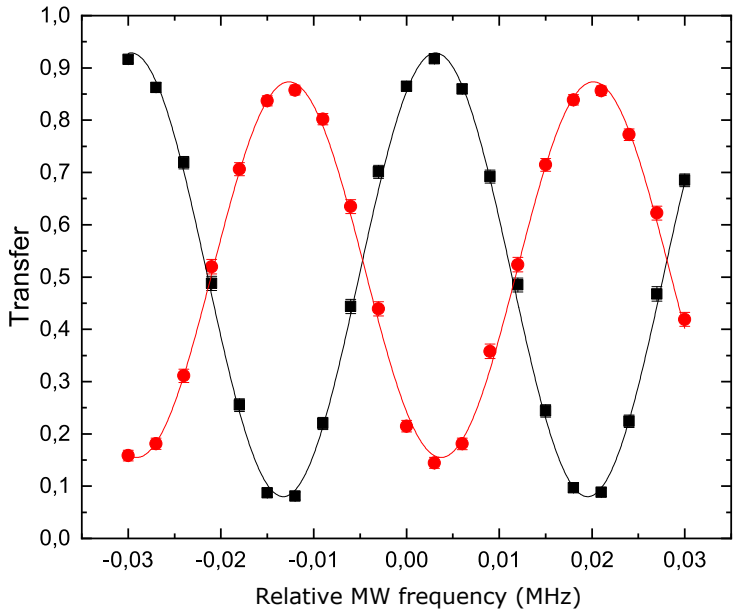

Figure 4.19: Ramsey fringes on the $|51c\rangle \rightarrow |49c\rangle$ transition. Black data are taken in absence of the repumper pulses. Red data are taken in presence of repumper pulses. Solid lines are sinusoidal fits.

As a conclusion, we provide the reader with a brief outlook of the developments of the electric-quadrupole experiment. We briefly discuss a Raman experiment, allowing us to measure the splitting $\delta^{(12)}_{n,m_{l_1}}$ between the $|4d_{3/2}\rangle$ for the circular state case, and a Ramsey experiment where we control the state of the Rydberg electron with a laser pulse.

The electric-quadrupole effect paves the way to fascinating perspectives. For circular atoms individually trapped in optical tweezers, the electric-quadrupole effect makes it possible to individually address a circular atom in an array with tightly focused laser beams, an essential tool for quantum simulation and quantum information, lacking with the usual MW addressing of circular states. One can use the fluorescence emitted after the spontaneous decay $|5p_{1/2},51c\rangle \rightarrow |5s_{1/2},51c\rangle$ to optically detect the circular states with remarkable spatial sensitivity and in a selective way, therefore importing some techniques from the experimental research of ions. Our experiment thus shows that alkaline-earth circular Rydberg states have the potential to combine the best features of the ion traps and Rydberg atoms worlds. In the next section, we are going to present these perspectives in more detail, together with other experiments, currently underway, representing the "next generation" of manipulations on circular states of Strontium.

CHAPTER 5

CONCLUSION

> And that's when I realize that, at the end, we'd all wish for the same thing. Just a little more time.
>
> *Marie Lu, Wildcard*

This work has presented a series of experimental investigations concerning the physics of alkaline-earth circular Rydberg states. In this last chapter, we are going to summarize what this manuscript has added to the state-of-the-art of the atomic physics world.

The results presented to this point are to be seen as steps towards the realization of a programmable Rydberg quantum simulator exploiting alkaline-earth circular states as platforms for the qubits. However, while aiming for such an ambitious goal, the experiment also offers some short-term, interesting perspectives. We shortly present them in the last part of this chapter.

5.1 Summary of the results

Chapter 2 discusses the experimental circularization of Strontium. This is realized on an atomic beam leaving from a high-temperature oven, crossing a cryogenic environment at 4 K and reaching a detector ionizing the atoms. First, we present the Rydberg excitation to $|52^1F_3, m_{l_1} = 2\rangle$ via three optical photons. Unfortunately, the $|F\rangle$ states are known to join the respective manifold at very high electric field. Therefore, we apply a MW pulse to transfer the atoms to a $|G\rangle$ state joining the manifold at lower electric field (112.2 V/m). We opt for $|51^1G_4, m_{l_1} = +2\rangle$. Next, we discuss the calibration of a square rf pulse able to transfer the population from $|51^1G_4, m_{l_1} = +2\rangle$ to the circular state. This rf pulse is at 110 MHz, 189 ns long and $\sigma+$ polarized. All in all, our

circularization reaches 85% of efficiency.

Chapter 3 shows that the circular Rydberg states are impervious to the autoionization effect. To prove this, we first present an optical pumping process allowing us to prepare the metastable $|4d_{3/2}\rangle$ states of the core electron. It involves the excitation of the core electron from $|5s_{1/2}\rangle$ to $|5p_{1/2}\rangle$ via a 422 nm laser pulse and the fast, spontaneous decay from $|5p_{1/2}\rangle$ to the $|4d_{3/2}\rangle$ states. The $|4d_{3/2}\rangle$ states are considered as degenerate at this stage of the work, since we assume all the energy levels of the core electron as equivalent to those of the Sr^+ ion. We then measure the amount of circular atoms when the core is in the ground state $|5s_{1/2}\rangle$ or excited to any of the $|4d_{3/2}\rangle$ states. The number of circular states is showed not to vary as a function of the state of the core, implying that the optical pumping from $|5s_{1/2}\rangle$ to $|4d_{3/2}\rangle$ preserves the population of the circular Rydberg electron. On the contrary, when performing the experiment with the Rydberg electron in a low-l_1 state, the autoionization effect makes the amount of Rydberg atoms drop. We verify in this way the dependency of the autoionization effect with respect to the angular momentum of the Rydberg electron. The same conclusions hold in an analogous experiment investigating the autoionization of the Rydberg atoms with the core in a $|4d_{5/2}\rangle$ state.

Chapter 4 presents some optical manipulations on the Rydberg atoms via the coupling with the second valence electron. We lift the approximation on the equivalence between states of the core and states of the Sr^+ ion and study the effect of the electron-electron interaction on the energy levels of the core. We see that the electric-quadrupole term of the multipole expansion of the electron-electron potential leads to a degeneracy lifting among the $|4d_{3/2}\rangle$ states. They are split in two sets, one with $|m_{j_2}| = 1/2$ and the other with $|m_{j_2}| = 3/2$, separated by an amount $\delta^{(12)}_{n,m_{l_1}}$. This quantity is 760 kHz for $|51c\rangle$. We then measure $\delta^{(12)}_{n,m_{l_1}}$ in the experiment. This is first done via MW spectroscopy between the Rydberg states. More specifically, this experiment allows us to measure the difference between the value of $\delta^{(12)}_{n,m_{l_1}}$ for a given Rydberg state of the $n = 51$ manifold and the value of $\delta^{(12)}_{n,m_{l_1}}$ associated to another Rydberg state of the $n = 49$ manifold. Next, $\delta^{(12)}_{n,m_{l_1}}$ is measured by analysing the efficiency of the repumping process from the $|4d_{3/2}\rangle$ states to $|5s_{1/2}\rangle$ as a function of time. The experiment confirms the predictions made by theory on the value of $\delta^{(12)}_{n,m_{l_1}}$ and its dependency with respect to the principal quantum number of the circular states. Indeed, we verify that $\delta^{(12)}_{n,m_{l_1}}$ rigorously follows a n^{-6} power law as indicated by theory. Finally, we prove that $\delta^{(12)}_{n,m_{l_1}}$ is also dependent on the magnetic quantum number of the Rydberg states. This is done by measuring $\delta^{(12)}_{n,m_{l_1}}$ after performing the experiment on several spin-coherent-states prepared along the circularization ladder. The results show $\delta^{(12)}_{n,m_{l_1}}$ to increase as a function of the rf duration preparing the spin-coherent-state, therefore as a function of m_{l_1}. Our model presents solid predictions of this dependency as well.

5.2 Perspectives

There has been a long tradition of experiments concerning circular states of alkali atoms. While they led to fascinating results, they also suffered from strong limitations. One of them is the destructive detection of the Rydberg states, another is the impossibility to mitigate the heating mechanisms arising in the spin chain studied via the simulator. Short-term experiments on alkaline-earth circular states can help to tackle these constraints and establish new protocols to work with the Rydberg atoms. In this conclusion, we shortly discuss two of these protocols, concerning the cooling and the imaging of the circular states. Both are strongly inspired by the experimental research of ions.

As for cooling, when working with an atomic beam, one can achieve the first laser cooling of a circular Rydberg state. After the circularization, the in-axis scattering of the 422 nm laser and the atomic beam can slow the atoms. They would receive a "kick" from the blue photon in the direction opposite to that of the atomic beam. This event would result in a one-dimensional slowing of the velocity class and therefore of the circular Rydberg state. This experiment is in progress in our research group.

Within the cold atoms context, one can use the fluorescence of the core to optically detect the circular state. After the circularization and the trapping of the Rydberg atoms, one can excite the core with the 422 nm laser and produce fluorescence via the $|5p_{1/2}\rangle \rightarrow |5s_{1/2}\rangle$ spontaneous decay. The process leading to the emission of fluorescence would be non-destructive for the Rydberg electron, since the circular atoms do not present autoionization effect. Then, the blue photons emitted by the core would be captured by a sensitive camera, enabling us to image the circular state.

Both the cooling and the optical detection of the circular state will then come together in the realization of a Rydberg quantum simulator. The use of Strontium, instead of Rubidium, would make this machine more efficient. First, it would enable us to optically detect non-destructively the circular states located in the optical lattice of the simulator and perform spatially selective measurements with great sensitivity. Second, the laser cooling of the core would help us to counterbalance the heating in the system during the long simulation times accessible with the remarkable properties of circular states.

APPENDIX A

THE HYPERFINE STRUCTURE OF THE STRONTIUM ATOM

The spin-orbit coupling is not the last degree of complexity for the Hamiltonian of an atom. One can consider a further mechanism of coupling, this time between the total angular momentum of the electrons and the nuclear spin. It is the hyperfine interaction [89, 90]. We are going through this physics shortly in this appendix.

A.1 The Hamiltonian

We model the hyperfine interaction via a new component of the atomic Hamiltonian. It reads

$$\hat{H}_{hf} = A_{hf}\hat{\mathbf{I}}\cdot\hat{\mathbf{J}}, \tag{A.1}$$

where A_{hf} is the hyperfine structure constant and $\hat{\mathbf{I}}$ is the nuclear spin operator. It is associated to the nuclear spin quantum number I. This number depends on the amounts Z and A of protons and neutrons of the atom, where each nucleon contributes with +1/2. As a general rule, if A and Z are even, $I = 0$. If A is even but Z is odd, I is half-integer. If both A and Z are odd, I is integer.

The inclusion of $\hat{H}_{hf}$ in the total Hamiltonian makes J unsuitable as a quantum number. It is replaced by the quantum number F, obeying the selection rule

$$|J - I| \leq F \leq J + I. \tag{A.2}$$

As a consequence, the degeneracy of the levels with equal J is lifted. Notably, the new set of energy levels now depends on the isotopic species of the atom, since every isotope has its own value of the nuclear spin (figure A.1).

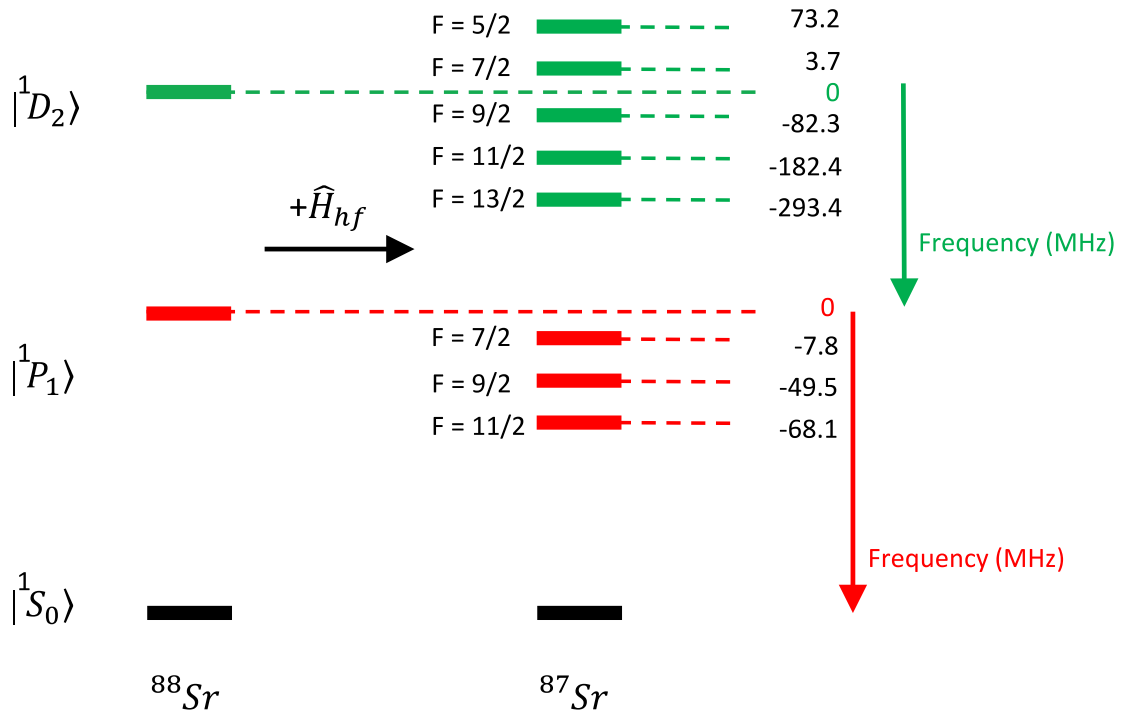

Figure A.1: Energy levels of ^{87}Sr and ^{88}Sr.

A.2 Experimental results

Natural strontium presents a broad diversity of isotope species. We count four in total, ^{84}Sr, ^{86}Sr, ^{87}Sr, ^{88}Sr, with natural abundances of 0.56%, 7.00%, 9.86%, 82.58% respectively. Our experiment does not use isotopically pure Sr, but the excitation laser frequencies are set at resonance with the transitions of ^{88}Sr only [91].

The isotope shift of the $|5s5p\,^1P_1\rangle$ and $|5s5d\,^1D_2\rangle$ levels of ^{84}Sr and ^{86}Sr, with respect to ^{88}Sr, is larger than 100 MHz. We verify this by sweeping the frequency of the 896 nm laser and recording the number of Rydberg atoms produced. We repeat this experiment for different values of the 767 nm laser frequency, driving the $|5s5p\,^1P_1\rangle \rightarrow |5s5d\,^1D_2\rangle$ transition, which is tuned by varying the frequency of the EOM placed on the 767 nm laser line going to the ultra-stable cavity (figure A.2a). We detect a peak in the atomic counts at around -90 MHz of detuning from the 896 nm laser frequency used for the Rydberg excitation of ^{88}Sr. The atomic counts are maximized for a frequency of the 767 nm laser shifted by -254 MHz with respect to the frequency used for the Rydberg excitation. Ultimately, the distance between the spectral lines of ^{88}Sr and ^{86}Sr is large enough so as to safely select ^{88}Sr in our Rydberg excitation process.

As for ^{86}Sr, the isotope ^{87}Sr has a non-negligible natural abundance. The 461 nm and 767

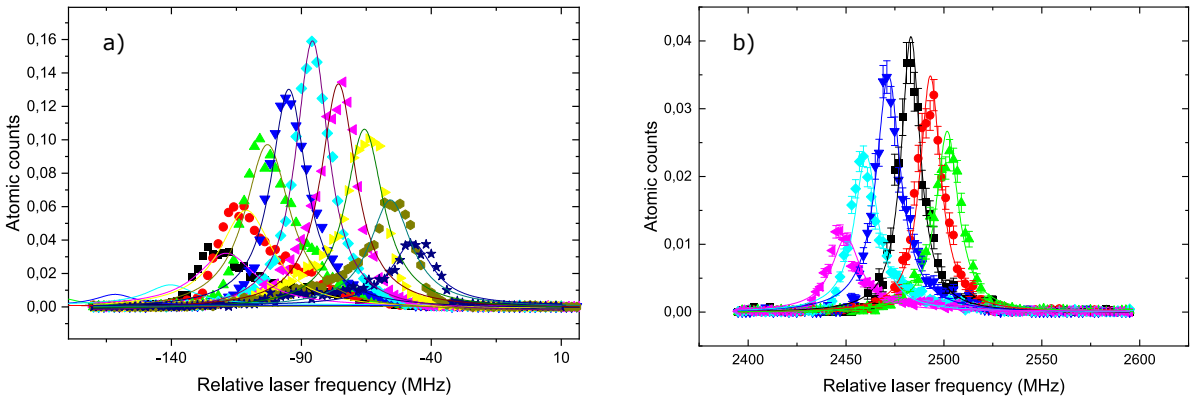

Figure A.2: a) Laser spectra of the $|5s5d\,^1D_2\rangle \rightarrow |52^1F_3, m_{l_1} = +2\rangle$ transition of ^{86}Sr for different 767 nm frequencies. The 767 nm frequency is shifted by −214 MHz (black data), −224 MHz (red data), −234 MHz (green data), −244 MHz (blue data), −254 MHz (light blue data), −264 MHz (magenta data). b) Laser spectra of the $|5s5d\,^1D_2\rangle \rightarrow |52^1F_3, m_{l_1} = +2\rangle$ transition of ^{87}Sr for different 767 nm frequencies. The 767 nm frequency is shifted by −244 MHz (black data), −254 MHz (red data), −264 MHz (green data), −234 MHz (blue data), −224 MHz (light blue data), −214 MHz (magenta data), −274 MHz (yellow data), −284 MHz (dark green data), −294 MHz (dark blue data). The "zero" of the laser frequency is set at the 896 nm laser frequency exciting the $|52^1F_3, m_{l_1} = +2\rangle$ state of ^{88}Sr. Similarly, the zero for the EOM governing the 767 nm laser frequency is set at that value used for the Rydberg excitation of ^{88}Sr. Solid lines are Gaussian fits.

nm laser frequencies are nearly resonant with the transitions $|5s5s\,^1S_0\rangle \rightarrow |5s5p\,^1P_1, F = 7/2\rangle \rightarrow |5s5d\,^1D_2, F = 7/2\rangle$ of ^{87}Sr. However, in ^{87}Sr, the exchange energy in the $|5snf\rangle$ level is smaller than the core hyperfine interaction (the splitting between the $|F = 4\rangle$ and $|F = 5\rangle$ ground states of the $^{87}Sr^+$ ion is 5 GHz). We thus expect two lines for the $|5s5d\rangle$ to $|5snf\rangle$ transition located at approximately ±2.5 GHz from that of ^{88}Sr. We verify this feature by scanning the 896 nm laser and observing the line of the ^{87}Sr isotope at +2.48 GHz (figure A.2b). As a result, this laser is not resonant with the transition in ^{87}Sr. Our conclusion is that only the isotope ^{88}Sr with $I = 0$ is concerned by the measurements.

APPENDIX B

THE PREPARATION OF THE CIRCULAR RYDBERG STATE OF STRONTIUM VIA AN ADIABATIC PASSAGE

The Rabi rf pulse is not the only technique allowing us to access the circular Rydberg state of a given manifold. We briefly present here an alternative strategy, based on an adiabatic passage accomplishing the same task and starting from the same starting level as the Rabi rf pulse. However, the adiabatic passage is not in use to get the results mentioned in this work, given the much shorter duration of the Rabi pulse. Unfortunately, the adiabatic passage takes 11 μs, thus reducing the time available for the ionic-core manipulation.

The strategy to circularize via the adiabatic passage is detailed in [69] for the case of Rubidium. The core of that technique is ramping the amplitude of the electric field applied to the atoms across that value making the $|51^1G_4, m_{l_1} = +2\rangle \rightarrow |51c\rangle$ transition resonant with a single-frequency, rf pulse. This pulse has a trapezoidal envelope and obviously share the same starting time and duration as the electric field ramp.

Figure B.1 presents the sequence of our circularization to the $|51c\rangle$ state of Strontium via an adiabatic passage. The beginning of the sequence emulates that of the Rabi passage. We first laser excite $|52^1F_3, m_{l_1} = +2\rangle$ and transfer the population to $|51^1G_4, m_{l_1} = +2\rangle$. Next, we ramp the vertical electric field while applying a long rf pulse. An adiabatic passage performed as for Rubidium, with only one ramp of the vertical electric field, is not efficient. We opt for a triple ramp (the first is 2 μs long, the intermediate one 5 μs and the last one 1 μs), which makes the preparation of the circular state more adiabatic. The variation of the electric field is coupled with a rf pulse long ~ 8 μs, resonant at 110 MHz, switched on and off with two ramps of 1 μs each. As a final step, we set the electric field back to that value used for the calibration of the probe for the

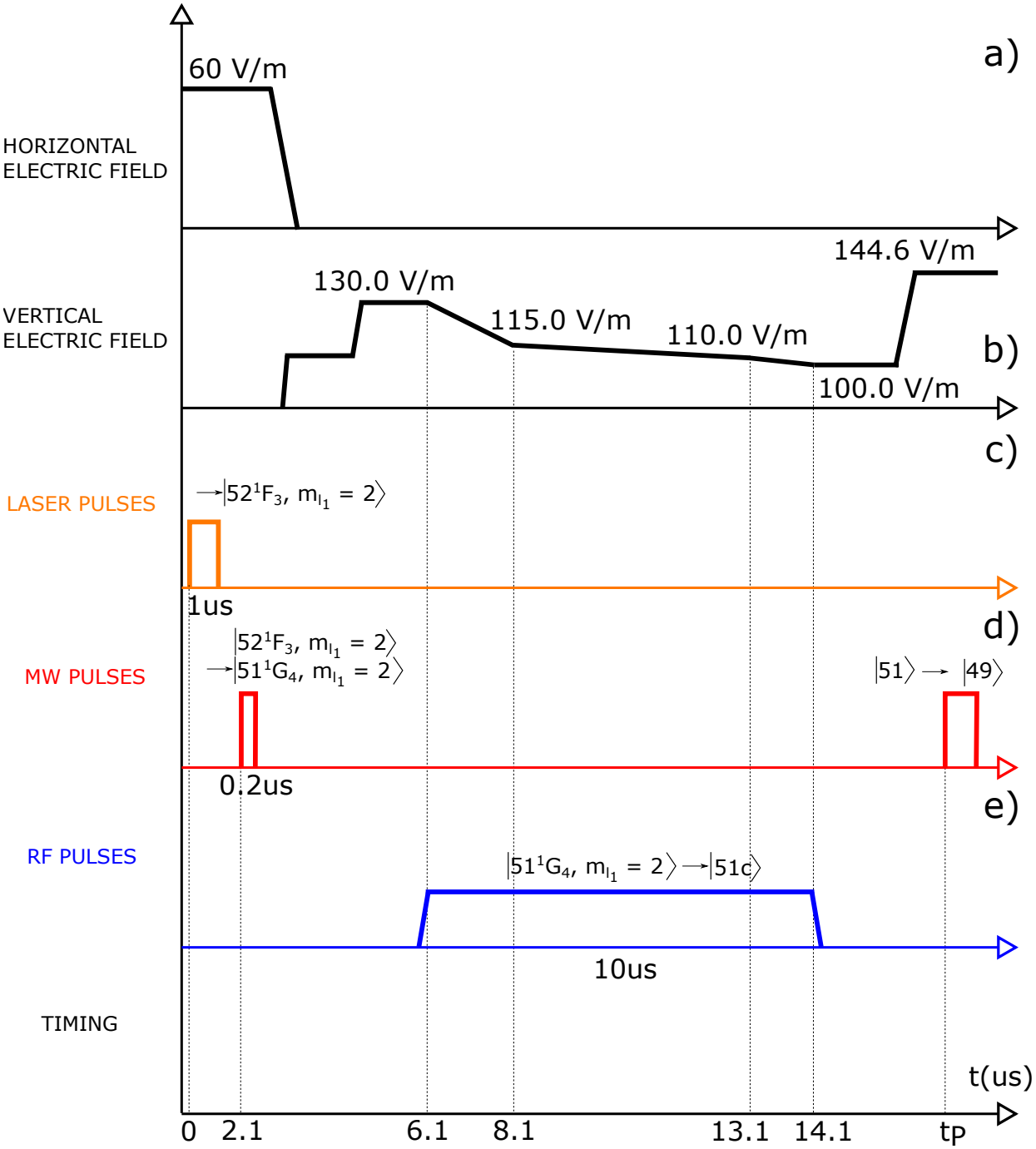

Figure B.1: Sequence or laser, MW, rf and static electric fields used to prepare $|51c\rangle$ via an adiabatic passage.

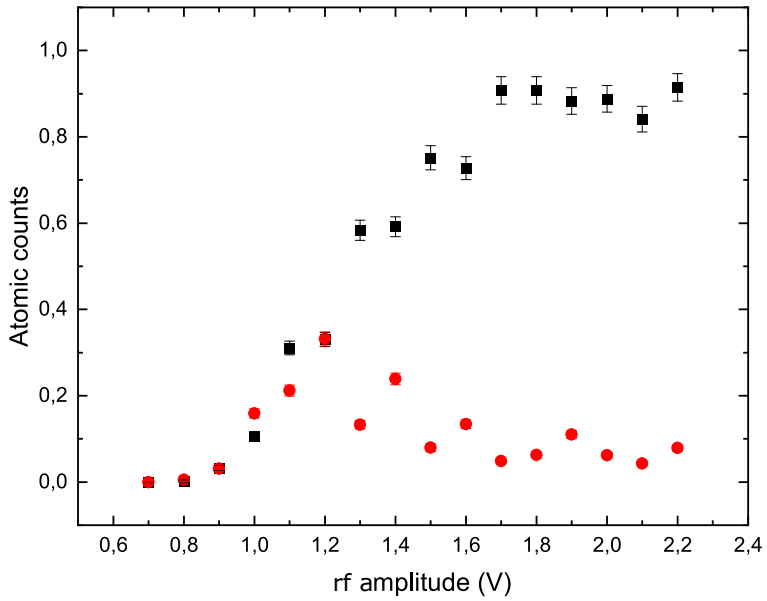

Figure B.2: Scan of the amplitude of the rf pulse transferring the atoms to $|51c\rangle$ with an adiabatic evolution. We detect the populations of $|51c\rangle$ (black points) and $|51, n_1 = 0, m_{l_1} = 49\rangle$ (red points).

circular state. We apply the MW probe and measure the circular population transferred from $|51^1G_4, m_{l_1} = +2\rangle$.

Figure B.2 presents the results of the circularization via the adiabatic passage. We measure the populations of $|51c\rangle$ and $|51, n_1 = 0, m_{l_1} = 49\rangle$, by use of the respective probes, as a function of the rf amplitude. This quantity is expressed in terms of the voltage delivered by the waveform generator to the rf synthesizer. We normalize the atomic counts with respect to the population of $|51^1G_4, m_{l_1} = +2\rangle$.

APPENDIX C

LASER SPECTROSCOPY FOR THE IDENTIFICATION OF THE RESONANCE FREQUENCIES OF THE CORE ELECTRON

The manipulations of the ionic-core electron require us to measure the atomic transition frequencies between the $|5s_{1/2}\rangle$, $|5p_{1/2}\rangle$ states and between the $|4d_{3/2}\rangle$, $|5p_{1/2}\rangle$ states. We perform laser spectroscopy in order to know the resonances of the transitions between all these levels and lock accordingly the frequency of the 422 nm and 1092 nm laser beams.

C.1 The $|5s_{1/2}\rangle \rightarrow |5p_{1/2}\rangle$ resonance frequency of the core

We start by accessing the Rydberg state $|51^1G_4, m_{l_1} = +2\rangle$ and increase (decrease) the vertical (horizontal) component of the electric field. The vertical component is set to an high value (> 200 V/m) to lift the degeneracy of the states composing the Rydberg ladder. Next, we apply the 422 nm laser beam and sweep its frequency via an EOM. We measure the number of Rydberg atoms in $|51^1G_4, m_{l_1} = +2\rangle$ by direct ionization.

The interaction of the laser beam with the atoms, when it is resonant with the $|5s_{1/2}\rangle \rightarrow |5p_{1/2}\rangle$ transition, causes autoionization. This event results in a reduction of the number of Rydberg atoms recorded when the 422 nm laser in on resonance with the $|5s_{1/2}\rangle \rightarrow |5p_{1/2}\rangle$ transition. The measurement shows the signal drop in correspondence with the resonance frequency of the 422 nm laser ($\sim$ 710.9618 THz) (figure C.1). On the contrary, the interaction of the laser beam with the atoms, when out of resonance, has no consequences on the atomic counts.

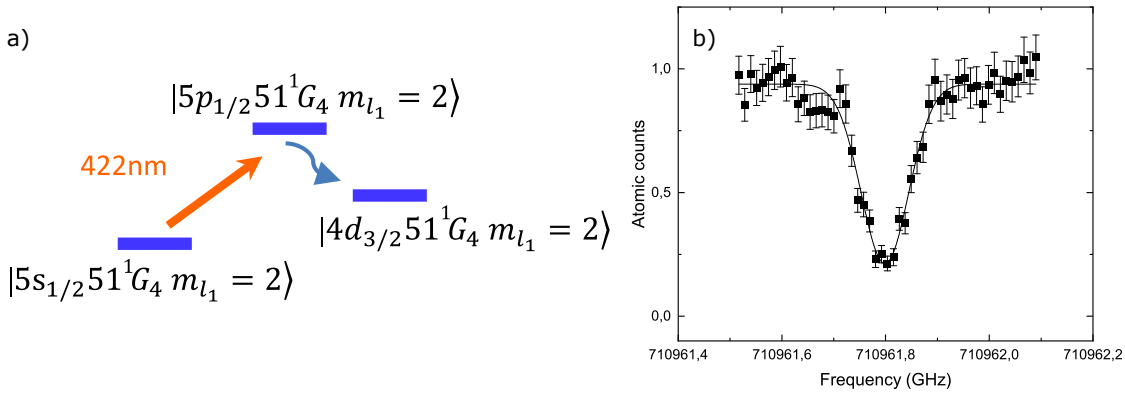

Figure C.1: a) Manipulation of the ionic-core electron. b) Scan of the 422 nm laser frequency on the atoms prepared in the $|51^1G_4, m_{l_1}=+2\rangle$ state and drop of the atomic counts (black points) due to autoionization. The solid line is a Gaussian fit.

C.2 The $|4d_{3/2}\rangle \rightarrow |5p_{1/2}\rangle$ resonance frequency of the core

The 422 nm laser beam brings the population to the $|5p_{1/2}, nl_1\rangle$ state. There, the atoms autoionize. When considering a high l_1 though, we expect some atoms to decay in the metastable $|4d_{3/2}, nl_1\rangle$ states. To remove the atoms from the metastable $|4d_{3/2}\rangle$ trapping states, we can apply the 1092 nm repumper laser beam. To that end, we must know the resonance frequency of the $|4d_{3/2}, nl_1\rangle \rightarrow |5p_{1/2}, nl_1\rangle$ transition to fix the frequency of the 1092 nm laser. Standard laser spectroscopy is again applied to determine the resonance frequency of the transition.

We consider the situation where the core excitation to the $|5p_{1/2}\rangle$ state is performed with the outer electron in a low-m_{l_1} Rydberg state. The application of the repumper brings the population from $|4d_{3/2}, nl_1\rangle$ back to $|5p_{1/2}, nl_1\rangle$ only if the spontaneous decay to $|4d_{3/2}, nl_1\rangle$ took place. Since we deal with low-l_1 states, the autoionization is much faster than the decay, resulting in an immediate autoionization of all atoms. This fact prevents the repumper from having any effect. On the other hand, testing the autoionization effect on an high-m_{l_1} state can be hard since there is negliglible autoionization. Thus, it would be also hard to see an action of the repumper. Our strategy is therefore to prepare the outer electron within an intermediate Rydberg state along the ladder. This state is less likely to autoionize before the spontaneous decay between the $|5p_{1/2}\rangle$ and the $|4d_{3/2}\rangle$ states of the core occurs.

We apply a σ+, 52 ns long rf pulse producing a spin-coherent-state, centered on $|5s_{1/2}, n=51, n_1=0, m_{l_1}=12\rangle$. Next, we scan the frequency of a 0.7 μs, MW pulse across a span including the frequencies of the two-photon transitions between the spin-coherent-state and the $\hat{\mathbf{J}}_1$ ladder of the $n=49$ manifold (figure C.2a). The power of the MW source is calibrated so as to maximize the transfer rate on these transitions. We set the MW frequency on the central $|5s_{1/2}, n=51, n_1=0, m_{l_1}=12\rangle \rightarrow |5s_{1/2}, n=49, n_1=0, m_{l_1}=10\rangle$ transition. We have now a probe

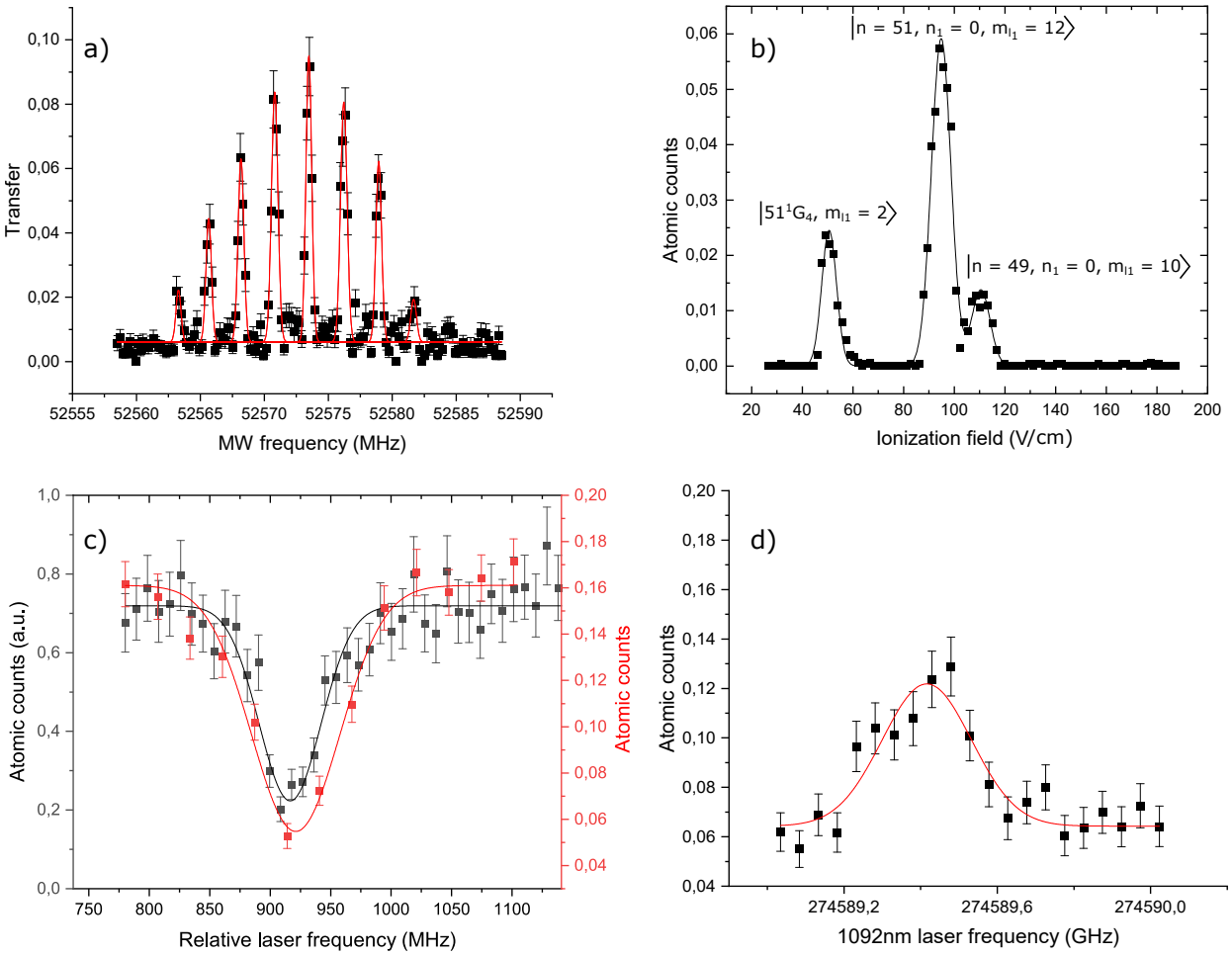

Figure C.2: Setting of the resonance frequency of the 1092 nm laser. a) MW spectrum of the transition between a spin-coherent-state prepared along the circularization ladder and another in the $n = 49$ manifold. b) Ionization signals of the atoms in the $|5s_{1/2}, n = 51, n_1 = 0, m_{l_1} = 12\rangle$ state (central, bell-shaped signal) and in the $|5s_{1/2}, n = 49, n_1 = 0, m_{l_1} = 10\rangle$ state (right, bell-shaped signal). Some atoms (left, bell-shaped signal) are not transferred by the rf pulse. c) Scan of the 422 nm laser frequency on $|5s_{1/2}, n = 51, n_1 = 0, m_{l_1} = 12\rangle$ (red points) and comparison of the resonance frequency with that measured when working with $|5s_{1/2}, n = 51, n_1 = 0, m_{l_1} = 2\rangle$ (black points). d) Scan of the 1092 nm laser frequency and detection of the atomic counts in $|5s_{1/2}, n = 51, n_1 = 0, m_{l_1} = 12\rangle$ (black points). All solid lines are Gaussian fits.

for the $|5s_{1/2}, n = 51, n_1 = 0, m_{l_1} = 12\rangle$ state (figure C.2b).

After accessing $|5s_{1/2}, n = 51, n_1 = 0, m_{l_1} = 12\rangle$, we apply the 422 nm laser beam and scan its frequency. We see the atoms autoionizing as already done for $|51^1G_4, m_{l_1} = 2\rangle$. We compare the resonance frequency of the core $|5s_{1/2}\rangle \rightarrow |5p_{1/2}\rangle$ transition when the Rydberg electron is prepared in two different m_{l_1} states (figure C.2c). The experiment does not evidence a strong difference in the resonance frequency when the Rydberg electron is in two different m_{l_1} states. For a simplicity of the laser frequency locking, we keep the same value of the resonance frequency used when testing the autoionization for $|51^1G_4, m_{l_1} = 2\rangle$. Finally, we keep the 422 nm laser in resonance, apply the repumper at maximum power, 19.2 mW, and scan its frequency while monitoring the population of the $|5s_{1/2}, n = 51, n_1 = 0, m_{l_1} = 12\rangle$ state by use of the probe. We observe an increase of the number of atoms detected around 274.5894 THz. This is the laser frequency resonantly driving the $|4d_{3/2}\rangle \rightarrow |5p_{1/2}\rangle$ core transition and preserving some atoms from the autoionization (figure C.2d).

APPENDIX D

CALIBRATION OF MW PROBES FOR THE DISCRIMINATION OF SINGLET AND TRIPLET STATES

We need to determine the frequency of two MW probes enabling us to discriminate between the triplet and singlet states. Calibrating them by using two atomic transitions between high-l_1 states is not possible. Singlet and triplet states with high-l_1 present the same transition frequencies, since the exchange energy is zero. We must forcefully opt for two atomic transitions between low-l_1 states. On the other hand, populating a triplet state is possible only by using the leak from the $|5p_{1/2}\rangle$ state, which is accessed via a 422 nm pulse. However, exciting the core when the outer electron is directly prepared in a low-l_1 state causes the autoionization of the atom. Therefore, the only option remaining is populating the triplet states when the circular state is prepared, thus guaranteeing the survival of the Rydberg electron to the autoionization effect, and only later diminishing its l_1 by decircularization.

We prepare two sequences of events to be applied on the atoms. Both involve the circularization and the decircularization. Only one of them (figure D.1) presents the excitation of the core between the rf pulses. We record the MW spectrum near the transition $|5s_{1/2}, n = 51, n_1 = 0, m_{l_1} = 2\rangle \rightarrow |5s_{1/2}, n = 49, n_1 = 0, m_{l_1} = 1\rangle$. This scan is performed at 144.6 V/m, as for all the other probes.

Figure D.2a presents the navigation in the Hilbert space following the interaction of the atoms with the sequence of events applied to calibrate the MW probes. Figure D.2b presents the number of atoms detected in $|5s_{1/2}, n = 49, n_1 = 0, m_{l_1} = 1\rangle$, as a function of the MW frequency. We observe a single peak at $\nu_{MW} = 52.4678$ GHz, when the 422 nm laser pulse is not applied. It corresponds to the transition from the $|5s_{1/2}, n = 51, n_1 = 0, m_{l_1} = 2\rangle$ to the $|5s_{1/2}, n = 49, n_1 = 0, m_{l_1} = 1\rangle$ singlet states. We observe an additional transfer peak at $\nu_{MW} = 52.4728$ GHz, when the 422 nm laser

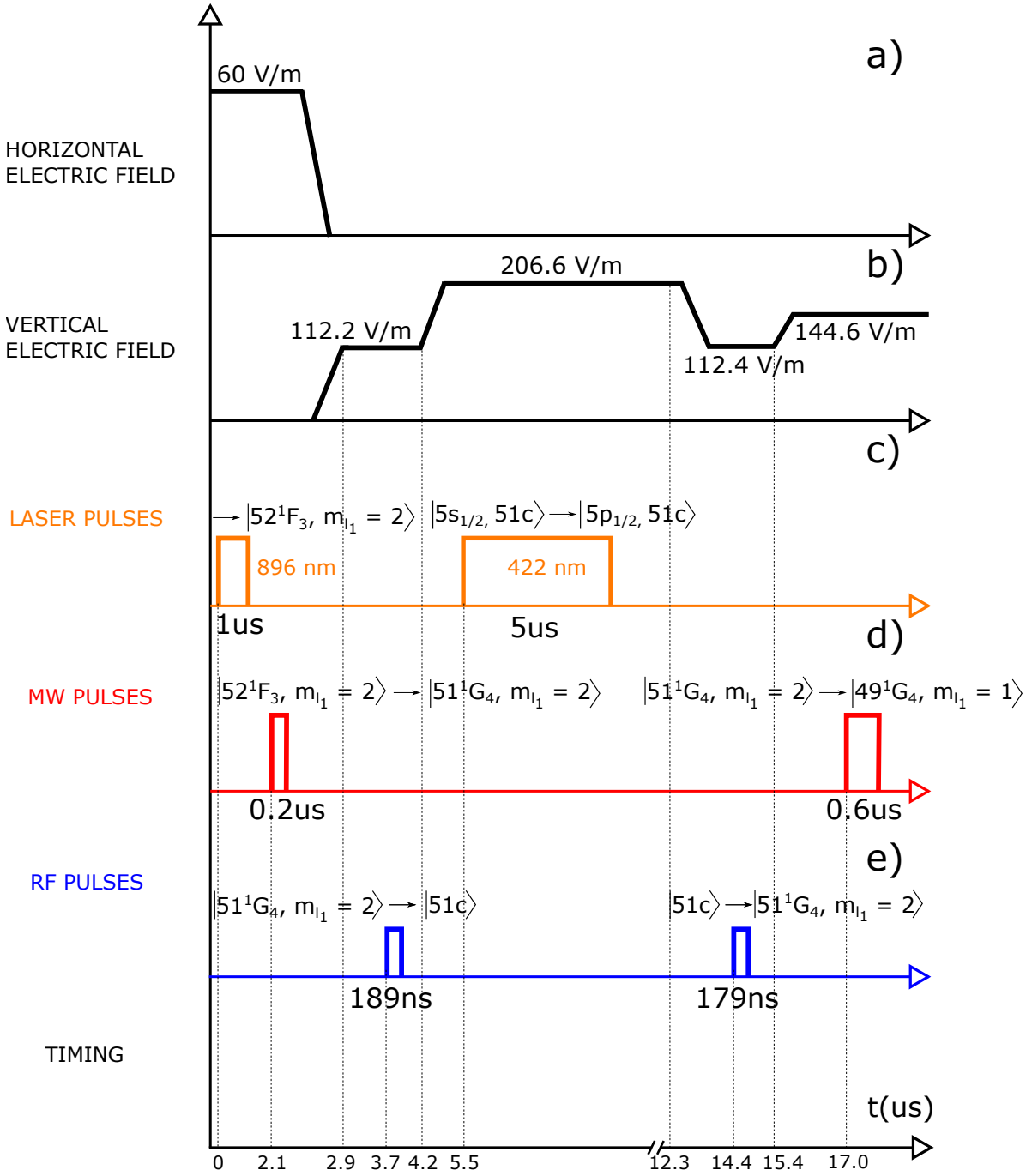

Figure D.1: Sequence of laser, MW, rf and static electric fields used to calibrate the low-l_1 probes.

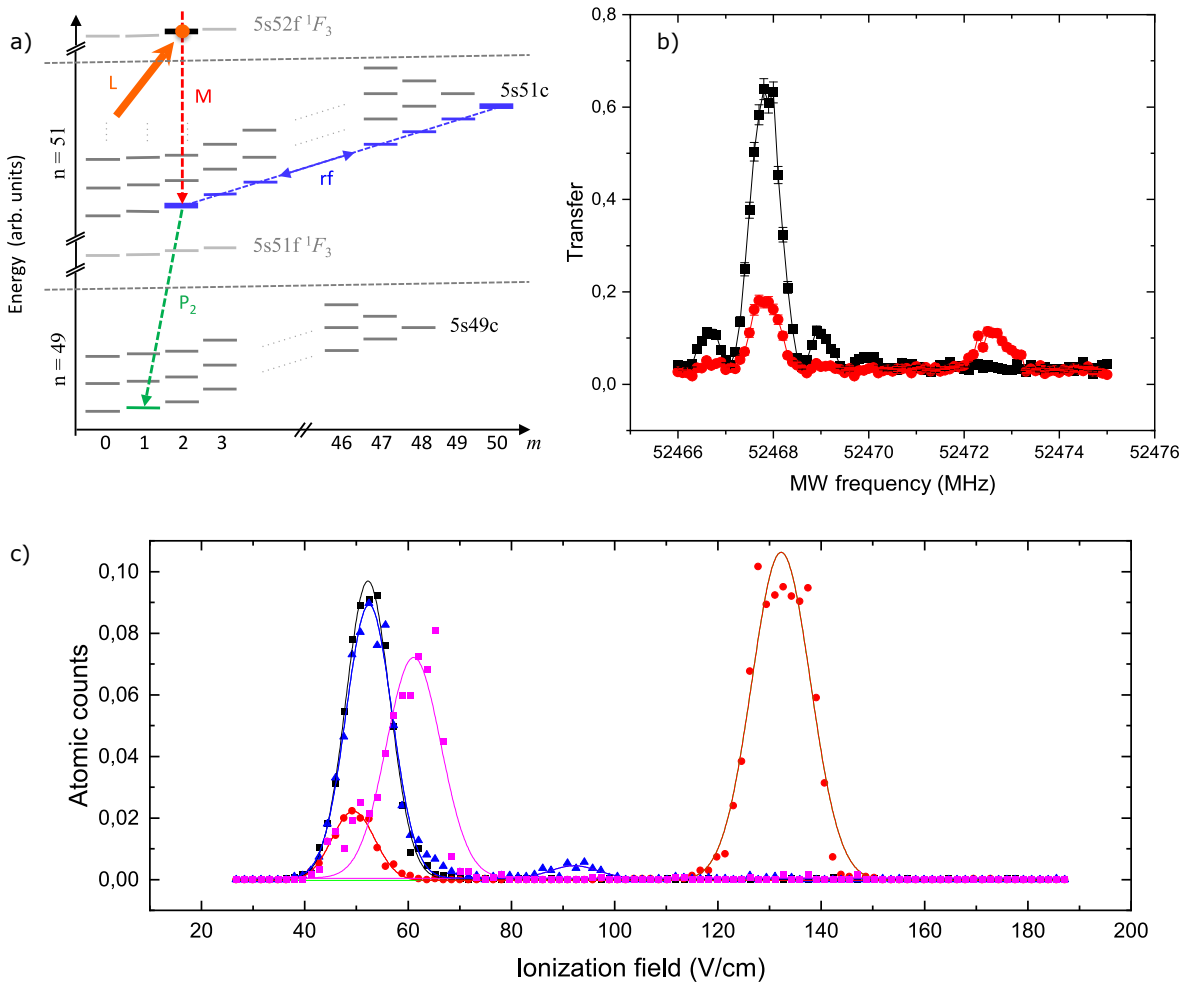

Figure D.2: a) Navigation in the Hilbert space. b) MW spectrum of the $|5s_{1/2}, n = 51, n_1 = 0, m_{l_1} = 2\rangle \rightarrow |5s_{1/2}, n = 49, n_1 = 0, m_{l_1} = 1\rangle$ transition when the 422 nm laser excites (red points) or not (black points) the core. Red data show two peaks and we interpret the right one as that of the triplet state, the left one as that of the singlet state. Solid lines are Gaussian fits of the data. c) Ionization signal before the circularization (black data), after the circularization (red data, with some atoms ionizing at around 50 V/cm, not transferred by the rf field, and some circularized), after the decircularization (blue data) and after the decircularization followed by the MW probe for the singlet state (magenta data). Solid lines are Gaussian fits.

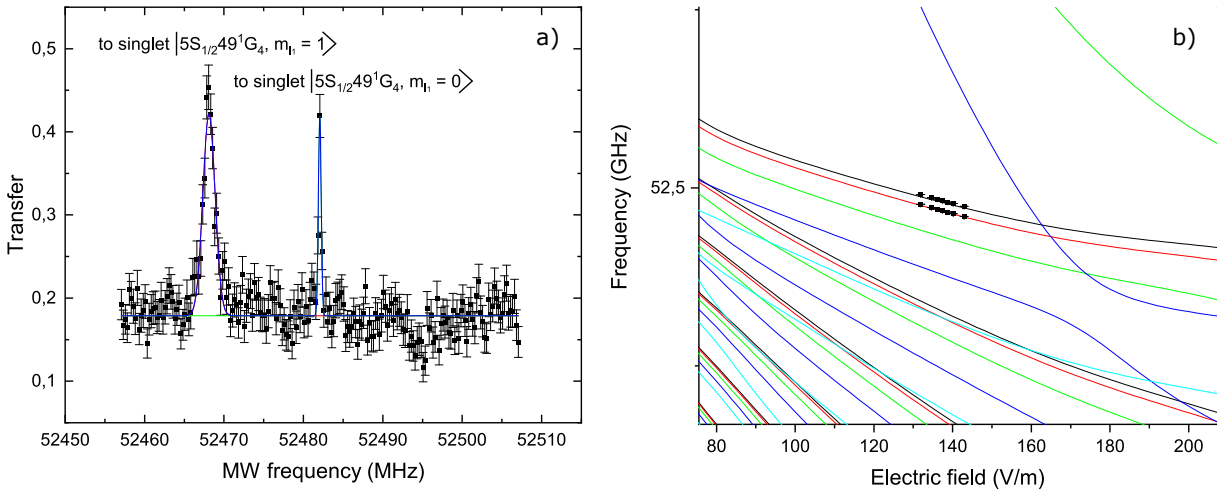

Figure D.3: a) MW spectra of the $|51^1G_4, m_{l_1} = 2\rangle \rightarrow |49^1G_4, m_{l_1} = 0\rangle$ and $|51^1G_4, m_{l_1} = 2\rangle \rightarrow |49^1G_4, m_{l_1} = 1\rangle$ transitions. Solid lines are Gaussian fits. b) Stark diagram for the $|49^1G_4\rangle$ set of states (lines. Black: $|49^1G_4, m_{l_1} = 0\rangle$, red: $|49^1G_4, m_{l_1} = 1\rangle$, green: $|49^1G_4, m_{l_1} = 2\rangle$, blue: $|49^1G_4, m_{l_1} = 3\rangle$) and experimental data (points). The zero is set at the energy of $|51^1G_4, m_{l_1} = +2\rangle$.

is applied on the atoms before the decircularization. We attribute it to the transition between the $|5s_{1/2}, n = 51, n_1 = 0, m_{l_1} = 2\rangle$ and $|5s_{1/2}, n = 49, n_1 = 0, m_{l_1} = 1\rangle$ triplet states. The MW pulse duration is set to 0.6 μs after a Rabi experiment (undisplayed here). It is too short to resolve the atomic transition frequencies between the triplet states of the $n = 51$ manifold and those, chosen as targets of the triplet probe, in the $n = 49$ manifold. Figure D.2c shows the decircularization process and the transfer from the $n = 51$ to the $n = 49$ manifold, caused by the probe, on the ionization signal. First, it proves that the decircularization brings back the atoms from the circular state to a low-l_1 Rydberg state (blue data). Second, it shows that the probe transfers the decircularized population to another state, whose ionization field is far from that of the level accessed after the decircularization (pink data).

The identification of the transfer peaks is done via the Stark diagrams. We record the frequency of the singlet transition $|5s_{1/2}, n = 51, n_1 = 0, m_{l_1} = 2\rangle \rightarrow |5s_{1/2}, n = 49, n_1 = 0, m_{l_1} = 1\rangle$, together with the one of $|5s_{1/2}, n = 51, n_1 = 0, m_{l_1} = 2\rangle \rightarrow |5s_{1/2}, n = 49, n_1 = 0, m_{l_1} = 0\rangle$, (figure D.3a). We do this for several electric fields. The dependencies of the two transition frequencies follow those predicted by the Stark diagrams. Figure D.3b shows the simulations of the Stark effect for the $|49G\rangle$ family of states and the experimental data.

APPENDIX E

CALIBRATION OF THE DURATION OF A SHORT LASER PULSE DEPLETING THE $|5s_{1/2},51c\rangle$ STATE

The 422 nm pulse used to study the autoionization effect and to calibrate the core selective MW probes were 5 - 7 μs long respectively. The sequences presented in chapter 4 involve the application of two repumper pulses and occasionally of a MW pulse at the electric field amplitude where the 422 nm pulse is set. It is therefore important to reduce the duration of the 422 nm pulse to save time for the repumper and the MW. On the other hand, we do not want to lose the efficiency of the depletion of the $|5s_{1/2},51c\rangle$ state.

In order to have a good efficiency of depletion and a shorter pulse, we circularize, excite the core with a 422 nm laser pulse at 9 mW and measure the amount of circular atoms with unexcited core as a function of the duration of the 422 nm pulse.

Figure E.1 shows the result of this measurement. When the repumper is off, we see that the amount of atoms in $|5s_{1/2},51c\rangle$ becomes low for a duration > 2 μs (and then saturates at 5%). This is the duration that we choose for the 422 nm pulse to optically pump the atoms in the $|4d_{3/2}\rangle$ states. Note that, when the duration of the 422 nm pulse exceeds 2 μs, the transfer of the atoms repumped in $|5s_{1/2},51c\rangle$ saturates. In the case of vertical polarization of the repumper, this happens at a transfer of 0.4. It is close to 0.5, the expected value after that the optical pumping distributes the population equally in $|4d_{3/2}|m_{j_2}| = 1/2,51c\rangle$ and $|4d_{3/2}|m_{j_2}| = 3/2,51c\rangle$ and the repumper acts on the only $|4d_{3/2}|m_{j_2}| = 1/2,51c\rangle$. The mismatch with such an ideal case is due to the power of the repumper which was low due to experimental limitations. In the case of horizontal polarization, we reach the saturation of transferred atoms at 0.65, away from the 1.00 ideal case due to the same problem of laser power at the moment of the experiment.

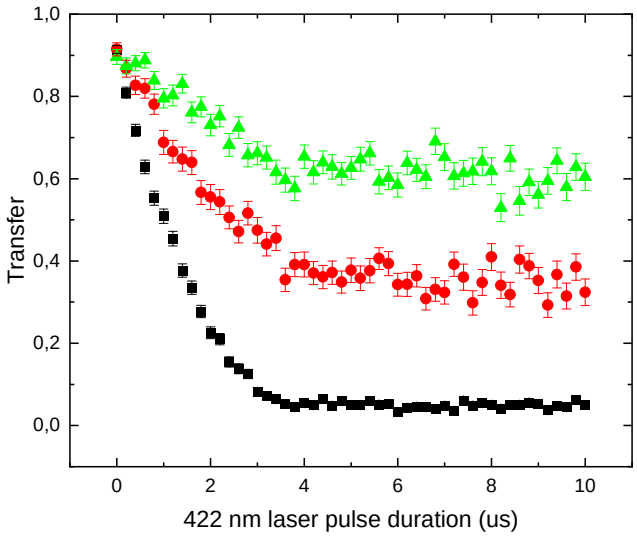

Figure E.1: Scan of the duration of the 422 nm laser pulse, when the repumper is off (black data) or on (red data are for an horizontal polarization of the repumper, green data for a vertical polarization).

APPENDIX F

IDENTIFICATION OF THE ELLIPTICAL RYDBERG STATE ACCESSED VIA A RADIO-FREQUENCY PULSE OF DURATION τ

A $\sigma+$ polarized, resonant radio-frequency pulse prepares a spin-coherent-state along the Rydberg ladder of a given manifold. Notably, the magnetic quantum numbers of the elliptical Rydberg states composing the spin-coherent-state depend on the duration τ of the radio-frequency pulse. We present here an experiment leading us to identify which is the dominant elliptical component of the spin-coherent-state as a function of τ.

F.1 Principle of the experiment

When preparing the spin-coherent-state, the average magnetic quantum number $\langle m_{l_1} \rangle$ of the Rydberg components reads

$$\langle m_{l_1} \rangle = \frac{j_{1,max}}{2}\Big(1+\cos\Omega t\Big), \tag{F.1}$$

where $j_{1,max} = 50$ is the maximum j_1 associated to the Rydberg ladder, as presented in chapter 1, and Ω is the Rabi frequency. We need the experimental value of Ω to understand which elliptical states compose the spin-coherent-state. A first indication on the value of Ω is given by the Rabi passage presented in chapter 2. We extract $\Omega = 2\pi \cdot (2.8832 \pm 0.0048)$ MHz from figure 2.21a. Unfortunately, when inserting this value in (F.1), we cannot fit well the data of figure 4.17c.

We opt for another strategy to get the Rabi frequency. The main feature of this new method consists of using two rf pulses, sharing the same power and frequency, instead of one. The first pulse has duration τ, the other $\tau_{rec} = 189$ ns $-\tau$, where 189 ns is the optimal duration of the Rabi pulse performing the circularization. We apply the first rf pulse on a low-m_{l_1} state of the

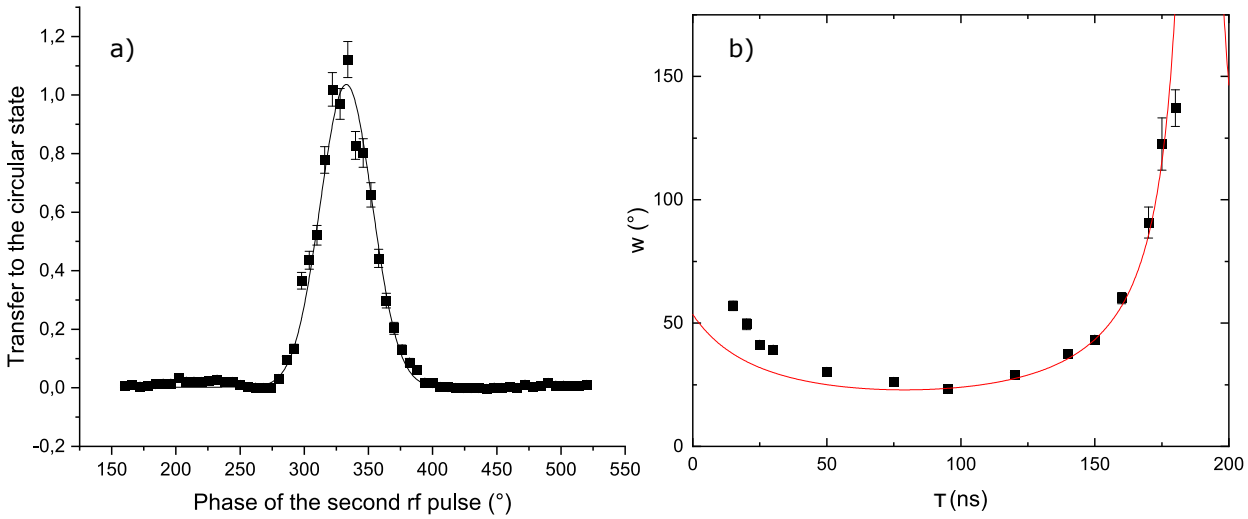

Figure F.1: Phase-sweep experiment for the identification of the Rabi frequency. a) Phase sweep of the second rf pulse and measurement of the circular state for $\tau = 25$ ns and $\tau_{rec} = 164$ ns. Black squares are experimental data, the solid line is a Gaussian fit. b) Phase width w as a function of τ (experimental points) and fit of the evolution (solid line).

circularization ladder. This implies to rotate the Rydberg state across the Bloch sphere via a rotation operator $R(\theta, 0)$. In this way, we prepare a spin-coherent-state. We let its phase evolve for a certain amount of time and apply a second rf pulse, corresponding to a rotation operator $R(\theta, \phi_{rf})$, to conclude the circularization. Notably, the dispersion of the phase in the waiting time between the two pulses depends on which spin-coherent-state is accessed via the first rf pulse only. It is a function of $\sin(\Omega(189-\tau))$. Our goal is recording that dispersion of phase by monitoring the number of circular atoms prepared, as a function of ϕ_{rf}, at the end of the sequence. We do this for several values of τ and extract the width w of the circular population distribution at every repetition of the experiment. This reads

$$w = \sqrt{\left(\frac{2}{\sqrt{\frac{j_{1,max}}{2}}} \cdot \frac{180}{\pi \sin(\Omega(189-\tau))}\right)^2 + \xi^2}, \tag{F.2}$$

where ξ takes into account the noise in our experiment. We are therefore going to measure w to deduce the Rabi frequency.

F.2 Experimental result

The experiment is divided into three parts. We start by splitting the rf pulse performing the circularization in two, $\sigma+$ polarized rf pulses with square envelopes. To produce them, we employ two synthesizers, both connected to the same ring electrodes inside the cryostat. One pulse is prepared by the synthesizer H, the other by the synthesizer N. Each synthesizer imposes a

frequency (equal for the two pulses), a power and a phase to the rf pulse produced. The duration of each pulse is assigned by us. The delay between the two pulses is 10 ns. Next, we apply the pair of rf pulses on the atoms and prepare the circular state $|51c\rangle$. Finally, we measure the circular population with a MW probe, while sweeping the phase of the second rf pulse. Note that, since we use different synthesizers, the phase sweep of the second rf pulse does not affect the first one.

Figure F.1a presents the result of this experiment. We record the circular population as a function of the phase of the second rf pulse and fit the signal via a Gaussian lineshape. We are interested in the phase width of the fit. We want it to be as precise as possible to estimate the width, so as to study its evolution as a function of τ to deduce a new value of the Rabi frequency. This fact motivates the very thin phase step of the sweep and the high number of experimental data recorded. The same procedure is repeated for different values of τ and τ_{rec} but always keeping the same delay between the pulses. Figure F.1b shows the normalized phase width of the circular state signal as a function of τ. The agreement between the data recorded when $\tau > 70$ ns and the theoretical formula of the phase width is met for $\Omega = 2\pi \cdot 2.28$ MHz. We insert this value in equation (F.1) to obtain equation (4.31) and finally convert τ into $\langle m_{l_1} \rangle$.

BIBLIOGRAPHY

[1] M. Saffman, T. G. Walker, K. Mölmer, Quantum information with Rydberg atoms, *Reviews of Modern Physics*, **82**, 2313, 2010

[2] H. Fan, S. Kumar, J. Sedlacek, H. Kbler, S. Karimkashi, and J. P. Shaffer, Atom based RF electric field sensing, *Journal of Physics B: Atomic, Molecular, Optical Physics*, **48**, 202001, (2015)

[3] A. Facon, E. -K. Dietsche, D. Grosso, S. Haroche, J.-M. Raimond, M. Brune, and S. Gleyzes, A sensitive electrometer based on a Rydberg atom in a Schrödinger-cat state, *Nature*, **535**, 262-265, (2016)

[4] H. Labuhn, D. Barredo, S. Ravets, S.de Léséleuc, T. Macr, T. Lahaye, and A. Browaeys, Tunable two dimensional arrays of single Rydberg atoms for realizing quantum Ising models, *Nature*, **534**, 667–670, (2016)

[5] H. Bernien, S. Schwartz, A. Keesling, H. Levine, A. Omran, H. Pichler, S. Choi, A. S. Zibrov, M. Endres, M. Greiner, V. Vuletic, and M. D. Lukin, Probing many body dynamics on a 51-atom quantum simulator, *Nature*, **551**, 579–584, (2017)

[6] Sabrina Patsch, Daniel M. Reich, Jean-Michel Raimond, Michel Brune, Sébastien Gleyzes, and Christiane P. Koch, Fast and accurate circularization of a Rydberg atom, *Physical Review A*, **97**, 053418, (2018)

[7] Arthur Larrouy, Sabrina Patsch, Rémi Richaud, Jean-Michel Raimond, Michel Brune, Christiane P. Koch, and Sébastien Gleyzes, Fast Navigation in a Large Hilbert Space Using Quantum Optimal Control, *Physical Review X*, **10**, 02105, (2020)

[8] A. Omran, H. Levine, A. Keesling, G. Semeghini, T. T. Wang, S. Ebadi, H. Bernien, A. S. Zibrov, H. Pichler, S. Choi, J. Cui, M. Rossignolo, P. Rembold, S. Montangero, T. Calarco, M. Endres, M. Greiner, V. Vuletić, and M. D. Lukin, Generation and manipulation of Schrödinger cat states in Rydberg atom arrays, *Science*, **365**, 570-574, (2019)

[9] F. B. Dunning, T. C. Killian, S. Yoshida, and J. Burgdörfer, Recent advances in Rydberg physics using alkaline-earth atoms, *Journal of Physics B: Atomic,Molecular, Optical Physics*, **49**, 112003, (2016)

[10] D. Leibfried, C. Roos, P. Barton, H. Rohde, S. Gulde, A. B. Mundt, G. Reymond, M. Lederbauer, F. Schmidt-Kaler, J. Eschner, and R. Blatt, Experiments towards quantum information with trapped Calcium ions, *AIP Conference Proceedings*, **551**, 130, (2001)

[11] M. A. Sepiol, A. C. Hughes, J. E. Tarlton, D. P. Nadlinger, T. G. Ballance, C. J. Ballance, T. P. Harty, A. M. Steane, J. F. Goodwin, and D. M. Lucas, Probing Qubit Memory Errors at the Part-per-Million Level, *Physical review letters*, **123**, 110503, (2019)

[12] B. Merkel, K. Thirumalai, J. E. Tarlton, V. M. Schäfer, C. J. Ballance, T. P. Harty, and D. M. Lucas, Magnetic field stabilization system for atomic physics experiments, *The Review of scientific instruments*, **90**, 044702, (2019)

[13] R. Le Targat, L. Lorini, Y. Le Coq, M. Zawada, J. Guéna, M. Abgrall, M. Gurov, P. Rosenbusch, D. G. Rovera, B. Nagórny, R. Gartman, P. G. Westergaard, M. E. Tobar, M. Lours, G. Santarelli, A. Clairon, S. Bize, P. Laurent, P. Lemonde, and J. Lodewyck, Experimental realization of an optical second with strontium lattice clocks, *Nature communications*, **4**, 2109, (2013)

[14] Laurent Stephenson, David Nadlinger, Bethan Nichol, Peter Drmota, Timothy Ballance, Keshav Thirumalai, Joseph Goodwin, David Lucas, and Christopher Ballance, High-rate high-fidelity entanglement of qubits across an elementary quantum network, *Physical Review Letters*, **124**, 110501, (2020)

[15] P. G. Westergaard, J. Lodewyck, L. Lorini, A. Lecallier, E. A. Burt, M. Zawada, J. Millo, and P. Lemonde, Lattice-induced frequency shifts in Sr optical lattice clocks at the 10^{-17} level, *Physical Review Letters*, **106**, 210801, (2011)

[16] J. Lodewyck, P. G. Westergaard, and P. Lemonde, Nondestructive measurement of the transition probability in a Sr optical lattice clock, *Physical Review A*, **79**, 061401(R), (2009)

[17] I. Manai, A. Molineri, C. Fréjaville, C. Duval, P. Bataille, R. Journet, F. Wiotte, B. Laburthe-Tolra, E. Maréchal, and M. Cheneau, Shelving spectroscopy of the strontium intercombination line, *Journal of Physics B: Atomic Molecular and Optical Physics*, **53**, 085005, (2020)

[18] D. Antypas, A. Fabricant, J. E. Stalnaker, K. Tsigutkin, V. V. Flambaum, and D. Budker,

Isotopic variation of parity violation in atomic ytterbium, *Nature Physics*, **15**, 120-123, (2019)

[19] S. Saskin, J. T. Wilson, B. Grinkemeyer, and J. D. Thompson, Narrow-Line Cooling and Imaging of Ytterbium Atoms in an Optical Tweezer Array, *Physical Review Letters*, **122**, 143002, (2019)

[20] Mouktik Raha, Songtao Chen, Christopher M. Phenicie, Salim Ourari, Alan M. Dibos, and Jeff D. Thompson, Optical quantum nondemolition measurement of a single rare earth ion qubit, *Nature communications*, **551**, 1605, (2020)

[21] L. Gil, R. Mukherjee, E. Bridge, M. Jones, and T. Pohl, Spin Squeezing in a Rydberg Lattice Clock, *Physical Review Letters*, **112**, 103601, (2014)

[22] R. Mukherjee, J. Millen, R. Nath, M. P. A. Jones, and T. Pohl, Many-body physics with alkaline-earth Rydberg lattices, *Journal of Physics B: Atomic,Molecular, Optical Physics*, **44**, 184010, (2011)

[23] V. D. Ovsiannikov, A. Derevianko, and K. Gibble, Rydberg Spectroscopy in an Optical Lattice: Blackbody Thermometry for Atomic Clocks, *Physical Review Letters*, **107**, 093003, (2011)

[24] W. Bowden, R. Hobson, P. Huillery, P. Gill, M. P. A. Jones, and I. R. Hill, Rydberg electrometry for optical lattice clocks, *Physical Review A*, **96**, 023419, (2017)

[25] T. Cantat-Moltrecht, R. Cortiñas, B. Ravon, P. Méhaignerie, S. Haroche, J.-M. Raimond, M. Favier, M. Brune, and C. Sayrin, Long-lived circular Rydberg states of laser-cooled Rubidium atoms in a cryostat, *Physical Review Research*, **2**, 022032(R), (2020)

[26] G. Lochead, D. Boddy, D. P. Sadler, C. S. Adams, and M. P. A. Jones, Number-resolved imaging of excited-state atoms using a scanning autoionization microscope, *Physical Review A*, **87**, 053409, (2013)

[27] P. McQuillen, X. Zhang, T. Strickler, F. B. Dunning, and T. C. Killian, Imaging the evolution of an ultracold strontium Rydberg gas, *Physical Review A*, **87**, 013407, (2013)

[28] A. Bounds, N. Jackson, R. Hanley, R. Faoro, E. Bridge, P. Huillery, and M. Jones, Rydberg-Dressed Magneto-optical Trap, *Physical Review Letters*, **120**, 183401, (2018)

[29] J. Wilson, S. Saskin, Y. Meng, S. Ma, A. Burgers, and J. Thompson, Trapped arrays of

alkaline earth Rydberg atoms in optical tweezers, arXiv:1912.08754, (2019)

[30] A. Cooper, J. P. Covey, I. S. Madjarov, S. G. Porsev, M. S. Safronova, and M. Endres, Alkaline-Earth Atoms in Optical Tweezers, *Physical Review X*, **8**, 041055, (2018)

[31] M. Norcia, A. Young, and A. Kaufman, Microscopic Control and Detection of Ultracold Strontium in Optical Tweezer Arrays, *Physical Review X*, **8**, 041054, (2018)

[32] Ivaylo S. Madjarov, Jacob P. Covey, Adam L. Shaw, Joonhee Choi, Anant Kale, Alexandre Cooper, Hannes Pichler, Vladimir Schkolnik, Jason R. Williams, and Manuel Endres, High-fidelity entanglement and detection of alkaline-earth Rydberg atoms, *Nature Physics*, **16**, 857–861, (2020)

[33] J. Millen, G. Lochead, G. R. Corbett, R. M. Potvliege, and M. P. A. Jones, Spectroscopy of a cold strontium Rydberg gas, *Journal of Physics B: Atomic, Molecular, Optical Physics*, **44**, 184001, (2011)

[34] S. Ye, X. Zhang, T. C. Killian, F. B. Dunning, M. Hiller, S. Yoshida, S. Nagele, and J. Burgdörfer, Production of very-high-n strontium Rydberg atoms, *Physical Review A*, **88**, 043430, (2013)

[35] S. Ye, X. Zhang, F. B. Dunning, S. Yoshida, M. Hiller, and J. Burgdörfer, Efficient three-photon excitation of quasi-one-dimensional strontium Rydberg atoms with n ~ 300, *Physical Review A*, **90**, 013401, (2014)

[36] J. Millen, G. Lochead, and M. P. A. Jones, Two-Electron Excitation of an Interacting Cold Rydberg Gas, *Physical Review Letters*, **105**, 213004, (2010)

[37] G. Fields, X. Zhang, F. B. Dunning, S. Yoshida, and J. Burgdörfer, Autoionization of very-high-n strontium Rydberg states, *Physical Review A*, **97**, 013429, (2018)

[38] F. Niyaz, J. Nunkaew, and T. F. Gallagher, Microwave spectroscopy of the Yb 6 s (n + 3) d 6 s n g ,6 s n h, and 6 s n i transitions, *Physical Review A*, **99**, 042507, (2019)

[39] W. E. Cooke, T. F. Gallagher, S. A. Edelstein, and R. M. Hill, Doubly Excited Autoionizing Rydberg States of Sr, *Physical Review Letters*, **40**, 178, (1978)

[40] R. R. Jones, and T. F. Gallagher, Autoionization of high l Ba 6 p 1 / 2 nl states, *Physical Review A*, **38**, 2846, (1988)

[41] L. Pruvost, P. Camus, J. M. Lecomte, C. R. Mahon, and P. Pillet, High angular momentum 6pnl, 6dnl doubly excited Rydberg states of barium, *Journal of Physics B: Atomic,Molecular, Optical Physics*, **24**, 4723-4741, (1991)

[42] D. Wehrli, M. Génévriez, and F. Merkt, Autoionization rates of core-excited magnesium Rydberg atoms in electric fields using the core fluorescence as a reference, *Physical Review A*, **100**, 012515, (2019)

[43] H. Lehec, X. Hua, P. Pillet, and P. Cheinet, Isolated core excitation of high orbital quantum number Rydberg states of ytterbium, *Physical Review A*, **103**, 022806, (2021)

[44] R. G. Hulet, and D. Kleppner, Rydberg Atoms in "Circular" States, *Physical Review Letters*, **51**, 1430, (1983)

[45] A. Signoles, E. Dietsche, A. Facon,D. Grosso, S. Haroche, J. Raimond, M. Brune, and S. Gleyzes, Coherent Transfer between Low-Angular-Momentum, Circular Rydberg States, *Physical Review Letters*, **118**, 253603, (2017)

[46] J. M. Raimond, M. Brune, and S. Haroche, Manipulating quantum entanglement with atoms, photons in a cavity, *Reviews of Modern Physics*, **73**, 565, (2001)

[47] K. Kleinbach, F. Engel, T. Dieterle, R. Lw, T. Pfau, and F. Meinert, Ionic Impurity in a Bose-Einstein Condensate at Submicrokelvin Temperatures, *Physical Review Letters*, **120**, 193401, (2018)

[48] A. Ramos, K. Moore, and G. Raithel, Measuring the Rydberg constant using circular Rydberg atoms in an intensity-modulated optical lattice, *Physical Review A*, **96**, 032513, (2017)

[49] T. Nguyen, J. Raimond, C. Sayrin, R. Cortiñas, T. Cantat-Moltrecht, F. Assemat,I. Dotsenko, S. Gleyzes, S. Haroche, G. Roux, T. Jolicoeur, and M. Brune, Towards Quantum Simulation with Circular Rydberg Atoms, *Physical Review X*, **8**, 011032, (2018)

[50] F. Roussel, M. Cheret, L. Chen, T. Bolzinger, G. Spiess, J. Hare, and M. Gross, Observation of Circular Metastable Doubly Excited States of Barium, *Physical Review Letters*, **65**, 1199-1202, (1990)

[51] F. Meinert, C. Hlzl, M. A. Nebioglu, A. D'Arnese, P. Karl, M. Dressel, and M. Scheffler,

Indium tin oxide films meet circular Rydberg atoms: prospects for novel quantum simulation schemes, *Physical Review Research*, **2**, 023192, (2020)

[52] P.H. Moriya, M.O. Araújo, F. Todão, M. Hemmerling, H. Kessler, R.F. Shiozaki, R. Celistrino Teixeira, and Ph. W. Courteille, Comparison between 403 nm and 497 nm repumping schemes for strontium magneto-optical traps, *Journal of Physics communications*, **2**, 125008, (2018)

[53] Millen James, A cold strontium Rydberg gas, Durham theses, Durham University. Available at Durham E-Theses Online: http://etheses.dur.ac.uk/849 (2011)

[54] R. Feynman, Simulating physics with computers, *Int. J. of Theor. Phys.*, **21**, 467–488, (1982)

[55] S. Lloyd, Universal quantum simulators, *Science*, **273**, 1073-1078, (1996)

[56] I. M. Georgescu, S. Ashhab, and F. Nori, Quantum simulation, *Reviews of Modern Physics*, **86**, 153, (2014)

[57] Ehud Altman, Kenneth R. Brown, Giuseppe Carleo, Lincoln D. Carr, Eugene Demler, Cheng Chin, Brian DeMarco, Sophia E. Economou, Mark A. Eriksson, Kai-Mei C. Fu, Markus Greiner, Kaden R. A. Hazzard, Randall G. Hulet, Alicia J. Kollar, Benjamin L. Lev, Mikhail D. Lukin, Ruichao Ma, Xiao Mi, Shashank Misra, Christopher Monroe, Kater Murch, Zaira Nazario, Kang-Kuen Ni, Andrew C. Potter, Pedram Roushan, Mark Saffman, Monika Schleier-Smith, Irfan Siddiqi, Raymond Simmonds, Meenakshi Singh, I. B. Spielman, Kristan Temme, David S. Weiss, Jelena Vuckovic, Vladan Vuletic, Jun Ye, and Martin Zwierlein, Quantum Simulators: Architectures and Opportunities, *Physical Review X Quantum*, **2**, 017003, (2021)

[58] E. Manousakis, A quantum-dot array as model for 21 copper-oxide superconductors: A dedicated quantum simulator for the many-fermion problem, *J. Low Temp. Phys.* **126**, 1501-1513, (2002)

[59] I. Buluta, and F. Nori, Quantum simulators, *Science*, **326**, 108-111, (2009)

[60] Pascal Scholl, Michael Schuler, Hannah J. Williams, Alexander A. Eberharter, Daniel Barredo, Kai-Niklas Schymik, Vincent Lienhard, Louis-Paul Henry, Thomas C. Lang, Thierry Lahaye, Andreas M. Läuchli, and Antoine Browaeys, Quantum simulation of 2D antiferromagnets with hundreds of Rydberg atoms, *Nature*, **595**, (2021)

[61] Sepehr Ebadi, Tout T. Wang, Harry Levine, Alexander Keesling, Giulia Semeghini, Ahmed Omran, Dolev Bluvstein, Rhine Samajdar, Hannes Pichler, Wen Wei Ho, Soonwon Choi, Subir Sachdev, Markus Greiner, Vladan Vuletić, and Mikhail D. Lukin, Quantum phases of matter on a 256-atom programmable quantum simulator, *Nature*, **595**, 233–238, (2021)

[62] R. G. Cortiñas, M. Favier, B. Ravon, P. Méhaignerie, Y. Machu, J.-M. Raimond, C. Sayrin, and M. Brune, Laser Trapping of Circular Rydberg Atoms, *Physical Review Letters*, **124**, 123201, (2020)

[63] D. Stevens, J. Brochard, and A. M. Steane, Simple experimental methods for trapped-ion quantum processors, *Physical Review A*, **58**, 2750, (1998)

[64] H. Haken and H.C. Wolf, Quantum Mechanics of the Hydrogen Atom, *Springer*, 149-166, (1994)

[65] Kyle W. Martin, Benjamin Stuhl, Jon Eugenio, Marianna S. Safronova, Gretchen Phelps, John H. Burke, and Nathan D. Lemke, Frequency shifts due to Stark effects on a rubidium two-photon transition, *Physical Review A*, **100**, 023417, (2019)

[66] K.J.Kollath and M. C. Standage, Progress in Atomic Spectroscopy Part B, *Hanle W., Kleinpoppen H. (eds)*, 955-997, (1979)

[67] E. K. Dietsche, Quantum sensing with Rydberg Schrödinger cat states, *Ph.D. thesis*, (2017)

[68] A. Signoles, Manipulations cohérentes d'états de Rydberg elliptiques par dynamique Zénon quantique, *Ph.D. thesis*, (2014)

[69] J. Han, Y. Jamil, D. V. L. Norum, P. J. Tanner, and T. F. Gallagher, Rb nf quantum defects from millimeter-wave spectroscopy of cold 85Rb Rydberg atoms *Physical Review A*, **74**, 054502, (2006)

[70] M. L. Zimmermann, M. G. Littman, M. M. Kash, and D. Kleppner, Stark structure of the Rydberg states of alkali-metal atoms, *Physical Review A*, **20**, 2251, (1979)

[71] A. Facon, Chats de Schrodinger d'un atome de Rydberg pour la métrologie quantique, *Ph.D. thesis*, (2015)

[72] C. L. Vaillant, M. P. A. Jones, and R. M. Potvliege, Long-range Rydberg–Rydberg interactions in calcium, strontium and ytterbium, *Journal of Physics B: Atomic Molecular and Optical Physics*, **45**, 135004, (2012)

[73] C. L. Vaillant, M. P. A. Jones, and R. M. Potvliege, Multichannel Quantum Defect Theory of Strontium Rydberg Series, *Journal of Physics B: Atomic Molecular and Optical Physics*, **47**, 155001, (2014)

[74] X.-W. Liu, and Z.-W. Wang, Multichannel quantum-defect theory of lifetimes for highly excited states of atoms: Calculation of Yb lifetimes in the perturbed 6snd^1, ^{3}D$_2$ sequences, *Physical Review A*, **40**, 1838-1842, (1989)

[75] W.E. Cooke and C.L. Cromer, Multichannel quantum-defect theory and an equivalent N-level system, *Physical Review A*, **32**, 2725, (1985)

[76] M.J. Seaton, Quantum defect theory, *Rep. Prog. Phys.*, **46**, 167, (1983)

[77] Ph.D. thesis of Dr. Moriya, Universidade de Sao Paulo.

[78] Master thesis of Ph.D. student Léa Lachaud.

[79] D. J. Berkeland, and M. G. Boshier, Destabilization of dark states and optical spectroscopy in Zeeman degenerate atomic systems, *Physical Review A*, **65**, 033413, (2002)

[80] G. J. Long, Mössbauer Spectroscopy Applied to Inorganic Chemistry, Volume 1, *Modern Inorganic Chemistry*, (1984)

[81] N. Ramsey, Molecular Beams, *Oxford University Press*, (1956)

[82] W. M. Itano, External-Field Shifts of the ^{199}Hg$^+$ Optical Frequency Standard, *Journal of Research of the National Institute of Standards and Technology*, **105**, 829–837, (2000)

[83] K. T. Hecht, The Wigner—Eckart Theorem. In: Quantum Mechanics. *Graduate Texts in Contemporary Physics. Springer, New York, NY*, (2000)

[84] W. M. Itano, Quadrupole moments and hyperfine constants of metastable states of Ca+, Sr+, Ba+, Yb+, Hg+, and Au, *Physical Review A*, **73**, 022510, (2006)

[85] Dansha Jiang, Bindiya Arora, and M. S. Safronova, Electric quadrupole moments of metastable states of Ca+, Sr+, and Ba+, *Physical Review A*, **78**, 022514, (2008)

[86] Chiranjib Sur, K. V. P. Latha, Bijaya K. Sahoo, Rajat K. Chaudhuri, and B. P. Das, Electric quadrupole moments of the D states of Alkaline-Earth-Metal Ions, *Physical Review Letters*, **96**, 193001, (2006)

[87] R. Shaniv, N. Akerman, and R. Ozeri, Atomic Quadrupole Moment Measurement Using Dynamic Decoupling, *Physical Review Letters*, **116**, 140801, (2016)

[88] H. Lehec, X. Hua, P. Pillet, and P. Cheinet, Isolated core excitation of high-orbital-quantum -number Rydberg states of ytterbium, *Physical Review A*, **103**, 022806, (2021)

[89] C. Schwartz, Theory of Hyperfine Structure, *Physical Review*, **106**, 380, (1957)

[90] H. Sunaoshi, Y. Fukashiro, M. Furukawa, M. Yamauchi, S. Hayashibe, T. Shinozuka, M. Fujioka, I. Satoh, M. Wada, and S. Matsuki, A precision measurement of the hyperfine structure of ^{87}Sr+, *Hyperfine Interactions*, **78**, 241–245, (1993)

[91] B. A. Bushaw, and W. Nörtershäuser, Resonance ionization spectroscopy of stable strontium isotopes and ^{90}Sr via $5s^2\ {}^1S_0 \rightarrow 5s5p\ {}^1P_1 \rightarrow 5s5d\ {}^1D_2 \rightarrow 5s^{11}f\ {}^1F_3 \rightarrow$ Sr+, *Spectrochimica Acta Part B Atomic Spectroscopy*, **55**, 1679-1692, (2000)

RÉSUMÉ

Les atomes de Rydberg alcalino-terreux sont des outils très prometteurs pour les technologies quantique. Ils profitent des propriétés remarquables des atomes de Rydberg et, notamment, un énorme couplage aux champs externes ou à d'autres atomes de Rydberg tandis que le noyau ionique conserve un électron optiquement actif. Cependant, les états de Rydberg de faible moment angulaire subissent une auto-ionisation presque immédiate lorsque le noyau est excité. Classiquement, les deux électrons « entrent en collision » et un est expulsé. Cependant, ce n'est pas le cas pour les états circulaires. Ici, nous démontrons que les atomes de Strontium où un électron est dans un état de Rydberg circulaire, avec un noyau excité dans un niveau métastable 4d sont stables pendant plus de quelques millisecondes. Nous vérifions cette propriété pour un noyau ionique soit dans un état 4d, j = 3/2, soit dans un état 4d, j = 5/2. Aussi, nous mesurons la différence d'énergie entre les états 4d métastables de l'électron du noyau ionique, résultant du couplage électrostatique entre les deux électrons de valence, avec l'un préparé dans un état Rydberg. Nous montrons que cette différence d'énergie est fonction des nombres quantiques principaux et magnétiques de l'électron de Rydberg. Nous montrons que le couplage électrostatique entre les deux électrons de valence amène à contrôler l'état de l'un par l'état de l'autre. Cela ouvre la voie à la détection non destructive de l'état de l'atome de Rydberg. L'utilisation de la fluorescence émise par l'électron du cœur permet d'envisager la détection optique selective des états circulaires avec une sensibilité remarquable. Les résultats présentés dans ce travail sont importants dans le cadre de la réalisation d'un simulateur quantique Rydberg, exploitant les états circulaires du Strontium pour construire les qubits.

MOTS CLÉS

Rydberg, Strontium, autoionization, simulation quantique.

ABSTRACT

Alkaline-earth Rydberg atoms are very promising tools for quantum technologies. They benefit from the remarkable properties of Rydberg atoms and, notably, a huge coupling to external fields and to other Rydberg atoms while the ionic core retains an optically active electron. However, low angular-momentum Rydberg states suffer almost immediate autoionization when the core is excited. Classically, the two electrons "collide" and one is expelled. However, this is not the case for circular states. Here, we demonstrate that Strontium circular Rydberg atoms with a core excited in a 4d metastable level are stable for more than a few milliseconds. We verify this property while the ionic core is either in a 4d, j = 3/2 state or a 4d, j = 5/2 state. Furthermore, we measure the energy difference between the Zeeman sublevels of metastable 4d states of the ionic-core electron, resulting from the electric-quadrupole coupling between the two valence electrons, with one prepared in a Rydberg state. We show that that the energy difference is a function of the principal and magnetic quantum numbers of the Rydberg electron. We show that this coupling between the two valence electrons leads to control the state of one depending on the state of the other. This opens the way to detect non-destructively the state of the Rydberg atom. Using the fluorescence emitted by the core electron allows us to envision a selective, optical detection of the circular states with remarkable sensitivity. The results presented in this work are important in the context of the realization of a Rydberg quantum simulator, exploiting the circular states of Strontium to build the qubits.

KEYWORDS

Rydberg, Strontium, autoionization, quantum simulation.